8-8-2024 10:00 AM

Predictive Models of Polymer Composites: A Thesis

Navid Afrasiabian, *Western University*

Supervisor: Colin Denniston, *The University of Western Ontario*

A thesis submitted in partial fulfillment of the requirements for the Doctor of Philosophy degree in Physics

Recommended Citation

Afrasiabian, Navid, "Predictive Models of Polymer Composites: A Thesis" (2024). *Electronic Thesis and Dissertation Repository*. 10368.
https://ir.lib.uwo.ca/etd/10368

Abstract

Predictive models are a powerful tool to understand and improve physical systems. Predictive models not only can be used to improve current materials, but they also gain fundamental understanding of the underlying processes. There are numerous theoretical and numerical models introduced in the field of polymer composites and nanocomposites. Different methods best describe a system at a specific time and length scale. In this thesis, I utilize coarse-grained Molecular Dynamics (CGMD), multiphase-field (MPF), and Lattice Boltzmann (LB) methods to study different aspect of polymer composites and nanocomposites.

Starting at the nanoscale, we study the dispersion and orientation patterns of nanorod-polymer systems using coarse-grained Molecular Dynamics. We particularly focus on the phase behaviour of nanorods in an unentangled polymer melt as a function of the nanorod concentration. The system is comprised of flexible polymer chains and multi-thread nanorods that are equilibrated in the isothermal-isobaric (NPT) ensemble. All interactions are purely repulsive except for those between polymers and rods. Results with attractive vs repulsive polymer–rod interactions are compared and contrasted. The concentration of rods has a direct impact on the phase behavior of the system. At lower concentrations, rods phase separate into nematic clusters, whereas at higher concentrations more isotropic and less structured rod configurations are observed. A detailed examination of the conformation of the polymer chains near the rod surface shows extension of the chains along the director of the rods (especially within clusters). The dispersion and orientation of the nanorods are a result of the competition between depletion entropic forces responsible for the formation of rod clusters, the enthalpic effects that improve mixing of rods and polymer, and entropic losses of polymers interpenetrating rod clusters.

Physical and mechanical properties of semi-crystalline polymers depend on their degree of crystallization and crystal morphology. Producing semi-crystalline material with desired properties is only possible when the crystallization process and structure is well-understood and can be predicted. We introduce a coarse-grained model of polymer crystallization using a multiphase-field approach. The model combines a multiphase-field method, Nakamura's kinetic equation, and the equation of heat conduction for studying microstructural evolution of crystallization under isothermal and non-isothermal conditions. The multiphase-field method provides flexibility in adding any number of phases with different properties making the model effective in studying blends or composite materials. We apply our model to systems of neat PA6 and study the impact of initial distribution of crystalline grains and cooling rate on the morphology of the system. The relative crystallinity (conversion) curves show qualitative agreement with experimental data. We also investigate the impact of including carbon fibers on the crystallization and grain morphology. We observe a more homogeneous crystal morphology around fibers. This is associated with the higher initial volume fraction of crystal grains and higher heat conductivity of the fiber (compared to the polymer matrix). Additionally, we observe that the crystalline grains at the fiber surface grow perpendicular to the surface. This indicates that the vertical growth observed in experiments is merely due to geometrical constraints imposed by the fiber surface and neighbouring crystalline regions.

The production of fiber-reinforced thermoplastics involves processes performed under flow conditions. Therefore, it is crucial to understand the dynamics of fibers in flow to obtain high quality fiber-reinforced composites. We introduce a new LBM where the continuous distribution function is discretized using distribution mass function that in addition to a mean value also has a variance. This introduces extra independent degrees of freedom to recover the second and third moments of Maxwell-Boltzmann equation fully. This eliminates the error terms that appear in the standard LBM and extends the applicability of LBM to compressible flows. The variance terms can further be utilized to incorporate thermal and viscoelastic features. As the variance terms appear as part of the discretization scheme, they consistently appear in the derivation and no ad-hoc manipulation of the equations is required to recover the correct second and third moments. Furthermore, there are only 6 extra terms (or 9 for a non-symmetric general stress tensor) introduced in this model. Thus, we expect the algorithm to be more memory efficient and have shorter runtimes than multi-lattice models.

Keywords: Polymer Composite, Molecular Dynamics, Multiphase-Field, Lattice Boltzmann, Conformational Entropy, Crystal Morphology

Summary for Lay Audience

One approach to addressing issues like global warming and transportation safety is through lightweighting. This involves replacing materials used in vehicles with lighter alternatives without sacrificing performance. Composite materials, which combine the best properties of different substances, enable the creation of high-performance lightweight materials. However, achieving the desired end product requires the testing of diverse ingredient materials and processing techniques. This is financially demanding due to the substantial requirement for materials and labour.

This is where mathematics and technology offer a solution: computer simulations. Computer simulations enable the execution of numerous virtual experiments across a wide range of conditions. This not only enhances our comprehension of the underlying physics that drives the real-world observations, but it also reduces the range of possibilities that must be tested in the laboratory. As a result, they save both material usage and labour hours. In this thesis, I use 3 different simulation methods to study polymer composites (polymers are long and chain-like molecules).

The properties of materials are determined by the behaviour of their molecules. So, it is important to understand how materials work at the molecular level to predict their properties and improve them. In the first simulation, I looked at the shape and arrangement of the molecules in a material that is a mix of a polymer melt and fibers.

In the second simulation, I combined different mathematical models to reproduce how a polymer looks under the microscope when it crystallizes. It is important to understand how crystal regions are distributed in a polymer material because the degree of crystallinity and distribution of the crystals affect the performance of the material.

The production of fiber-reinforced polymers involves the liquid mixture flowing through pipes and/or into molds. Therefore, it is crucial to understand how fibers behave in a flow to obtain high quality fiber-reinforced composites. For the third simulation, I expanded a previous simulation method that only applied to simple fluids like water to account for compressible fluids. The model can be further expanded to reproduce viscoelastic flows like polymers.

Co-authorship statement

The work presented in chapter 2 was done in collaboration with Venkat Balasumbramanian and my supervisor, Colin Denniston. This work has been published in the Journal of Chemical Physics (DOI:10.1063/5.0122174).

The work presented in chapter 3 was done in collaboration with Ahmed Elmoghazy, Juliane Blarr, Benedikt Scheuring, Andreas Prahs, Daniel Schneider, Wilfried V. Liebig, Kay A. Weidenmann, Colin Denniston, and Britta Nestler. The author contributions for this work were as follows: **Navid Afrasiabian:** Conceptualization; investigation; methodology; formal analysis; visualization; project administration; writing - original draft; writing - editing and review **Ahmed Elmoghazy:** Parameter identification; methodology; simulation; visualization; writing - original draft; writing - editing and review **Juliane Blarr:** Experiments; writing - original draft **Benedikt Scheuring:** Parameter identification; experiments; writing - original draft **Andreas Prahs:** Supervision; conceptualization; project administration; methodology; writing - editing and review **Daniel Schneider:** Supervision; Conceptualization; project administration; methodology; writing - original draft **Wilfried V. Liebig:** Supervision; funding acquisition; writing - original draft **Kay A. Weidenmann:** Supervision; funding acquisition; writing - original draft **Colin Denniston:** Supervision; funding acquisition; Conceptualization; writing - original draft; writing - editing and review **Britta Nestler:** Supervision; funding acquisition; writing - original draft. This work, in the form a manuscript, has been submitted for publication and is currently under review.

The work presented in chapter 4 was done in collaboration with my supervisor, Colin Denniston. This work will be the basis for a publication that will be co-authored with my supervisor. Section 4.4.2 and 4.4.3 are done in Collaboration with Colin Denniston, MG Cole-André, FE Mackay, Santtu TT Ollila, and Tyson Whitehead and are published in the journal of Computer Physics Communications (DOI:10.1016/j.cpc.2022.108318)

Acknowledgment

This work is the culmination of four years of hard and passionate work. However, this would not have been possible without the support I received from everyone. First and foremost, I would like to thank my supervisor, Dr Colin Denniston, for providing a lab environment that fosters curiosity and kindness. I have learnt a lot, professionally and personally, from him.

I would not have been here if it weren't for all the effort and sacrifices my parents, Omid and Farideh, have made. Their support and encouragement have been a main source of motivation and energy for me through my PhD journey. There are no words to say this but I thank you!

And I would like to thank my sister, Nasim, for all the funny memes and stories! If you've ever done a PhD, you know you need those to survive the days that research is not working out.

I also would like thank my partner, Meghan. She has been my rock, although she didn't get enough time to spend with me because I was writing this thesis! I am very lucky to have her. And I would like to thank Meghan's parents, Jim and Connie, for their support and kindness.

As I am writing I am realizing how lucky I have been to have met many wonderful people through my PhD program. I would like to thank all my good friends at the Physics and Astronomy department: Sheyda Alavi, Farshid Soltani, Mateo Pascual, Ramtin Babiepour, Adrien Helias, Mark Suffak, Ariel Chitan, Peter Quigely, Jamie Griffiths, Rina Rast, Nadia Aiaseh, Charmi Bhatt, Setareh Changizrezaei, Hannah Christie, Nicholas Clark, Dilanjan Diyabalanage, Louis Fang, Pietropaolo Frisoni, Diego Martinez, Yasamin Modabber, Anusha Ravikumar, Noah Stocek, Claudia Tugulan, Kasia Wisniewski, Sage Bechanan.

I had the opportunity of visiting Dr Britta Nestler's lab at Karlsruhe Institute of Technology during my PhD. I had the pleasure of working with Ahmed Elmoghazy, Andreas Prahs, and Daniel Schneider and meeting other lab members Simon Daubner, Martin Reder, and Paul Hoffrogge. I would like to thank them all for their hospitality. I greatly miss our daily trips for lunch to the Mensa.

Contents

List of Figures

List of Tables

Acronyms

AIMD *ab initio* Molecular Dynamics. 3, 5

BGK Bhatnagar–Gross–Krook. 11

C-DFT Classical Density Functional Theory. 14, 15, 18, 23

CG coarse-grained. 5

CGMD coarse-grained Molecular Dynamics. 3, 20, 21, 31

DFT Density Functional Theory. 23, 24

DPD Dissipative Particle Dynamics. 8, 23

HL Hoffman-Lauritzen. vii, 26–28

HNC Hyper-netted chain. 17

LB Lattice Boltzmann. 10, 11, 29, 55–57, 60, 61, 66, 71, 73

LBGK Lattice Bhatnagar-Gross-Krook. 55

LBM Lattice Boltzmann Method. 3, 11, 12, 29, 55, 56, 60, 79

LHS left hand side. 9

LJ Lennard-Jones. 8

MC Monte Carlo. 7, 15, 21, 22

MD Molecular Dynamics. 3–5, 20, 24, 29

MPF multiphase-field. 14

MRT Multi-Relaxation Time. 12

MS Martynov-Sarkisov. 17

MV triple-modified Verlet. 17

ODE ordinary differential equation. 11

OZ	Ornstein-Zernike. 16
PA6	PolyAmide-6. 12
PCs	polymer composites. 3, 19, 21
PDE	partial differential equation. 11
PF	Phase-Field. 3, 29
PNCs	polymer nanocomposites. 3, 19–21
PRISM	Polymer Reference Interaction Site Model. 15–17, 24
PY	Percus-Yevick. 17
Q-DFT	Quantum Density Functional Theory. 14
RHS	right hand side. 11, 14, 28, 56, 58, 66
RISM	Reference Interaction Site Model. 16, 17
RVE	representative volume element. 18
SCMFT	Self-Consistent Mean-Field Theory. 18, 24
SRT	Single-Relaxation Time. 57, 58, 73
TEM	transmission electron microscopy. 22
THLB	Thermal Lattice Boltzmann. 55
WDA	weighted density approximation. 15, 16

Chapter 1

Introduction

Polymer composites are made up of a polymeric matrix and a reinforcement component like fibers. Polymer composites are high performance material with applications in a variety of industries such as the automotive and aerospace industries. These hybrid material offer a lightweight alternative to traditional materials. Substituting the material used in vehicles with lighter counterparts without compromising their performance is known as lightweighting and is one of the main applications of polymer composites. Lightweighting improves efficiency of vehicles and provides a way to tackle problems such as global warming, and transportation safety. However, producing such high performance materials is more complicated than a simple mixing of the components and requires a deep understanding of interactions and assembly of different components on different length scales as well as the impact of processing on the final product.

1.1 A pinch of history

Material science has had a profound historic significance, shaping the course of human civilization and revolutionizing various industries, throughout the ages. The discovery of materials like iron and steel propelled societies into the Iron Age, leading to advancements in warfare, agriculture, and transportation. During the industrial revolution, the invention of new materials, such as alloys, enabled the mass production of consumer goods, transforming economies and improving living standards. Later in the 19th century, John Wesley Hyatt and his brother, Isaiah, invented a new material called Celloloid in hopes of winning a $10,000 prize announced by a New York billiard ball manufacturer [1]. This extravagant prize was offered as the manufacturers were dealing with a shortage of Ivory, the main ingredient of billiard balls. Apparently, John and Isaiah never received their prize but they definitely changed the course of material industry.

Celluloid was made out of natural cellulose. It took another 40 years before fully synthetic polymers were introduced with the work of Leo Baekland. Baekeland and Thurlow, his lab assistant, knew the potential of phenol-formaldehyde resins. Particularly, they tried to find a replacement for shellac—used to insulate electrical cables in the early years of the 20th century. In February 1909, Baekeland announced the successful production of “Bakelizers” and went on to mass production in his house lab in 1910. By 1930, his company, Bakelite Corporation, grew to a large corporation with a 128-acre plant in Bound Brook, New Jersey [1].

Bakelite could be molded and exhibited better properties than Celloloid even though it was cheaper. However, the pure resin was very brittle. To overcome this, Baekland had to blend it with strengthening substances, particularly, cellulose. In this way, Baekland also introduced the concept of plastic composites [1].

As plastics were becoming more and more pertinent in the industry and to everyday living, understanding polymers attracted increasing numbers of scientists and engineers. The pioneering work of Hermann Staudinger with the title "*Ü*ber Polymerisation" set up the field of "polymer science" just over a 100 years ago [2]. 2 years later, in 1922, Staudinger and his colleague, Jakob Fridschi, published a paper "Über Isopren und Kautschuk" that showed experimental evidence that caoutchouc and its hydrogenated derivative have similar colloidal properties, despite the fact that the hydrogenated derivative did not show colloidal aggregation due to lack of double-bonds. This paper is where for the first time the terminology "Macromolecule" is used.

Polymeric materials have many advantages such as high impact and energy dissipation, formability, and are particularly lightweight. This makes them a perfect candidate to be used in the industries like automotive and aerospace to improve efficiency of vehicles. However, polymers are not as strong as metals which poses a safety risk and limits their use [3]. A solution to this challenge is the use of polymer composite materials. Composites are materials with two or more distinct components with a distinct interphase [3]. Composites typically offer not only better strength but also improved corrosion and fatigue resistance. Additionally, the variety of matrix and reinforcement materials provides flexibility in design.

The concept of composites might initially come across as far-fetched, but the fundamental concept behind their creation is deeply intuitive and has been understood by humans for a long time. We frequently blend diverse elements, like different ingredients in our food, to produce novel substances that inherit qualities from each constituent. This practice can even be observed in mythological narratives, where superior beings are often portrayed as a fusion of human and animal attributes, symbolizing the amalgamation of mental and physical strengths. So as we see the notion of combining diverse elements to yield a new substance with the favourable attributes of its constituents is far from novel. Composite materials emerged based on this very principle.

However, the creation of mixtures is a more intricate task than mere ingredient mixing. The proportions of various ingredients and the mixing process itself significantly influence the final blend. Likewise, in the realm of polymer composites, achieving the desired end product necessitates the exploration of diverse ingredient materials and processing techniques. This endeavour is financially demanding due to the substantial requirement for materials and labour.

Another obstacle in the manufacturing of high-performance polymer composites, especially nanocomposites, lies in their complex hierarchical structure and the involvement of various phenomena occurring across different time and length scales. This complexity imposes difficulties on the quantity of data attainable through experiments, consequently curtailing both the ability to design these materials intentionally and control the properties of the final product.

This is where technology and mathematics offer a solution through the utilization of mathematical models and computer simulations. Predictive models enable the execution of numerous virtual experiments across a wide range of conditions. This approach not only enhances our comprehension of the underlying physical processes driving real-world observations, but it also reduces the range of possibilities that must be tested in the laboratory. As a result, predictive models play a pivotal role in advancing our understanding of the relationship between structure and properties in composite materials, while also significantly saving both material usage and time expenditure.

In this thesis, I utilize coarse-grained Molecular Dynamics (CGMD), the Lattice Boltzmann Method (LBM), and Phase-Field (PF) methods to study different aspects of polymer composites and nanocomposites from molecular phase separation to microstructure distribution. But before going into details of the models used and new results obtained from my research, in this chapter, I provide a brief background and review of the existing work in the field. The rest of this chapter is organized as follows: An introduction and description of different available computational and theoretical models is given in 1.2. In 1.3, I provide examples of how these methods are applied in the field of polymer composites (PCs) and polymer nanocomposites (PNCs). The purpose of section 1.2 is to provide a brief background for the readers who are new to the field and for sake of completeness.

1.2 Mathematical models of polymer composite

As mentioned before, polymer composites (PCs) and polymer nanocomposites (PNCs) have a hierarchical structure meaning that they have two or more critical length scales [4]. Therefore, a complete understanding of their physical and mechanical properties is only achievable when studied across all the relevant scales. A variety of theoretical and computational methods have been applied to such systems [5]. In Fig.1.1, a simple diagram of different computational methods with their relevant time and length scale is shown. In this thesis, I emphasize bottom-up approaches to modelling polymer composites. As a result, I start by discussing simulation methods at smaller scales such as *ab initio* Molecular Dynamics (AIMD) and Molecular Dynamics (MD) first and move on to larger scales as the chapter proceeds. Bottom-up modelling refers to an approach where the parameters required for a practical model are obtained from smaller scale simulations rather than experimental data. Bottom-up methods are easier to generalize as they are governed by first-principle models of physics and chemistry.

1.2.1 Molecular Dynamics

Imagine a system of N nuclei with coordinates $\{\boldsymbol{R}_1, ..., \boldsymbol{R}_N\} = \boldsymbol{R}$, momenta $\{\boldsymbol{P}_1, ..., \boldsymbol{P}_N\} = \boldsymbol{P}$, and masses $M_1, ..., M_N$ and N_e electrons described by coordinates $\{\boldsymbol{r}_1, ..., \boldsymbol{r}_{N_e}\} = \boldsymbol{r}$, momenta $\{\boldsymbol{p}_1, ..., \boldsymbol{p}_{N_e}\} = \boldsymbol{p}$, masses $m_1 = ... = m_{N_e} = m$, and spins $\{s_1, ..., s_{N_e}\} = s$. Nuclear spin is ignored in the present discussion. The non-relativistic Hamiltonian of this system is

$$\begin{aligned}
\mathcal{H} &= K(\boldsymbol{P}_1, ..., \boldsymbol{P}_N, \boldsymbol{p}_1, ..., \boldsymbol{p}_{N_e}) + U(\boldsymbol{R}_1, ..., \boldsymbol{R}_N, \boldsymbol{r}_1, ..., \boldsymbol{r}_{N_e}) && (1.1)\\
&= \sum_{i=1}^{N} \frac{\boldsymbol{P}_i^2}{2M_i} + \sum_{i=1}^{N_e} \frac{\boldsymbol{p}_i^2}{2m_i} + \sum_{i>j} \frac{e^2}{|\boldsymbol{r}_i - \boldsymbol{r}_j|} + \sum_{i>j} \frac{Z_i Z_j e^2}{|\boldsymbol{R}_i - \boldsymbol{R}_j|} - \sum_{i,j} \frac{Z_i e^2}{|\boldsymbol{R}_i - \boldsymbol{r}_j|} && (1.2)\\
&= K_N(\boldsymbol{P}) + K_e(\boldsymbol{p}) + U_{ee}(\boldsymbol{r}) + U_{NN}(\boldsymbol{R}) + U_{eN}(\boldsymbol{R}, \boldsymbol{r}) && (1.3)
\end{aligned}$$

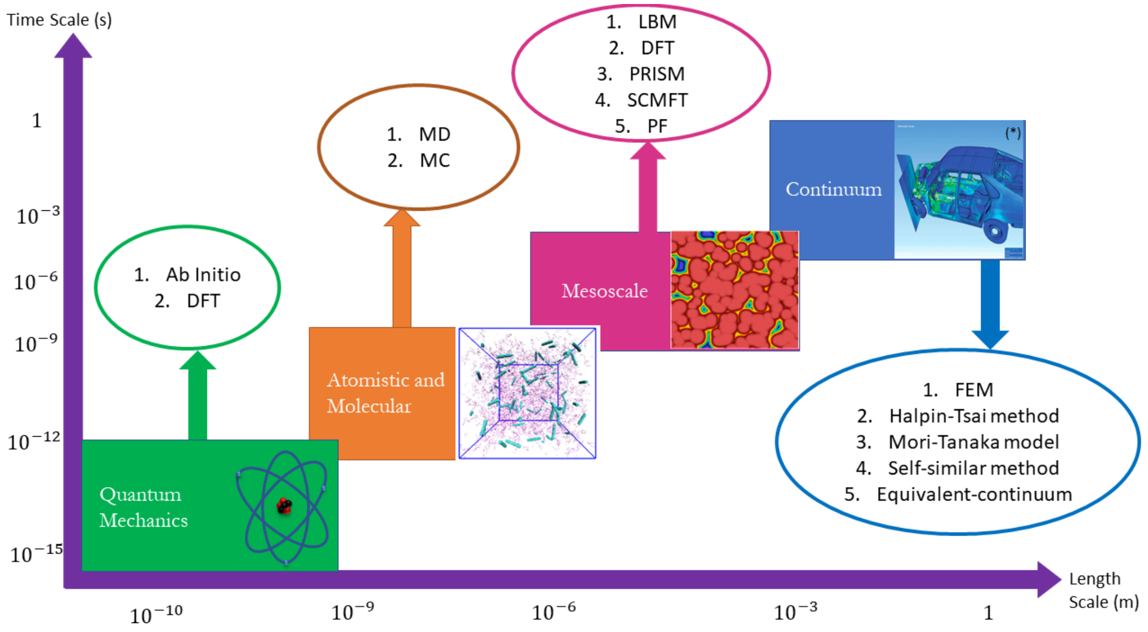

Figure 1.1: Computational and simulation methods and their corresponding time and length scales. The various methods noted in the figure will be discussed in the text. (*) is retrieved from [6].

where e is the charge of an electron, and Z_ie is the charge of the ith nucleus. To determine the state of the system, we have to solve the time-independent Schrödinger's equation:

$$\mathcal{H}\Psi(\boldsymbol{x},\boldsymbol{R}) = E\Psi(\boldsymbol{x},\boldsymbol{R}) \tag{1.4}$$

where $\boldsymbol{x} = (\boldsymbol{r}, s)$ is the full set of electron positions and spins, and Ψ is an eigenfuntion of $\mathcal{H}$ with eigenvalue E. Taking advantage of the fact that $M_i >> m$ for $i = 1, ..., N$ and therefore nuclei move considerably slower than electrons, one could simplify Eq. 1.4. This approximation is known as the Born-Oppenheimer approximation [7] and is the basis of Molecular Dynamics (MD) methods. With this assumption, we can separate the wave function as follows:

$$\Psi(\boldsymbol{x},\boldsymbol{R}) = \psi(\boldsymbol{x},\boldsymbol{R})\chi(\boldsymbol{R}) \tag{1.5}$$

where $\chi(\boldsymbol{R})$ is the nuclear wave function and $\psi(\boldsymbol{x},\boldsymbol{R})$ is the electronic wave function. Plugging (1.5) into (1.4), we get a new eigenvalue equation

$$\mathcal{H}_e\psi(\boldsymbol{x},\boldsymbol{R}) = \varepsilon(\boldsymbol{R})\psi(\boldsymbol{x},\boldsymbol{R}) \tag{1.6}$$

where

$$\varepsilon(\boldsymbol{R}) = E - \frac{(K_N + U_{NN})\chi(\boldsymbol{R})}{\chi(\boldsymbol{R})}. \tag{1.7}$$

and

$$\mathcal{H}_e = K_e + U_{ee} + U_{eN} \tag{1.8}$$

is the electronic Hamiltonian. K_N and K_e are the kinetic energy contributions of nuclei and electrons, respectively. U_{ab} denote potential energy interactions between components a and b. The new eigenvalue equation then gives a set of eigenfunctions $\psi_n(\boldsymbol{x}, \boldsymbol{R})$ and eigenvalues $\varepsilon_n(\boldsymbol{R})$ which parametrically depends on the positions of the nuclei. For each solution, there is a corresponding nuclear eigenvalue equation:

$$(K_N + U_{NN} + \varepsilon(\boldsymbol{R}))\chi(\boldsymbol{R}) = E\chi(\boldsymbol{R}). \tag{1.9}$$

The nuclear dynamics can be determined by solving the time dependent Schr$\ddot{o}$dinger's equation for the time dependent nuclear wave function $X(\boldsymbol{R}, t)$ on the surface of the electronic potential corresponding to eigenvalue $\varepsilon_n(\boldsymbol{R})$. In other words, we assume that electrons instantaneously respond to the nuclear motion and the wave function takes the adiabatic form. Now, if we also assume that the nuclei move in a classical regime, we end up with the classical equations of motion on the ground-state surface for the nuclei:

$$\begin{aligned} \dot{\boldsymbol{R}}_i &= \frac{\boldsymbol{P}_i}{M_i} \\ \dot{\boldsymbol{P}}_i &= -\nabla_i E_0(\boldsymbol{R}) \end{aligned} \tag{1.10}$$

where $E_0(\boldsymbol{R}) = \varepsilon_0(\boldsymbol{R}) + U_{NN}(\boldsymbol{R})$. As can be seen, Eq. 1.10 is Newton's equations of motion (in the Hamiltonian form). The potential $E_0(\boldsymbol{R})$ can be specified empirically or from ab initio methods, or a combination of both [8]. The functional forms that describe the potential $E_0(\boldsymbol{R})$, or the interatomic interactions, are called force fields. Therefore, this type of MD simulation is known as the force-field method. There are newer MD algorithms where the ab initio calculations are done on the fly as the simulation progresses (known as *ab initio* Molecular Dynamics (AIMD))[9, 10]. AIMD offers flexibility in including reactions and electronic polarization at the price of computation time and simulation domain size. This limits the application of *ab initio* methods, either as a way to compute force-field parameters or in form of AIMD, but with advances in computer hardware and algorithms, I see such methods being utilized more often.

The properties of real world materials are usually relevant to the average atomic behaviour on a much longer time scale than the rapid electron motion or even atomic motion. Moreover, performing ab initio or MD simulations on such long time-scales is computationally extremely expensive. A solution to this problem can be achieved by mapping the fine electronic/atomic system to a coarser system of reduced resolution. This approach is called coarse-graining. In the coarse-grained (CG) system, the sites correspond to a group of atoms in the original system. The effective interactions between different CG sites then needs to be defined such that the main properties of the fine-grained system are retained. Coarse-graining is a complicated process as the mapping between the microscopic details and the CG space is not trivial and not always clear [11]. However, it offers insight into molecular features that are the origin of mesoscopic and macroscopic behaviours.

1.2.2 Monte Carlo

The macroscopic thermodynamic observables originate from the microscopic features of the system. However, it is daunting to solve the equations of motion for every single particle in a system of realistic length scale and this level of detail is not necessary to recover equilibrium macroscopic variables. The equilibrium thermodynamic observables can, in fact, be computed from the ensemble averages of the relevant microscopic functions [12].

Take $a(\boldsymbol{x})$ to be a microscopic phase space function where $\boldsymbol{x} = (\boldsymbol{r}_0, ..., \boldsymbol{r}_N, \boldsymbol{p}_0, ..., \boldsymbol{p}_{3N})$ and A is the corresponding macroscopic (equilibrium) observable. Then, we can write

$$A = \langle a(\boldsymbol{x})\rangle = \frac{1}{Z}\int a(\boldsymbol{x}) f(\mathcal{H}(\boldsymbol{x}))d\boldsymbol{x} \tag{1.11}$$

where $\mathcal{H}(\boldsymbol{x})$ is the Hamiltonian of the system and

$$Z = \int f(\mathcal{H}(\boldsymbol{x}))d\boldsymbol{x} \tag{1.12}$$

is the normalization factor which is better known as the partition function. f is called the distribution function and its form depends on the choice of ensembles. The partition function plays a fundamental role in statistical physics and is directly related to different equilibrium macroscopic variables.

There are different ways one could calculate the integrals above to determine the equilibrium macroscopic quantities. One way is to approximate the integrals by a summation over a subset of the phase space points, also known as a sample of the phase space. Imagine an integral of the form Eq. 1.11 in 1 dimension

$$I = \int g(x)f(x)dx \tag{1.13}$$

where $f(x)$ is a probability distribution function (not necessarily the same as the f in Eq. 1.12) such that

$$f(x) \geq 0, \tag{1.14}$$

$$\int f(x)dx = 1. \tag{1.15}$$

In this case, one can define an estimator

$$G = \frac{1}{M}\sum_{i=1}^{M} g(x_i) \tag{1.16}$$

where x_i is the ith random variable of a set of drawn random variables $\{x_1, ..., x_M\}$. The random variables are drawn randomly from the distribution function $f(x)$. Then,

$$\langle G\rangle = \langle\frac{1}{M}\sum_{i=1}^{M} g(x_i)\rangle \approx \frac{1}{M}\sum_{i=1}^{M}\langle g(x)\rangle = \langle g(x)\rangle = I. \tag{1.17}$$

According to the central limit theorem, it is then guaranteed that

$$I = \lim_{M\to\infty} G. \tag{1.18}$$

This class of probabilistic algorithms are called Monte Carlo algorithms. The method was first introduced by Ulam and Metropolis after the second World War [13].

Now, one question that may occur to you is: How would one pick the M phase space points to then calculate the above summations? This problem is known as sampling. A sampling method is an algorithm that can produce a sequence of values of random variables $X = \{X_1, X_2, ...\}$ such that for any subset Ω of Ω_0

$$P\left\{X_k \in \Omega\right\} = \int_{\Omega} f(x)dx \leq 1 \tag{1.19}$$

where P is the probability, and $f(x)$ is a probability distribution function defined on Ω_0. Imagine our 1D probability distribution function $f(x) \geq 0$ to be defined on $[a, b]$ such that

$$\int_a^b f(x)dx = 1. \tag{1.20}$$

Then the cumulative distribution function $F(x)$ can be defined as

$$F(X) = \int_a^X f(x)dx \leq 1 \tag{1.21}$$

where $X \in [a, b]$ and

$$f(x) = \frac{dF}{dX}. \tag{1.22}$$

Consider $y(x)$ to be a nondecreasing function of x. Since y and x map into each other, we have

$$X \geq x \iff y(X) \geq y(x). \tag{1.23}$$

Consequently, the cumulative probability distributions are the same

$$F_X(X) = \int_x^X f(x)dx = \int_{y(x)}^{y(X)} \tilde{f}(y)dy = F_Y(Y). \tag{1.24}$$

Typical random number generators generate sequences that are uniformly distributed on the interval $[0, 1]$:

$$r(n) = \begin{cases} 1 & 0 \leq r \leq 1, \\ 0 & \text{otherwise.} \end{cases} \tag{1.25}$$

with cumulative distribution

$$R(\xi) = \begin{cases} 0 & \xi < 0, \\ \xi & 0 \leq \xi \leq 1, \\ 1 & \xi > 1. \end{cases} \tag{1.26}$$

Now, if we assume that there exists a transformation such that $n = y(x)$ where $y(x)$ is a nondecreasing function of x, based on above discussion, the cumulative probabilities should be the same for n and x

$$F(X) = \xi \tag{1.27}$$

where $\xi \in [0, 1]$. Therefore, one can solve Eq. 1.27 for a set of random numbers $\{\xi_1, ..., \xi_M\}$ to find $\{X_1, ..., X_M\}$. By setting $x_i = X_i$, then we get a sampling of M values of the distribution $f(x)$. This type of sampling is called "simple sampling". Simple sampling is the most basic method but there are other algorithms such as Metropolis method that can be utilized to sample the phase space.

The Metropolis method was inspired by the independence of equilibrium states of a system from the kinetic of the system [13, 14]. This technique explores the phase space by a Markov chain where at each step, the system either moves to a new state (accepted move) or the move is rejected and it stays at the current state (rejected move). The probability of a move being accepted must follow the detailed balance relation [15]. The advantage of Metropolis method is that almost all probability distributions can be sampled by it regardless of the complexity of the distribution. However, the Markov chain nature of the algorithm creates correlations between successive states and the sampling is correct only asymptotically. Further information on the Metropolis method and other Monte Carlo methods can be found in the literature [12, 15, 16].

1.2.3 Dissipative Particle Dynamics

MD and MC methods are typically utilized to study nano and micro scale properties of systems. Moving up to more mesoscopic methods, we start with Dissipative Particle Dynamics (DPD). DPD is a mesoscopic particle based method where the "particles" represent regions of the fluid rather than atoms. The equation of motion of particle i is

$$\dot{\boldsymbol{r}}_i = \boldsymbol{v}_i = \boldsymbol{p}_i/m_i \tag{1.28}$$

$$\dot{\boldsymbol{p}}_i = \sum_{j \neq i} \boldsymbol{F}_{ij}^C + \boldsymbol{F}_{ij}^D + \boldsymbol{F}_{ij}^R \tag{1.29}$$

where $\boldsymbol{r}$ is the position of the particle, $\boldsymbol{p}$ is the momentum vector, and "$\dot{}$" represents time derivative [17]. There are three types of force applied to the particles, conservative ($\boldsymbol{F}^C$), dissipative ($\boldsymbol{F}^D$), and random ($\boldsymbol{F}^R$). The forces are assumed to be pairwise additive. The conservative force is usually defined as a linear function of particle separation such that

$$F_{ij}^C = a_C w_C(\boldsymbol{r}_{ij})\hat{\boldsymbol{r}}_{ij} \tag{1.30}$$

where a_c is a coefficient related to fluid compressibility, $w_C(\boldsymbol{r}_{ij})$ is the conservative weight function, and $\hat{\boldsymbol{r}}_{ij}$ is the unit vector connecting particle i to j. The weight function is typically softer than molecular potentials such as LJ potentials allowing for larger time steps. This is one of the main attractions of DPD as it makes simulations on longer time scales possible [16].

The dissipative forces are defined as

$$F_{ij}^D = -\gamma w_D(\boldsymbol{r}_{ij})(\boldsymbol{r}_{ij} \cdot \boldsymbol{v}_{ij})\hat{\boldsymbol{r}}_{ij} \tag{1.31}$$

where γ is the friction coefficient, and $w_D(\boldsymbol{r}_{ij})$ is the dissipative weight function. The random forces are defined as

$$F_{ij}^R = \sigma \zeta_{ij} w_R(\boldsymbol{r}_{ij})\hat{\boldsymbol{r}}_{ij} \tag{1.32}$$

where σ is the amplitude of the noise, and $w_D(\boldsymbol{r}_{ij})$ is the random weight function. ζ_{ij} is a Gaussian noise with the following stochastic properties:

$$\langle \zeta_{ij}(t) \rangle = 0 \tag{1.33}$$

$$\langle \zeta_{ij}(t)\zeta_{kl}(t') \rangle = (\delta_{ik}\delta_{jl} + \delta_{jk}\delta_{il})\delta(t-t'). \tag{1.34}$$

ζ_{ij} is symmetric to conserve momentum and $w_D(\boldsymbol{r}_{ij})$ and $w_R(\boldsymbol{r}_{ij})$ are chosen to satisfy the fluctuation–dissipation theorem [18, 19].

While DPD was originally proposed as a method to simulate fluids on a mesoscale, often now, it is used as a momentum conserving thermostat (e.g. in place of Langevin thermostat) in Molecular Dynamics simulations.

1.2.4 Lattice Boltzmann

Historically, the Lattice Boltzmann model was developed as a successor of the Lattice Automata where the boolean variables on each grid point were replaced by particle distributions [20]. But as was later shown [21], it is possible to derive the lattice Boltzmann equation directly from discretizing the Boltzmann equation in velocity space, time, and space. In this section, I will cover the fundamental theory behind the model and leave the algorithmic and implementation details to chapter 4.

The continuous linearized Boltzmann Equation is written as

$$\frac{Df}{Dt} \equiv \partial_t f(\boldsymbol{\xi}, \boldsymbol{x}, t) + \xi_\alpha \partial_\alpha f(\boldsymbol{\xi}, \boldsymbol{x}, t) = C\left(f - f^{eq}\right) \tag{1.35}$$

where Df/Dt is the material derivative of the distribution function f. $f(\boldsymbol{\xi}, \boldsymbol{x}, t)$ represents the density normalized probability of finding a particle at position $\boldsymbol{x}$ and time t with microscopic velocity ξ and is a function of microscopic velocity $\boldsymbol{\xi}$, space $\boldsymbol{x}$, and time t. For sake of brevity, I replace all $f(\boldsymbol{\xi}, \boldsymbol{x}, t)$ with f and use the expanded form only when necessary. The Einstein summation convention is used in $\xi_\alpha \partial_\alpha f(\boldsymbol{\xi}, \boldsymbol{x}, t)$. The $C\left(f - f^{eq}\right)$ is the collision operator and f^{eq} is the particle distribution at equilibrium. The collision operator$C$ is a linear function of $(f - f^{eq})$. The macroscopic properties then are defined as the moments of the f

$$\rho = \int f d\boldsymbol{\xi}, \tag{1.36}$$

$$\rho \boldsymbol{u} = \int f \boldsymbol{\xi} d\boldsymbol{\xi}, \tag{1.37}$$

$$\rho k_B T = \frac{1}{2} \int f (\boldsymbol{\xi} - \boldsymbol{u})^2 d\boldsymbol{\xi}. \tag{1.38}$$

where $\boldsymbol{u}$ is the macroscopic velocity, T is the temperature, ρ is the mass density, k_B is the Boltzmann constant. It can be shown that the equilibrium distribution for an ideal gas f^{eq} takes a Maxwell-Boltzmann form [22]

$$f^{eq}(\rho, \boldsymbol{\xi}, \boldsymbol{u}, T) = \frac{\rho}{(2\pi k_B T)^{d/2}} \exp\left(\frac{(\boldsymbol{\xi} - \boldsymbol{u})^2}{2 k_B T}\right) \tag{1.39}$$

where d is the dimension. Writing out the moments of this equilibrium distribution function while imposing conservation of mass, momentum, and energy, we see that the macroscopic variables indeed turn out to be the moments of f^{eq}

$$\rho = \int f^{eq} d\boldsymbol{\xi}, \tag{1.40}$$

$$\rho \boldsymbol{u} = \int f^{eq} \boldsymbol{\xi} d\boldsymbol{\xi}, \tag{1.41}$$

$$\rho k_B T = \frac{1}{2} \int f^{eq} (\boldsymbol{\xi} - \boldsymbol{u})^2 d\boldsymbol{\xi}. \tag{1.42}$$

The moments of the collision operator C can also be determined applying conservation of mass, momentum, and energy

$$0 = \int C(f) d\boldsymbol{\xi}, \tag{1.43}$$

$$0 = \int C(f) \boldsymbol{\xi} d\boldsymbol{\xi} \tag{1.44}$$

$$0 = \frac{1}{2} \int C(f) (\boldsymbol{\xi} - \boldsymbol{u})^2 d\boldsymbol{\xi}. \tag{1.45}$$

Now to derive the Lattice Boltzmann equations from 1.35, we need to discretize f in velocity space, physical space, and time.

Velocity discretization

Hermite polynomials are a great candidate for discretization of the Boltzmann equation in phase/velocity space as their generating function is a Gaussian resembling the form of the equilibrium distribution f^{eq}. In addition, they form a complete basis in $\mathbb{R}$ [20, 21]. It also can be shown that the expansion coefficients of the series are directly related to the moments of the distribution f^{eq}. Thus, using the Gauss-Hermite quadrature rule, one can recover the exact moments up to a certain degree using a model with sufficient number of discrete velocities. For example, the truncated equilibrium distribution

$$f^{eq} \approx \rho g(\boldsymbol{\xi}) \Big\{ 1 + \xi_\alpha u_\alpha + (u_\alpha u_\beta + (T-1)\delta_{\alpha\beta}) (\xi_\alpha \xi_\beta - \delta_{\alpha\beta}) \Big\} := \rho g(\boldsymbol{\xi}) Q(\rho, \boldsymbol{\xi}, T), \tag{1.46}$$

where $g(\boldsymbol{\xi})$ is the Hermite generating function, would be a good approximation to recover macroscopic behaviour of a simple fluid. Then, the discretized version of this distribution would take the form

$$f_i^{eq} = \rho w_i Q(\rho, \boldsymbol{\xi}_i, T) = \rho w_i \Big\{ 1 + \xi_{i\alpha} u_\alpha + (u_\alpha u_\beta + (T-1)\delta_{\alpha\beta}) (\xi_{i\alpha} \xi_{i\beta} - \delta_{\alpha\beta}) \Big\}. \tag{1.47}$$

where w_i is the quadrature weight associated with the ith discrete velocity. The change of variable $\boldsymbol{e}_i = \boldsymbol{\xi}_i / \sqrt{3}$ is typically done to avoid appearance of extra factors of $\sqrt{3}$ in the moments:

$$f_i^{eq} = \rho w_i \Big\{ 1 + \frac{e_{i\alpha} u_\alpha}{c_s^2} + \frac{(u_\alpha u_\beta + (T-1)\delta_{\alpha\beta}) (e_{i\alpha} e_{i\beta} - \delta_{\alpha\beta})}{2 c_s^4} \Big\}. \tag{1.48}$$

where c_s is the speed of sound.

The first two moments are explicitly

$$\rho = \sum_{i=0}^{q-1} f_i^{eq} \tag{1.49}$$

$$\rho u_\beta = \sum_{i=0}^{q-1} f_i^{eq} e_{i\beta} \tag{1.50}$$

where u_β is the βth component of the velocity. Different LB models in a d-dimensional space are distinguished by the number of velocities q that they use which is reflected in the name of the model $DdQq$. The most commonly used LB models are $D1Q3$ in 1D, $D2Q9$ in 2D, and $D3Q15$, and $D3Q19$ in 3D.

The discretization of the distribution function f can be done similarly

$$f_i(\boldsymbol{x}, t) = \frac{w_i}{g(\boldsymbol{e}_i)} f(\boldsymbol{e}_i, \boldsymbol{x}, t) \tag{1.51}$$

where $g(\boldsymbol{e}_i)$ is added to satisfy the quadrature as fs do not necessarily have a Maxwellian form, unlike f^{eq}. We can finally rewrite the Boltzmann equation with the discrete-velocity distributions

$$\partial_t f_i + e_{i\alpha}\partial_\alpha f_i = C_i \tag{1.52}$$

where C_i is the discrete collision operator.

Space and time discretization

The discrete-velocity Boltzmann Equation is a first-order hyperbolic partial differential equation (PDE) which can be reduced to an ordinary differential equation (ODE) along the characteristic curves $x_{0\alpha} = x_\alpha - e_{i\alpha}\Delta t$ where $e_{i\alpha}$ is the discrete velocity by which f_i travels to neighbouring sites ($x_{0\alpha} + e_{i\alpha}\Delta t$ falls on a lattice site). Thus,

$$\frac{df_i}{dt} := \partial_t f_i + e_{i\alpha}\partial_\alpha f_i = C_i(\boldsymbol{x}, t). \tag{1.53}$$

This ODE can be integrated along the characteristics to get

$$f_i(\boldsymbol{x} + \boldsymbol{e}_i\Delta t, t + \Delta t) - f_i(\boldsymbol{x}, t) = \int_0^{\Delta t} C_i(\boldsymbol{x} + \boldsymbol{e}_i s, t + s)ds. \tag{1.54}$$

Using the Euler's method, one gets

$$f_i(\boldsymbol{x} + \boldsymbol{e}_i\Delta t, t + \Delta t) - f_i(\boldsymbol{x}, t) = C_i(\boldsymbol{x}, t)\Delta t \tag{1.55}$$

which is known as the Lattice Boltzmann equation. The Lattice Boltzmann equation can also be recovered using a second order discretization in space and time. We will discuss this and the consequences in chapter 4.

A careful look at Eq. 1.55 reveals that the operations on the RHS all take place at time t and the results are then propagated to the neighbouring sites at $t + \Delta t$. Therefore, the lattice Boltzmann algorithm is naturally divided into two steps:

1. A local step where distributions are repopulated after relaxation, known as the collision step,
2. The streaming step where the populations are propagated to the neighbouring sites.

Collision Operator

So far, I have used the linear collision operator C_i without discussing its exact form. The original collision operator of the Boltzmann equation is a complicated integral accounting for binary collision of particles. Although there are methods suggested in the literature to numerically solve this integral [23, 24], they tend to be computationally costly. Moreover, as it only accounts for binary collisions, it is limited to modelling gases. One could instead use approximations for the collision operator that provide reasonable macroscopic results. The linearized collision operator, also known as Bhatnagar–Gross–Krook (BGK) approximation, is the most commonly used approximation.

The most commonly used BGK collision operator is the single relaxation time

$$C_i = -\frac{1}{\tau}(f_i - f_i^{eq}) \tag{1.56}$$

where τ is the relaxation time [25]. This approximation usually provides satisfactory results and it's commonly used due to its simplicity. More complicated collision operators with multiple relaxation times can be introduced to improve stability and/or expand LBM to model more complicated systems.

The Lattice Boltzmann Method (LBM) has been successfully used to study a wide range of simple and complex fluids [26–29]. We further discuss the method and its history in chapter 4.

1.2.5 Phase-field

Phase-field models are a class of mesoscopic models used to describe materials with heterogeneous structure [30]. The main characteristic/advantage of this modelling technique is the diffuse treatment of interfaces. This approach allows tracking the evolution of the (multi-domain) system without the need to track every individual interface which makes it faster and easier to implement and therefore more attractive compared to conventional sharp-interface models.

The diffuse interface treatment of binary systems goes back over a century ago to van der Waals's liquid-gas model [31]. Later, Cahn and Hilliard derived an expression for the free energy of a flat interface between coexisting phases using the diffuse interface approach and studied the spinodal decomposition of the system [32]. Langer introduced the concept of non-conserved order parameters for separating coexisting phases [33]. Allen and Cahn extended the Cahn-Hilliard approach to non-conserved order parameters to study the kinetics of an interface, particularly an antiphase boundary[1] [34]. The flexibility and capability of the phase-field method has made it a popular tool to study microstructure evolution [35–37].

The applications of the phase-field method are usually divided into two types, one where the order parameters correspond to well-defined physical quantities and the other where the field variables are defined for the mere purpose of avoiding tracking of boundaries [37, 38]. The phase-field model used in Chapter 3 to study the crystallization of PolyAmide-6 (PA6) falls into the second category. For this purpose, I utilize the multiphase-field model introduced by Steinbach et al. and Nestler et. al [35, 39–41]. In the rest of this subsection, I provide a brief introduction to the multiphase-field model and leave more detailed description of the crystallization model for chapter 3.

For sake of simplicity, at this point I only apply the model to 2 phases and no bulk driving force. In this case, the system can be described in terms of a single order parameter ϕ. The free energy of such a system can be written as

$$\mathcal{F}(\phi, \nabla\phi) = \int_V f(\phi, \nabla\phi) d\boldsymbol{r} \tag{1.57}$$

---

[1] An antiphase boundary (APB) refers to a specific interface within a crystalline material where there is a transition between two regions characterized by opposite atomic arrangements. In other words, on one side of the boundary, the atomic structure exhibits a specific pattern, while on the other side, it is the exact opposite arrangement

where f is the free energy density, and

$$\sum_{\alpha=1}^{N=2} \phi_\alpha(\boldsymbol{r}, t) = 1 \tag{1.58}$$

where $\boldsymbol{r}$ is the position vector and t is the time. Thus, if phase 1 is described by ϕ, the second phase would be described by $1 - \phi$.

The free energy density can be split into two main contributions: interfacial and bulk

$$f(\phi, \nabla\phi) = f_{int}(\phi, \nabla\phi) + f_b(\phi, c). \tag{1.59}$$

For now, I ignore bulk contributions $f_b(\phi, c) = 0$ and the impact of conservative field c. The interfacial contribution is defined as

$$f_{int}(\phi, \nabla\phi) = \epsilon a(\phi, \nabla\phi) + \frac{1}{\epsilon}\omega(\phi) \tag{1.60}$$

where ϵ is a constant related to the length of the diffuse interface, and the first term on the RHS is

$$a(\phi, \nabla\phi) = \gamma_{12}(\nabla\phi \cdot \nabla\phi) \tag{1.61}$$

where γ_{12} is the interfacial energy density between two phases [42]. The most commonly used potential terms $\omega(\phi)$ are double-well and double-obstacle potentials:

$$\omega_{well}(\phi) = \gamma_{12}\phi^2(1-\phi)^2, \tag{1.62}$$

$$\omega_{obs}(\phi) = \gamma_{12}\phi(1-\phi). \tag{1.63}$$

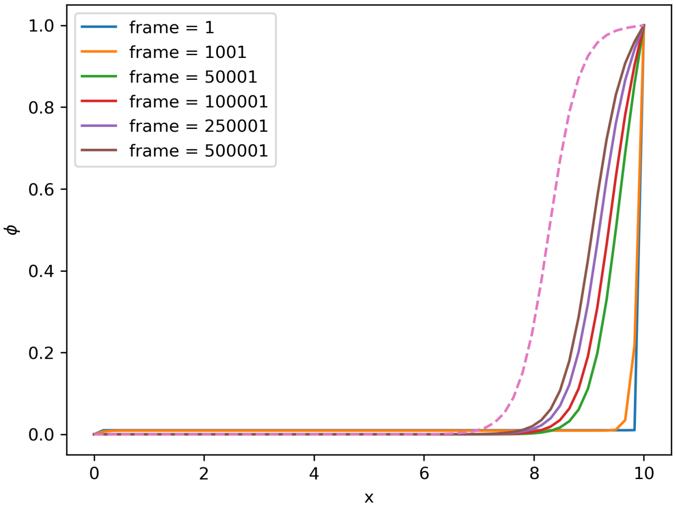

Figure 1.2: The evolution of the phase field profile is shown. ϕ is initially 0 everywhere except at $x = 10$ where it is 1. The phase corresponding to $\phi = 1$ grows and the boundary between the phases moves into the domain until it reaches its equilibrium (dashed pink curve)

Based on “model A” of Hohenberg and Halperin [30], the evolution equation of the non-conserved order parameter is

$$\frac{\partial \phi}{\partial t} = -\frac{1}{\epsilon} M_{12} \frac{\delta \mathcal{F}}{\delta \phi} \tag{1.64}$$

where M_{12} is the mobility for interface between the two phases. Then, from variational calculus [43], we have

$$\frac{\partial \phi}{\partial t} = -\frac{M_{12}}{\epsilon} \left(\frac{\partial f}{\partial \phi} - \nabla \cdot \frac{\partial f}{\partial (\nabla \phi)} \right). \tag{1.65}$$

Plugging in the free energy functional into this equation, we get the evolution equation of the order parameter ϕ

$$\frac{\partial \phi}{\partial t} = -\frac{\gamma_{12}}{\epsilon^2} M_{12} \left(\phi(1-\phi)(1-2\phi) - 2\epsilon^2 \nabla^2 \phi \right) \tag{1.66}$$

when the double-well potential is used. As an example, the evolution of ϕ in 1D ($x \in [0, 10]$ in unit length) is shown in Fig. 1.2. The system is initialized so that $\phi(10\sigma) = 1$ and ϕ is zero everywhere else. We see that the phase corresponding to $\phi = 1$ grows and the boundary between the phases moves into the domain until it reaches its equilibrium (dashed pink curve). In chapter 3, we will discuss the generalization of the phase-field model to many phases, namely, the multiphase-field (MPF) model and how it can be utilized to study the crystal morphology of neat and fiber-reinforced polymers.

1.2.6 Classical Density Functional Theory

The Classical Density Functional Theory (C-DFT) is based on the variational principle that the functional derivative of the free energy with respect to density should be zero at equilibrium [44]. This method is found attractive by the scientific community as it recovers and connects microscopic details of a system to its macroscopic properties, but it is computationally faster than molecular simulations. Its formalism also has roots in statistical mechanics making the model mathematically more robust compared to phenomenological models [45]. The model was originally adopted from Hohenberg and Kohn's Quantum Density Functional Theory (Q-DFT) and used to predict interfacial behaviour of classical liquids at interfaces and near hard walls [46]. Since then the model has been applied to a variety of physical phenomena such as phase transition [47], polymeric systems [48], polymer nanocomposites [49, 50], and biological systems [45, 51].

Consider a system of N particles in the presence of external field ψ. The Hamiltonian for such a system is defined as

$$\mathcal{H}(\boldsymbol{r}^N, \boldsymbol{p}^N) = K(\boldsymbol{p}^N) + U(\boldsymbol{r}^N) + \Psi(\boldsymbol{r}^N) \tag{1.67}$$

where

$$\Psi(\boldsymbol{r}) = \sum_{i=1}^{N} \psi(\boldsymbol{r}_i) = \int \psi(\boldsymbol{r}) \rho(\boldsymbol{r}) d^N \boldsymbol{r}. \tag{1.68}$$

The microscopic density $\rho(\boldsymbol{r})$ is then defined as

$$\rho(\boldsymbol{r}) = \sum_{i=1}^{N} \delta(\boldsymbol{r} - \boldsymbol{r}_i) \tag{1.69}$$

with equilibrium value

$$\rho^{(1)}(\boldsymbol{r}) = \langle\sum_{i=1}^{N}\delta(\boldsymbol{r}-\boldsymbol{r}_i)\rangle. \tag{1.70}$$

The angle brackets $\langle\cdot\rangle$ shows ensemble averages and $\delta(\boldsymbol{r})$ is the Dirac delta function. From statistical mechanics, the grand canonical potential of our system is

$$\Omega_G = F - \mu N = \mathcal{F} + \int \psi(\boldsymbol{r})\rho^{(1)}(\boldsymbol{r})d^N\boldsymbol{r} - \mu N \tag{1.71}$$

where $\mathcal{F}$ is the intrinsic free energy. Now let us define a functional Ω of an average density $n(\boldsymbol{r})$:

$$\Omega[n(\boldsymbol{r})] = \mathcal{F}[n(\boldsymbol{r})] + \int \psi(\boldsymbol{r})n(\boldsymbol{r})d^N\boldsymbol{r} - \mu\int n(\boldsymbol{r})d^N\boldsymbol{r} \tag{1.72}$$

where $n(\boldsymbol{r})$ does not necessarily have to be the equilibrium density. It can be shown that for a functional of this form the minimum of the functional occurs at the equilibrium phase space density [52]. Moreover, the intrinsic free energy functional $\mathcal{F}$ can be proven to be a unique functional of the equilibrium single-particle density $\rho^{(1)}(\boldsymbol{r})$. Therefore, from the combination of these theorems (also known as Hohenberg-Kohn theorems), we have

$$\Omega_G = \Omega[\rho^{(1)}(\boldsymbol{r})] \leq \Omega[n(\boldsymbol{r})]. \tag{1.73}$$

The above theorems and results provide a tool to calculate density profiles and the grand canonical potential using variational calculus. But in order to do so, one has to know the form of the free energy. The exact form of the free energy is only known for non-interacting hard spheres (ideal fluids):

$$\mathcal{F}^{id} = k_BT\int \rho^{(1)}(\boldsymbol{r})\left[\ln\left(\Lambda^3\rho^{(1)}\right) - 1\right]d\boldsymbol{r} \tag{1.74}$$

where Λ is the de Broglie thermal wavelength [52]. For more complicated systems, the free energy functional needs to be approximated. As the exact form is known for ideal fluids, it seems logical to split the free energy into the known ideal contribution, and an excessive part that contains all the other contributions (due to interactions):

$$\mathcal{F} = \mathcal{F}^{id} + \mathcal{F}^{ex}. \tag{1.75}$$

As the excessive part is formally unknown, it needs to be approximated. Various approaches have been introduced to approximate the excess free energy functional for atomic fluids and a detailed description of such methods can be found in the literature [53, 54].

In the case of polyatomic molecules, finding the free energy functional is a trickier task as interparticle interactions are present even in the ideal case. In 1986, Chandler, McCoy, and Singer extended the application of C-DFT to polyatomic systems using a segment-based method [55]. In this model, the ideal free energy includes contributions from a gas of non-interacting polymers as well as the intramolecular bonding between the particles while the excessive free energy contains all the intermolecular couplings. The intramolecular correlation functions are determined using single chain Monte Carlo simulations. The intermolecular correlation functions, on the other hand, are expanded to a linear order around the uniform fluid reducing their calculation to finding the pair correlation functions of the bulk fluid. This is typically done using the Polymer Reference Interaction Site Model (PRISM) which will be discussed in more depth in the next section. In this scheme, the attractive interactions are usually dealt with using a mean-field approach. This version of C-DFT shares conceptual similarities with the simpler self-consistent mean field theory with the advantage of accounting for local packing effects.

The weighted density approximation (WDA) is commonly used to approximate free energy functionals for both polymeric and atomic systems [49, 53, 54]. The main idea is to replace the density $\rho(\boldsymbol{r})$ with a local average density $\bar{\rho}(\boldsymbol{r})$ so that the excessive free energy could be well approximated by a local function even when the local density may surpass that of close packing. In this case, the average (smoothed) density is defined as

$$\bar{\rho}(\boldsymbol{r}) = \int d\boldsymbol{r}'\rho(\boldsymbol{r}')w(|\boldsymbol{r}-\boldsymbol{r}'|r, \bar{\rho}(\boldsymbol{r})) \tag{1.76}$$

where w is a weight function. The excessive free energy then is

$$\mathcal{F}^{ex}\left[\rho(\boldsymbol{r})\right] = \int d\boldsymbol{r}\rho(\boldsymbol{r})f^{ex}(\bar{\rho}(\boldsymbol{r})) \tag{1.77}$$

where f^{ex} is the nonideal free energy of a bulk fluid. A variety of weighting functions have been developed for different physical problems leading to different versions of WDA [53].

1.2.7 Polymer Reference Interaction Site Model

In the previous section, I mentioned that the free energy functional is often split into two contributions: ideal and excessive. I also mentioned that the excessive part is the contribution that is formally unknown and needs to be either found from microscopic simulations or be approximated. It can be shown that the excess free energy and grand canonical functionals are generating functionals for a hierarchy of density correlation functions $h^{(n)}(\boldsymbol{r}^n)$ and direct correlation functions $c^{(n)}(\boldsymbol{r}^n)$, respectively [52]. After some functional calculus and algebra, one can derive an integral equation, famously known as the Ornstein-Zernike (OZ) relation, relating density and direct correlation functions:

$$h^{(2)}(\boldsymbol{r},\boldsymbol{r}') = c^{(2)}(\boldsymbol{r},\boldsymbol{r}') + \int c^{(2)}(\boldsymbol{r},\boldsymbol{r}'')\rho^{(1)}(\boldsymbol{r}'')h^{(2)}(\boldsymbol{r}'',\boldsymbol{r}')d\boldsymbol{r}''. \tag{1.78}$$

where $h^{(2)}(\boldsymbol{r},\boldsymbol{r}') = g^{(2)}(\boldsymbol{r},\boldsymbol{r}') - 1$ and

$$g^{(2)}(\boldsymbol{r},\boldsymbol{r}') = \frac{1}{\rho^{(1)}(\boldsymbol{r})\rho^{(1)}(\boldsymbol{r}')}\langle\sum_i\sum_j\delta(r-r_i)\delta(r'-r_j)\rangle \tag{1.79}$$

is the pair distribution function. In an isotropic system, $g^{(2)}(\boldsymbol{r},\boldsymbol{r}')$ only depends on the separation $|\boldsymbol{r}-\boldsymbol{r}'|$ and is specifically called the radial distribution function or $g(r)$. The direct pair correlation function $c^{(2)}(\boldsymbol{r},\boldsymbol{r}')$ is defined as the functional derivative of the single-particle direct correlation function $c^{(1)}(\boldsymbol{r})$

$$c^{(2)}(\boldsymbol{r},\boldsymbol{r}') = \frac{\delta c^{(1)}(\boldsymbol{r})}{\delta\rho^{(1)}(\boldsymbol{r}')} = -\frac{1}{k_BT}\frac{\delta^2\mathcal{F}^{ex}\left[\rho^{(1)}\right]}{\delta^2\rho^{(1)}(\boldsymbol{r})} \tag{1.80}$$

where

$$c^{(1)}(\boldsymbol{r}) = -\frac{1}{k_B T}\frac{\delta \mathcal{F}^{ex}\left[\rho^{(1)}\right]}{\delta \rho^{(1)}(\boldsymbol{r})}. \tag{1.81}$$

The OZ equation can be solved recursively to get

$$\begin{aligned} h^{(2)}(\boldsymbol{r}_1,\boldsymbol{r}_2) = c^{(2)}(\boldsymbol{r}_1,\boldsymbol{r}_2) &+ \int c^{(2)}(\boldsymbol{r}_1,\boldsymbol{r}_3)\rho^{(1)}(\boldsymbol{r}_3)c^{(2)}(\boldsymbol{r}_3,\boldsymbol{r}_2)d\boldsymbol{r}_3 \\ &+ \int\int c^{(2)}(\boldsymbol{r}_1,\boldsymbol{r}_3)\rho^{(1)}(\boldsymbol{r}_3)c^{(2)}(\boldsymbol{r}_3,\boldsymbol{r}_4)c^{(2)}(\boldsymbol{r}_2,\boldsymbol{r}_4)d\boldsymbol{r}_3 d\boldsymbol{r}_4 \\ &+ \ldots. \end{aligned} \tag{1.82}$$

This shows that the correlation between two particles is a result of their direct correlation plus an indirect correlation through their interaction with other particles in the medium.

The above equations are derived for atomic fluids. Andersen and Chandler extended the idea to molecular fluids and introduced the Reference Interaction Site Model (RISM) [56, 57]. Schweizer and Curro further generalized the RISM to describe polymeric fluids resulting in the Polymer Reference Interaction Site Model (PRISM) [58, 59].

In the RISM formalism, each molecule is represented by spherically symmetric interaction sites and the structure of the fluid is described in terms of site-site distribution functions. As the interaction sites on a molecule can interact with the other sites on the same molecule as well as sites on other molecules, the governing equations of the PRISM are generalized OZ equations that relate the site-site intermolecular pair correlation function $h_{ij}(\boldsymbol{r})$ to intramolecular pair correlation function $w_{ij}(\boldsymbol{r})$ and direct correlation function $c_{ij}(\boldsymbol{r})$:

$$h(\boldsymbol{r}) = \int d\boldsymbol{r}' \int d\boldsymbol{r}'' w(|\boldsymbol{r}-\boldsymbol{r}'|)c(|\boldsymbol{r}-\boldsymbol{r}''|)\left(w(\boldsymbol{r}'') + \rho^{(1)}h(\boldsymbol{r}'')\right) \tag{1.83}$$

where $h(\boldsymbol{r})$, $c(\boldsymbol{r})$, and $w(\boldsymbol{r})$ are $N \times N$ matrices (for N total sites) with site-site correlation functions $h_{ij}(\boldsymbol{r})$, $c_{ij}(\boldsymbol{r})$, and $w_{ij}(\boldsymbol{r})$ as elements. This equation is commonly presented in its Fourier space form for sake of simplicity:

$$\hat{h}(\boldsymbol{k}) = \hat{w}(\boldsymbol{k})\hat{c}(\boldsymbol{k})\left(\hat{w}(\boldsymbol{k}) + \rho^{(1)}\hat{h}(\boldsymbol{k})\right) \tag{1.84}$$

where the hat sign shows the functions in Fourier space and $\boldsymbol{k}$ is the wavevector. Detailed derivation of the RISM/PRISM equations can be found in the literature [52].

Since the correlation functions in 1.83 are unknown, a closure relation, relating $h(\boldsymbol{r})$, $w(\boldsymbol{r})$, $c(\boldsymbol{r})$ and the intermolecular potential, is required. There are different closure relations that one can use depending on the physical system. The closure relations are divided into two classes of atomic and molecular. The Percus-Yevick (PY), Hyper-netted chain (HNC), and Martynov-Sarkisov (MS) are the commonly used atomic closures [60]. The site-site PY approximation relates the direct correlation function to the pair distribution function

$$c_{ij}(\boldsymbol{r}) = \left(1 - e^{\beta U_{ij}}\right) g_{ij}(\boldsymbol{r}),\ |\boldsymbol{r}| > d_{ij} \tag{1.85}$$

where $\beta = 1/k_B T$, U_{ij} is the total site-site interaction potential, and d_{ij} is the distance of closest approach between site i and j.

On the other hand, the site-site HNC describes the direct correlation function as

$$c_{ij}(\boldsymbol{r}) = h_{ij}(\boldsymbol{r}) - \ln\Big(g_{ij}(\boldsymbol{r})\Big) - \beta U_{ij}(\boldsymbol{r}),\ |\boldsymbol{r}| > d_{ij}. \tag{1.86}$$

Certain closure approximations perform better for certain systems and conditions. For instance, the HNC closure has proven to be more accurate than the PY closure when Coulomb interactions and significant disparities in site diameters are present. On the other hand, the PY closure typically yields more accurate predictions when hard-core and short-range pairwise interactions are the only interactions in the system [60].

Molecular closure relations were invented to incorporate chain connectivity correlations (manifesting in $w(\boldsymbol{r})$) and tackle some inconsistencies arising from using atomic closure relations [61]. For polymer nanocomposites, it has been shown that the Percus-Yevick (PY) closure for polymer-polymer and polymer-particle sites with the Hyper-netted chain (HNC) for the particle-particle sites provides reasonable results [49, 50, 59, 62–65]. Recently, a new closure approximation, known as triple-modified Verlet (MV), was introduced by Zhou and Schweizer that showed improvements compared to combined PY-HNC method [66].

One of the challenges of generalizing the RISM formalism to polymers is the dependency of $h_{ij}(\boldsymbol{r})$ and $w_{ij}(\boldsymbol{r})$ on each other. Originally, this was overcome by the ideal chain assumption and Flory ideality theorem [49, 50, 59, 62–65, 67–70]. Although this is a reasonable assumption for homopolymer melts, in other cases, the nonideality and excluded volume effects play an important role and need to be considered. For this purpose, a self-consistent PRISM model was introduced by Schweizer, Honnell, and Curro [71]. This model is being used to study homopolymer melts, and polymer-nanoparticle melts with bare and grafted particles as well as anisotropic particles [72–76].

1.2.8 Self-Consistent Mean-Field Theory

Generally, in field-theoretic approaches, a free energy $\mathcal{F}$ is defined as a non-local functional of one or more potential fields $\psi(\boldsymbol{r})$ [77]. Then, the partition function of the system is expressed as a functional integral of the Hamiltonian:

$$Z = \int e^{-\mathcal{F}[\psi]}\ \mathcal{D}\psi \tag{1.87}$$

where $\int \mathcal{D}\psi$ is the integral over all possible functions $\psi(\boldsymbol{r})$. By extension, the ensemble average of some observable A is defined as

$$\langle A\rangle = \frac{1}{Z}\int e^{\mathcal{F}[\psi]} A[\psi]\ \mathcal{D}\psi. \tag{1.88}$$

Evaluating the above equations for practical models of fluids is difficult and cannot be done in closed form. Therefore, approximations are necessary to be able to utilize these equations and find the thermodynamic variables of interest. The mean-field approximation, commonly referred to as Self-Consistent Mean-Field Theory (SCMFT) in the polymer community, is one way to do so. This approximation is based on assuming that a single field configuration ψ_0 dominates the integrals above. The free energy functional $\mathcal{F}[\psi]$ is typically generalized to be complex and since we have an exponential integrand, then the mean-field ψ_0 corresponds to the saddle points of $\mathcal{F}$ such that

$$\left.\frac{\delta \mathcal{F}[\psi]}{\delta \psi(\boldsymbol{r})}\right|_{\psi=\psi_0} = 0. \tag{1.89}$$

Due to neglect of all other configurations (i.e. coarse-graining or homogenizing), mean-field models do not determine density correlations. Consequently, they do not successfully treat local packing or interaction effects in dense melts [49]. SCMFT is however relatively accurate when dealing with polymer melts at the mesoscale due to screening effects of intermolecular interactions. This is especially true for systems of concentrated high-molecular-weight polymer melts as the concentration fluctuations become insignificant [78].

The effective Hamiltonian is typically a function of the local density $\rho(\boldsymbol{r})$. Therefore, Self-Consistent Mean-Field Theory relates the local density and mean-field potential. By solving the SCMFT equations, one finds the density profile for the system. This is similar to Classical Density Functional Theory in that the structure and thermodynamic properties of the system are described in terms of a local density function [78, 79]. The difference lies in how the effective Hamiltonian or Free energy functional is defined and treated. Further information on Self-Consistent Mean-Field Theory models in different context and its relation to Classical Density Functional Theory (C-DFT) can be found in the literature [50, 77, 78, 80, 81].

1.2.9 Continuum models

In the models considered so far, the internal structure of materials at nano- or meso-scale was explicitly taken into account. Another class of modelling tools, perhaps the oldest, known as continuum or micromechanical models exist that study mechanics of materials as continuous media. The idea of a representative volume element (RVE) is central to such models as it has to statistically represent the local mechanical properties [82]. Micromechanical models have the capability of including interfaces, discontinuities, and couple mechanical and thermodynamic properties.

In the context of fiber-reinforced polymers, linear elasticity is usually assumed for both the fibers and the polymeric matrix:

$$\boldsymbol{\sigma}^f = \boldsymbol{C}^f \boldsymbol{\varepsilon}^f \tag{1.90}$$

$$\boldsymbol{\sigma}^p = \boldsymbol{C}^p \boldsymbol{\varepsilon}^p \tag{1.91}$$

where $\boldsymbol{\sigma}$ is the stress tensor, $\boldsymbol{C}$ is the stiffness tensor, and $\boldsymbol{\varepsilon}$ is the strain tensor. The superscripts f and p stand for fiber and polymer, respectively. As the microstructures are homogenized or coarse-grained in such models, they usually ignore the interfacial matrix-fiber effects and only work with average stress $\bar{\boldsymbol{\sigma}}$ and strains $\bar{\boldsymbol{\varepsilon}}$:

$$\bar{\boldsymbol{\sigma}} = \frac{1}{V}\int \boldsymbol{\sigma}(\boldsymbol{x}) d\boldsymbol{x}, \tag{1.92}$$

$$\bar{\boldsymbol{\varepsilon}} = \frac{1}{V}\int \boldsymbol{\sigma}(\boldsymbol{x}) d\boldsymbol{x}. \tag{1.93}$$

A linear relation between the average stress and strain, like the component-wise quantities, is considered:

$$\bar{\boldsymbol{\sigma}} = \boldsymbol{C}\bar{\boldsymbol{\varepsilon}} \tag{1.94}$$

The total average stress and strain is then assumed to be the superposition of contributions from the fibers and the matrix:

$$\bar{\boldsymbol{\sigma}} = v_f \bar{\boldsymbol{\sigma}}^f + v_p \bar{\boldsymbol{\sigma}}^p, \tag{1.95}$$

$$\bar{\boldsymbol{\varepsilon}} = v_f \bar{\boldsymbol{\varepsilon}}^f + v_p \bar{\boldsymbol{\varepsilon}}^p. \tag{1.96}$$

where v_f and v_p are the volume fractions of the fiber and polymer. The concentration of stress and strain at the fiber is associated with tensors that relate the stress and strain of the fiber to the average stress and strain:

$$\bar{\boldsymbol{\varepsilon}}^f = \boldsymbol{A}\bar{\boldsymbol{\varepsilon}}, \tag{1.97}$$

$$\bar{\boldsymbol{\sigma}}^f = \boldsymbol{B}\bar{\boldsymbol{\sigma}}. \tag{1.98}$$

Finite Element, Halpin-Tsai, Mori-Tanaka, and Equivalent-continuum models are some of the popular continuum models used for polymer-fiber composites. As the next chapters of this thesis are mostly focused on micro- and meso-scale models of polymer-fiber composites, I do not go into details of continuum models. The more in-depth descriptions of such models can be found in the literature [82–87].

In section 1.2, a brief discussion of the theoretical foundations of different modelling approaches that are commonly used in studying fiber-reinforced polymers was provided. The subsequent section will summarize studies conducted in the field of polymer composites and polymer nanocomposites using these methods.

1.3 Application of Mathematical methods in polymer composite modelling

In the last quarter century, there has been significant attention from both industry and academia towards polymer nanocomposites, driven by their superior properties when compared to polymer blends. In this section, I provide a survey of the literature in the field with a focus on theoretical and computational studies. I would like to note that this list is not exhaustive and studies most relevant to the topic of the thesis are presented here. However, there are excellent review articles available for interested readers [50, 82, 84, 88–91].

1.3.1 Molecular Dynamics

In the field of polymer nanocomposites (PNCs), *ab initio* Molecular Dynamics simulations are conducted to analyze interfacial interactions between nanofillers and polymers [92], and to calculate structural and electronic properties [93–95]. However, AIMD is most commonly used to parametrize MD force fields [84, 90]. The force fields then can be used in all-atom Molecular Dynamics simulations to study polymer nanocomposites.

All-atom Molecular Dynamics simulations are a popular tool for studying and predicting properties of nanocomposites with specific chemistry. Schwab and Denniston studied the curing and thermodynamic properties of a UPPH resin by means of all-atom Molecular Dynamics [96]. The measured material properties from their simulations showed good agreement with reported values for the same class of material. In a follow-up work, Schöller et al. investigated the impact of fiber surface and sizing on the distribution and degree of crosslinking [97]. They found that adding the fiber surface reduces the diffusivity in the normal direction to the surface resulting in a lower overall conversion degree of the radical reaction of the final system, compared to a pure resin.

Milano et al. investigated the interfacial behaviour of Polystyrene and gold nanoparticles with and without coating by performing all-atom MD simulations [98]. They observed ordering of polymer chains at the interface of the nanoparticles in both cases. However, the ordering was less significant for the coated nanoparticles.

Ndoro and colleagues studied the interfacial properties of grafted and ungrafted silica nanoparticles in a Polystyrene matrix using all-atom MD [99]. Their nanoparticles were spherical and grafted polymer chains had the same length as the matrix chains. They found that flatter surfaces induce more structure compared to ones with more curvature. They also found that higher densities of grafting limits penetration of matrix chains, as one would expect.

All-atom MD provide a great insight into the interfacial and microscopic properties of PNCs. However, systems that are of industrial interest are at much larger length and time scales and it is not clear how the microscopic interfacial behaviours affect the overall properties of the material. One way to bridge between different length scales is by coarse-graining as defined previously.

coarse-grained Molecular Dynamics (CGMD) is another class of MD simulations that is commonly used in the field of polymer composites and nanocompsites [82, 89, 90]. Starr et al. studied the structural and conformational effects as well as the dynamics of systems with attractive and repulsive polymer-nanoparticle interactions [100]. To this end, they conducted CGMD simulations of a single icosahedral nanoparticle embedded in a polymer melt. They found that the chains near the nanoparticle surface are elongated and flattened. This behaviour was found to be almost independent of temperature, or the interaction nature and strength, for the range of interactions applied in their study.

Liu et al. studied the impact of polymer-nanoparticle interaction, nanoparticle size, and nanoparticle loading on the interfacial properties of polymer nanocomposites [101]. They found that the nanoparticle interfacial layer consists of different segments of different polymer chains which was found to be in good agreement with experimental results of Chen et al. [102].

One of the main barriers in producing high performance PCs and PNCs is the phase separation of the reinforcement agents from the matrix. Smith and colleagues investigated the nanoparticle aggregation and depletion effects of spherical nanoparticles in an unentangled melt by means of CGMD simulations [103]. They used two or five nanoparticles in their simulations. They determined the potential of mean force of the nanoparticles as a function of molecular weight and strength of the polymer–nanoparticle interaction. For weaker nanoparticle–polymer interactions, they observed strong depletion effects caused by the polymer matrix that promoted aggregation. An analysis of the nanoparticle second virial coefficient showed that nanoparticle aggregation increased with molecular weight for relatively weak polymer–nanoparticle interactions.

The shape of nanoparticles can play an important role in the properties of the composite. Toepperwein et al. studied the impact of inclusion of nanorods on the structure and entanglement network of a polymer matrix [104]. For this purpose, they utilized MC and CGMD simulations. All interactions in the system (i.e. rod-rod, polymer-polymer, and rod-polymer) were attractive. The polymer-nanorod interactions were stronger to mimic a more realistic system (i.e. $\epsilon_{pp} = \epsilon_{nn} \leq \epsilon_{np}$). They found that increasing the aspect ratio of the nanorods promotes their cluster aggregation. Performing a primitive path analysis [105], they also found that the inclusion of nanoparticles does not alter the underlying primitive path mesh of the polymer itself. They then concluded that mechanical enhancement in polymer nanocomposites should not be associated with the alteration in the polymer network but with contact and entanglement of the polymer and the inclusion.

Using coarse-grained Molecular Dynamics, Gao et al. investigated the effect of inter-component interaction strength, temperature, filler concentration, cross-linking density, external shear, aspect ratio, and nanorod grafting on the dispersion patterns and kinetics of polymer nanocomposites [106]. For a system in which the polymers were attracted to both rods and polymers, and rods repelled rods, they found that there exists an optimum polymer-rod attraction strength that promotes good dispersion. On the other hand, adding attractive interactions between the rods facilitated formation of nanorod clusters. They also examined the impact of nanorod loading on the dispersion for the system with attractive nanorod-nanorod interactions. They varied the loading from 4.7% to 36.3%. They observed an increase in aggregation with increase in nanorod loading. Moreover, they found that higher cross-linking density or adding an external shear can be used to improve dispersion of the nanorods.

In a recent article, Lu, Wu, and Jayaraman conducted coarse-grained Molecular Dynamics simulations on polymer-rod nanocomposites with homogeneous and patchy surface to understand the effect of nanorod design on final PNCs morphology [107]. In this study, the polymer-polymer, and polymer-nanorod interactions were purely repulsive while the nanorods interacted with an attractive potential. For short nanorods, they observed percolated nanorod structure for the system with patchy rods whereas the simple nanorods phase-separated to a cluster. In the case of long nanorods, both designs exhibited formation of ordered aggregates, either finite-sized or percolating. They also looked into the conformation of polymers at the nanorod interface where they discovered that although the average radius of gyration (R_g) of the polymers remained the same as that of a pure melt, the interfacial chains stretched out and expanded.

Li et al. studied the morphology and mechanical properties of polymer-nanorod composites where nanorod networks are formed due to nanorod attractive interactions [108]. They found that in the presence of the nanorod networks, the stress transferred along the backbone of the network rather than the polymer-nanorod interface. Moreover, they observed improved nanorod structures upon increasing the nanorod volume fraction as well as increasing the length-to-diameter ratio which in turn, led to improved mechanical properties.

CGMD is a great tool to study properties material at larger scales than All-atom MD. However, even at this level of CGMD, performing simulations of highly concentrated PNCs is quite costly. Therefore, such systems have been studied less compared to dilute systems.

1.3.2 Monte Carlo

Monte Carlo (MC) technique is a stochastic method that is used to study interfacial behaviour and structural properties of PNCs [109–118].

In a series of papers, Vacatello utilized MC simulations to study structural properties and chain dimensions of polymer melts in the presence of spherical particles [111, 112, 119]. They studied the impact of particle diameter, and particle volume fraction. They observed that the interfacial polymer segments were densely packed near particle surface similar to planar solid surfaces. The average size of the polymer chains was found to decrease in the presence of particles regardless of the size of the particle. They also examined the order parameter of chain segments (of size 5 beads) with respect to nearest particles and concluded that the interfacial segments align with the surface of the particle.

Termonia studied the conformation of polymer chains at the nanoparticle interface for dense melts of high molecular weight [120]. They used a Lattice Monte Carlo with the unit lattice length being equal to that of a statistical segment for the chains. Their results showed the presence of an interfacial region within which the chains orient tangentially to the filler surface. In addition, they studied the polymer density as a function of the distance from the filler surface. They found that in the interfacial region defined above the density of the polymer is lower. However, the density of the chain-ends were found to be higher in this region.

Pandey et al. studied the conformational characteristics of a Polyethylene melt near a silica slab and highly curved silica nanoparticles using preferential sampling techniques [121] combined with a connectivity-altering Monte Carlo algorithm [122]. They examined the local density of the polymer in proximity of the filler surface. They observed that an increase in the curvature of the particles (decrease of radius) results in a decrease in the length of the train segments (sequences in actual contact with the surface [123]). However, the number of polymer segments in contact with nanoparticles increased. They found that the increased number of contacts stems from more chains interacting with the particle (not different segments of the same chain.) This also appeared to affect the influence of curvature on the bound layer (interfacial region) thickness. Compared to previous studies, Pandey and coworkers observed a more modest decrease in the bound layer thickness as a result of increased curvature.

The number of Monte Carlo studies dedicated to systems of polymer-nanorod mixtures is underwhelming compared to that of polymer-nanoparticle systems. Savenko and Dijkstra studied the phase behaviour of a polymer-nanorod system for different polymer-to-nanorod diameter ratios. In this study, they conducted Monte Carlo simulations of a polymer-nanorod system using an effective Hamiltonian that accounted for the effect of the polymer matrix implicitly [124]. The polymers were assumed to be noninteracting but excluded from the surface of the rods by a distance equal to their radius of gyration. Their phase diagrams showed regions of the isotropic (I), nematic (N), smectic-A (Sm), and crystalline (K) phases. They observed that the phase diagram for large polymer chains exhibits an isotropic gas-liquid type phase separation. Moreover, the phase diagram showed I-N-Sm and I-Sm-K triple points and broad coexistence of I-N, I-Sm, and I-K phases. A decrease in the polymer-to-nanorod diameter ratio resulted in a shift of the I-N-Sm triple point to higher values of polymer packing fractions leading to a broad I-K coexistence region. At the lowest polymer-to-nanorod diameter ratio, they observed an I-N-K and an N-Sm-K triple point.

Jiang and colleagues studied physical and optical properties of films of gold nanorods and Poly(2-vinylpyridine) using transmission electron microscopy (TEM) and MC simulations [125]. They observed that the dispersion of nanorods evolves from side-by-side alignment to end-to-end linking as the volume fraction of the nanorods is increased.

Monte Carlo methods provide a computationally efficient approach to study equilibrium properties of PNCs. However, MC simulations have been less commonly employed to investigate the structural characteristics of dense mixtures of nanoparticles and polymers. This is due to the inherent difficulties in executing moves that involve nanoparticles. As a result, MC simulations have been predominantly employed in scenarios where nanoparticles remain stationary.

1.3.3 Dissipative Particle Dynamics

Dissipative Particle Dynamics (DPD) is a popular mesoscopic method to study soft matter [16, 17, 126]. Polymers and polymer nanocomposites have not been an exception [50, 82, 127–130].

Lin et al. studied the self-assembly of grafted nanoparticles (i.e. nanoparticles with polymer chains grafted onto them) with different shapes [131]. The results showed a positive relationship between the length (L_g) and number (N_g) of grafted polymers with the dispersion of the nanoparticle, i.e. dispersion improves when L_g and N_g of grafted polymers is increased. Different superstructures were observed for different nanoparticle geometries. In the case of nanorods, spherical structures formed at low L_g and N_g and transformed to side-by-side packing as length and number of grafted polymers was increased. The interplay of enthalpic solvophilicity and excluded volume effect resulted in "fillet-like" shapes at large N_g and small L_g while at large N_g and L_g, ribbon-like structures appeared (see Fig. 7 in Ref. [131]). Further increase in the length and number of grafted chains led to complete dispersion of the nanorods in the polymer.

Khani and coworkers studied the self-assembly and phase behaviour of grafted nanorods in a homopolymer matrix [132]. The length and density of grafted chains as well as graft-matrix interactions were chosen as control parameters. For a non-interacting graft-matrix system, at low grafting densities, the graft length did not have a significant impact on the phase behaviour leading to the conclusion that the depletion forces are dominant in this limit. However, beyond this limit, increasing the length and density of the grafted chains resulted in better dispersion due to the balance between excluded volume and depletion effects. The graft-matrix attractions did not affect the dispersion patterns at low grafting densities. But they observed a larger dispersion window with dispersion occurring at relatively lower degrees of grafting when the attractions were stronger. Rich and complicated structures were observed in the presence of repulsive forces between the matrix and the grafted chains.

Dissipative Particle Dynamics is a mesoscopic method that recovers hydrodynamics and can be applied to larger time scales than molecular simulations as it allows for larger time steps. However, like any coarse-grained model, care should be taken setting parameters to get correct hydrodynamic behaviour. DPD was originally proposed as a method to simulate fluids on a mesoscale. However, it is more often used as a momentum conserving thermostat (e.g. in place of Langevin thermostat) in Molecular Dynamics simulations.

1.3.4 Classical Density Functional Theory

Classical Density Functional Theory (C-DFT) has been used to study the depletion effects in polymer-nanoparticle systems [49, 133–135]. Patel and Egorov conducted C-DFT simulations of two hard spheres in a solution of freely jointed polymers [133, 134]. They measured the colloid-colloid excess mean force, potential of mean force, and the second virial coefficient for different polymer densities, chain lengths, and colloid/polymer size ratios. They observed an increase in the depletion attraction, pushing the spheres closer, when the density was increased. The colloid-colloid second virial coefficient was found to monotonically decline with the solution density. For a specific density, however, the second virial coefficient decreased when either the polymer chain length or the colloid size was increased, corresponding to higher tendency towards forming colloidal aggregates for larger colloids or longer chains.

Frischknecht and Yethiraj performed the first three-dimensional DFT calculations to determine two- and three-body interactions among nanoparticles in an athermal polymer melt [136]. They found three-body interactions to have a significant role in such systems even with purely repulsive interactions. They then conclude that systems of polymer nanocomposites cannot be modelled accurately unless these interactions are accounted for.

Shou et al. studied morphological properties of a rod-diblock copolymer system using a SCMFT/DFT technique [137]. They found that the aspect ratio of the rods affects their spatial distribution. A transition from cylindrical to lamellar morphology was observed when the length of the rods was increased. To determine the mechanical properties of the mixture, the final configuration of the simulations were imported into a Lattice Spring model and the elastic response of the system was measured. They found that higher rod aspect ratios result in an improvement of the Young's modulus.

Bryk developed a DFT model to study mixtures of polymer and hard rods [138]. The model was then applied to study the phase separation of such systems. A demixing similar to hard-sphere-rod systems is predicted. They observed that the critical packing fraction decreased as a function of the chain length.

1.3.5 Polymer Reference Interaction Site Model

Hooper and Schweizer performed Polymer Reference Interaction Site Model (PRISM)-based simulations of a pair of spherical nanoparticles in a homopolymer melt and studied the structural properties of the system [63]. They investigated the impact of the particle-to-monomer size ratio, chain length, and monomer-particle interaction strength and range. They observed four nanoparticle arrangements. For weak polymer-particle attractions, direct contact aggregation of the particles was dominant due to depletion effects. At moderate attraction ranges, polymer-bridged contact between the particles was observed while for long range attractions, a stable polymer bound layer around the nanoparticles was formed and led to steric stabilization. For long range and strong attractions, They found particles arrangements similar to polymer-bridged case but this time with a bound layer around the particles. This configuration was called a tele-bridged configuration.

Hall and Schweizer extended the application of PRISM to study the morphology and phase behaviour of anisotropic nanoparticles in a dense absorbing polymer melt [139]. They compared the result for 3 nanoparticle geometries, namely, rods, disks, and cubes. At the infinitely dilute regime, the second virial coefficient curves as a function of interaction strength took a concave shape with small variations in the middle and sharp declines at low and high interaction strengths. This was associated with depletion effects at low interaction strengths, steric stabilization at intermediate strengths, and polymer-induced bridging at high strengths. In this work, they also studied the effect of nonzero filler concentration on the nanoparticle Potential of mean-field, and depletion and bridging induced phase separation. However, the filler concentration and aspect ratio (for the rods) were picked under the threshold for isotropic-nematic transition which were not addressed in this work. They observed that the miscibility region broadened (larger range of interaction strengths) with a decrease in the dimensionality of the nanoparticles (cubes being least miscible). The tendency to phase separation via polymer bridging showed a monotonic behaviour as a function of nanoparticle dimensionality, i.e. rods required a much higher interfacial attraction to induce strong bridging.

Tripathy and colleagues studied the structure and phase behaviour of athermal and attractive nanorods in a dense polymer matrix [140]. They studied polymers of diameter $d = 0.5$ and rods with diameters, $D = 0.5,\ 1,\ 2,$ and 5 (in LJ units). The aspect ratio of the rods was varied in the range of 1 to 100. The polymer nanocomposite has a total volume fraction of 0.4, and the volume fraction of nanoparticles was 0.004. They observed nanoparticle arrangements similar to those described by Schweizer et al. [63, 139]. However, they found the limits of these regimes sensitive to the aspect ratio, surface roughness, and nanorod thickness. The region of miscibility between depletion-driven and bridging-driven phase separations diminished rapidly with increasing aspect ratio, particularly when the interactions between polymer and nanoparticles were attractive.

In a follow-up work, they compared the structure and phase behaviour obtained from PRISM theory and MD simulations of 1% volume fraction of nanorods in a polymer melt [141]. They found that PRISM theory predicts a slower narrowing of the dispersion window as a function of nanorod aspect ratio which was attributed to using the equivalent-site approximation for rigid rods.

Polymer Reference Interaction Site Model has been widely used to study dispersion and morphology of PNCs. The advantage of using PRISM lies in equilibrium nature of the model as the equilibration time of polymer nanocomposites systems, especially in the presence of long polymer chains, is considerably long. However, PRISM theory has limitations when applied to PNCs. As a liquid-state theory, PRISM cannot predict the behaviour of the crystalline state, particularly at higher filler loadings [60].

1.3.6 Self-Consistent Mean-Field Theory

Self-Consistent Mean-Field Theory (SCMFT) has commonly been used to study phase behaviour of polymer nanocomposites [49, 50, 82, 142–148]. Surve et al. studied the polymer adsorption characteristics, pair-interaction potentials, and phase and percolation behaviour of a mixture of spherical nanoparticles in a polymer melt using a combination of Self-Consistent Mean-Field Theory and McMillan-Mayer framework [149]. For low polymer concentrations, their results showed a phase separation between the polymer and nanoparticles due to a bridging attraction while at higher polymer concentrations, the mixture was stabilized by the polymer excluded volume effects. The particle-to-polymer size ratio was found to directly affect the pair interactions and phase behaviour such that smaller particles improved the stability of the mixtures.

They further extended their model to study the phase behaviour of polymer-nanorod systems [150]. The effect of polymer adsorption strength, polymer concentration, the relative sizes of rods and polymer, and rod aspect ratio on the isotropic-nematic phase transition as well as percolation transition was studied. In the presence of non-adsorbing polymer, they found that the depletion forces led to a large two-phase region, expanding with increased polymer concentration. On the other hand, the addition of adsorbing polymers resulted in a more diverse phase behaviour, with high polymer concentrations causing repulsive interactions that stabilized the rods. At a fixed volume fraction of rods and polymers, they observed the dispersion to go from immiscible at weak interactions to stable and then immiscible again as strength of polymer-particle interaction was increased. Further increase of the interactions led to another stable phase for the highest attractions. This phase behaviour was called "reenterant".

Self-Consistent Mean-Field Theory is highly effective for describing long-wavelength concentration patterns. However, due to its mean-field nature, the intermolecular pair correlations are not determined. This limits the ability of the method to address local packing or polymer-particle interfacial behaviour.

1.3.7 Summary and Motivation

In this section, I reviewed some of the computational and theoretical studies that have been done in the field of polymer composites and nanocomposites. A majority of the literature is dedicated to understanding systems of spherical particles in a polymer matrix under athermal conditions (i.e. only excluded volume interactions were applied). In addition to depletion forces, the structural properties of the polymer chains at the interface and the phase behaviour of the mixtures were investigated. In spite of providing a great insight into depletion effects, athermal systems are not commonly adopted in practice due to poor performance. Some of the studies mentioned above examined the impact of polymer-particle and particle-particle attractions on the phase behaviour of polymer nanocomposites. The presence of such interactions and their interplay with depletion effects was found to significantly affect the phase and mechanical behaviour of the system.

Surface treatments like functionalization or adding sizing agents not only result in more uniform dispersion of nanoparticles but also improve the interfacial interactions between the rods and the polymer matrix which is critical for achieving good mechanical properties [3, 151–154]. Stronger interfacial adhesion facilitates the stress transfer from the matrix to the nanorods thus improving the interfacial shear stress (IFSS) strength and performance of the nanocomposite [155–159]. Therefore, it is interesting and useful to investigate polymer nanocomposites (PNCs) systems with attractive polymer-rod interactions. In chapter 2, we study the phase behaviour of a polymer-nanorod melt where the interactions between the polymer and the nanorods is attractive. Additionally, we investigate the interfacial behaviour of the polymers at the nanorod surface.

High- and ultrahigh-density (>50%) polymer nanocomposites have been less studied due to the practical difficulties in their production. However, recently several methods have been implemented to overcome some of these barriers [160–162]. Moreover, performing simulations, especially molecular simulations, of dense systems of polymer nanocomposites were too computationally costly until recently. Therefore, most of the computational studies have focused on dilute systems. It has also been shown that high- and ultrahigh-density polymer nanocomposites exhibit exceptional properties such as improved toughness [163] and have potential to be used in energy storage and conversion devices [164]. Therefore, they are of high interest. Since both lower and higher concentrations are practically relevant, it is important to understand the impact of concentration on the properties of a polymer-nanorod composite system and discover any possible behaviour changes from lower to higher concentrations. Hence, in chapter 2, we utilize coarse-grained Molecular Dynamics (CGMD) simulation to study the effect of concentration on the phase behaviour of a polymer-nanorod melt over a wide range of concentrations up to 0.44 particle fractions.

1.4 Models of polymer crystallization

Crystalline polymers are versatile materials with many applications. For example, polyethylene is known for its excellent chemical resistance and is used in pipes and tubes to transport water and chemicals. Dry-cleaning covers are also thin films of polyethylene. Other examples include polypropylene which is often used for packaging, polyamides and polyesters which play an important role in the fashion industry and clothing [165].

Unlike small molecules, polymeric materials never reach 100 percent crystallinity and therefore are usually referred to as semi-crystalline polymers. As the degree of crystallinity directly impacts the properties of the product, there has been a lot of effort dedicated to understand mechanisms of polymer crystallization experimentally [166–168], computationally [169–171], and theoretically [165, 172–174].

As the conditions of processing affect the crystallization of the polymer, it is important to understand the kinetics of crystallization to be able to predict the degree of crystallization of the final product. A long line of kinetic theories of polymer crystallization started with Avrami equation which was independently derived by Andrei Kolmogorov in 1937, Melvin Avrami in 1939, and Robert Franklin Mehl and his graduate student W.A. Johnson in 1939 [175–177]. The original Avrami kinetic equation was derived based on an instantaneous nucleation assumption, that is, a certain number of germ nuclei exist at the beginning which may, or may not, grow into crystalline grains through the process. Two modes of transformation are considered: growth and ingestion by growing nuclei of crystals. Then, the changes in the number of germ nuclei $N(t)$ can be related to the volume of the new/crystalline phase by

$$N(\tau) = \bar{N}(1 - V(\tau)) \tag{1.99}$$

where $\bar{N}$ is the initial number of germ nuclei, $\tau = ndt$ is the characteristic time and n is probability of formation of growth nuclei per germ nucleus per unit time, and $V(\tau)$ is the volume of the new phase per unit volume of space. Avrami then defined extended volumes V_{ex} based on the Taylor expansion of the functional $V[N(\tau)]$ in terms of N. Conceptually, these extended volumes correspond to the volume of the growing nuclei without considering any overlap between them (undisturbed nuclei). Avrami showed that if there are $N(t')$ nuclei at time t' that each grow to volume $v(t, t')$ at later time t, then the total transformation volume is found to be

$$V_{ex}(t) = \int_0^t N(t')v(t, t')dt' \tag{1.100}$$

where $V_{ex}(t)$ is the total (extended) volume. In the subsequent paper, he considered the case where the centre of the grains are randomly distributed. Using this assumption, he derived a relation between the transformed volume and the extended volume as

$$V = 1 - \exp(-V_{ex}). \tag{1.101}$$

Often in the literature, it is mentioned that the Avrami equation (Eq. 1.101) is specific to isothermal conditions despite the fact that it is explicitly mentioned in the original papers that no condition was used to derive the above equation except for the local random distribution of grains [172, 178].

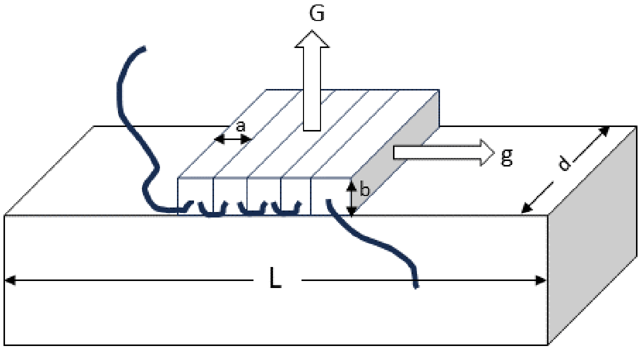

Figure 1.3: The Hoffman-Lauritzen model and relevant dimensions are illustrated.a and b are the width and thickness of the stem, respectively. L is the length of the growth front, and d is the length of the stem. g shows the rate of lateral growth and G shows the rate of perpendicular growth (crystal growth rate) [188].

However, he further derived the equations for the isothermal case arriving at the equation below:

$$V(t) = 1 - \exp\left(-k(\theta)t^m\right) \tag{1.102}$$

where V is the relative crystallinity (transformed volume) at time t, m is the Avrami index, θ is the temperature, and k is the isothermal crystallization rate accounting for nucleation and growth rate. Eq. 1.102 although successful in providing a clearer picture of crystallization mechanisms, has limited application in modelling crystallization during processing of materials as such processes are almost always non-isothermal. This was the motivation for introducing non-isothermal models such as Ozawa and Nakamura models [179, 180].

Another theory broadly used in the polymer community to model crystallization is the Hoffman-Lauritzen (HL) model [173, 181, 182]. In the framework of classical nucleation theory [174, 183, 184], this model was proposed to theoretically describe the crystallization of linear polymer chains into chain-folded lamellae observed in the experiments by Keller et al. and other groups in the late 1950's [185–187]. In this model, the crystallization starts with deposition of a polymer segment onto a crystal surface. The polymer segments that crystallize onto the substrate are called stems and are used to describe the crystallization process. In this sense, the HL model is a coarse-grained model. An illustration of the HL model is shown in Fig. 1.3.

After the formation of the first stem, the attached segments fold regularly next to each other and grow in the lateral direction g. If σ_l and σ_f are respectively the lateral and folding surface free energy, then the free energy of formation for an n-fold layer is

$$\Delta F = 2bd\sigma_l + 2bdn\sigma_f - 2bd(n+1)\Delta H_f \tag{1.103}$$

where b is the thickness of a stem, d is the length of the stem, and ΔH_f is the heat of fusion. Different chains may crystallize onto the substrate until the entire length of the substrate (denoted by L) is filled with crystallized chains. The completion of the growth front can either happen very quickly before formation of new nuclei or numerous nuclei form and growth front grows slowly. Hoffman and Lauritzen defined two different regimes to address each case. In regime I, corresponding to rapid completion of layers, the growth rate is found to be

$$G = r_d bL = \frac{S_T}{aN_A} bL \tag{1.104}$$

where r_d is the stem deposition rate, S_T is the total flux of nucleating polymers (stem formation), and N_A is Avogadro's number. In regime II, where numerous nuclei form and spread slowly, the growth rate is

$$G = b\sqrt{r_d g} = b\sqrt{\frac{S_T g}{aN_A}} \tag{1.105}$$

where $r_d g$ is the surface nucleation rate. It is worth mentioning that Hoffman and Lauritzen did not consider chain-end effects in their derivations. In the above equations, S_T needs to be found in terms of model quantities. I do not go into details of the derivation of this quantity here but it is important to point out that they split the contribution of the free energy of fusion into the activation energy of forward and backward reactions [188, 189]. This leads to a Turnbull and Fisher type [190] equation for the growth rate:

$$G = G_0 \exp\Big(-\frac{U}{R(T - T_\infty)}\Big) \exp\Big(-\frac{K_g}{T\Delta T\zeta}\Big) \tag{1.106}$$

where U is the activation energy for segmental jump rate [189, 191], R is the universal gas constant, $\zeta = 2T/(T_m^o + T)$, and $\Delta T = (T_m^o - T)$ where T_m^o is the equilibrium melting temperature. For regime I,

$$K_g = \frac{4b\sigma_l\sigma_f T_m^o}{\Delta H_f k_B}, \tag{1.107}$$

and for regime II,

$$K_g = \frac{2b\sigma_l\sigma_f T_m^o}{\Delta H_f k_B}. \tag{1.108}$$

Hoffman et al. also showed that under appropriate conditions, i.e. heterogeneous and instantaneous formation of nucleation sites, the bulk rate constant Z_3 in the bulk crystallization isotherm

$$\chi = \chi_0 \Big[1 - \exp(Z_3 t^3)\Big] \tag{1.109}$$

is related to the growth rate as

$$Z_3 = \frac{4\pi v_0}{3} G^3 \tag{1.110}$$

where χ_0 is the maximum crystallinity at the end of stage 1, and v_o is the number of growth centres per volume. In this model, Hoffman divided the crystallization process into two stages: stage 1 where crystallization is nucleation-controlled and stage 2 where crystallization of short chains is driven towards completion and interlamellar links are removed. Stage 2 is considered to be diffusion-controlled. This idea was later used by Patel and Spruiell to find the half-time factor in the non-isothermal kinetic model of Nakamura [192].

The above models have had a reasonable amount of success in predicting the evolution of the overall crystallinity of polymer samples. However, they do not provide much information about the shape or distribution of the crystalline microstructure. Microstructures generally refer to compositional or structural inhomogeneities in materials caused by processing and are known to directly influence the properties of the final product [38].

Huang and Kamal presented a model for the morphological solidification of polymers, addressing the challenging multi-scale nature of polymer crystals and the complexities in their modeling [193]. They assessed existing morphological modeling approaches at the time, including Voronoi, modified Avrami-Evans, cellular automata, and phase-field models, highlighting their geometric, phenomenological, and computationally demanding nature. Emphasizing the necessity for more quantitative and computationally manageable models, they incorporated insights from phase-field and nucleation theories to define their model variables and set up the model. The model involved coupled equations of an envelope growth equation tracking spherulite boundaries and impingement, and a lamellar orientation equation replicating the Maltese cross morphology of the spherulites. The growth velocity of the envelope was determined by the HL equation and lamellar orientation was reproduced using the Frank equation [194]. To address nucleation, they embedded nucleation seeds and defined a critical nucleus radius larger than which nuclei would be stable and grow. The chain conformation effects in the initial crystallization stages were ignored in this model. The results were compared to Polyethylene experiments. The obtained spherulitic growth and impingement kinetics showed good agreement with the experiments. In these simulations, the growth velocity and the position of the nuclei were measured from experiments and used as an input.

Molnar and coworkers introduced a probabilistic method of polymer crystal nucleation and growth [195]. The model, in conjunction with experimental data, was used to estimate spherulite size, distribution, and nucleus density in the absence and presence of nucleating agents. In their model, the growth front of the spherulites was not tracked and the conversion degree and spherulite size distribution was estimated based on the phase transition time. The conversion curves generated by their model under isothermal conditions showed good agreement with experimental results.

Phase-field models are a powerful tool to study free boundary problems and systems with different phases [37, 38, 196]. Xu et al. studied spatio-temporal growth of isotactic polystyrene single crystals during isothermal crystallization using a phase-field model [197]. Wang et al. introduced a phase-field model to study isothermal crystallization of polymer melts [198]. Their model was able to reproduce various single crystal morphologies found in isotactic polystyrene such as dendritic, lamellar branching, faceted hexagonal, and spherulitic structures.

Bahloul et al. modified the phase-field model proposed by Kobayashi for solidification and dendritic growth [199] to account for crystallization characteristics of polymeric material [200]. The main equations of the model are the phase-field and heat equations:

$$\frac{\partial \phi}{\partial t} = -M \frac{\delta \mathcal{F}(m(T), \phi)}{\delta \phi}, \tag{1.111}$$

$$\frac{\partial T}{\partial t} = \frac{\kappa}{\rho C_p} \nabla^2 T + \frac{\Delta H}{C_p} \frac{\partial \phi}{\partial t} \tag{1.112}$$

where ϕ is the phase-field order parameter or crystallinity, M is the mobility corresponding to the inverse of the characteristic time of attachment of atoms at the interface, and $\mathcal{F}$ is the free energy functional. In the heat equation, T stands for the temperature and κ, ρ, and C_p are respectively the thermal conductivity, density, and heat capacity. The second term on the right hand side of the heat equation is the source term corresponding to the latent heat of crystallization. The phase-field equation is coupled to the heat equation through function $m(T)$ in the local free energy. The heat equation is coupled to the phase-field parameter through the source term. Anisotropy and noise are added to the interface to reproduce dendritic patterns of crystalline areas. The improvement to Kobayashi's model was made by modifying the mobility M and the source coefficient $\frac{\Delta H}{C_p}$ to incorporate Hoffman-Lauritzen theory. Comparing their results to experiments [201, 202], they state that their model quantitatively predicts the growth rate and reproduces accurate morphologies in a specific range of temperatures. Later in a follow-up work, Bahloul and colleagues performed full-field micromechanical simulations on the microstructures generated by their modified phase field model to predict the effective mechanical properties [203]. As will be discussed, the main challenge in using Kobayashi-type models in modelling polymer composites is the computational cost associated with reproducing details like dendritic branches.

Polymers often show up in the industry in form of composite materials due to improved functionality and performance. However, the addition of reinforcing components such as fibers affects the crystallization process. Therefore, new assumptions and methods are required in their modelling. Krause et al. studied the spherulitic growth of a fiber-reinforced polymer using computer simulations [204]. Mehl and Rebenfeld generalized the Avrami model to account for the influence of fibers in the presence of both thermal and athermal nucleation [205, 206]. Benard et al. took on an analytical approach based on the geometric method of Avrami to study the impact of fiber inclusion on isothermal crystallization polymers [207]. Haudin and Chenot developed a set of differential equations based on the Avrami model [208]. This allowed them to numerically solve spherulite evolution in polymer injection molding without oversimplifying assumptions. They also studied the size distribution of the spherulites using their model. Later, they extended their model to long-fiber thermoplastic composites including the impact of fiber surface transcrystallinity [209]. Galeski et al. proposed an analytical model of crystallization kinetics for polymer composites with fibers and nanofibers [210]. Ruan and co-workers investigated the crystallization of short fiber-reinforced composites during the cooling phase by means of a multi-scale model that coupled the macroscopic heat equation to the mesoscopic crystal morphology [211, 212].

1.4.1 Summary and Motivation

In this section, I reviewed some of the most commonly used crystallization models for polymeric systems. Avrami's model and its derivatives have shown great success in modelling the crystallization kinetics of polymers. Although crystal structure and processing conditions are accounted for in the derivation of such models, they do not explicitly reproduce the microstructure of the semi-crystalline polymer. But, they only describe the overall kinetics and degree of crystallinity of the material. The Hoffman-Lauritzen (HL) model describes the nucleation and growth of crystals assuming that chain folding is the main mechanism of crystallization. This model provides a relation to calculate crystal growth rate of crystal lamellae. However, it does not provide a method to locate and track crystal microstructure.

Phase-field methods offer a convenient way to track boundaries of multi-phase systems. Kobayashi proposed a phase-field model for solidification and dendritic growth. To achieve this, he coupled the evolution equation of the order parameter with heat conduction equation. He also introduced a noise term at the diffuse boundaries to reproduce the dendritic shapes. This model has been adopted by the polymer community to model spherulitic growth and polymer crystallization. The results obtained from such models show good agreement with experiments. The main challenge in using Kobayashi-type models in modelling polymer composites is the computational cost. The dendritic branches reproduced by such models is at the nanoscale. The length fibers in fiber-reinforced polymers can be between several microns to several millimetres. Therefore, simulating such systems would require a massive amount of memory and time.

In chapter 3, we propose a coarse-grained model of polymer crystallization using a multiphase-field approach. The multiphase-field method (MPF) is coupled with the Nakamura model and the equation of heat conduction to model the non-local crystallization of polymeric materials on a microstructural length scale. The MPF is a generalization of the classical phase-field method to numerous locally present phases [39]. This readily allows for the inclusion of extra phases such as fibers and the study of their impact on the crystallization of the polymeric material. In our model, rather than tracking the evolution of every single nucleus, we define crystalline regions the crystallinity of which are predicted by the Nakamura model. The coarse-grained definition of our crystalline region enables us to model larger domains relevant to fiber-reinforced systems.

1.5 Chapter Outline

In this chapter, I provided an overview of different theoretical and computational methods commonly used to study soft material particularly polymers and polymer composites. In this thesis, I will apply three of the methods discussed, namely, Molecular Dynamics, Lattice Boltzmann, Phase-Field to study different aspects of polymer composites and nanocomposites.

In chapter 2, I employ coarse-grained Molecular Dynamics (MD) simulations to shed light on the phase-behaviour of nanorods in a polymer melt at the nanoscale. The chapter addresses the impact of nanorod concentration on their dispersion and orientation in the melt. I start the chapter with describing the methodology and simulation details followed by a results section.

Chapter 3 addresses the non-isothermal crystallization of polymers and their crystal morphology. In this chapter, I present a novel coarse-grained model that can capture certain microstructural properties of the material while keeping computational costs low. This chapter is arranged as follows: In section 3.2, we describe our model and the comprising equations. In section 3.3, we share our experimental findings of our Differential Scanning Calorimetry (DSC) and Polarized Light Microscopy (PLM). We discuss the numerical implementation of the model and details regarding numerical constants and parameters in section 3.4.1 followed by 3.4 where we share the results of our simulations and the comparisons to experimental data. We finish off the article with a summary of the model and the results in 3.5.

In chapter 4, we introduce a new velocity discretization method for the Lattice Boltzmann Method (LBM) which allows for systematic extension of the LBM to compressible flows as well as conserved energy and viscoelastic fluids. We first derive the evolution equations for the new LBM. This is followed by several test cases including sound wave propagation and Poiseuille flow. We also show that our model satisfies Galilean invariance, even when a density gradient is present, by reproducing a Couette flow in the presence of gravity.

Chapter 2

Dispersion and Orientation patterns in polymer-nanorod melts

Mixtures of anisotropic fillers, especially nano-fibers (NFs) and nano-tubes (NTs) in polymer matrices have shown a great potential to produce high performance materials and therefore have received a lot of attention from scientific and engineering communities [84, 88, 213–220]. On top of the intrinsic properties of the nanorods, their distribution and orientation in the polymer matrix, interaction with the matrix, and aspect ratio play a crucial role in the overall performance of the material [154, 221–223]. A larger aspect ratio of the nanofillers is known to increase the efficiency of the polymer nanocomposite [154, 223] and previous computational works have studied the effect of nanorod length [104, 224]. However, in this study, we have polymer chains and nanorods with fixed lengths in all simulations and instead turn our focus to the effect of concentration on dispersion patterns of nanorods in a system with polymer-rod attractions.

One of the main barriers in enhancing properties of polymeric materials through adding NTs or NFs is the formation of aggregates which leads to problems such as non-uniform stress distribution and slippage [225, 226]. In spite of the development of preparation and processing techniques such as in situ polymerization and surface modification that have been successful in promoting better dispersion of nanorods in a polymer matrix [217, 221, 225, 227–234], there is a need for a deeper understanding of the underlying physics that leads to the observed phase behaviour in nanorod-polymer systems. As a result, it has been under an extensive examination both theoretically [109, 139, 150, 235] and computationally [100, 104, 106, 107, 124, 140, 141, 236–238]. An overview of the studies in this field was provided in chapter 1.

The dispersion patterns of nanorods in a pool of attracting polymer chains is a less explored field and is the focus of this paper. To get a better idea of what is driving the phase behaviour in the system we contrast our results with those of a system with purely repulsive nanorod-polymer interactions but otherwise identical. Using coarse-grained Molecular Dynamics (CGMD), we simulated a polymer-nanorod melt where all interactions were repulsive except for polymer-rod and looked at the dispersion and orientation of rods as well as the conformation of polymer chains at the rod interface. This work is the result of my collaboration with Venkat Balasubramanian, and Colin Denniston and it has been published in the Journal of Chemical Physics [239].

This chapter is designed as follows: In section 2.1, we go over the simulation setup and details.

Section 2.2 is dedicated to results and discussion where we first describe the dispersion patterns of the rods by means of auto-correlation of a number density, and rod-rod distances and then delve into orientational behaviour of the nanocomposite melt. We sum up the paper by pointing out the main findings in section 2.3.

2.1 Methodology

In this work, we adopt a coarse-grained approach to model the polymer-nanorod mixture. The melt is comprised of a mix of polymer chains and rigid nanorods. Each polymer molecule is composed of $n_p = 32$ consecutive beads (monomers) connected via Finitely Extensible Non-linear Elastic (FENE) bonds (cf. Fig. 2.1a). The Kremer-Grest FENE potential[240]

$$U_b = -\frac{1}{2}KR_b^2 \ln\left[1-\left(\frac{r}{R_b}\right)^2\right] + 4\epsilon_b\left[\left(\frac{\sigma}{r}\right)^{12}-\left(\frac{\sigma}{r}\right)^{6}+\frac{1}{4}\right]H\left(2^{\frac{1}{6}}\sigma\right) \tag{2.1}$$

is used to implement all the bonded interactions necessary for the monomer inter-connectivity. The first term on the RHS is attractive in nature with $K = 30\epsilon_b\sigma^{-2}$ being the effective elastic constant where $\epsilon_b = 1.0\epsilon$ and $\epsilon = \frac{m\sigma^2}{\tau^2}$ is the Lennard-Jones energy constant. Here, m is the Lennard-Jones(LJ) unit mass, σ is the LJ length scale, and τ is the LJ time scale. $R_b = 1.5\sigma$ is the maximum bond extension in any direction [240]. On the other hand, the second term on the RHS represents the repulsive portion of the potential with the cut-off length $r_c = 2^{1/6}\sigma$, at the minimum if the LJ potential, enforced through the Heaviside function $H(x)$ (i.e. shifted-truncated LJ). This form of potential also eliminates nonphysical bond crossings [240]. The excluded volume of the polymer chains is implemented through a repulsive $12-6$ LJ potential similar to the one used for the FENE bonds between the polymer beads. The interaction cutoff of the polymer-polymer interactions is also set to $r_{pp} = 2^{1/6}\sigma$ and the strength is $\epsilon_{pp} = 1.0\epsilon$. Interactions between the polymers and rods are also of a $12-6$ LJ potential form with strength $\epsilon_{rp} = 1.0\epsilon$. However, the cutoff length for these interactions is set to $r_{rp} = 2.5\sigma$ creating attraction between the polymer chains and the nanorods. To help understand the effect of attractive forces, we compare our results to systems that are identical except for lacking the attractive part of the potential by setting $r_{rp} = 2^{1/6}\sigma$ (and adding a constant shift so that they are zero at the cutoff).

The rigid rods in our system consist of four individual threads (sub-rods) which are assembled in a helical pattern as shown in Fig.2.1b. Each thread is comprised of $n_r = 16$ point particles (monomers) of mass m and diameter σ where m and σ are the LJ unit mass and length, respectively. The monomers are interconnected along the backbone via the FENE bonds described in Eq. 2.1 and rigidity of the rods is ensured by a harmonic angle potential U_h for every monomer *triad* along the backbone

$$U_h = k\left(\theta-\theta_0\right)^2 \tag{2.2}$$

where $k = 1000$ (LJ units) is the spring constant, θ is the angle formed by a triad at any given time during the simulation and θ_0 is its equilibrium value. A rigid conformation is obtained by penalizing any bending of the rods by setting $\theta_0 = 180°$ during the energy minimization step. However, at equilibration and production stages, each rod is treated as a rigid body to reduce computational cost of the simulation without compromising the physics. The diameter and length of the rods are respectively $D \approx 2.35\sigma$ and $L \approx 13.35\sigma$ giving them an aspect ratio of about 5.5. Atoms are spaced

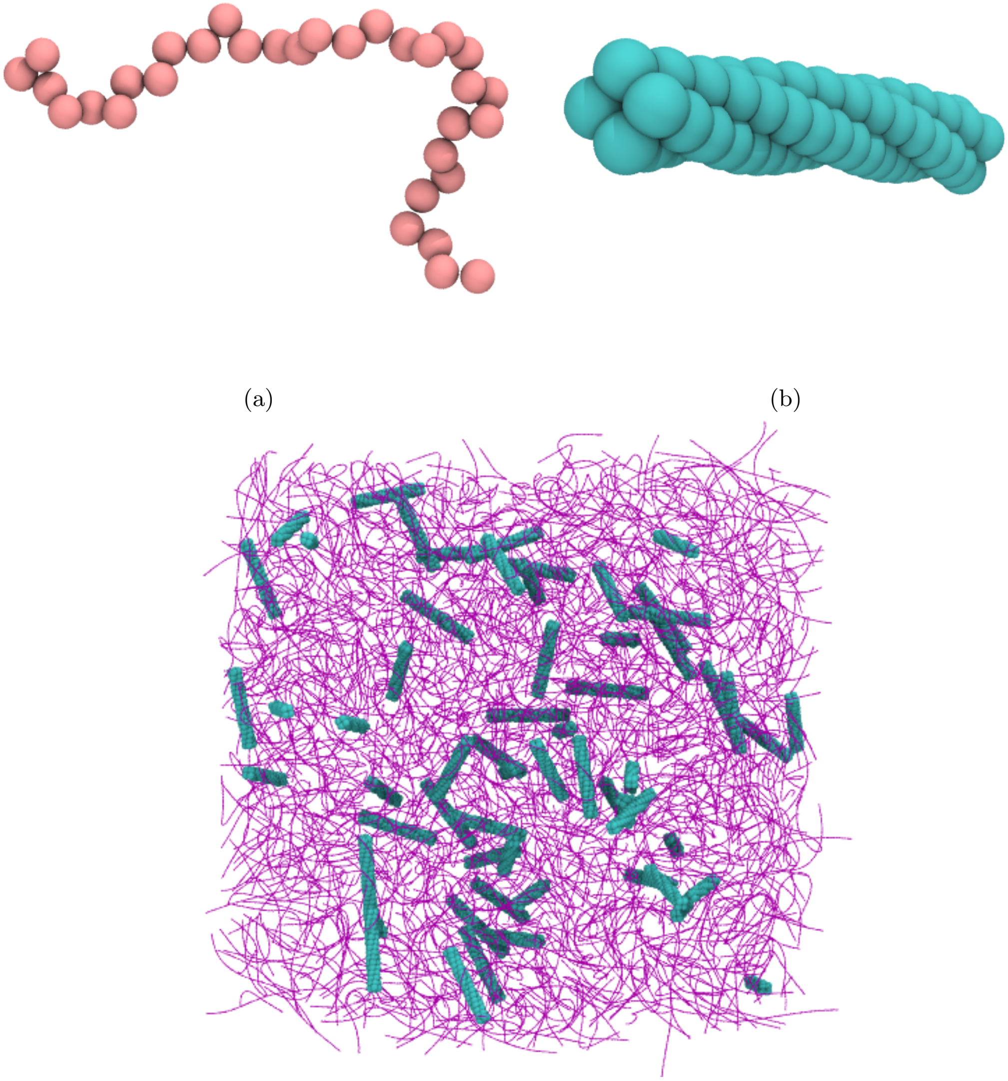

(a) (b)

(c)

Figure 2.1: An example of polymer chain is shown in (a) while (b) shows a lateral view of a nanorod. A random initial configuration shown in (c) (before energy minimization), is generated using moltemplate package for each realization. The nanorods are shown in cyan(green) and the polymer chains are shown as purple lines. The VMD software was used for visualizations [241].

approximately 1.15σ along the rod and 0.85σ between atoms in neighboring threads. The multi-thread design of the nanorods is different from most previous studies where single thread nanorods [104, 106, 107, 140, 155, 238, 242–246], hollow nanotubes [89, 247], or smooth (sphero)cylinders were used [109, 248, 249]. This gives the nanorods a new surface roughness, which has been shown to play a role in the phase behaviour of polymer-nanorod composites [250]. Moreover, the multi-threaded nanorods are incommensurate with the polymers (where the typical atomic spacing is around 1.35σ) eliminating possible artificial adhesion at the surface [251, 252]. This makes the multi-threaded design a good candidate for further studies of fibre pullout and interfacial slippage. All the simulations are done using the open source package LAMMPS [253]. The details of the simulation and equilibration procedures are discussed in the next subsection.

One of the main objectives of the present work is to investigate the effect of nanorod inclusion on the conformation of the polymer chains in the melt, especially the chains at the interface of the nanorods. As a measure of the shape and size of the polymers, we calculated the radius of gyration tensor $\boldsymbol{R}_g$ of a chain from the particle coordinates as

$$R^2_{g_{\alpha\beta}} = \frac{1}{M^2}\left[\sum_{i=1}^{n_p} m_i(r_{i,\alpha} - r_{com,\alpha})(r_{i,\beta} - r_{com,\beta})\right] \tag{2.3}$$

where $R^2_{g_{\alpha\beta}}$ is the element of the tensor $\boldsymbol{R}^2_g$ on the αth row and βth column, M is the total mass of the chain, n_p is the number of beads in the chain, and m_i is the mass of the ith bead. The $r_{i,\alpha}$ represents the position of the ith bead in $\alpha = x, y, z$ direction and similarly, the $r_{i,\beta}$ is the position of the ith bead in $\beta = x, y, z$ direction. The r_{com} is the position of the centre of mass of the polymer chain. Then the $|R_g|$ was found by

$$|R_g| = \sqrt{\lambda_1^2 + \lambda_2^2 + \lambda_3^2} \tag{2.4}$$

where λ_i is the ith eigenvalue of the gyration tensor. A set of 10 realizations of a pure melt, at the same temperature and pressure as the production runs examined in the results section, are run and the average radius of gyration of the polymer is measured to be $R_0 \approx 3\sigma$. This value is used as a reference throughout the paper.

A fixed number of polymer chains $N_p = 1000$ is used across realizations whereas the total number of rigid rods N_r in the melt is varied in order to achieve different concentrations of nanofillers. We quantify the concentration of the rods ϕ_c by simply taking the ratio of the total number of rod monomers to the total number of particles N

$$\phi_c = \frac{\text{number of rod beads}}{\text{total number of beads}} = \frac{(4 \cdot N_r)n_r}{N} \tag{2.5}$$

where $n_p = 32$, $n_r = 16$, $N_p = 1000$, $N = N_p n_p + (4 \cdot N_r)n_r$, $60 \leq N_r \leq 500$, and $0.1 \leq \phi_c \leq 0.5$.

Lastly, to improve results statistically, for each value of ϕ_c, 10 independent realizations were carried out and the results were averaged over the realizations. Throughout the paper, all quantities are presented in dimensionless LJ units.

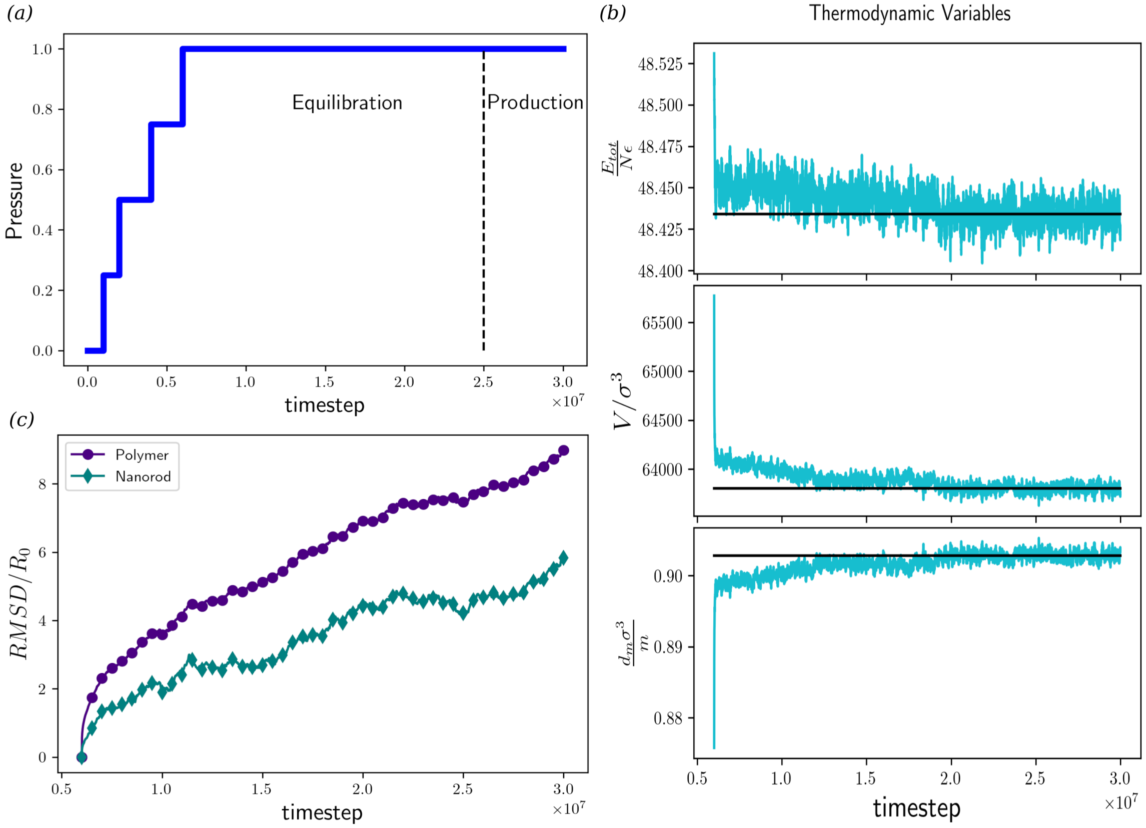

Figure 2.2: The equilibration scheme is shown in (a). (b) shows the total energy, volume, and mass density during the last stage of equilibration and the production for a system of $\phi_c = 0.44$. In (c), the RMSD for the nanorods and polymers as a function of time are demonstrated. The value of the RMSD is normalized by the pure melt average radius of gyration R_0.

2.1.1 Equilibration procedure

The simulation is started from a random initial configuration (see Fig.2.1c) generated using the *moltemplate* package [254]. Following the procedure in [255], a soft interaction of the form

$$U = A\left[1 + \cos\left(\frac{\pi r}{r_c}\right)\right] \quad \text{for } r < r_c \tag{2.6}$$

is then applied between all the components where r_c is the cut-off length. The potential amplitude A is linearly increased from 0 to 100ϵ over 1000τ. This allows for the overlapping particles to rearrange themselves without making the simulation unstable. At this point, the molecules are at a reasonable separations to be able to turn on the LJ interactions (and the soft potential U is turned off). As the last step before equilibration, the box (system) is relaxed.

The equilibration procedure consists of 4 stages as shown in Fig. 2.2a. We start off the equilibration with a short NVT run where a Langevin thermostat [256, 257] is applied to keep the temperature at $T = 1$ in all subsequent steps. In the next step, we turn on a Berendsen barostat [258] at the target pressure of $P = 0.25$ and let the system evolve under the isothermal-isobaric (NPT) ensemble for 1 million steps. Then the system is compressed by increasing the pressure stepwise in three more steps up to the final $P = 1$. The packing density of the mixture is defined as $d_p = \frac{\text{Total Volume of particles}}{\text{Volume of simulation box}}$ and the final pressure is chosen to achieve a melt-like packing density of $0.3 \leq d_p \leq 0.5$ [65, 107, 139]. The system is run at $P = 1$ and $T = 1$ for 9 million steps (or 19 million steps for the highest concentration) before the production. This careful stepwise protocol ensures that the mixture does not get trapped in a kinetically favourable state. To confirm that the system is in true equilibrium, we monitored the thermodynamic parameters as well as the root-mean-squared-displacement (RMSD). In Fig. 2.2 (b), the total energy, volume, and mass density of the system at the last stage of equilibration and the production for a typical system at $\phi_c = 0.44$ are illustrated. The values of these thermodynamic variables are levelled off and fluctuating around a mean value by the end of equilibration and during production. As the equilibration time increases with concentration, especially when nanorod-polymer attractions are at play, here, we only present the data for the highest concentration.

The structural equilibration of polymeric systems is a slower process compared to relaxation of thermodynamic variables [259]. Therefore, we also measured the root-mean-squared-displacement of the particles as a function of time to make sure that the polymers and the rods move reasonable distances during equilibration [255, 260]. In Fig. 2.2 (c), we show the evolution of the RMSD for the nanorods and polymers. As can be seen, both the rods and the polymers move multiple R_0, the average radius of gyration of a polymer in the pure melt, during the process validating the fact that the system is not stuck in a glassy state. We should mention that the particle RMSD is different from the RMSD of the centre of mass (COM). This takes into account the rotational motion of the molecules as well as the COM displacement which are both crucial to the equilibration process. However, we tracked the RMSD of the centre of mass of the constituents to make sure that the rotational motion is not taking over in the above graphs. The RMSD of COM for the rods and the polymers are plotted in Fig. A.2 (a) in the Appendix demonstrating they also move several R_0.

To investigate the effect of attractive interactions on the phase behaviour of the nanorod-polymer melt, we compare some of the results for our system to a system with all repulsive interactions. The all-repulsive system is equilibrated following the same protocol as the attractive system. Similar to

Fig. 2.2, in Fig. A.1 of the Appendix, the evolution of the thermodynamic variables and particle RMSD at the highest concentration $\phi_c = 0.44$ are shown. The RMSD of centre of mass for the all-repulsive case is presented in Fig. A.2 (b).

In addition to the equilibration procedure described above, we also tested equilibration procedures involving parallel tempering (with up to 8 replicas) and just letting systems evolve for much longer time periods. The final states found were the same to those described here but did not find those states any faster than the procedure described above.

2.2 Results

2.2.1 Dispersion and phase Separation

Rigid rods and nano particles have long been known to have poor dispersion in polymer melts. However achieving optimal dispersion of the rods throughout the melt is extremely important when considering the mechanical and structural properties of the resulting material. As mentioned earlier, chemically treating the surfaces of the rigid rods has shown to improve dispersion as it boosts their interactions with the polymer matrix [227, 233, 261, 262]. Therefore, due to their practical relevance, we mainly focus on a system of nanorod-polymer composite in which the polymer-rod interactions are attractive while all other interactions are hard-core repulsive. To understand the effect of the attractive polymer-rod interaction, the results are compared and contrasted with systems that have purely repulsive polymer-rod interactions but are otherwise identical.

In Fig. 2.3, we present snapshots of our system at the lowest concentration, i.e. $\phi_c = 0.1$, as it equilibrates. Fig. 2.3a (a) shows the system at an initial stage of the equilibration. As can be seen, the system starts out in a fairly random configuration with a lot of empty space between the components (lower packing density and larger box size). Fig. 2.3 (b) shows the system after 2.5 million timesteps at $P = 0.5$. We can see the early stages of the agglomeration of rods with a few clusters of rods appearing. Fig. 2.3 (c) depicts a later stage when 5 million timesteps have elapsed and at $P = 0.75$. As can be seen, the evolution of clusters continues and the shape of the clusters changes. Fig. 2.3 (d) shows the system at $P = 1.0$ and packing density $d_p = 0.33$ after 20 million steps. We can see that distinct aggregates are formed and some regions are filled with only polymers (at lower concentrations). This phase separation has been observed in experiments [232, 237] as well. In most previous computational studies where formation of such clusters were studied, an attractive interaction between rods were at play [107, 242]. However, the formation of such clusters in a system with rod-rod repulsive forces suggests the significance of entropic effects in this phenomenon.

To quantitatively investigate the phase separation visually observed in the simulations, we divide the system into voxels and in each voxel we compute an order parameter related to the number density difference defined as

$$\rho_n = \frac{p_n - r_n}{p_n + r_n} \tag{2.7}$$

where p_n is the number of polymer monomers and r_n the number of rod monomers in the voxel.

To examine the ordering in the system it is useful to look at various spatial correlation functions. Most studies examine the radial distribution function $g(r)$ (a mass-density correlation function). Some of the correlation functions we examine are similar, namely the density autocorrelation and rod-rod centre of mass correlation functions, but we will also analyze orientational correlation functions

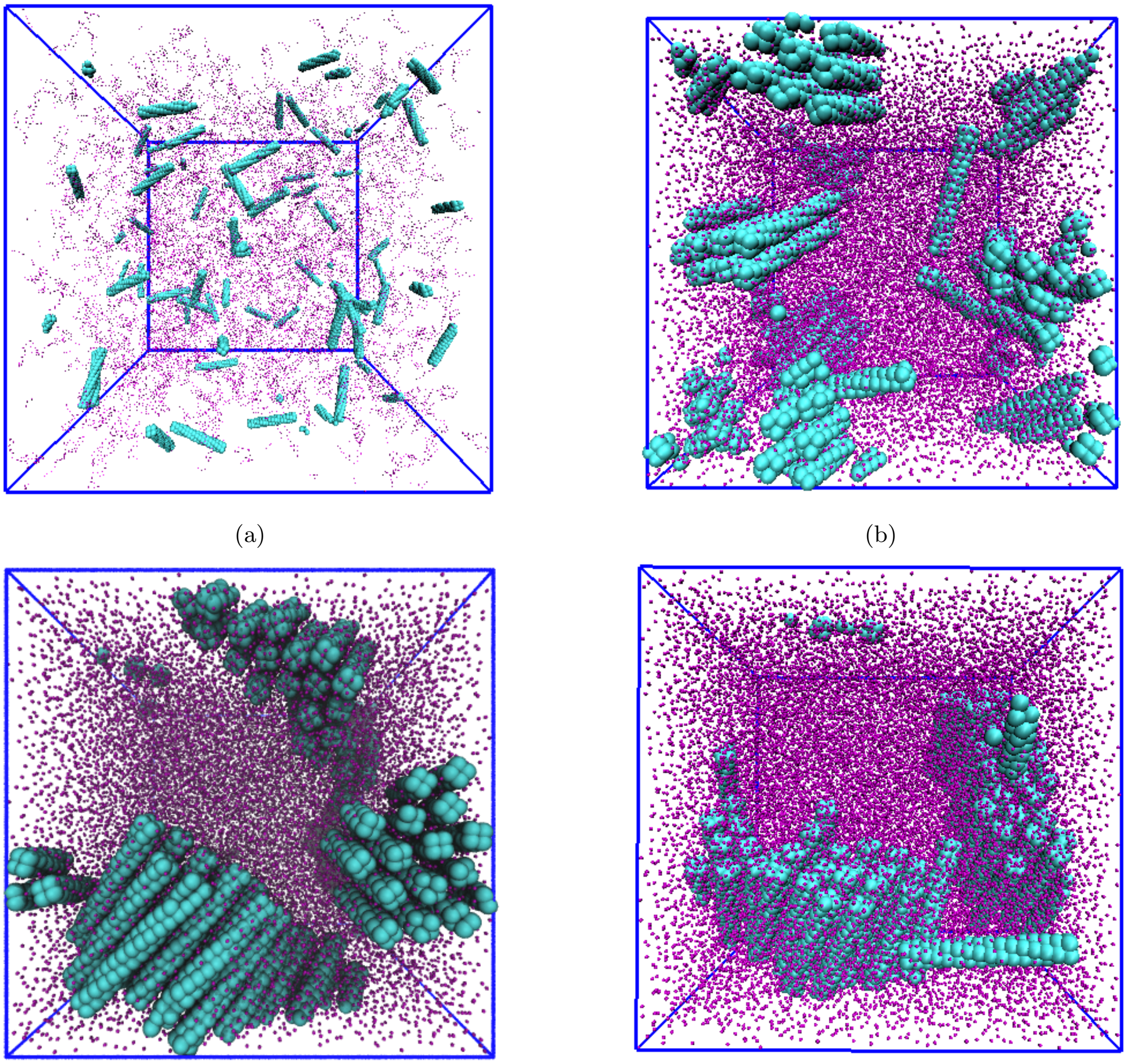

(a) (b)

(c) (d)

Figure 2.3: A nanorod-polymer melt with nanorod concentration $\phi = 0.1$ and nanorod-polymer interaction strength $\epsilon_{rp} = 1$. As the system evolves, the (a) initial random configuration at $P = 0$ progress to phase separate and form (d) distinct rod aggregates after equilibration at $P = 1$. (b) and (c) show intermediate stages at $P = 0.5$ and $P = 0.75$ respectively. The considerable change in the system configuration is partial evidence of full equilibration of the system. (d) shows the final configuration of the system after 9×10^6 equilibration steps and 10^6 production steps. The matrix polymer chains are shown as purple dots for illustration purposes.

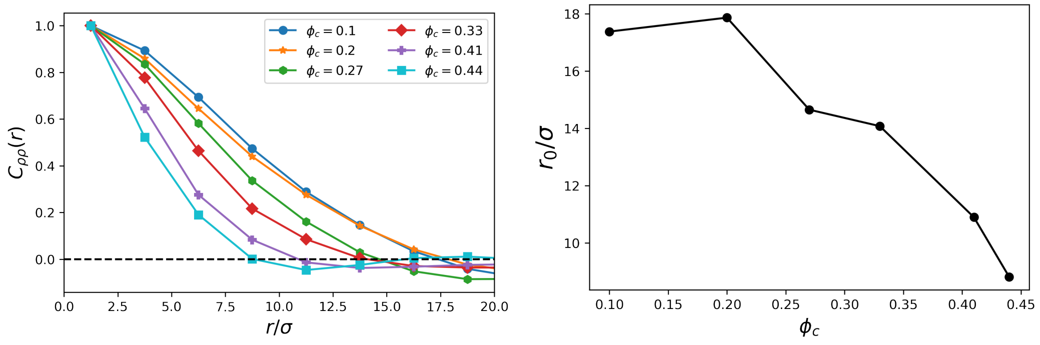

(a) (b)

Figure 2.4: (a) shows the auto-correlation function of the number density difference ρ_n as a function of radial distance from the origin for selected concentrations while (b) shows the intercept of the auto-correlation function with $C_{\rho\rho}(r) = 0$ axis as a function of concentration.

to provide a complete picture of the spatial correlation of the system. First, the auto-correlation function of the density-difference characterizes the distribution of particles inside the simulation box. The auto-correlation function for ρ_n is

$$C_{\rho\rho}(r) = \frac{\langle \rho_n(0).\rho_n(r) \rangle - \langle \rho_n \rangle^2}{\langle \rho_n^2 \rangle} \tag{2.8}$$

and is found using Fast Fourier Transforms, and the Wiener-Khinchin theorem [263]. Fig. 2.4(a) shows the $C_{\rho\rho}(r)$ as a function of radial distance from the reference point ($r = 0$). Since we have a periodic boundary condition, we only plot the function for one octant of the simulation box. The 3D distribution obtained from the calculations is mapped onto the radial distance by averaging all the discrete values of the $C_{\rho\rho}(r)$ within distance r and $r + \delta r$, where $\delta r = 2.5\sigma$, and assigning the mean value to the point at r.

At lower concentrations, $C_{\rho\rho}$ drops from 1 at low r and becomes negative beyond a characteristic length r_0. In Fig. 2.4(b), the characteristic length r_0 corresponding to the zero-crossing of $C_{\rho\rho}$ as a function of the concentration is illustrated. We observe an overall decrease in $C_{\rho\rho}$ as we increase the concentration of rods which is reflected in r_0 going down as concentration goes up. From the definition of ρ_n, the decrease at higher concentrations shows that the correlation between the composition of voxels decreases as function of concentration which implies that the polymers and the rods are becoming better mixed in systems with higher rod concentrations.

Another important indicator of the structure of the system is the distance of nanorods from each other in the melt. In Fig. 2.5(a), we show the probability of finding the centre of mass of the nanorods at a distance Δr from each other. By increasing this shell radius to include larger distances, the number of rods within the shell increases just due to the larger volume. Therefore, we normalize the probability by the volume of the shell. Similar to $g(r)$ graphs, peaks in the rod-rod distance plot show spatial order in the system. As can be seen, the graphs show a first peak around 3.15σ at all concentrations which corresponds to the distance between neighbouring rods. Since this value is larger than the direct contact distance of two rods, this shows that polymers interpenetrate the space between the rods. Polymers between the rods were also observed directly in snapshots of the system configurations, such as the ones shown in Fig. 2.6. Fig. 2.6 shows the snapshots of systems at concentrations (a) $\phi_c = 0.1$, (b) $\phi_c = 0.2$, (c) $\phi_c = 0.33$, and (d)$\phi_c = 0.44$.

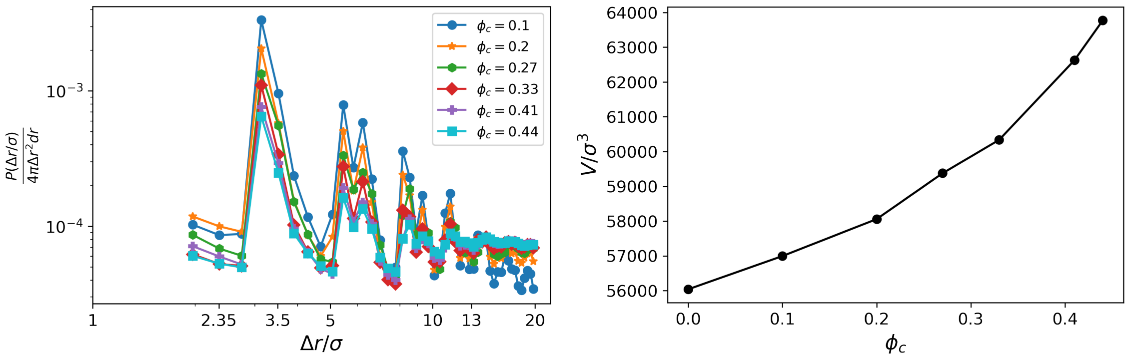

(a) (b)

Figure 2.5: In (a), probability density function is shown for the pairwise distance between the centre of mass of the rigid rods in the melt. (b) shows the average volume of the system as a function of the concentration. The patterns in (a), and (b) suggest that the melt becomes more mixed and less ordered at concentrations higher than $\phi_c \approx 0.25$.

Moreover, in Fig. 2.5(a), the peaks slowly diminish as the concentration goes up which implies there is less order at higher concentrations. The system becoming more mixed is also manifested in the average volume of the system. In Fig. 2.5(b), we see the average volume versus concentration. The volume initially grows linearly, but beyond $\phi_c \approx 0.25$, as the system becomes less ordered (particularly the rods), the rate of growth increases. This is likely related to the well-known fact that a system of orientationally disordered rods require more volume than orientationally ordered rods at equilibrium. The orientation of rods and the corresponding order of the system will be discussed in greater depth in the next section.

To provide a better picture of the processes responsible for the above results, we compare the result of our system (with rod-polymer attractive interactions) to a system with all repulsive interactions. Fig. 2.7(a) shows the $C_{\rho\rho}(r)$ for a system with repulsive forces between all components. Compared to Fig. 2.4(a), the graphs cross $C_{\rho\rho}(r) = 0$ at larger distances and we do not observe as significant a decrease in the zero-crossing as concentration increases. As a matter of fact, while the correlation curves at first decrease with concentration, they go up again beyond $\phi_c = 0.27$. The slower drop of $C_{\rho\rho}$ suggests that neighbouring voxels contain similar type of atoms. In other words, the rods and polymers are more fully phase separated. This is also observed from direct visualizations. Fig. 2.7 (c) shows snapshots of an all-repulsive system at a concentration of $\phi_c = 0.44$. A full phase separation is observed for the all-repulsive system.

The lack of any attractive forces implies the phase separation for the system with all purely repulsive forces is entirely driven by entropic effects (excluded volume) similar to depletion forces seen in systems of spherical colloids of two different sizes [264–267]. This type of depletion-induced phase separation is also observed in mixtures of nanorods in non- or weakly-adsorbing polymer solutions [109, 124, 139, 140, 236].

In contrast, the rods in the corresponding system with attractive rod-polymer interactions are better dispersed in the polymer melt as shown in Fig. 2.6(d). In order to increase their contact surface with the rods, the polymers break up the large clusters of rods into smaller ones as well as penetrate into the space between rods within the clusters. This becomes more evident if we compare the rod-rod centre of mass results for the repulsive and attractive cases. Similar to Fig.

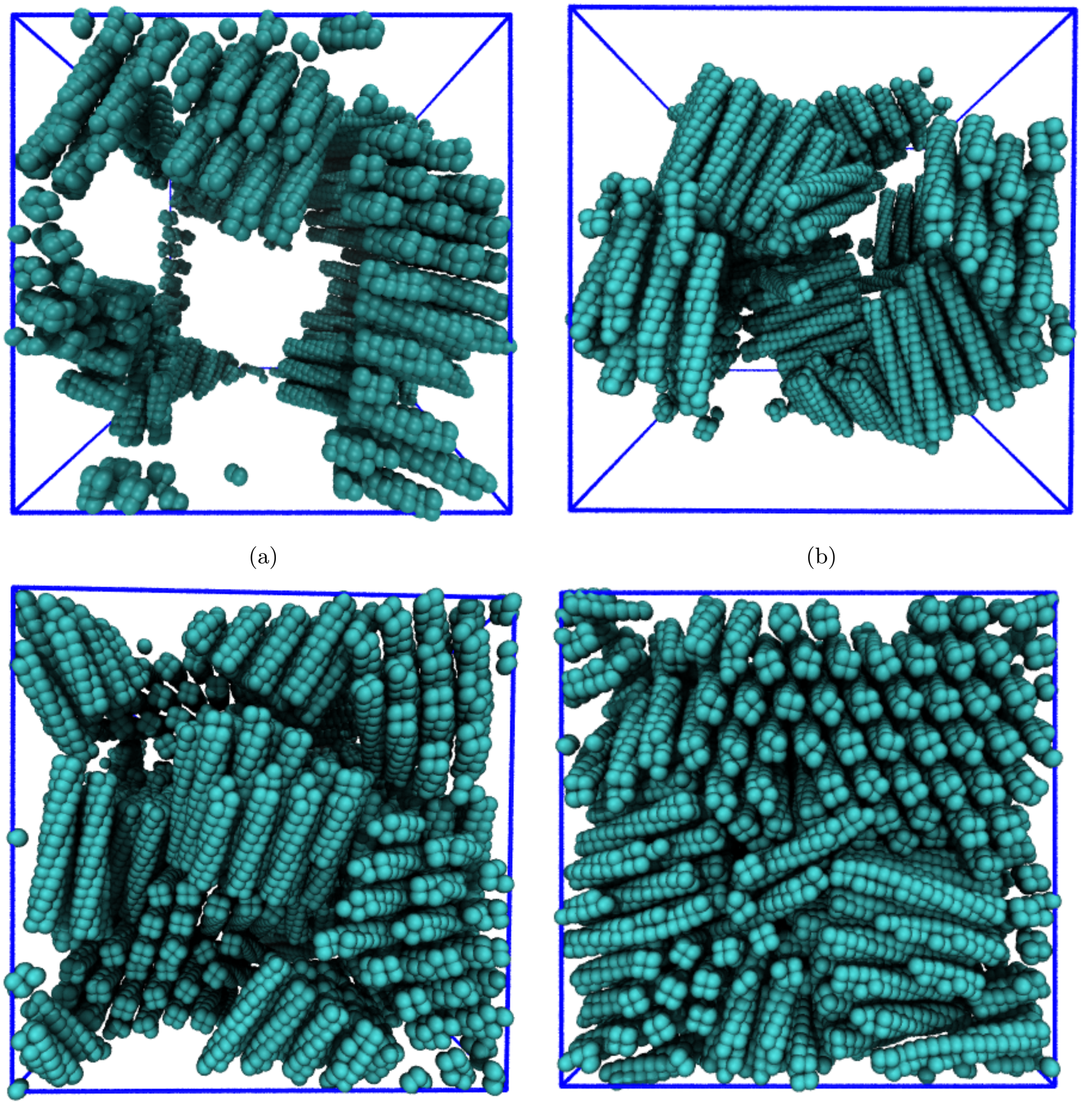

(a) (b) (c) (d)

Figure 2.6: Snapshots of the rod-polymer system at concentrations (a) $\phi_c = 0.1$, (b) $\phi_c = 0.2$, (c) $\phi_c = 0.33$, and (d)$\phi_c = 0.44$ are shown. Initially, increasing the concentration of the rods results in the growth of the size of the clusters, but further increase breaks the clusters up and makes the system more uniformly mixed. This is attributed to the interplay of entropic and enthalpic effects.

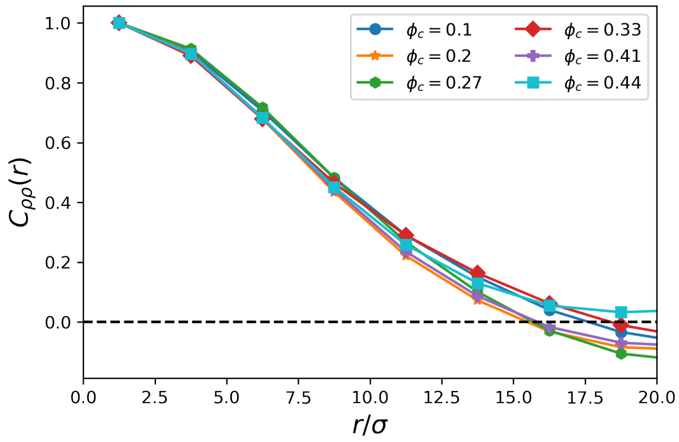

(a)

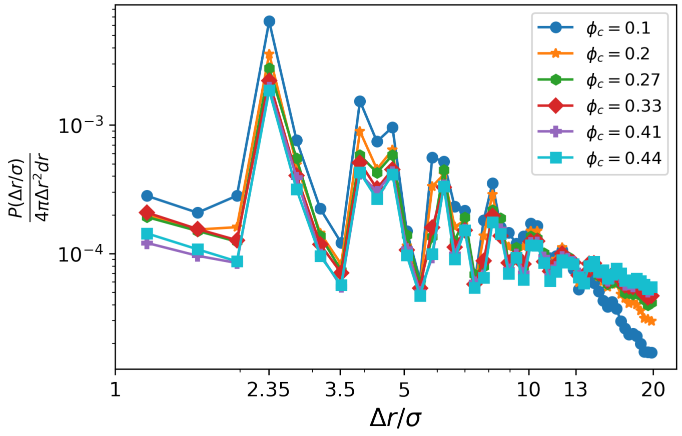

(b)

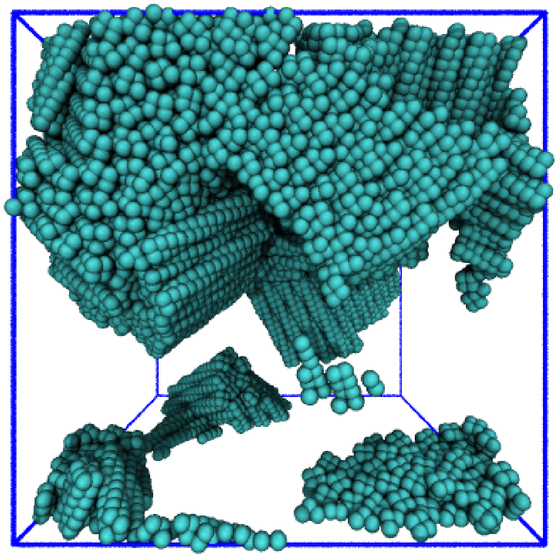

(c)

Figure 2.7: The auto-correlation function of the number density (a), and the rod-rod centre of mass distance (b) for a system with all-repulsive interactions are illustrated. In (c), a system at $\phi_c = 0.44$ with repulsive interactions between all components is visualized. (a)-(c) show both quantitatively and visually that rods aggregate via direct contact in the fully repulsive system. Regardless of the rod concentration, all the rods phase separate into a single cluster in this case.

2.5 (a), Fig. 2.7(b) shows the probability density of rod-rod centre of mass distance. The maximum probability happens at a distance close to the diameter of the rods $\Delta r \approx 2.35\sigma$ which means the rods directly touch within a cluster for the repulsive system while for the system with rod-polymer attractions, the first peak happens at a larger distance which suggests that polymers are present between the rods within a cluster. One might interpret this as polymers gluing the rods together and therefore determine formation of cluster to be energetically driven [106, 141]. However, as shown by the $C_{\rho\rho}(r)$ graphs, introducing the rod-polymer attraction splits the larger clusters into smaller ones and does not promote formation of clusters. Although the polymers are present within clusters (polymer-bridged), polymer-bridging does not seem to be the source of aggregation at the specific interaction strengths studied in this work. The details of the effect of the rod-polymer attraction strength on the phase behaviour will be studied in a future work.

The difference in the behaviour of the fully repulsive system and attractive system can be interpreted as follows. The phase separation of the polymers and the rods in the repulsive system is an entropic process and since there is no other processes to compete with, increasing the number of rods does not alter the behaviour of the system significantly. However, in the presence of the rod-polymer attractive interactions, the enthalpic effect that tries to increase the contact surface of rods and polymers competes with the entropic effect pushing the system away from phase separation, and formation of clusters. As a result, increasing the number of rods steers the attractive system towards a more mixed configuration as it boosts the energetic interactions.

Another interesting result illustrated in Fig. 2.3c is the orientation of rods within the aggregates. As can be seen, the rods within a cluster align laterally and in parallel. In other words, they form a nematic phase within each cluster. The formation of a nematic phase of nanorods in solutions of polymers has been mentioned in the literature [235, 268] and is the topic of the next section.

2.2.2 Orientation and Order

Rod clusters

In the previous section, we observed that the nanorods tend to phase separate into clusters that visually seem to have nematic order. In this section, we further investigate this possible ordering and phase behaviour. We start with an examination of the orientational order of the rods as a function of their position. An orientational correlation C_{rr} can be defined as

$$C_{rr}\left(|\Delta \boldsymbol{r}|\right) = \left\langle \left|\hat{\boldsymbol{e}}_i^r(\boldsymbol{r}) \cdot \hat{\boldsymbol{e}}_j^r(\boldsymbol{r} + \Delta\boldsymbol{r})\right| \right\rangle \tag{2.9}$$

where $\hat{\boldsymbol{e}}_i^r$ and $\hat{\boldsymbol{e}}_j^r$ are the end-to-end vectors of the ith and jth nanorods and $\Delta r = |\Delta \boldsymbol{r}|$ is the distance between the centre of mass of the nanorods. The value of C_{rr} is 1 for a fully orientationally ordered state and 0.5 for an isotropic state.

Fig. 2.8 shows C_{rr} as a function of Δr for a range of concentrations for the attractive system (a) and repulsive system (b). In both systems, the neighbouring rods at short distances are very correlated and C_{rr} takes values near one. However, moving away from a reference rod, the orientational correlation between the rod and other rods fades away and C_{rr} decreases. At lower concentrations, this decay is slower in the presence of the attractive forces while in the all-repulsive system, C_{rr} stays near 1 before a sharp drop at $\Delta r \approx 8\sigma$. Moreover, we can see a shift towards smaller C_{rr} values as the concentration of rods increases in the attractive system. This is on par with what

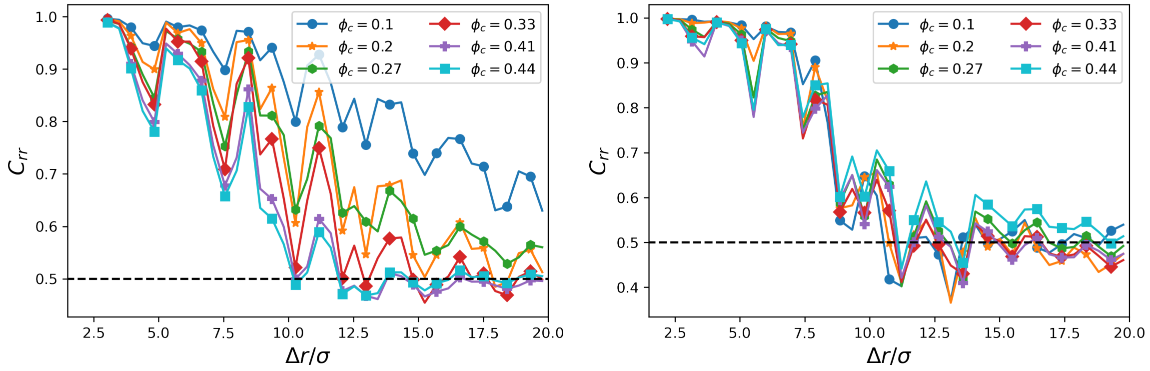

(a) (b)

Figure 2.8: Orientational correlation between different rigid rod directors. (a) and (b) are the attractive and repulsive cases, respectively. The nearby rods align in the same direction which results in values close to 1 in low Δr for both cases, but this value decreases as Δr increases more gradually in the attractive case. The concentration seems to have small to nothing impact on the C_{rr} pattern in the all repulsive system.

we have already seen in Fig. 2.5: the order of the nanocomposite melt diminishes somewhat as the concentration of the rods increases. In contrast, the concentration does not seem to have much effect on the orientational correlation of the all-repulsive system.

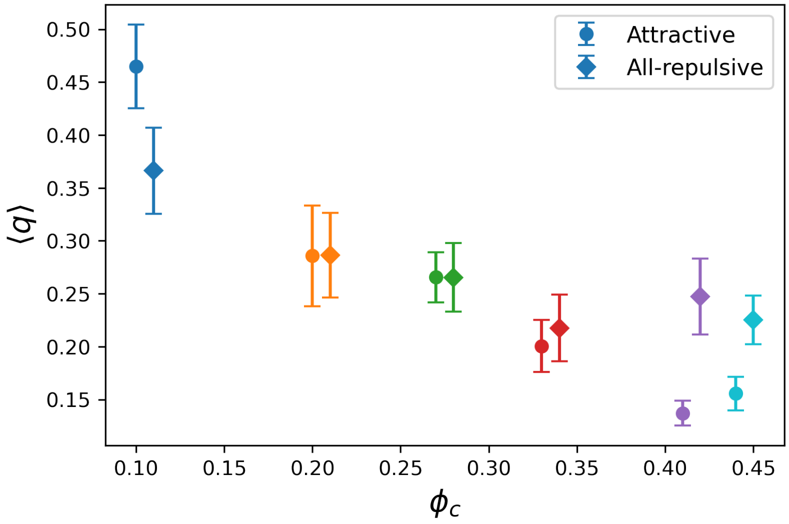

Figure 2.9: The order parameter $\langle q \rangle$ as a function of rod concentration is depicted. For the attractive system (solid circles) we see a distinct decreasing pattern in the value of $\langle q \rangle$. For the all-repulsive system (diamonds), the decreasing pattern is similarly observed, but it is not as monotonic and distinct. Values for the all-repulsive system have been shifted right by 0.01 to make them easier to distinguish from the values for attractive system.

To further investigate the order of the system, we look at the order parameter tensor $\boldsymbol{Q}$ and its eigenvalues. The $\boldsymbol{Q}$ is a traceless tensor defined as

$$Q_{\alpha\beta} = \left\langle \hat{e}_\alpha \hat{e}_\beta - \frac{1}{3}\delta_{\alpha\beta} \right\rangle \tag{2.10}$$

where $\hat{e}$ is the unit vector (along the length) of a rod, $\alpha, \beta = x, y, z$, and the angle brackets denote the expectation value over all rods [28]. The eigenvalues of this matrix show the order along the corresponding eigenvectors. The average value of the largest eigenvalue $\langle q \rangle$ over several realizations is plotted as a function of concentration in Fig. 2.9 where the attractive and repulsive cases are represented by circles and diamonds, respectively. One more time, we see that the overall order of the nanocomposite decreases as a function of concentration. Although this decrease is observed in both (a) and (b), it is more pronounced in the attractive case (a change from lowest to highest concentrations of around 0.3 for the attractive case versus 0.15 for the all-repulsive).

Although $\langle q \rangle$ shows the order along the global director (corresponding eigenvector), it does not provide a lot of information on the uni- or bi-axiality of the system and a look at the other eigenvalues of tensor $Q_{\alpha\beta}$ is necessary. We use a pair of order parameters (s_1, s_2) as defined in [269, 270]

$$s_1 = q_1 - q_3 \tag{2.11}$$

$$s_2 = q_2 - q_3 \tag{2.12}$$

where $q_3 \leq q_2 \leq q_1 = q$ are the eigenvalues of the $\boldsymbol{Q}$-tensor. Based on definition, the eigenvalues take values on the interval $\left[\frac{-1}{3}, \frac{2}{3}\right]$ which in turn translates to $s_1, s_2 \in [-1, 1]$. However, since we have the condition $q_3 \leq q_2 \leq q_1 = q$, all the points lie in the region $s_1, s_2 \in [0, 1]$. Therefore, we only show this region of the $s_1 - s_2$ triangle. In Fig. 2.10, the order parameter pairs are plotted for different concentrations. The origin $(0, 0)$ corresponds to the isotropic state, the dashed-lines represent uniaxial states, the rest show biaxial states. The boundaries of the triangle (black solid lines) are physically impossible states. In Fig. 2.10(a), for the attractive system, we see a monotonic decrease in the value of s_1 as a function of concentration and the points move towards the origin as the concentration is increased. Similar to $\langle q \rangle$, the decrease in s_1 as a function of concentration is again about half as much over the range of concentrations studied for the all-repulsive system compared to the system with attractive rod-polymer interactions.

Comparing Fig. 2.10 (a) and (b), we can also see that overall, the attractive system has a more uniaxial order (the points are closer to the x-axis or the dashed-line). This agrees with what we have seen in Fig. 2.8 where C_{rr} of the attractive system in Fig. 2.8 (a) shows deeper valleys compared to C_{rr} of the all-repulsive case in Fig. 2.8 (b).

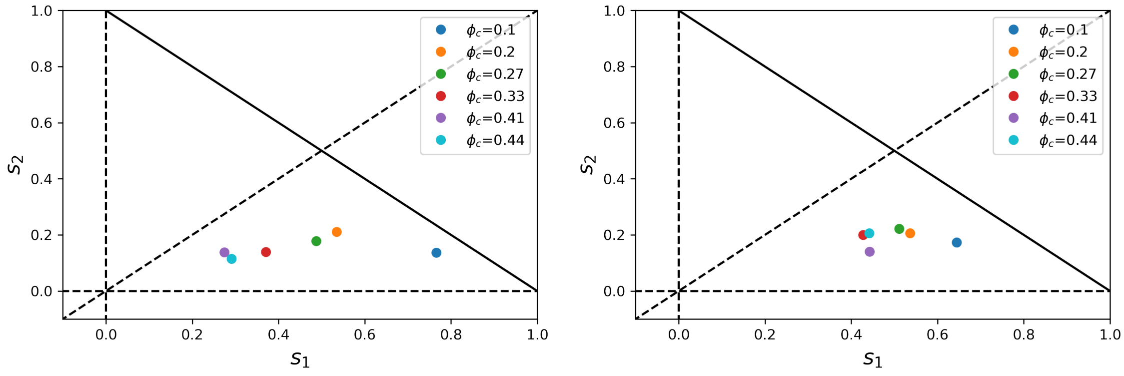

(a) (b)

Figure 2.10: The eigenvalues of the order parameter $\boldsymbol{Q}$ are plotted in $s_1 - s_2$ space. (a) shows the system with rod-polymer attractions and (b) shows the all-repulsive system. The isotropic state is at the origin $(0, 0)$, the dashed-lines represent uniaxial states, and the rest of the region inside the triangle corresponds to biaxial states.

To summarize, at low concentrations, the system with attractive interactions has more orientational order and correlations over a longer range than the all-repulsive system. This appears to be due to the presence of ribbon-like configurations of orientationally aligned rods stretching across the system (cf. Fig. 2.6a) in the attractive case whereas the rods are in more of a compact clump in the repulsive case. At intermediate concentrations, the ribbons break up into clusters which are internally orientationally aligned and with sizes similar to those seen in the repulsive case (cf. Fig. 2.8). The size of these clusters seems related to that of the rod length (the correlations in Fig. 2.8b drop at a length scale that is almost exactly half of the rod length). This seems likely to be due to the fact, apparent in the snapshots (cf. Fig. 2.6 and Fig. 2.7c), that the rods do not just orient with their neighbour but also form layer-like clusters where the rod centers-of-mass line up in a plane with their long axis oriented normal to the plane. Within the layer, the rods form close-packed structures. However, the orientation and layering of neighboring clusters are not correlated. As such, as we add slightly more rods we primarily just add new clusters so the decay of the order parameter at intermediate concentrations is primarily due to averaging over more clusters. At high concentrations, the orientational order for the all-repulsive system starts to level off, and perhaps even start to increase (cf. Fig. 2.9). At the same time, the all-repulsive system starts to pick up some small longer range correlations in orientational order ($C_{rr} > 0.5$ in Fig.2.8b). i.e. as we pack in more rods the all-repulsive system starts to gain some true long range liquid crystal-like ordering. In contrast, the system with attractive interactions becomes more orientationally isotropic as we increase the number of rods. As we saw in the previous subsection, the attractive system also becomes more mixed as we increase the number of rods whereas the all-repulsive system fully phase separated into a single clump of rods separate from the polymer melt. This suggests that the interfacial polymers play a role in this difference in behaviour between the attractive and all-repulsive rod-polymer systems.

Interfacial polymers

The phase separation of rods, and nematic ordering within the aggregates, has important ramifications for the nanocomposite's mechanical properties, for example non-uniform stress distribution and slippage [225, 226]. However, another factor that plays a determining role in understanding the mechanics of fracture of polymer-nanorod composites is the behaviour of polymer chains at the polymer-nanorod interface. Unlike nanorod dispersion patterns, the interfacial behaviour has not been studied significantly in the literature which is the motivation for the work in this section. In their recent MD article, Lu et. al found that the polymer chains near nanorod surfaces take on more extended conformations while the chains far away behave like chains in a pure melt [107]. Our simulations tell a similar story.

In a polymer melt, the radii of gyration of individual chains are distributed in a Gaussian distribution with mean R_0. We measure the radius of gyration of the polymer chains within a distance of 5σ from the surface of rods ("nearby") and compare them to those in a melt (polymers far from the rods are still in the polymer melt phase so are distributed nearly identical to those in a pure melt). The difference in probability density of the radius of gyration for nearby chains from pure melt is shown for all concentrations in Fig. 2.11. If we look at the difference between the probability densities for polymers near rods and the pure melt for the attractive polymer-rod interactions, as shown in Fig. 2.11(a), we see a clear pattern where $\Delta\mathcal{P}$ is negative for $R_G/R_0 < 1$ and positive for $R_G/R_0 > 1$. This can be interpreted as near-rod polymers have fewer compact

($R_G < R_0$) and more expanded ($R_G > R_0$) chains. We also observe a longer tail in Fig. 2.11(b) which means there are polymers that are extended up to twice their pure melt conformation. The system with purely repulsive interactions shows completely opposite behavior (cf. Fig. 2.11b). In this case, near-rod polymers have more compact ($R_G < R_0$) and fewer expanded ($R_G > R_0$) chains.

Note that while both of these case involve polymers nearby rods, we have seen earlier that in the attractive case these polymers completely interpenetrate the rod clusters whereas in the repulsive case these polymers are at the interfacial surface between a melt-like region of polymers and a single big cluster of rods (with no polymer interpenetration). In other words, in the repulsive case the near-rod polymers are effectively experiencing the effect of a hard wall that they cannot penetrate and so if we think of the polymer configuration as a random walk, when this walk "hits" the wall (formed by the cluster of rods) it is just reflected back into the melt. These reflections result in the observed more compact configurations seen here and in most other polymer melts near hard walls [271].

By contrast, the presence of the rods in the melt results in stretching of polymer chains for the attractive system. However, we have not yet addressed the direction in which the polymers stretch. The chains can extend along the length of the rods or perpendicular to the direction of clusters. Therefore it is interesting to see if there is also some kind of orientational correlation between the rods and polymers. To measure this, we defined a rod-polymer correlation function such that

$$C_{rp}\left(|\Delta \boldsymbol{r}|\right) = \left\langle |\hat{\boldsymbol{e}}_i^r(\boldsymbol{r}) \cdot \hat{\boldsymbol{e}}_j^p(\boldsymbol{r} + \Delta \boldsymbol{r})| \right\rangle \tag{2.13}$$

where $\hat{\boldsymbol{e}}_i^r$ and $\hat{\boldsymbol{e}}_j^p$ are the director of the ith rod and the end-to-end vector of the jth polymer and $\Delta r = |\Delta \boldsymbol{r}|$ is the distance between the centre of mass of the rod and polymer. Fig. 2.12 shows the values of this correlation parameter at different concentrations.

As can be seen, for all concentrations in the attractive case shown in Fig. 2.12a, polymers near rods are most elongated along the rod and the correlation decays as the distance increases. An interesting feature of this plot is the behaviour of C_{rp} as a function of concentration. The overall correlation goes up as the concentration increases up to $\phi_c \approx 0.3$ and then declines. By fitting an exponential, we have defined a length scale ℓ_{rp} which is plotted in the inset as a function of concentration. The ℓ_{rp} inclines at the beginning which corresponds to growth of cluster size and reaches a peak around $\phi_c = 0.3$. This agrees with what we have already seen in the previous sections. The initial rise in the number of rods results in larger ordered clusters where polymers sneak in between the rods and stretch along the director of the cluster. However, further increase in the number of rods leads to a less ordered system, particularly in the rod orientations, with an abundance of rod surfaces for the polymers to interact with. Therefore, the polymer chains show less preference to align with any specific rod.

The correlations for the repulsive case, Fig. 2.12b, are much lower in magnitude and are shorter range, dropping sharply to 0.5 at fixed distance similar to what is seen for the rod-rod correlations in Fig. 2.8b. As noted above, these polymers are at the surface of a rod cluster that, due to the rod-rod correlations, forms a corrugated surface. It would appear that these polymers have a small tendency to follow these corrugations which results in the observed C_{rp} correlations, which just die off at distances where the rods that form these corrugations are no longer correlated.

Lastly in this section, we look at the orientation of polymers with respect to each other by introducing a polymer-polymer segmental correlation function like the ones defined for rod-rod and

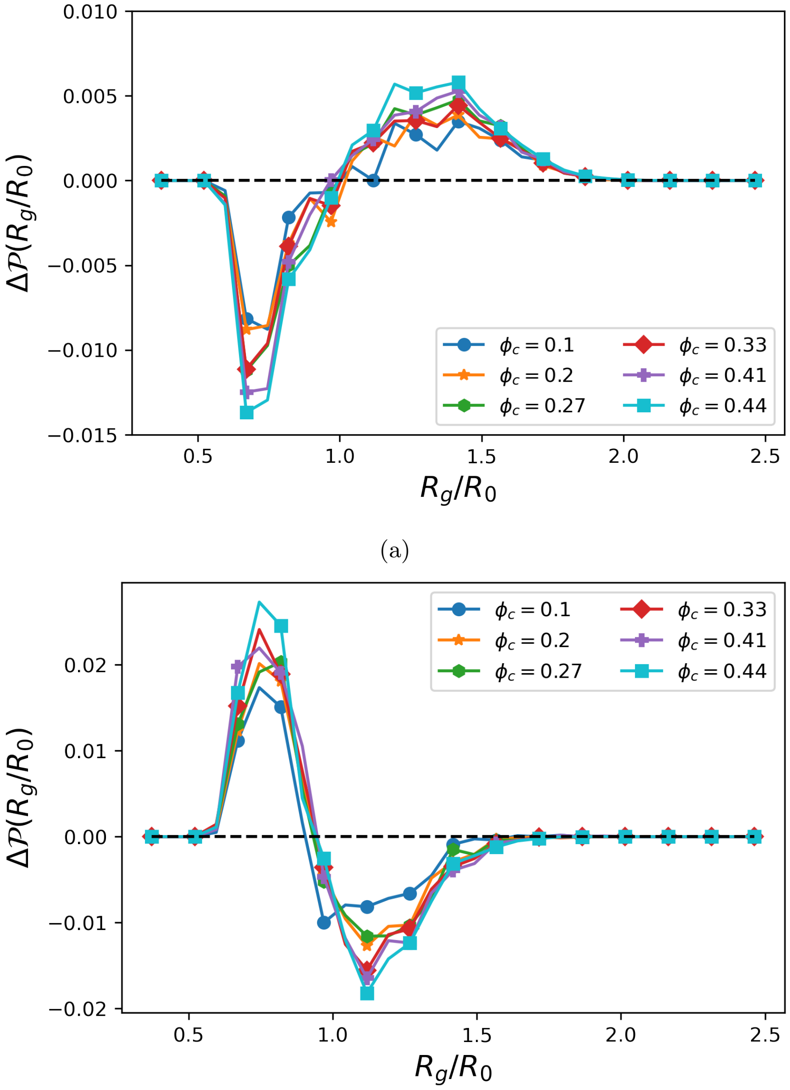

(a)

(b)

Figure 2.11: (a) depicts the difference of probability densities of the normalized radius of gyration of the near polymer chains and the pure melt in the original system while (b) shows the same quantity in the all-repulsive one.

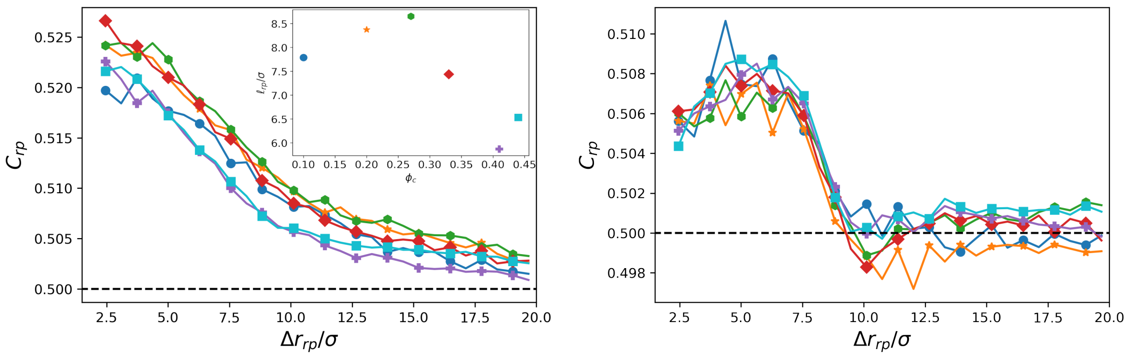

(a)

(b)

Figure 2.12: Orientational correlation C_{rp} between director of rods and polymers' end-to-end vector are shown for (a) the original system and (b) the all-repulsive system. The inset in (a) shows the length scale ℓ_{rp} as a function of concentration.

rod-polymer

$$C_{pp}\left(|\Delta \boldsymbol{r}|\right) = \left\langle \left|\hat{\boldsymbol{e}}_i^p(\boldsymbol{r}) \cdot \hat{\boldsymbol{e}}_j^p(\boldsymbol{r} + \Delta \boldsymbol{r})\right|\right\rangle \tag{2.14}$$

where e_i and e_j are the end-to-end vectors of the ith and jth polymer segments and $\Delta r = |\Delta \boldsymbol{r}|$ is the distance between the centre of mass of the segments. Here, we show the results for segments of length 16 beads (half of a polymer length). In Fig. 2.13(a), the relative orientational correlation, $\Delta C_{pp} = C_{pp} - C_{pp_{melt}}$, is shown for the attractive system. While this is typically quite small implying there is only a slight tendency for polymers to align, it is clearly nonzero. At lower concentrations, the behaviour is very close to the melt. However, as more rods are added to the system, ΔC_{pp} increases and the polymers are more orientationally correlated. This is because the polymers that are aligned with a certain rod are aligned with each other. This becomes even more obvious when ΔC_{pp} is scaled by the concentration ϕ_c as illustrated in Fig. 2.13(b). As can be seen, the scaled correlation functions collapse implying that the increase in the correlation is a direct result of increase in the number of rods.

In contrast, for the all-repulsive system shown in Fig. 2.13(c), the increase in the number of rods does not affect ΔC_{pp} by much and its value only fluctuates around zero. This agrees with what we have seen so far: the rods in the all-repulsive system aggregate into a big cluster with no polymers in between, i.e. direct contact. Therefore, due to lack of contact with the polymers, they cannot alter the conformation of the polymers. This being said, we see some positive values at smaller distances. This is attributed to the polymers at the surface of the large cluster.

An interesting comparison can be made to work by Gorkunov and Osipov [272] who looked at adding nanoparticles into a liquid crystal matrix. They found that adding isotropic nanoparticles into the liquid crystal dilutes the liquid crystal and lowers order of the system and consequently, the nematic-isotropic transition temperature. On the other hand, they found that anisotropic particles mimic their nematic host, aligning with the liquid crystal, and as a result improving the nematic ordering of the system. We see a similar effect here: In the absence of polymer-nanorod attractive forces, the polymer chains form random walk blobs (see Fig.2.11b) and effectively, play the role of the isotropic nanoparticles in a pool of nanorods. However, when the attractive interactions are present, the polymers attempt to increase their contact surface with the rods. As a result, they take

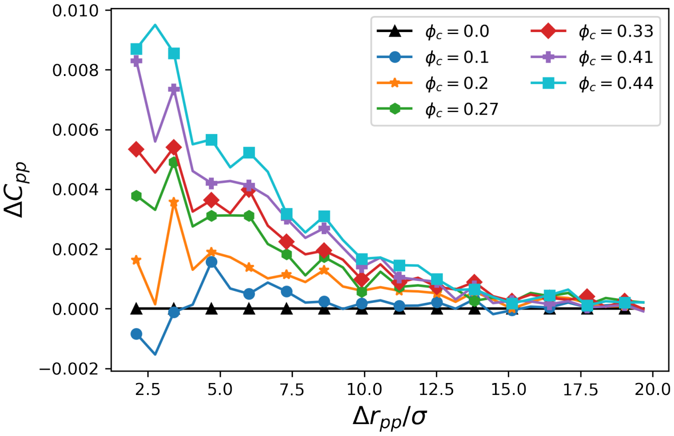

(a)

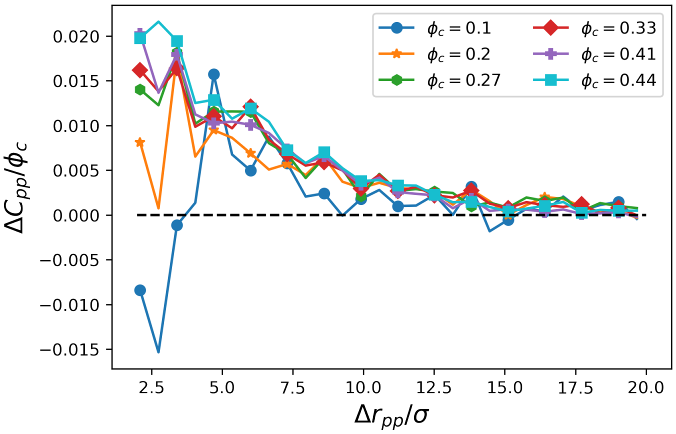

(b)

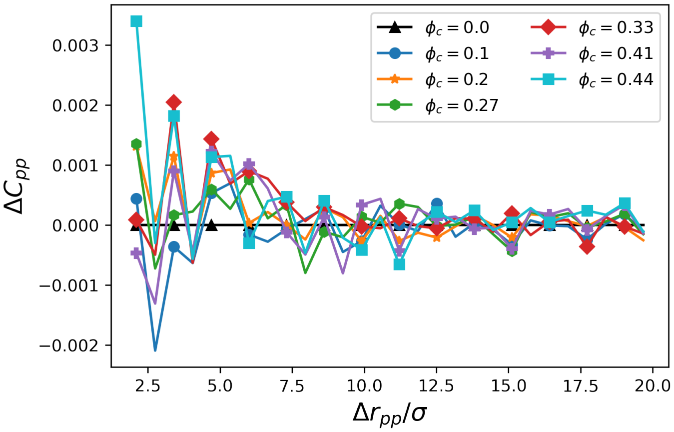

(c)

Figure 2.13: The relative orientational correlation parameter $\Delta C_{pp} = C_{pp} - C_{pp_{melt}}$ as a function of the polymer-polymer pairwise distance Δr_{pp}. (a) shows the relative orientational correlation ΔC_{pp} for the original system while (b) shows the scaled relative orientational correlation $\Delta C_{pp}/\phi_c$ for the same system. (c) shows ΔC_{pp} for the all-repulsive system (not scaled).

on more elongated conformations (see Fig.2.11a) and like anisotropic nanoparticles, they reinforce the nematic ordering of the nanorods. This is reflected in the difference between $\langle q \rangle$ for attractive and repulsive cases in Fig. 2.9.

There is one caveat in this comparison. Single molecule nanoparticles only have degrees of freedom associated with translation and rotation, but polymer chains have significantly more degrees of freedom (they can change shape). Although aligning with the rods can be favourable, the polymer pays the cost in loss of conformational entropy. At lower concentrations, the population of elongated chains is low enough that the ordering effects can easily compensate for it. However, by adding considerable number of rods, the conformational entropy decreases deeply and drives the system towards a less ordered configuration. As a result, we see a change of trend as the concentration goes up and $\langle q \rangle$ of the attractive system becomes less than that of the all-repulsive system for high ϕ_c.

2.3 Discussion and Conclusions

The dispersion and orientation patterns of nanorods in polymer melts with either attractive or repulsive rod-polymer interactions has been examined as a function of the rod concentration. We see three competing effects: i) entropy of the rods; ii) energetic interactions between the rods and polymers and; iii) entropy of the polymers. The all-repulsive interaction system completely phase separates at all rod concentrations whereas the system with attractive polymer-rod interactions does not. This strongly implicates the role of entropy, in the form of the depletion effect (related to the free volume per particle), as the main driver of phase separation in the system.

The attractive polymer-rod interactions set up a competition between entropic and enthalpic effects (as this is a constant pressure system it is more appropriate to discuss in terms of enthalpy than energy). Since the strength of the enthalpic effects are proportional to the number of rods in the system, the dispersion patterns show direct correlation with the rod concentration. At lower concentrations, entropic processes are dominant and ordered clusters of nanorods are created. However, due to the presence of the attractive forces, the rods do not completely phase separate and polymers interpenetrate between the rods of a cluster. At higher concentrations, the energetic effects become significant and the dispersion of the rods improves with the overall cluster size diminishing with concentration. The polymer interpenetration between the rods is typically referred to as "polymer bridging" and, at least at very strong polymer-rod interactions, is often argued to create an effective rod-rod attraction leading to the formation of rod clusters. As mentioned above, this does not appear to be the case here as the phase separation seems entirely entropically driven at the strength of polymer-rod interaction we have studied here.

The orientational ordering of the rods also appears to be strongly affected by a competition between entropy of the rods and entropy of the polymers. In all systems, the global orientational order of the rods decreases as the concentration of rods increases. However, in the system with repulsive rod-polymer interactions at low concentrations there is no long-range correlations in the rod orientations implying that the observed system averaged orientational order is primarily a function of having a limited number of oriented clusters and as we add more rods to the system the number of uncorrelated clusters increases hence lowering the average orientational order. However, at the highest concentrations of rods we do start to see weak long-range correlations in the rod orientations implying true orientational order may start to set in at these concentrations. The polymers in the repulsive interaction system show no orientational order and are somewhat compacted at the boundary between the rod phase and polymer melt phase. Such compaction is consistent with the depletion effect being responsible for the full phase separation seen in that system. As the concentration of rods increases, the long range orientational order of the rods decreases. In contrast, the system with attractive rod-polymer interactions shows true long range orientational order at low concentrations of rods. As the concentration of rods increases, these clusters break up and the orientational order decreases to the point where, at the highest concentrations, there is no long range correlations between rod orientations. In the system with attractive interactions the polymers close to and interpenetrating rod clusters are stretched out and oriented along the rods. As a result, increased rod ordering, while entropically favorable for the rods, would result in a considerable loss of entropy for the polymers in the system which prevents the long range orientational order at high rod concentrations. This competition between the entropy of the rods and that of the polymers seems to be a under appreciated facet of these systems.

Chapter 3

Polymer Crystallization: A multiphase-field study

3.1 Introduction

Polymer composites are commonly used in various industries due to their multifaceted advantages. These materials offer a compelling combination of enhanced mechanical properties, including high strength and durability, often surpassing those of traditional materials [273, 274]. Their lightweight nature makes them particularly desirable in aerospace and automotive applications, contributing to fuel efficiency and improved overall performance.

The main ingredients of polymer composites are a polymer-based matrix and a reinforcing material such as fibers, and nanofibers. Over the recent decades, semi-crystalline polymers have become increasingly popular as the matrix material due to their ease of manufacture and recyclability. Products made from these polymers are commonly shaped through extrusion or injection molding. As the properties of a product derived from semi-crystalline polymers heavily rely on the formed morphology and the degree of crystallization during the manufacturing process, investigations into the kinetics of crystallization and crystal morphology hold significant importance [83, 200, 212, 275]. An introduction to crystallization models of polymers and their history is provided in chapter 1. The work presented in this chapter was led by the author in collaboration with Ahmed Elmoghazy, Juliane Blarr, Benedikt Scheuring, Andreas Prahs, Daniel Schneider, Wilfried V. Liebig, Kay A. Weidenmann, Colin Denniston, and Britta Nestler. This work, in the form a manuscript, has been submitted for publication and is currently under review.

Motivation and Originality As mentioned above, microstructure and morphology have a direct impact on the physical and mechanical properties of the material. The typical kinetics used to model and predict crystallization of polymers are at a macroscopic and industrial scale. Experiments, including our own (discussed in section 3.3.2), indicate that crystallization results in intricate microstructures. Therefore, understanding the evolution and distribution of these microstructures is imperative.

The previous attempts to reproduce crystallization at microstructure level are mostly based on Kobayashi based phase-field models or probabilistic Avrami-based models. In Kobayashi-based models, the order parameter describes the crystallinity. This allows for the development of models for spherulitic and dendritic growth but limits the application of such models to larger scales. Particularly, simulating systems with fibers becomes extremely costly computationally as the fibers are several orders of magnitude larger than the dendritic branches. The probabilistic Avrami-based models generate randomly dispersed nuclei and model their evolution based on the Avrami equation. The main challenge for such models is tracking of the boundaries and their interaction. This becomes even more challenging when applied to a system with several components.

In this work, the multiphase-field method (MPF) is coupled with the Nakamura model and the equation of heat conduction to model the non-local crystallization of polymeric materials on a microstructural length scale. The MPF is a generalization of the classical phase-field method to numerous locally present phases [39]. This readily allows for the inclusion of extra phases such as fibers and the study of their impact on the crystallization of the polymeric material. MPF has been successfully used to study mircostructral behaviour of materials [276–279].

In our model, the phase-field order parameter defines the crystalline areas, whereas the crystallization kinetic, within a crystallizing phase, is governed by the Nakamura model. This allows for a more coarse-grained description of the system compared to models at spherulitic level but still accounts for the inhomogeneities at the micro-scale. The dependency of crystallization on temperature is also accounted for through the Nakamura model and the crystallization rate constant (defined later).

Overall, our approach yields heterogeneous crystal morphologies observed in experiments of semicrystalline polymers and predicts the impact of the cooling process and non-isothermal crystallization on such morphologies. Moreover, the present model enables to account for phases that remain completely free of crystallinity such as fibers in fiber reinforced polymers.

Outline In section 3.2, we describe our model and the equations involved. In section 3.3, we share the experimental findings of our Differential Scanning Calorimetry (DSC) and Polarized Light Microscopy (PLM). In section 3.4, we discuss the numerical implementation of the model and details regarding numerical constants and parameters. This is followed by the results of our simulations and the comparisons to experimental data. We conclude the article with a summary of the model and the results in 3.5.

Notation In this chapter, we use a direct tensor notation. Thus, scalar fields are written as α and vectors as $\boldsymbol{a}$. The scalar product between two vectors is given by $\boldsymbol{a} \cdot \boldsymbol{b}$.

3.2 Modeling and theory

The main objective of the present work is to address the non-locality of crystalline structure in semicrystalline polymeric materials and composites. To achieve this, we use a multiphase-field (MPF) method to follow the evolution of crystalline grains while the crystallinity of each grain evolves according to an Avrami-type model. In this section, we explain each theory and how they have been utilized to successfully reproduce the crystallization of polymeric materials.

3.2.1 Multiphase-field Method

Free energy functional In this work, we employ a multiphase-field method to track the evolution of the crystalline phase. The starting point of the modeling is given by the free energy functional

$$\mathcal{F}(\boldsymbol{\phi}, \nabla\boldsymbol{\phi}, \chi) = \int_V f(\boldsymbol{\phi}, \nabla\boldsymbol{\phi}, \chi)\,\mathrm{d}V. \tag{3.1}$$

Here, f denotes the free energy density and $\boldsymbol{\phi}$ is the tuple of order parameters, i.e., $\boldsymbol{\phi} = \{\phi_1, \dots, \phi_\mathrm{N}\}$, where N is the number of phases. The tuple of the gradients of the order parameters is abbreviated by $\nabla\boldsymbol{\phi} = \{\nabla\phi_1, \dots, \nabla\phi_\mathrm{N}\}$ and the relative crystallinity is denoted by χ.

Since the order parameters are interpreted as the volume fractions of the corresponding subregions, the summation constraint

$$\sum_{\alpha=1}^{N} \phi_\alpha(\boldsymbol{x}, t) = 1 \tag{3.2}$$

has to be fulfilled where $\boldsymbol{x}$ is the position vector, and t is the time.

Subsequently, an additive decomposition of the free energy density is assumed:

$$f(\boldsymbol{\phi}, \nabla\boldsymbol{\phi}, \chi) = f_\mathrm{int}(\boldsymbol{\phi}, \nabla\boldsymbol{\phi}) + f_\mathrm{b}(\boldsymbol{\phi}, \chi), \tag{3.3}$$

with f_int as the interfacial contribution and f_b the bulk contribution. The interfacial contribution consists of the potential and gradient contributions:

$$f_\mathrm{int}(\boldsymbol{\phi}, \nabla\ \boldsymbol{\phi}) = f_\mathrm{pot}(\boldsymbol{\phi}) + f_\mathrm{grad}(\boldsymbol{\phi}, \nabla\ \boldsymbol{\phi}). \tag{3.4}$$

Following [35], we consider a gradient contribution f_grad of the following form

$$f_\mathrm{grad}(\boldsymbol{\phi}, \nabla\boldsymbol{\phi}) = \epsilon \sum_{\beta=2}^{\mathrm{N}} \sum_{\alpha=1}^{\beta-1} \gamma_{\alpha\beta} \left(\phi_\alpha \nabla\phi_\beta - \phi_\beta \nabla\phi_\alpha\right) . \left(\phi_\alpha \nabla\phi_\beta - \phi_\beta \nabla\phi_\alpha\right) \tag{3.5}$$

where $\gamma_{\alpha\beta}$ is the interfacial energy density between two phases, and ϵ is a constant related to the width of the diffuse interface [42]. Since it allows for stabilized interface kinetics [280] and it is numerically more efficient, we use a multi-obstacle potential for the potential contribution f_pot,

$$f_\mathrm{pot} = \frac{16}{\epsilon\pi^2} \sum_{\beta=2}^{\mathrm{N}} \sum_{\alpha=1}^{\beta-1} \gamma_{\alpha\beta} \phi_\alpha \phi_\beta \tag{3.6}$$

Anywhere the order parameters do not fulfill the Gibbs simplex, given by

$$\mathcal{G} = \left\{ \boldsymbol{\phi} : \sum_{\alpha=1}^{\mathrm{N}} \phi_\alpha(\boldsymbol{x}, t) = 1,\ \phi_\alpha \geq 0\,\forall\alpha \right\}, \tag{3.7}$$

$f_\mathrm{pot} = \infty$ is enforced. The bulk free energy f_b is defined as the interpolation of the phase-specific bulk free energies

$$f_\mathrm{b} = \sum_\alpha \phi_\alpha f_\mathrm{b}^\alpha(\chi_\alpha), \tag{3.8}$$

where f_b^α is the bulk free energy of phase α and it depends on the relative crystallinity of the corresponding phase. The phase-specific bulk free energy for each phase is defined as a quadratic function of the difference between relative crystallinity χ_α and its equilibrium value χ_α^{eq}, i.e.

$$f_{\mathrm{b}}^{\alpha}(\chi_\alpha) = A_\alpha(\chi_\alpha^{eq} - \chi_\alpha)^2 \tag{3.9}$$

where A_α is the driving force coefficient of phase α.

Evolution equation of the order parameter In this work, the order parameter evolution is described by

$$\frac{\partial \phi_\alpha}{\partial t} = -\frac{1}{\epsilon \mathrm{N}^*} \sum_{\alpha \neq \beta}^{\mathrm{N}^*} M_{\alpha\beta} \left(\frac{\delta \mathcal{F}}{\delta \phi_\alpha} - \frac{\delta \mathcal{F}}{\delta \phi_\beta} \right) \tag{3.10}$$

where $M_{\alpha\beta}$ is the individual mobility for each $\alpha - \beta$ interface [281] and $N*$ is the number of locally active phases. The mobility of the phase-field evolution can be set to that of a Hoffman-Lauritzen type model [188] to have the growth of the crystalline area to be consistent with the folded-chain crystal models. We further discuss the exact form of the mobility used in our model in section 3.4.1.

The variational derivatives in Eq. 3.10 are evaluated using the Euler-Lagrange equation [43]

$$\frac{\delta \mathcal{F}}{\delta \phi_\alpha} = \frac{\partial f}{\partial \phi_\alpha} - \mathrm{div}\left(\frac{\partial f}{\partial \nabla \phi_\alpha} \right) \tag{3.11}$$

where div stands for divergence operator $(\nabla \cdot)$.

3.2.2 Heat conduction and crystallization

Heat conduction Processing of thermoplastics always involves heat transfer. Therefore, it is crucial to account for its impact on crystallization. As crystallization is an exothermic phase transition, it is important to account for the heat generated during the process. In the present model, the heat source term that accounts for the crystallization enthalpy depends on the crystallization and cooling rates. Thus, the equation of heat conduction reads

$$\frac{\partial \theta}{\partial t} = \frac{\kappa}{\rho C_v} \nabla^2 \theta + \frac{X_\infty \Delta H_{\mathrm{f}}(\dot{\theta})}{C_v} \frac{\partial \bar{\chi}}{\partial t} \tag{3.12}$$

where θ is temperature, and $\nabla^2 \theta$ denotes the Laplacian of the temperature field. $\kappa(\phi)$ is the phase dependent heat conductivity coefficient, and $C_v(\phi)$ is the phase dependent specific heat. The phase dependent parameters are linearly interpolated at the interface. The numerical values of these parameters can be found in Table 3.4. The second term on the right hand side of Eq. 3.12 is the heat source term where X_∞ is the maximum crystallinity coefficient, $\Delta H_{\mathrm{f}}(\dot{\theta})$ is the cooling-rate dependent crystallization enthalpy. The dependency of the crystallization enthalpy on the cooling rate is found by fitting experimental data. The local average crystallinity $\bar{\chi}$ is defined as the interpolation of the phase dependent crystallinities:

$$\bar{\chi} = \sum_\alpha \chi_\alpha \phi_\alpha \tag{3.13}$$

where ϕ_α is the phase-field order parameter associated with phase α.

Crystallization described by the Nakamura model The multiphase-field model, discussed above, tracks the boundaries of the crystalline regions, i.e. where crystallization can happen and where it cannot. The degree of crystallinity inside the crystalline regions evolves following the Nakamura model. The Nakamura model can be directly derived from the Avrami model assuming a constant ratio of nucleus growth rate to spontaneous nucleation rate (isokinetic condition)[180]. We use the differential form of the Nakamura model to track the degree of crystallinity in the crystalline areas [192]

$$\frac{\partial \chi_\alpha}{\partial t} = n_\alpha K_\alpha(\theta, \dot{\theta})(1-\chi_\alpha)\left(\ln\left(\frac{1}{1-\chi_\alpha}\right)\right)^{(n_\alpha-1)/n_\alpha} \tag{3.14}$$

where χ_α is the crystallinity of phase α, n_α is the Avrami coefficient, and K_α is the crystallization rate constant which is a function of temperature and its rate of change. K_α is typically associated with the crystallization half-time and can be found from experimental data through a half-time analysis [192]. There are empirical [282] and theoretical [188] equations that describe the relation between half-time and temperature. In this work, we use Ziabicki's empirical formulation for our crystallization rate constant [282]

$$K_\alpha(\theta, \dot{\theta}) = K_{max,\alpha}(\dot{\theta})\mathrm{exp}\bigg(-4\mathrm{ln}(2)\frac{(\theta-\theta_{max,\alpha})^2}{D_\alpha^2}\bigg). \tag{3.15}$$

Here, the parameters $K_{max,\alpha}$, $\theta_{max,\alpha}$, and D_α can be found by fitting DSC measurements, as described in the subsequent sections. This equation has been successfully used in modelling similar systems [283, 284].

Governing equations The governing equations considered for modeling the non-local crystallization of the semi-crystalline PA6 are the evolution equation for the order parameter, the heat conduction and the Nakamura model in its differential form. They are collated in Tab. 3.1 for convenience.

Phase-field Evolution	$\frac{\partial \phi_\alpha}{\partial t} = -\frac{1}{\epsilon \mathrm{N}^*}\sum_{\alpha\neq\beta}^{\mathrm{N}^*} M_{\alpha\beta}\left(\frac{\delta\mathcal{F}}{\delta\phi_\alpha} - \frac{\delta\mathcal{F}}{\delta\phi_\beta}\right)$
Heat Conduction	$\frac{\partial\theta}{\partial t} = \frac{\kappa}{\rho C_v}\nabla^2\theta + \frac{X_\infty \Delta H(\dot{\theta})}{C_v}\frac{\partial\bar{\chi}}{\partial t}$
Crystallinity Evolution	$\frac{\partial\chi_\alpha}{\partial t} = n_\alpha K_\alpha(\theta,\dot{\theta})(1-\chi_\alpha)\left(\ln\left(\frac{1}{1-\chi_\alpha}\right)\right)^{(n_\alpha-1)/n_\alpha}$

Table 3.1: The governing equations, constituting the non-local crystallization model in this work, are the evolution of the order parameter, the equation of heat conduction, and the differential form of the Nakamura model.

3.3 Experimental Data and Results

Material Information TechnylStar XS 1352 BL PA6 was purchased from DOMO Chemicals GmbH (Leuna, Germany). Granules of weight of approximately 9 mg were used as samples. Since polyamide is a hygroscopic polymer and therefore tends to absorb water, the samples were dried in a vacuum oven at 50 °C for 24 h before testing. The experiments were carried out by Juliane Blarr and Benedikt Scheuring.

3.3.1 DSC Measurements

Experimental procedure of the DSC measurements Non-isothermal Differential Scanning Calorimetry (DSC) measurements were performed with a Mettler Toldeo DSC 3 series with automatic sample changer according to DIN EN ISO 11357-1 in aluminum trays and nitrogen atmosphere. Measurements were performed at heating and cooling rates of 0.6 K/min, 5 K/min, 20 K/min, and 50 K/min. To reduce the test time, all measurements were performed in a temperature range of 25 - 250 °C except for the experiments at 0.6 K/min cooling rate. At 0.6 K/min cooling rate, a temperature range of 100 - 250 °C was investigated. To account for fluctuations in the measurement data, at least two cooling processes were recorded for each cooling rate.

The results of the DSC measurements with cooling rates ranging from 0.6 K/min to 50 K/min are shown in Fig. 3.1 as a plot of heat flow versus temperature.

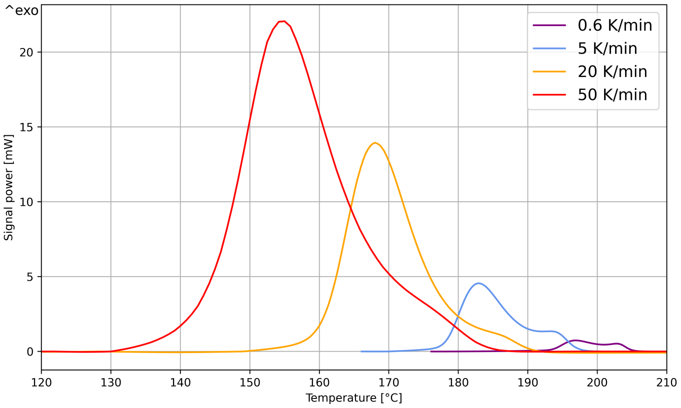

Figure 3.1: Non-isothermal DSC exotherms are shown at various cooling rates: (red) 50 K/min, (orange) 20 K/min, (blue) 5 K/min, and (purple) 0.6 K/min. The increase in cooling rate results in stronger signals, and lower crystallization temperature.

Results and discussion of the DSC measurements In Fig. 3.1, we observe that an increase in the cooling rate results in broadening of the DSC exotherms plus a significant increase in the DSC signal. The DSC signal is directly correlated with the crystallization rate such that a more pronounced DSC signal is detected at a higher crystallization rate [285]. Therefore, increasing the cooling rate seems to increase the overall rate of crystallization. The temperature where the peak signal is observed at is called the crystallization temperature T_c. We observe a shift of T_c to lower temperatures when the cooling rate is increased. The horizontal shift of the DSC curves to lower temperatures is attributed to the effect of the cooling rate on nucleation[286].

Crystallization begins after an initial delay which depends on the interplay between the incubation and residence time. The incubation time is the time required for the critical nucleus to form at that specific temperature. Dependent upon temperature, incubation time is longer at higher temperatures. The residence/induction time is the time it takes for the sample to sense the change in the temperature and adjust during a non-isothermal scan. Successful nucleation occurs when the residence time at a given temperature is more than the incubation time at that temperature [286, 287]. At lower cooling rates, this criterion is met at higher temperatures and hence the shift to the right in the DSC exotherms. Conversely at higher cooling rates, the residence time is no longer sufficient for stable nucleation at high temperatures and crystallization happens only at lower temperatures [286].

The absolute crystallinity of the sample is determined by the ratio

$$X_\infty = \frac{\Delta H_\mathrm{f} - \Delta H_\mathrm{cold}}{\Delta H_0} \times 100, \tag{3.16}$$

where ΔH_f corresponds to the enthalpy of fusion after the second heating and as shown in Fig. 3.1, it depends on the cooling rate. ΔH_cold is the enthalpy released during cold crystallization, and $\Delta H_0 = 204.8\ \mathrm{J\,g^{-1}}$ [288] is the enthalpy of fusion of perfect crystals of PA6. It is to be noted that no cold crystallization enthalpy was detected at any cooling rates in our experiments. The calculated X_∞ as well as crystallization temperature T_c and heat of fusion ΔH_f for different cooling rates are collated in table 3.2.

Cooling rate $[\mathrm{K\,min^{-1}}]$	T_c [°C]	ΔH_f $[\mathrm{J\,g^{-1}}]$	X_∞ [%]
0.6	196.9	67.22	32.8
5	183.2	58.17	28.4
20	168.88	62.28	30.4
50	156.61	55.20	26.9

Table 3.2: Crystallinity properties for PA6 for different cooling rates

3.3.2 Light Microscopy Experiments

Optical microscopy is a powerful method in analyzing the crystalline structure, defects, and orientation of materials such as polymers, liquid crystals, and semiconductors. Polarized light microscopy (PLM) is used in particular to examine crystals [289–293]. In PLM, the light from a transmitted light microscope passes through two polarization filters, each rotated by 90°, which ensure that the light is extinguished in the final image. In contrast to amorphous areas, crystals are optically anisotropic or birefringent objects which, when introduced into the beam path between the polarizers, cause a change in the plane of polarization. As a result, complete extinction no longer occurs and corresponding structures become visible. Hence, we utilize PLM with an integrated cooling/heating chamber to study the impact of cooling rate on spherulite size and distribution as well as the crystallization rate and crystallization temperature range.

Experimental setup and procedure Thin slices of thickness 7 µm were made from a granulate grain of PA6. This was done using a rotary microtome (HM 355 S, ThermoFisher Scientific). To avoid any undesirable reflections or refractions, the slices were wetted with kerosene oil before being placed on the slide. The temperature chamber was located externally and connected by a tube to the test area under the optical microscope, so that cooling could be performed directly under the microscope.

Experiments were performed on two samples. Each sample was heated and cooled at three different cooling rates: 50 K/min, 20 K/min and 5 K/min. The PLM was conducted using transmitted light with crossed polarizers on a BX-51 (Olympus) machine. In addition, a $\lambda/4$ plate was used to improve contrast. In images taken with a $\lambda/4$-plate, amorphous regions appear as magenta, while the crystalline regions generally appear as yellow or blue, depending on the orientation of the crystallites in the beam path. The microscopy images were taken at 9 frames per second (fps) at 50 × magnification. In the generated videos, the temperature was superimposed.

Results and discussion of Microscopy Experiments Fig. 3.2 shows the evolution of crystallization at the cooling rate 5 K/min captured by PLM. The images are chronologically arranged from left to right. We initially see a uniform magenta colour indicating that the entire sample is amorphous and liquid. Further cooling of the sample results in formation of crystalline regions. This can be seen in the middle image where several yellow regions appear. These regions seem to form linear stripes. The cooling is continued until no change in the structure of the sample is detected. The final structure of the sample is shown in the image on the right. The yellow stripes already visible in the second image are more pronounced, and the formerly magenta-coloured areas appear as blue dots. In the solid state, therefore, crystalline phases of either orientations (appearing in yellow or blue) have formed in the amorphous areas.

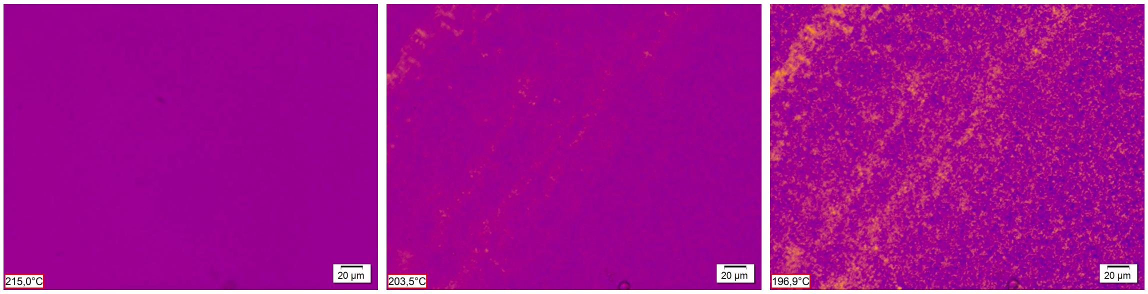

(a) (b) (c)

Figure 3.2: Images of a sample cooled down at 5 K/min (a) initial state ($\theta = 215°$C), (b) during the crystallization process ($\theta = 203.5°$C) and (c) final state ($\theta = 196.9°$C, after no change in the crystallization structure can be seen anymore.) Yellow and blue regions show crystalline areas while magenta demonstrates amorphous regions.

We observe that most of the crystallization sites form instantaneously at a start temperature followed by a relatively rapid growth. The stripe-like patterns of crystals were originally assumed to be the result of sample preparation. However, even after melting the sample and performing cooling experiments, these stripe-like crystalline areas are observed. This leads us to believe that such patterns are formed following the grooves of the cover glasses/slides. This is further confirmed after comparing the results to the experiments performed at 50 K/min cooling rate.

Fig. 3.3 shows PLM snapshots of the sample cooled at 50 K/min. Like before, the images are

(a) (b) (c)

Figure 3.3: Images of a sample cooled down at 50 K/min (a) initial state ($\theta = 205°\mathrm{C}$), (b) during the crystallization process ($\theta = 188°\mathrm{C}$) and (c) final state ($\theta = 173.3°\mathrm{C}$). Yellow and blue regions show crystalline areas while magenta demonstrates amorphous regions.

chronologically ordered from left to right. Similar stripes of crystalline areas are observed and they seem to form very early on in the crystallization process. However, we see slightly finer and milder yellow regions in the images for 50 K/min cooling rate. This is expected as the polymer chains do not have sufficient time to form folded crystals at high cooling rates resulting in smaller crystals.

There are advantages to using PLM but there are also barriers. Generally, in PLM images, it can be difficult to distinguish between different regions due to the changes caused by rotation of the sample. When the sample is rotated in the beam path, the colours of the crystalline regions interchange, and overall it could be difficult to clearly delineate amorphous and crystalline regions, especially in the presence of fine crystals.

Moreover, we could not obtain detailed material characteristic information of the star-branched PA6 used in our experiments. However, we suspect that the 7 µm thickness of our samples is probably considerably larger than a single crystal layer [294]. This can lead to superposition effects during imaging and some errors in the analysis of the images.

3.4 Numerical studies and results

3.4.1 Numerical implementations

Determination of crystallization parameters using Ziabicki model In 1968, Ziabicki extended the Turnbull-Fisher model to describe the kinetics of systems with anisotropic nuclei in isothermal and non-isothermal conditions [282]. Later, he further generalized his model to account for transient and athermal effects [282]. The extended crystallization kinetics function takes the form of a Gaussian function with the empirical parameters K_{max}, D and θ_{max}. The parameters could also be presented as cooling rate-dependent functions by evaluating the DSC measurements for different cooling rates and fitting the parameters on a power function for D and θ_{max}, and a linear function for K_{max} as suggested by Sierra et al. [295]. Since the crystallization enthalpy is also shown to be cooling rate-dependent, the term dH could also be linearly fitted in the same way. The crystallization rate constant parameter $K_c(\theta, \dot{\theta})$ takes the form:

$$K_c(\theta, \dot{\theta}) = K_{max,c}(\dot{\theta})\mathrm{exp}\left(-4\mathrm{ln}(2)\frac{(\theta - \theta_{max,c}(\dot{\theta}))^2}{D_c(\dot{\theta})^2}\right) \tag{3.17}$$

where subscript c stands for the crystalline phase and

$$\theta_{max,c}(\dot{\theta}) = C_1 \times \dot{\theta}^{-C_2} \tag{3.18a}$$

$$K_{max,c}(\dot{\theta}) = C_3 \times \dot{\theta} + C_4 \tag{3.18b}$$

$$D_c(\dot{\theta}) = C_5 \times \dot{\theta}^{C_6} \tag{3.18c}$$

$$dH(\dot{\theta}) = -C_7 \times \dot{\theta} + C_8. \tag{3.18d}$$

The value of the coefficients above are shown in table 3.3. A plot of K_c as a function of temperature for different cooling rates is shown in Fig. 3.4. To validate these values, the crystallization evolution predicted by the Nakamura model using the fitted coefficients are compared to the experimental results. Fig. 3.5 shows the relative crystallinity as a function of temperature (a) and time (b). The solid lines indicate the results of the Nakamura model using our fitted coefficients and the cross points indicate the experimental data (measured as explained in 3.3).

$C_1[1/s]$	$C_2[-]$	$C_3[s/K]$	$C_4[1/s]$	$C_5[1/s]$	$C_6[-]$	$C_7[s/K]$	$C_8[J/Kg]$
430.15	0.0207	0.0679	0.0063	29.78	0.2596	14.5	67.07

Table 3.3: Crystallization parameters for the Ziabicki model (Eq. 3.17) obtained from fitting the DSC measurements.

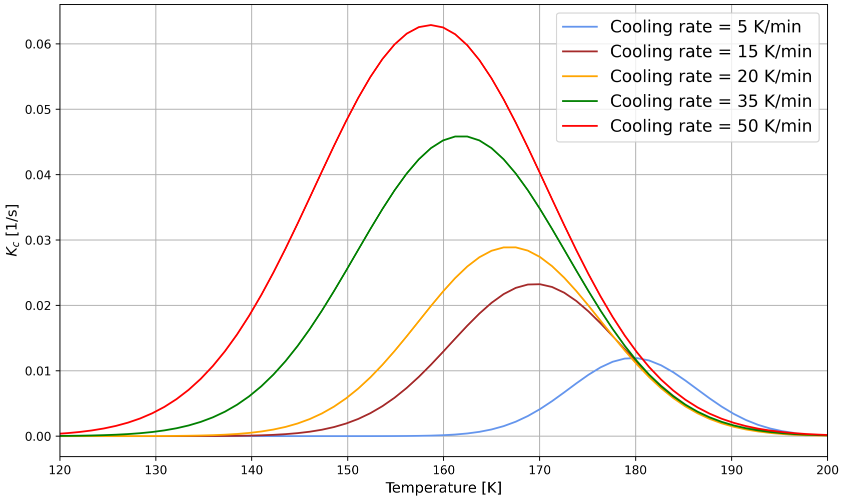

Figure 3.4: K_c parameter for different cooling rates as a function of temperature. The parameter is derived from the fitted empirical parameters. A clear trend of higher amplitude, wider base and a shift of the curves to the left is shown as the cooling rate increases.

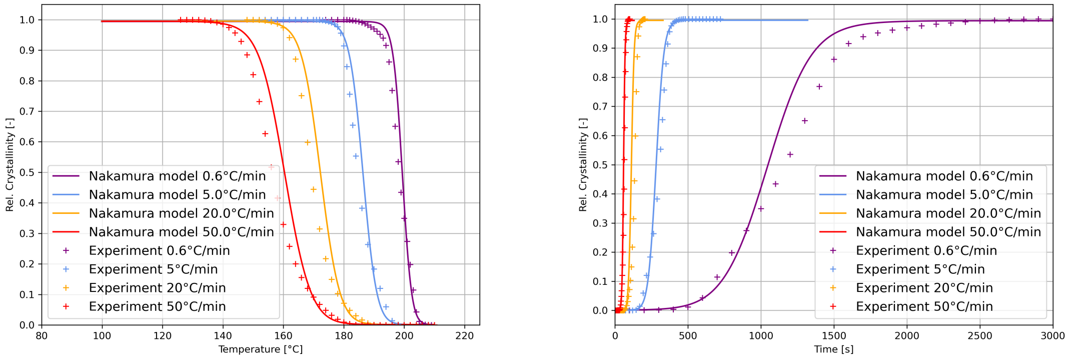

(a) (b)

Figure 3.5: Empirical crystallization parameters are validated by comparing the experimental results to the predictions of the model

Numerical implementation As mentioned in the theory section, our model consists of the heat conduction equation, the multiphase-field equation, and the Nakamura equation. The heat conduction and Nakamura equations are discretized using an implicit finite difference method. As the Nakamura model contains nonlinear terms, an iterative Newton method is utilized to find the crystallinity values.

The phase-field evolution equation is explicitly discretized using a second-order finite difference method. To avoid interface pinning and premature grain shrinkage, the driving force coefficient A_c (for crystal phase) in Eq. 3.9 is calibrated to always fulfill

$$\frac{|\Delta W_{bulk}^{\alpha\beta}|}{\frac{\gamma_{\alpha\beta}+\gamma^n}{\varepsilon}} \approx 1 \tag{3.19}$$

where $|\Delta W_{bulk}^{\alpha\beta}|$ is the driving force due to crystallization. $\gamma_{\alpha\beta}$ and γ^n are the surface tension in the tangential and normal directions, respectively. The value of A_c also directly affects the critical radius of the grains, meaning that the critical radius decreases when a larger A_c is applied. Fig. 3.6 shows the relation between A_c and the critical radius. This is expected as a larger driving force can overcome the higher surface tension of smaller crystalline grains.

In Eq. 3.9, the equilibrium crystallinity χ_α^{eq} is assumed to be 1, driving the system towards the maximum crystallinity. This means that initially, when crystallinity is low, we get the highest driving force and the driving force vanishes when full crystallinity is achieved.

We use a mobility M_{ca} between the crystalline and amorphous phase that is a function of the temperature and cooling rate, and has the same shape as the crystallization rate constant K. In order to improve the stability of the phase-field evolution a stabilizing factor is multiplied by the normalized K_c giving rise to the mobility

$$M_{ca} = \frac{(\Delta x)^2}{4\Delta t(\gamma_{ca}+\gamma^n)} \frac{K_c(\theta,\dot{\theta})}{K_{max,c}(\dot{\theta})} \tag{3.20}$$

where K_c is the crystallization rate constant for the crystal phase (see. Eq. 3.17), and $K_{max,c}$ is the

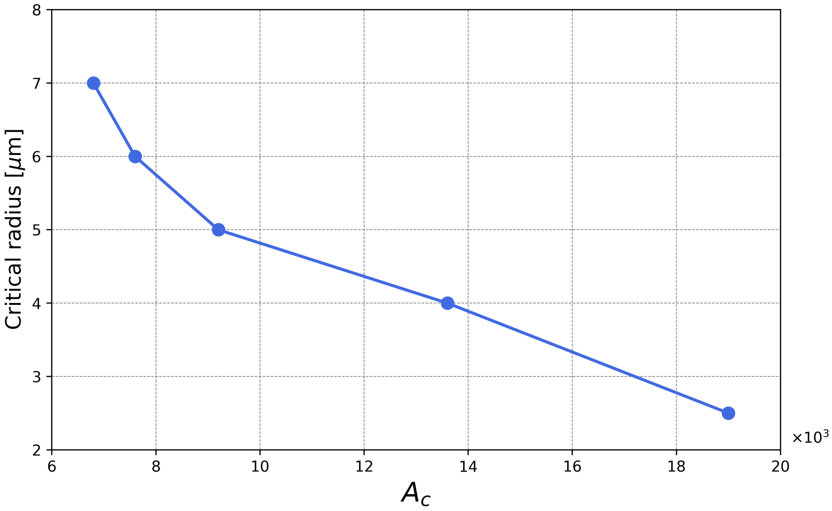

Figure 3.6: Graph relating the driving force prefactor (A_c) to critical radius

crystallization parameter obtained from Eq. 3.18b.

The mobility between the PA6 phases (crystalline and amorphous) and the fiber phase, $M_{\alpha f}$, is considered to be 0. This ensures the stability of the fiber phase and prevents the polymeric phases from leaking into and taking over areas occupied by the fiber phase. The details of the numerical values for each parameter can be found in Table 3.4.

In this work, we only consider instantaneous formation of crystalline regions at $t = 0$, i.e. crystalline regions are initially distributed in the amorphous phase. Since the Nakamura equation, which controls the degree of crystallinity of the crystalline areas, has to be non-zero to get any evolution, we initialize the crystallinity of the crystalline regions to a very small non-zero value.

The crystallinity only evolves in the crystalline phase and does not evolve in the amorphous phase nor the fiber phase. However, since the mobility between the amorphous and crystalline phase is not zero, the crystal grains can grow into and take over amorphous regions where the crystallization can then take place.

3.4.2 Pure Matrix

Single grain We begin by investigating the simplest system consisting of a single crystalline grain. The initial radius of the grain is 6 μm and the initial temperature of the domain is set to 200 °C. A Dirichlet boundary condition with a constant cooling rate is applied to the left and right boundaries, while the top and bottom boundaries are periodic. As mentioned before, an initial non-zero value of crystallinity is required for the crystallinity to evolve according to Nakamura model. Thus, we set the initial crystallinity degree of the crystalline areas to the small value 0.1%. As a result, the crystalline areas should not be interpreted as crystal nuclei but regions where some nuclei germs exist and there is potential for crystallization. Fig. 3.7 shows the phase-field order parameter field (upper row) and crystallinity field (lower row) after reaching the glass transition temperature T_g for different cooling rates, namely, 5, 20, 35, and 50 K/min. As can be seen, at higher cooling rates, the final size of the crystalline area is smaller compared to lower cooling rates. As the grain grows,

Table 3.4: Summary of all model parameters

Parameter	Value	Unit
	Thermal Properties	
Thermal Conductivity (κ)		
PA6	0.25 [296]	W/(m·K)
Carbon fiber	100 [297]	W/(m·K)
Specific Heat Capacity (C_p)		
PA6 (100% amorphous)	512	J/(kg·K)
PA6 (100% crystalline)	4310*	J/(kg·K)
Carbon Fiber	700 [297]	J/(kg·K)
Density (ρ)		
PA6	1130 [298]	kg/m^3
Carbon Fiber	1800[297]	kg/m^3
	PA6 Crystallinity Properties	
T_{max}	Eq. 3.18a	K
D	Eq. 3.18c	K
K_{max}	Eq. 3.18b	s^{-1}
	Phase-field Parameters	
Surface Tension (PA6)		
Normal component (γ^n)	37.19 [249]	mN/m
Tangential component ($\gamma_{\alpha\beta}$)	0.4·(γ^n)	mN/m
Mobility ($M_{\alpha\beta}$)		
PA6	Eq. 3.20	-
Carbon Fiber	0	-
	Numerical Parameters	
Mesh Size	0.5, 1	μm
Box Size	500	Cells
Time Step	0.01	s
Diffuse interface width	4	Cells

* Linearly approximated from 100% amorphous and 30% crystalline

the crystallinity evolves in the newly acquired areas by a rate determined by the temperature and cooling rate at these new areas. As crystallization at different locations happens at different times and temperatures, different levels of crystallinity are observed even inside a crystalline phase, leading to inhomogeneous crystallinity distributions.

The temperature field at different times during the simulation for the cooling rate of 15 K/min is shown in Fig. 3.8. At the beginning, the temperature field is more or less uniform stripes (in the vertical direction). After onset of crystallization, we observe higher temperatures around the crystalline area as a result of the released crystallization heat. As we reach the end of the simulation and crystallization slows down, we see the temperature gradient going back to an almost uniform pattern of stripes. We would like to point out that the effect of the crystallization heat is reduced by the influence of a Dirichlet boundary conditions which are predominant for a simulation box of this size.

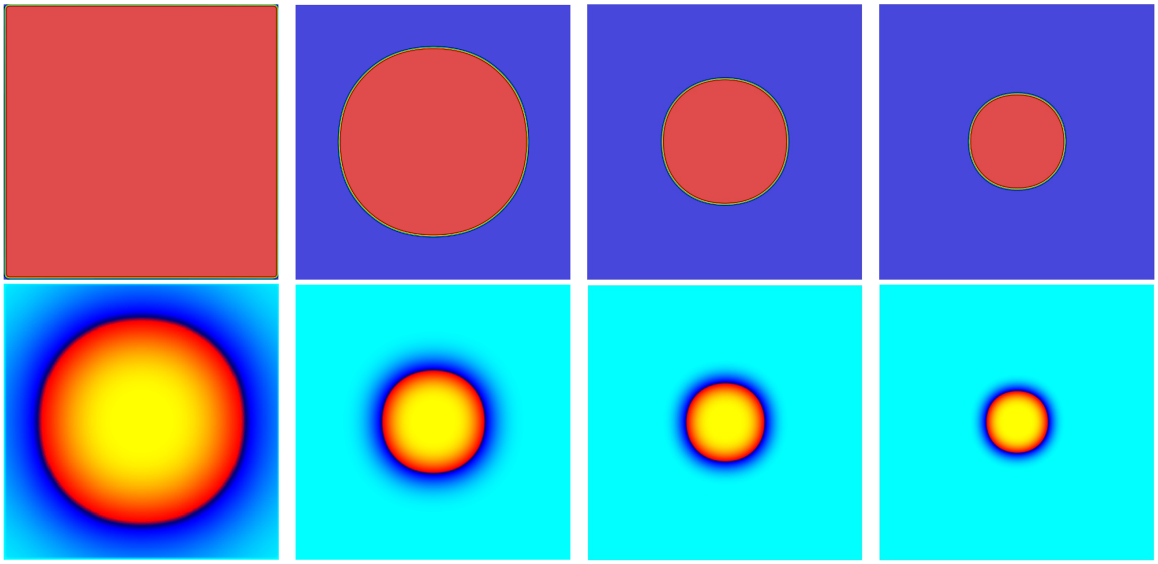

(a) 5 K/min (b) 20 K/min (c) 35 K/min (d) 50 K/min

Figure 3.7: The final morphologies of a single grain under different cooling rates are illustrated. The top row shows the phase-field order parameter field. The bottom row shows the crystallinity field.

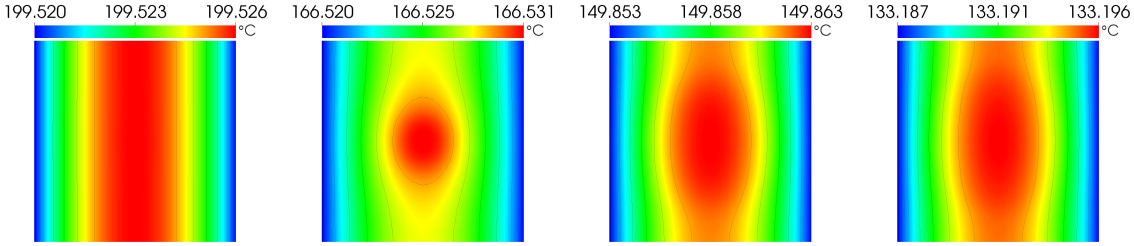

(a) (b) (c) (d)

Figure 3.8: The evolution of the temperature field for cooling rate 20 K/min is shown. (a) $t = 5s$, relative crystallinity ≈ 0 (b)$t = 100s$, relative crystallinity $= 0.003$ (c)$t = 150s$, relative crystallinity $= 0.54$ (d)$t = 200s$, relative crystallinity $= 1$

Case I: large grains The primary goal of this study is to develop a model that is capable of predicting the microstructure of semi-crystalline polymers and capturing the heterogeneous nature of such microstructures. Therefore, the natural next step is to study systems with multiple grains and the resulting microstructures. In this section, we investigate the crystallization behaviour of pure PA6 by simulating a 2D system of 500x500 cells and $dx = 1\mu$m under different cooling rates. The cooling rates selected for this study as with the single grain, are 5 K/min, 20 K/min, 35 K/min, and 50 K/min. Initially, 100 crystalline grains of radius between 4 and 10 μm and initial crystallinity degree of 0.1% are randomly dispersed in the amorphous phase leading to an initial crystal grain volume fraction of 6%. The initial morphology of the system is shown in Fig. 3.9a.

Fig. 3.10 shows the final (after reaching T_g) morphology of the system for different cooling rates. At the lowest cooling rate of 5 K/min, we observe fewer but larger grains covering almost the entire simulation box. We also see fewer grain boundaries. This is expected as the slower cooling rate provides sufficient time for the grains to grow and enough time for crystallinity to reach high values everywhere. As we increase the cooling rate, we see that the size of the grains becomes smaller and

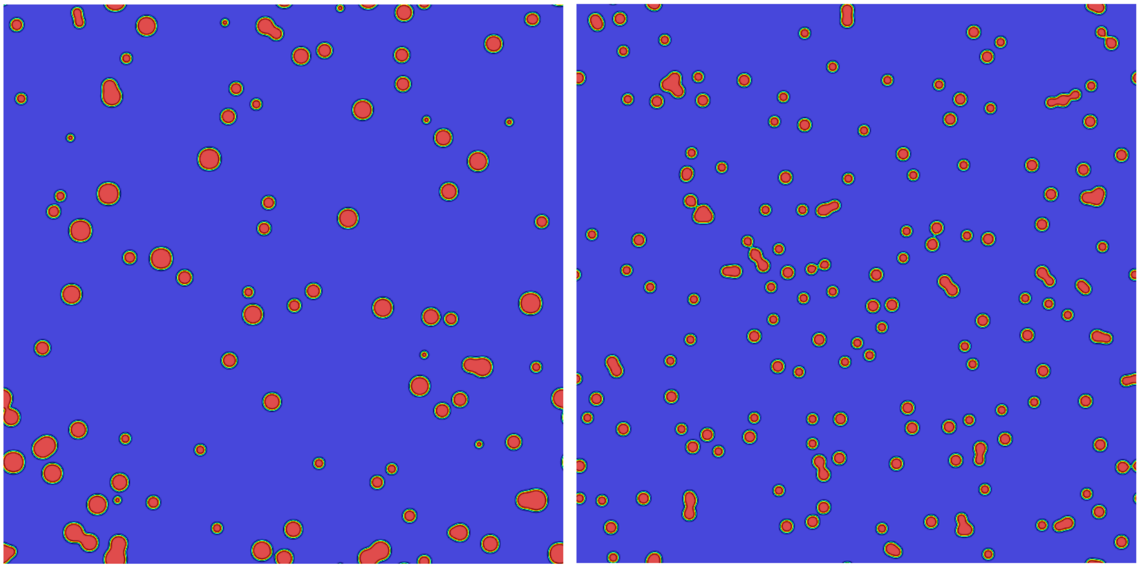

(a) (b)

Figure 3.9: The initial configuration of the system is shown for (a) 100 grains of radius between 4 and 10 μm (b) 185 grains of radius 2.5 and 3 μm.

gradients in crystallinity increase leading to fine grain morphologies. This prediction of the impact of cooling rate on morphology agrees with what we see in the experiments (see section 3.3.2) and other experimental work [286, 299].

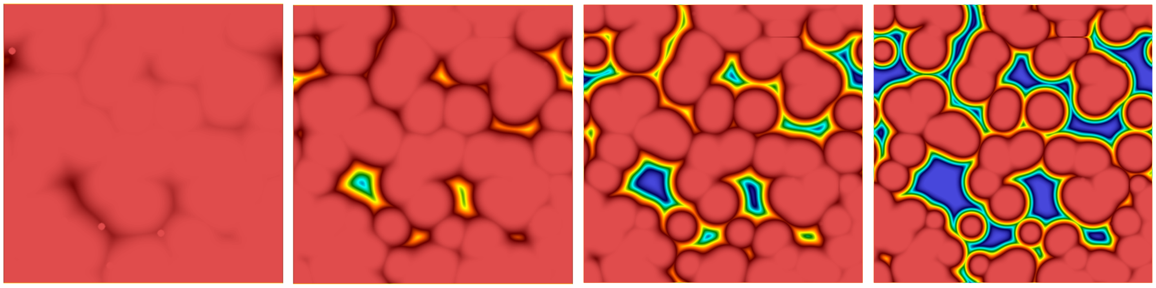

(a) 5 K/min (b) 20 K/min (c) 35 K/min (d) 50 K/min

Figure 3.10: Final morphologies under different cooling rate are shown. System is initialized with 100 grains of radius between 4 and 10 μm (6% area density). As expected, a higher conversion rate and larger crystalline areas are observed for lower cooling rates.

Case II: small grains To study the impact of initial grain structure on the final results, we examine the crystal morphology of pure PA6 for a system with higher number of initial crystalline grains and smaller radii. Initially, we randomly disperse 185 crystalline grains of radii between 2.5 and 3 μm, and initial crystallinity of 0.1%. This gives a similar initial crystal grain volume fraction as the previous example (6%). We apply and study the system under the same cooling rates as before. The simulation box is in 2D with 500x500 cells and $dx = 0.5\mu$m. The initial morphology of the system is shown in Fig. 3.9b.

Fig. 3.11 shows the final morphology of the system for different cooling rates. Similar to the other examples we have discussed so far, we see larger grains and more uniform crystallinity inside each grain when the cooling rates are lower. Increasing cooling rates results in smaller grains and larger variability in the crystallinity field.

Comparing the results in Fig. 3.10 and Fig. 3.11, in general, we see that more of the system crystallizes when more but smaller grains are embedded initially. However, we observe a more distinct difference between the morphologies in Fig. 3.10 and Fig. 3.11 at higher cooling rates. This is due to the fact that at lower cooling rates, the crystallinity has time to evolve to values near 1. Moreover, the temperature gradient across the simulation box is less steep and crystallization heat release is more uniform across the simulation box. All of these results in a more uniform growth of the grains and their crystallinity. In this case, the initial size of the grains has less of an impact compared to the number of initial grains on the total crystallinity as most grains reach their maximum size (considering impingement constraints).

Alternatively at high cooling rates, the number of initial grains and their size both play an important role in the final morphology. In this case, the grains do not have ample time to grow and are smaller in size. Also, due to the rapid decrease of temperature at the boundaries, there are steeper gradients across the simulation box. The combination of these leads to more localized crystallization (i.e. limited to the location of the initial grains) and therefore more heterogeneity in the morphology.

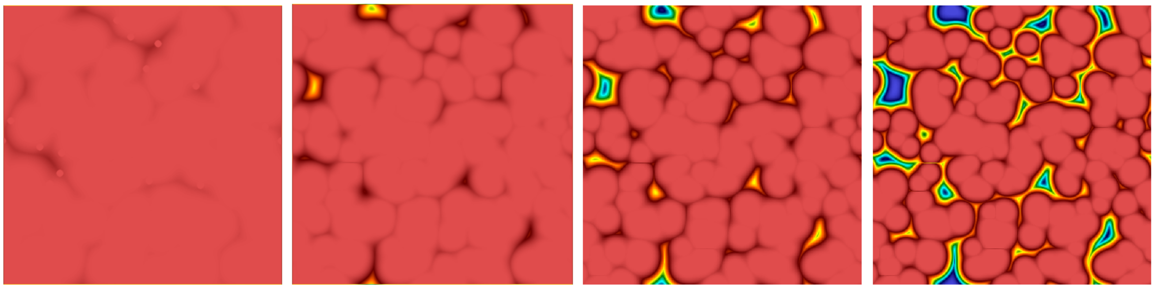

(a) 5 K/min (b) 20 K/min (c) 35 K/min (d) 50 K/min

Figure 3.11: Typical morphologies (after reaching T_g) for a system initialized with 185 crystalline grains of radius between 2.5 and 3 μm and at different cooling rates. At low cooling rates, a more uniform morphology is obtained while more inhomogeneous structures are observed for high cooling rates. Note that the box size is half of the one in Fig. 3.10.

Relative Crystallinity So far we discussed the resulting morphologies of our simulation and the impact of initial size and distribution of crystalline grains as well as cooling rate on these morphologies. It is informative to look at the relative crystallinity of our systems too as it can directly be compared to the results obtained from our DSC measurements. Fig. 3.12 shows the evolution of the relative crystallinity for case I and case II discussed above. The solid lines show the results of the simulations and the cross points show the results of the DSC measurements. The relative crystallinity is defined as the average crystallinity over the simulation box divided by the maximum:

$$\hat{\chi} = \frac{\langle \bar{\chi} \rangle}{max\{\bar{\chi}\}} \tag{3.21}$$

where

$$\langle \bar{\chi} \rangle = \frac{1}{A} \int_A \bar{\chi} da \tag{3.22}$$

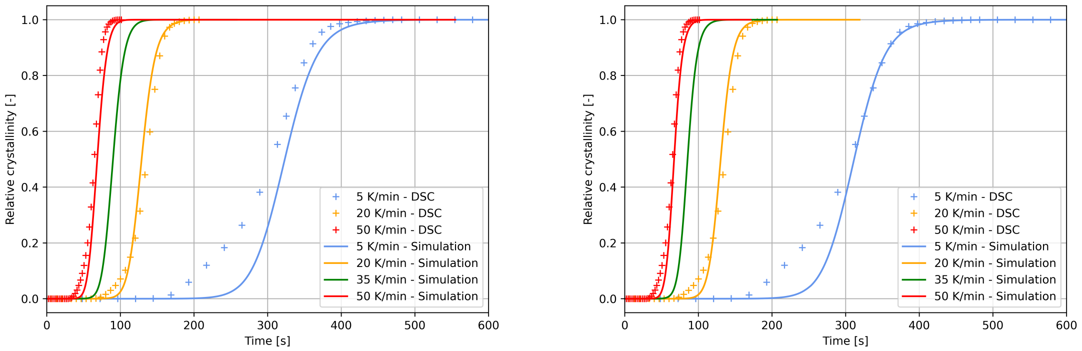

(a) (b)

Figure 3.12: Evolution curves of relative crystallinity are shown for different cooling rates. (a) is initialized with 100 crystalline grains while (b) is initialized with 185 crystalline grains. The curves provide qualitative agreements with experiments.

with A denoting the area of the simulation domain. As can be seen, our model correctly recovers the form of the crystallinity evolution curves. We also observe that lowering cooling rates results in the crystallization starting later and taking longer which is consistent with experimental DSC data. The gap between different curves grows as the cooling rate is decreased similar to the experimental curves. However, our model predicts a longer delay prior to the onset of crystallization compared to the experiments (a shift to the right). This difference is present in Fig. 3.5 but it is considerably smaller. Thus, this could be due to ignoring the smaller peaks that are observed in the DSC exotherms at the beginning of crystallization. Moreover, to compare the impact of cooling rate on the final morphology, we initialized all systems with similar density of grains, range of radii, and initial degree of crystallinity. In reality, the cooling rate and processing method affect the nucleation process as mentioned in section 3.3. One would expect a higher number of nuclei for systems with higher cooling rates [286] and we observe a better agreement with the experimental results for the system with larger number of initial nuclei (see Fig. 3.12b). The influence of nucleation is included through the Nakamura equation. However, further investigation on the relation between nucleation and initial crystalline grain distribution is required to obtain quantitatively accurate results, which will be investigated in future work.

The relation between relative crystallinity and temperature is also commonly investigated to collect information about the crystallization process. Fig. 3.13 shows the relative crystallinity as a function of temperature obtained from our simulations. Similar to evolution plots, we see a good qualitative agreement with Fig. 3.5. The shape of the curves and their order matches the experimental results. However, a shift to lower temperatures is observed in this case. We believe this has the same origin as the shift in the relative crystallinity evolution curves. Comparing Fig. 3.13a and Fig. 3.13b, we can clearly see the impact of the initial conditions. The curves for a system with lower number and larger size of grains are slightly shifted to higher temperatures and the slopes of the curves are marginally less steep.

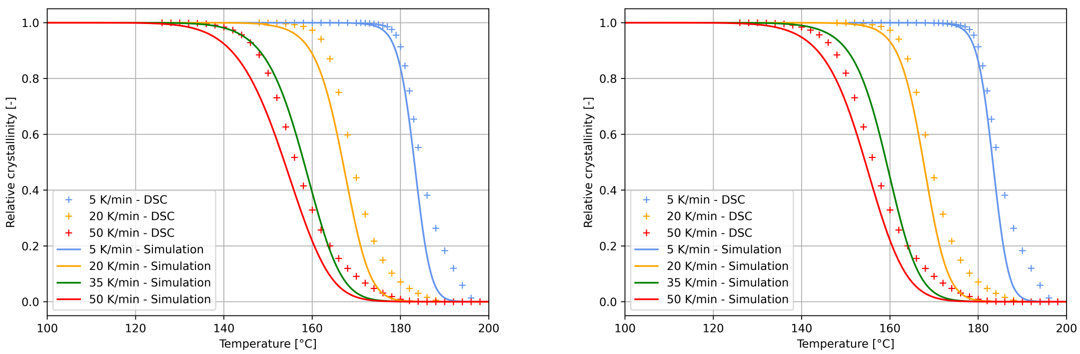

(a) (b)

Figure 3.13: Relative crystallinity is shown as a function of temperature for different cooling rates. (a) is initialized with 100 crystalline grains while (b) is initialized with 185 crystalline grains. The curves provide qualitative agreements with experiments.

3.4.3 Inclusion of Fibers

In this section we include different orientations a single discontinuous carbon fiber with a diameter of 15 μm and length of 150 μm in a PA6 matrix. The fiber is added to the multiphase-field model as a third phase that does not crystallize. As mentioned before, the mobility between the fiber and the other two phases (amorphous and crystalline) is 0. The thermal properties for the carbon fiber are shown in Table 3.4.The presence of fiber in a polymer matrix affects the nucleation process of the polymer. The surface of the fiber acts as a local nucleation site for the polymer around it. This phenomenon is called transcrystallinity. To account for this, we initialize the area at the interface and around the fiber in our simulations with a higher density of crystalline grains. We populate the interface of the fiber and the matrix with a maximum of 50% crystallinity. This value is chosen somewhat arbitrarily as we did not have access to experimental data for the specific matrix and fiber used in our experiments. This parameter can be simply adjusted for different systems and upon access to experimental or molecular data. The areas away from the fiber are initialized with 6% volume fraction of the crystalline grains similar to the pure matrix simulations.

Single fiber: Horizontal We first look at a single fiber placed horizontally in the centre of the box. Fig. 3.14 shows the initial and final distribution of grains for a typical system with the horizontal fiber. Results for two cooling rates, 25 K/min and 50 K/min, are shown. The higher number of initial grains inevitably lead to higher crystallinity around the fiber. The effect of the cooling rate discussed in the previous sections can also be seen here. The lower cooling rate allows for more time for the grains to grow and crystallize leading to less defined boundaries between them. On the other hand, the higher cooling rate exhibits more obvious heterogeneity in the crystallinity field.

Also, we observe that shape of the grains and their boundaries are perpendicular to the fibers. Fig. 3.15 shows an enhanced version of Fig. 3.14(b). The grains near the fiber take ellipsoidal shapes and the boundaries between them create vertical curves. This behaviour has also been observed in experimental works [300, 301]. We do not introduce any source of preferred directionality in our model. Thus, it seems that such patterns appear merely due to geometrical constraints imposed

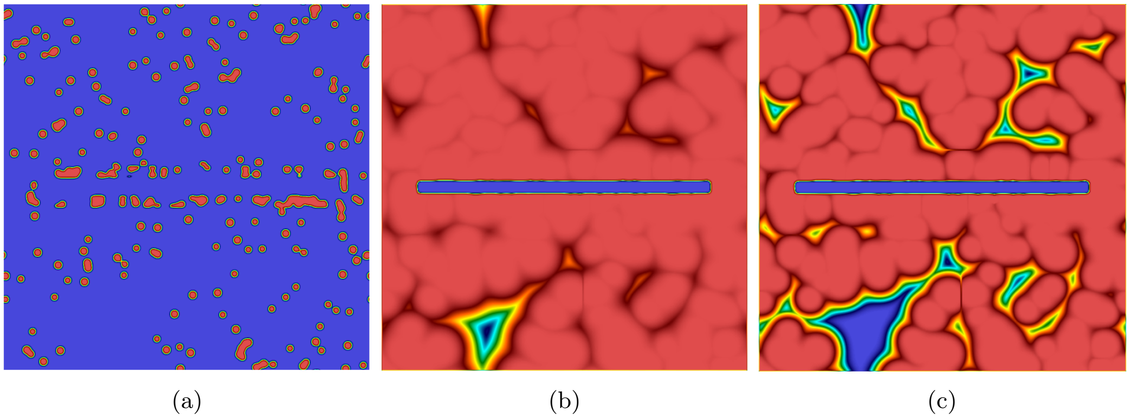
(a) (b) (c)

Figure 3.14: Initial and final morphology for crystallization field around a Carbon fiber horizontally placed in the middle of the domain. (a) Initial distribution, (b) 25 K/min, (c) 50 K/min

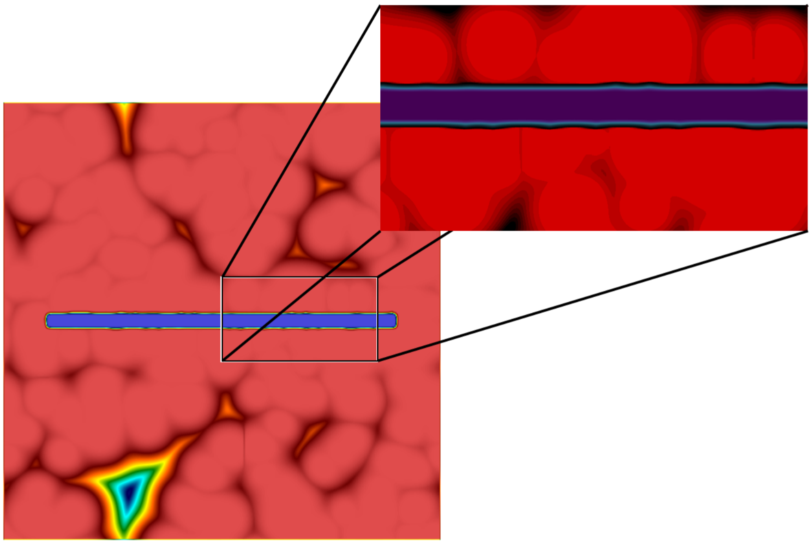

Figure 3.15: A magnified image of the fiber is shown. The vertical growth from the surface for the fiber is evident from the shape and boundaries of the crystalline grains.

by neighbouring grains and the fiber surface (the grain has no other space to grow except for perpendicular to the fiber and outwards).

The fiber also affects the heat conduction and the temperature field as it has different thermal properties compared to the matrix material. Fig. 3.16a shows the temperature field for a system with a horizontal carbon fiber in the centre of the box. The cooling rate for this system was 25 K/min. The carbon fiber has a higher thermal conductivity and a lower volumetric heat capacity than the PA6 matrix around it. The fiber acts as a heat conductor between the right and left boundaries of the domain and facilitates heat flow. This leads to lower but more uniform temperatures at and around the fiber. As a result, we expect a more uniform crystallization rate, especially around the fiber, leading to more homogeneous morphologies. We would like to point out that due to the small gradients of temperature in our system this effect might be subtle.

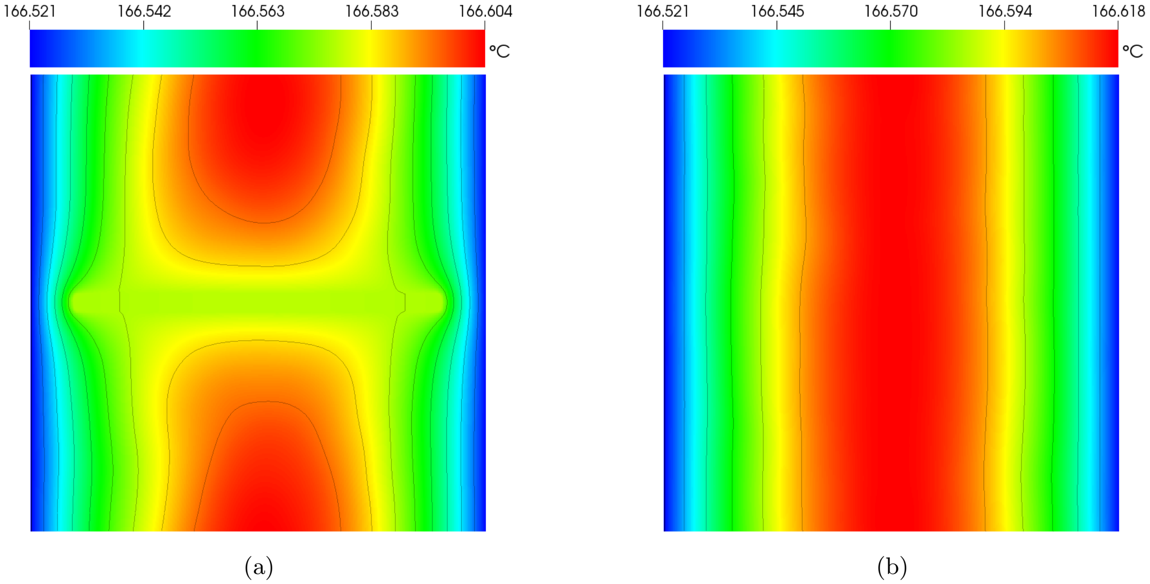

(a)

(b)

Figure 3.16: Temperature field for PA6 matrix with a horizontal (a) and vertical (b) fiber for cooling rate 25 K/min, at t= $80s$

Single fiber: Vertical Alternatively, one can place the fiber in the matrix in a vertical orientation. We place the fiber in the middle. The initial distribution of the crystalline grains as well as the final morphology of the crystallinity field for the different cooling rates are shown in Fig. 3.17. Similar to before, we see that the higher density of crystal grains around the fiber and the better heat conduction of the fiber result in more homogeneous crystallinity fields around the fiber. However, unlike the horizontal fiber, a vertical fiber in the middle does not facilitate the heat transfer across the entire sample as much (the Dirichlet BC dictates the heat transfer, see Fig. 3.16.) Thus, we see a more heterogeneous structure in this case. Ellipsoidal grain shapes with a tendency to grow perpendicular to the fiber surface are observed in this case as well.

3.5 Conclusion

Physical and mechanical properties of semi-crystalline polymers depend on their degree of crystallization and crystal morphology. In this work, we introduce a multiphase-field method coupled with the Nakamura model and heat conduction equation to model the non-local crystallization of polymeric materials on a microstructural length scale. The multiphase-field base of our model provides an efficient and easy way to track the boundaries of the crystalline areas. This makes it possible to study heterogeneous crystal structures. It also allows for adding any number of phases with different properties making the model a good candidate to study polymer blends and composites. The crystallization inside crystalline areas is controlled by a kinetic model, which was the Nakamura model in this work. The dependency of the crystal growth rate on temperature is added by a Turnbell-Fisher type of equation. The kinetic model and temperature dependency can be adjusted to match the processing conditions and specific materials under study.

We applied our model to neat PA6 and in the presence of fibers. For pure matrix, we observe that lower cooling rates result in more homogeneous structures with larger grains. More hetero-

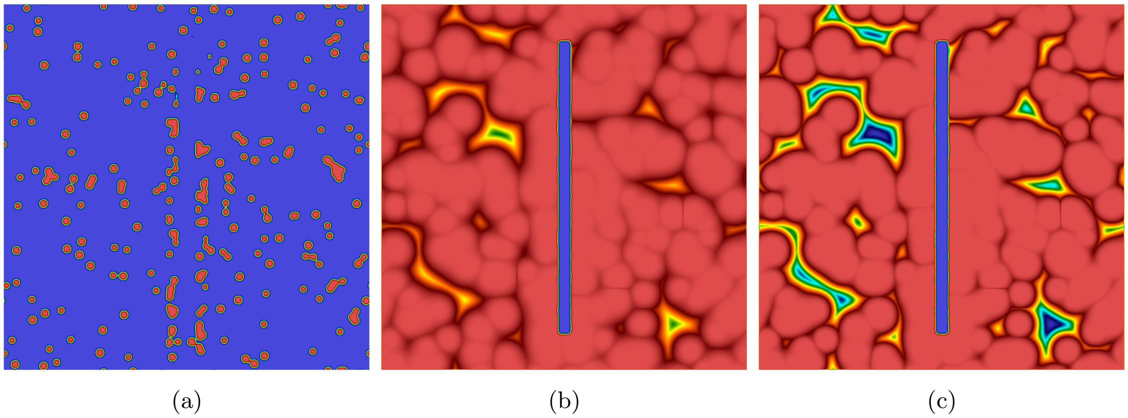
(a) (b) (c)

Figure 3.17: Initial and final morphology for crystallization field around a carbon fiber vertically placed in the middle of the domain. (a) shows the initial distribution. (b) depicts the final morphology for a system cooled at 25 K/min while (c) depicts the same for a system cooled at 50 K/min

geneous structures emerge as the cooling rate is increased. This heterogeneity stems from sharper temperature gradients and the short crystallization time available to the crystalline grains. At lower cooling rates, the initial size of the grains does not have a major impact on the final morphology as enough time is given for most grains to grow to their possible maximum crystallinity, considering impingement constraints. The initial number of grains does seem to have a more noticeable effect on the morphology. At higher cooling rates, both of these quantities seem to influence the final structure considerably.

In the presence of the carbon fiber, we observe a more homogeneous morphology around the fiber. This is associated with two effects: higher initial crystal grain volume fraction and high conductivity of the carbon fibers. All the crystalline grains near the fiber surface experience a similar cooling rate and crystallize at the same rate. The heat of crystallization is also transferred quickly from the region. The higher initial crystal grain volume fraction also means that most regions start crystallizing at the same time. These lead to the more homogeneous morphologies observed around the fiber. We also observe that the crystalline grains grow perpendicular to the fiber surface. This indicates that this vertical growth seen in experiments is merely because of the geometrical constraints applied to the interfacial grains.

Overall, our model provides results qualitatively in agreement with experiments. However, further understanding of the properties of the coarse-grained crystal grains and their relation to spherulites, and a detailed knowledge of the initial nuclei density is required to achieve better quantitative agreement with experiments.

Chapter 4

Compressible Lattice Boltzmann

The solutions of the equations of fluid dynamics are usually so complex that they are analytically only solvable in specific and limited cases. The field of computational fluid dynamics (CFD) emerged to address this problem by introducing and using numerical methods that can find the solutions of the fluid dynamics equations. The conventional CFD methods are numerical methods applied to the equations of fluid dynamics. The methods represent the fluid variables as values at various points throughout the domain. For example, in the Finite Difference method (FDM), the fluid field is discretized onto a grid of nodes. In the Finite Volume method (FVM), each node represents the average properties of its encompassing unit cell. In the Finite Element method (FEM), the system is divided to sub-domains and resulting vertcies. Then the continuous fluid field is approximated by interpolating the values on the vertices.

Despite their overall success, the conventional CFD models suffer from some shortcomings. The main challenge in using conventional CFD models lies in the difficulty of discretization of the non-linear terms in the Navier-Stokes equations and non-locality of the derivative approximations. The Lattice Boltzmann Method (LBM) offers an alternative to such methods.

Lattice Boltzmann Method (LBM), with its roots in kinetic theory, has proven to be a powerful tool to study fluid dynamics [20, 302]. One of the advantages of LBM over conventional CFD models is local nature of the node operations, i.e. the collision. This makes LBM easy to parallelize and implement. In addition, LBM recovers numerically exact conservation laws and offers excellent stability properties inherited from the implicit trapezoidal rule. A short introduction to standard LBM is provided in section 1.

The applications of LBM do not stop at simple fluids, but it has been used to study multiphase flows [26, 303–305], liquid crystals [28, 306, 307], flows in confined spaces [239, 308–310] as well as viscoelastic fluids [29, 311, 312], fluid-particle dynamics [27, 313, 314], and turbulence [315].

4.1 Introduction

Despite all the efforts, the majority of previous LBM based studies focus on isothermal flows in the incompressible limit while compressible, thermal, and viscoelastic systems are less studied. In this chapter, we introduce a new LBM capable of addressing some of the challenges in simulating compressible, thermal, and viscoelastic flows. As the first step, we apply our method to successfully model compressible flows.

High-speed compressible flows are commonly found in different fields such as explosion physics, aerophysics, and astrophysics. However, standard LBM is only valid at low Mach numbers and for weakly compressible flows. At high Mach number or in the presence of density variations, the compressibility effects and error terms in the method become significant. This poses challenges in modelling and simulating these compressible flows using the Lattice Boltzmann (LB) method, particularly those involving shocks and discontinuities [316].

Several attempts have been made to include compressibility effects in LBM. Alexander et al. proposed an LBM where the equilibrium distributions were adjusted so that a flexible speed of sound can be set [317]. As they pointed out, their model was limited to isothermal compressible flows. Yan and colleagues proposed a three-speed-three-energy-level lattice Boltzmann model for compressible Euler equation [318]. The model was found to simulate strong discontinuity phenomena but suffered from too many degrees of freedom and parameters to set. Kataoka and Tsutahara introduced an LBM on an extended lattice with an extra variable to adjust specific-heat of the fluid [319].

Ji et al. proposed a Finite Volume-Lattice Boltzmann method for compressible flows [320]. Finite Volume method (FVM) is one of the most popular methods in computational fluid dynamics. FVM is designed based on conservation of quantities inside a cell in the system. Therefore, any changes in a quantity is balanced by that quantity's flux. This requires that the fluxes are evaluated at the cell interface. There are different methods to evaluate the flux. The proposed method by Ji et al. used LB to solve the local Riemann problem across the interface. Their model showed superiority compared to the conventional Godunov scheme and was able to capture shock wave, contact discontinuity and rarefaction waves.

Sun formulated an adaptive-velocity LBM on a hexagonal lattice for compressible and thermal flows [8, 321]. In this model, the local velocity set is chosen dynamically allowing the mean flow to have a high Mach number. The model was able to capture shock waves. However, the model suffered from huge computational cost when the relaxation time was not set to 1.

The thermal LB models suggested so far can be divided two classes in terms of number of distribution functions used: single population and double population.

In an early attempt, Alexander and colleagues developed a Lattice Bhatnagar-Gross-Krook model to recover the full thermohydrodynamic equations. In this model, which counts as a single population model, an extended hexagonal lattice was employed and the equilibrium distribution was expanded up to second order in macroscopic velocity [322]. To test the model, they conducted 2D simulations of adiabatic sound propagation and Couette flow in the presence of heat transfer. Their results showed good agreement with theoretical predictions at low temperature differences. Qian introduced a similar multispeed model for 1D, 2D, and 3D on a standard lattice [323]. Chen et al. improved the conventional Thermal Lattice Boltzmann mentioned above by introducing higher-order expansion of the equilibrium distribution and higher number of discrete velocities [324]. As a result, they were able to eliminate the non-linear deviation present in the previous models. As a single-relaxation time was used in all of these models, they all suffered from constant Prandtl number. The boundaries and boundary conditions also imposed a challenge as multispeed models required access to neighbouring sites beyond the nearest neighbours. Moreover, the multispeed LB models were found to be unstable except for small variations in temperature. McNamara and coworkers addressed the instability issues of the multispeed models by introducing an extra relaxation time for the energy moments and using

Lax-Wendroff advection to provide an adjustable time step [325]. Despite their success in addressing the stability issues, they concluded that the model did not offer any advantage over explicit Navier-Stokes (NS) solvers as the stabilization methods used were shared between both approaches and computation time was similar.

Karlin et al. introduced the consistent Lattice Boltzmann model for weakly compressible flows. [326]. In this model, they used an $\mathcal{H}$-theorem and applied the Gauss-Hermite quadrature to the $\mathcal{H}$-function. By including the conservation of energy, they were able to remove the spurious bulk viscosity present in iso-thermal models. Also, they were able to achieve this on standard lattices which made their model more efficient compared to multispeed models. In a follow-up work, they extended the applicability of the consistent model to thermal flows [327]. In the original consistent model, the deviation terms generated by the low symmetry of the regular lattices was not addressed and limited the use of the model to weakly compressible fluids. These limitations were overcome by introducing new discrete equilibrium distributions obtained from the guided equilibria method [328] and correction terms that eliminated the deviation terms to recover Navier-Stokes and Fourier equations. A downside of this approach is the ad-hoc nature of the correction terms. As the finite-difference correction terms are derived to eliminate the deviations from the emerging macroscopic equation, they cannot be generalized to different LBMs.

Another approach proposed to overcome some of the challenges of multispeed models was by introducing a second distribution function. The extra distribution function is then used to solve for the energy equation [329]. This approach resulted in a more stable LBM and did not require extended lattices which made it attractive for simulating thermal flows. However, the momentum and energy equation had to be coupled via the source/force terms in the LB equations. The original double-population model suffered from complexity and non-locality [20]. Karlin et al. found that applying the conservation law to total energy rather than internal energy on the second lattice results in a local coupling between the two lattices and a major simplification of such models [330]. Generally, the double-population method requires large memory space, especially in 3D, and longer computation time as the LBE is solved for several distribution.

To address the lack of Galilean invariance in conventional LBM, Frapolli et al. proposed the co-moving Galilean Reference Frame [331]. They argued that the errors and numerical instabilities observed in conventional LBM for flows at high Mach numbers is due to streaming particle populations with fixed discrete velocities, i.e. using the "at rest" reference frame. The co-moving Galilean Reference Frame introduces uniformly shifted lattices, where the reference frame is consistently shifted across the numerical domain. They found that this approach works well for unidirectional compressible flows but is less effective for flows with significant variations in velocity and temperature [332].

Dorschner et al. suggested that these limitations can be removed if tailored discrete velocities rather than fixed velocities were used. Based on this principle, they introduced the "Particle on Demand" or the PonD model [333]. In the PonD model, the kinetic equations are reconstructed in local reference frames defined by the actual local fluid velocity and temperature. In the streaming step, a predictor-corrector iteration loop is implemented to find the particle populations in the co-moving reference frame. The co-moving reference frame is the reference frame/gauge in which the particle velocities are determined by the fluid velocity and temperature at the monitored site. Their model was able to capture Galilean invariance and conserve mass, momentum, and energy conservation.

Many biological and industrial fluids have viscoelastic properties. In order to understand and utilize such systems, one has to have a proper grasp of their viscoelastic properties. Designing predictive models facilitates both of these processes. To formulate a new model, one has to study different aspects of a system thoroughly. A model also can reveal the fundamental principles underlying a process. Moreover, predictive models can shed light on possible pathways to modify a system towards a desired outcome.

In an early work, Giraud et al. proposed an Lattice Boltzmann Method for simple viscoelastic fluids [334]. Two non-propagating parameters were introduced and coupled to the viscous stress tensor to include memory effects. The degree of viscoelasticity was controlled by a relaxation time. The model provided good qualitative results but it was suggested by the authors that further investigation and tuning was needed to achieve quantitative results. This model was further extended to two-component viscoelastic systems by Wagner et al. and was used to model rising of a bubble in a viscoelastic fluid [335].

The model was extended to 3D by Lallemand et al. [336]. In this case, they introduced 5 non-propagating parameters into the D3Q27 model leading to a D3Q32 model. They analyzed the model's dispersion equation to derive the hydrodynamic equations, establish conditions for isotropy and Galilean invariance, and optimize stability. Their findings indicated that their LBM exhibited memory effects and, in the linear regime, behaved like a viscoelastic fluid as described by the Jeffreys model [337].

In a different approach, Ispolatov and Grant introduced viscoelasticity to their LBM by adding a Maxwell stress tensor as a forcing term [338]. The model was found to predict viscoelastic behaviour but only for a limited range parameters and only qualitatively. The method appears constrained by stability requirements to small relaxation times [339]. Additionally, the macroscopic equations have not been derived to ensure that the body force was consistently incorporated.

Wagner derived a viscoelastic constitutive equation specifically for gases from the BGK model [311]. Unlike conventional viscoelastic models used for polymeric liquids, their model was non-objective, meaning it explicitly incorporates inertial effects. The difference between their model and Oldroyd-B were illustrated through exact solutions for simple shear and elongational flows, showing how the predicted viscoelastic responses for a gas differ from those in polymeric liquids.

Malaspinas and coworkers extended the approach of Denniston et al. [306] to incompressible viscoelastic fluids [29]. The mass and momentum equations were solved using standard LBM where the viscoelastic stress tensor was coupled through the forcing term. The viscoelastic stress tensor was then evolved by an advection-diffusion type LBM. The model was compared to a high accuracy Fourier pseudospectral algorithm for the Taylor–Green vortex case and the results for the energy decay of the solvent and of the polymers, using the Oldroyd-B constitutive equation, were found to be in good agreement. Their simulation of a Poiseuille flow was found to match the analytical solution. However, the model suffered from instabilities at high Weissenberg numbers which was attributed to the viscoelastic stress tensor boundary conditions.

As mentioned before, one of the challenges of using models with several distribution functions simultaneously on different lattices is the computational cost (memory and time). In this chapter, we introduce a new LBM where the continuous distribution function is discretized using distribution mass function that in addition to a mean value also has a variance. This introduces extra independent degrees of freedom to recover the second and third moments of the Maxwell-Boltzmann distribution fully. As will be discussed, this eliminates the error terms that appear in the standard LBM (see Eq. (5) in [340]) and extends the applicability of LBM to compressible flows. The variance terms can further be utilized to incorporate thermal and viscoelastic features. As the variance terms appear as part of the discretization scheme, they consistently appear in the derivation and no ad-hoc manipulation of the equations is required to recover the correct second and third moments. Furthermore, there are only 6 extra terms (or 9 for a non-symmetric general stress tensor) introduced in this model. Thus, we expect the algorithm to be more memory efficient and have shorter runtimes compared to multi-lattice models.

In the introduction chapter, we derived the most basic form of Lattice Boltzmann equation. However, our model for thermal and viscoelastic flows involves a more complicated form of the LBE with a new discretization. As a starting point, following Dellar [341], we derive the LB equation by discretizing a velocity-discretized Boltzmann equation in space and time for a generic distribution function, forcing term, and collision operator. Then, we introduce a new discretization method in the velocity space. Using a Chapman-Enskog expansion, we will show that this new discretization method recovers the macroscopic Navier-Stokes equations followed by a discussion of implementation and test runs. Finally, we conclude the chapter by summarizing the results and discussing the potentials and limitations of the model.

4.2 Theory

4.2.1 Multi-Relaxation Time Forced Lattice Boltzmann

Let us start with the discrete-velocity Boltzmann equation in the most general form

$$\partial_t f_i + e_{i\alpha}\partial_\alpha f_i = -\mathcal{L}_{ij}(f_j - f_j^{eq}) - \left[\frac{w_i}{g(\boldsymbol{\xi})}\boldsymbol{F}\cdot\frac{\partial f}{\partial \xi}\bigg|_{\boldsymbol{\xi}=\boldsymbol{e}_i}\right] \tag{4.1}$$

where f_i is the discrete-velocity distribution function, and $\boldsymbol{e}_i$ are the discrete velocities that f_i travels to neighbouring sites by. $\mathcal{L}_{ij}$ is the collision operator, $\boldsymbol{F}$ is an acceleration field, w_i is the quadrature weights, and g is the Hermite generating function. For sake of brevity, we call the RHS of the above equation C_i

$$-\mathcal{L}_{ij}(f_j - f_j^{eq}) - \left[\frac{w_i}{g(\boldsymbol{\xi})}\boldsymbol{F}\cdot\frac{\partial f}{\partial \xi}\bigg|_{\boldsymbol{\xi}=\boldsymbol{e}_i}\right] = -\mathcal{L}_{ij}(f_j - f_j^{eq}) + \Phi_i = C_i(\boldsymbol{x}, t) \tag{4.2}$$

As shown in the introduction, one can solve the above equation using the method of characteristics

$$\frac{df_i}{dt} = C_i \tag{4.3}$$

where d/dt is the complete derivative with respect to t. Taking the integral of both sides, we get

$$f_i(\boldsymbol{x} + \boldsymbol{e}_i\Delta t, t + \Delta t) - f_i(\boldsymbol{x}, t) = \int_0^{\Delta t} C_i(\boldsymbol{x}, t) \tag{4.4}$$

Now, if we perform the trapezoidal rule to solve the integral, we find

$$f_i(\boldsymbol{x}+\boldsymbol{e}_i\Delta t, t+\Delta t) - f_i(\boldsymbol{x},t) = \frac{C_i(\boldsymbol{x},t)+C_i(\boldsymbol{x}+\boldsymbol{e}_i\Delta t, t+\Delta t)}{2}\Delta t - \frac{\Delta t^3}{12}\frac{d^2C_i}{dt^2}\bigg|_t . \tag{4.5}$$

Reorganizing 4.5, we can write

$$f_i(\boldsymbol{x}+\boldsymbol{e}_i\Delta t, t+\Delta t) - \frac{C_i(\boldsymbol{x}+\boldsymbol{e}_i\Delta t, t+\Delta t)}{2}\Delta t = f_i(\boldsymbol{x},t) - \frac{C_i(\boldsymbol{x},t)}{2}\Delta t + C_i(\boldsymbol{x},t)\Delta t - \frac{\Delta t^3}{12}\frac{d^2C_i}{dt^2}\bigg|_t , \tag{4.6}$$

or

$$\bar{f}_i(\boldsymbol{x}+\boldsymbol{e}_i\Delta t, t+\Delta t) = \bar{f}_i(\boldsymbol{x},t) + C_i(\boldsymbol{x},t)\Delta t + \mathcal{O}\left(\Delta t^3\right) \tag{4.7}$$

where

$$\bar{f}_i(\boldsymbol{x},t) = f_i(\boldsymbol{x},t) - \frac{C_i(\boldsymbol{x},t)}{2}\Delta t. \tag{4.8}$$

Eq. 4.7 is the Lattice Boltzmann equation in terms of the auxiliary distributions $\bar{f}_i$. The fact that the Lattice Boltzmann can be recovered using the method above shows that the discretized (in space and time) Lattice Boltzmann equation is actually accurate up to the second order. To benefit from this higher order accuracy, one can use Eq. 4.7 instead of Eq. 1.55 as the LB evolution equation with the caveat that the macroscopic moments need to be corrected to match physical parameters. This is due to the fact that it is the moments of f_i and not $\bar{f}_i$ that were matched with the moments. We get to these correction terms soon but first, we have to make sure that Eq. 4.7 is all in terms of $\bar{f}_i$ for it to be used as an evolution equation.

We start with the definition of C_i:

$$\begin{aligned} C_i &= -\mathcal{L}_{ij}(f_j - f_j^{eq}) + \Phi_i \\ &= -\mathcal{L}_{ij}(\bar{f}_j - C_j\frac{\Delta t}{2} - f_j^{eq}) + \Phi_i \\ &= \frac{\Delta t}{2}\mathcal{L}_{ij}C_j - \mathcal{L}_{ij}(\bar{f}_j - f_j^{eq}) + \Phi_i \end{aligned} \tag{4.9}$$

Taking all the terms with C to one side and performing some linear algebra, we get

$$C_i - \frac{\Delta t}{2}\mathcal{L}_{ij}C_j = \left(\delta_{ij} - \frac{\Delta t}{2}\mathcal{L}_{ij}\right)C_j = -\mathcal{L}_{ij}(\bar{f}_j - f_j^{eq}) + \Phi_i, \tag{4.10}$$

and finally, we have C in terms of $\bar{f}_i$:

$$C_j = \left(\mathbb{I} - \frac{\Delta t}{2}\mathcal{L}\right)^{-1}_{ji}(-\mathcal{L}_{ik}(\bar{f}_k - f_k^{eq}) + \Phi_i). \tag{4.11}$$

Therefore, Eq. 4.7 can be rewritten fully in terms of $\bar{f}_i$ as

$$\bar{f}_i(\boldsymbol{x}+\boldsymbol{e}_i\Delta t, t+\Delta t) = \bar{f}_i(\boldsymbol{x},t) + \left(\mathbb{I} - \frac{\Delta t}{2}\mathcal{L}\right)^{-1}_{ij}\left(-\mathcal{L}_{jk}(\bar{f}_k - f_k^{eq}) + \Phi_j + \mathcal{O}\left(\Delta t^3\right)\right). \tag{4.12}$$

Operating the collision step for more complicated models than the simple Single-Relaxation Time

(SRT) is only manageable in moment space. So for a general collision operator, we can define it as

$$\mathcal{L} = \boldsymbol{M}^{-1}\boldsymbol{S}\boldsymbol{M} \tag{4.13}$$

where $\boldsymbol{M}$ is f-to-moment transformation matrix, and $\boldsymbol{S}$ is the relaxation time matrix. Plugging this definition into RHS of 4.12 and simplifying,

$$\begin{aligned}
&\left(\mathbb{I} - \frac{\Delta t}{2}\mathcal{L}\right)^{-1}_{ij}(-\mathcal{L}_{jk}(\bar{f}_k - f_k^{eq}) + \Phi_j) + \mathcal{O}\left(\Delta t^3\right) \\
&\quad = \left(\mathbb{I} - \frac{\Delta t}{2}\boldsymbol{M}^{-1}\boldsymbol{S}\boldsymbol{M}\right)^{-1}\left(\boldsymbol{M}^{-1}\boldsymbol{S}\boldsymbol{M}(\bar{\boldsymbol{f}} - \boldsymbol{f}^{eq}) + \boldsymbol{\Phi} + \mathcal{O}\left(\Delta t^3\right)\right) \\
&\quad = \left(\boldsymbol{M}^{-1}\boldsymbol{M} - \frac{\Delta t}{2}\boldsymbol{M}^{-1}\boldsymbol{S}\boldsymbol{M}\right)^{-1}\left(\boldsymbol{M}^{-1}\boldsymbol{S}\boldsymbol{M}(\bar{\boldsymbol{f}} - \boldsymbol{f}^{eq}) + \boldsymbol{\Phi} + \mathcal{O}\left(\Delta t^3\right)\right) \\
&\quad = \left(\boldsymbol{M}^{-1}(\mathbb{I} - \frac{\Delta t}{2}\boldsymbol{S})\boldsymbol{M}\right)^{-1}\left(\boldsymbol{M}^{-1}\boldsymbol{S}\boldsymbol{M}(\bar{\boldsymbol{f}} - \boldsymbol{f}^{eq}) + \boldsymbol{\Phi} + \mathcal{O}\left(\Delta t^3\right)\right) \\
&\quad = \left(\boldsymbol{M}^{-1}(\mathbb{I} - \frac{\Delta t}{2}\boldsymbol{S})^{-1}\boldsymbol{M}\right)\left(-\boldsymbol{M}^{-1}\boldsymbol{S}\boldsymbol{M}(\bar{\boldsymbol{f}} - \boldsymbol{f}^{eq}) + \boldsymbol{\Phi} + \mathcal{O}\left(\Delta t^3\right)\right) \\
&\quad = \left(\boldsymbol{M}^{-1}(\mathbb{I} - \frac{\Delta t}{2}\boldsymbol{S})^{-1}\boldsymbol{S}(\bar{\boldsymbol{m}} - \boldsymbol{m}^{eq})\right) + \left(\boldsymbol{M}^{-1}(\mathbb{I} - \frac{\Delta t}{2}\boldsymbol{S})^{-1}\right)\left(\boldsymbol{F} + \mathcal{O}\left(\Delta t^3\right)\right) \\
&\quad = \boldsymbol{M}^{-1}\left(\left(\boldsymbol{S}^{-1} - \frac{\Delta t}{2}\mathbb{I}\right)^{-1}(\bar{\boldsymbol{m}} - \boldsymbol{m}^{eq}) + \left(\mathbb{I} - \frac{\Delta t}{2}\boldsymbol{S}\right)^{-1}\left(\boldsymbol{F} + \mathcal{O}\left(\Delta t^3\right)\right)\right)
\end{aligned} \tag{4.14}$$

where $\boldsymbol{m}$ shows the moment vector, and $\boldsymbol{\Phi}$ is the force vector in f space while $\boldsymbol{F}$ is the forcing term in moment space. Eq. 4.14 shows the collision in moment space which is then returned to f space by an $\boldsymbol{M}^{-1}$ transformation.

For a Single-Relaxation Time (SRT) model, $\mathcal{L}_{ij} = \delta_{ij}/\tau$ and $\boldsymbol{S}$ is a diagonal matrix with all entries equal $1/\tau$. Then, the evolution equation simply turns to

$$\bar{f}_i(\boldsymbol{x} + \boldsymbol{e}_i\Delta t, t + \Delta t) = \bar{f}_i(\boldsymbol{x}, t) + \frac{\Delta t}{\tau + \frac{\Delta t}{2}}(\bar{f}_k - f_k^{eq} + \tau\Phi_i). \tag{4.15}$$

Since the discretization in velocity space is performed by matching the moments of f and f_i, the macroscopic quantities recovered by equation 4.12 would not provide the actual macroscopic values one would expect and need corrections. To find the relation between the moments of f_i and $\bar{f}_i$, we use Eq. 4.8. However, this equation involves the moments of the collision operator and the forcing term. For a system with conservation of mass, and momentum, the moments of the collision operator are

$$\sum_i \mathcal{L}_{ij}(f_j - f_j^{eq}) = 0 \tag{4.16}$$

$$\sum_i \mathcal{L}_{ij}(f_j - f_j^{eq})e_{i\alpha} = 0 \tag{4.17}$$

and the moments of the forcing term are

$$\sum_i \Phi_i = F_0 = 0 \tag{4.18}$$

$$\sum_i \Phi_i e_{i\alpha} = F_\alpha, \quad \alpha = x, y, z \tag{4.19}$$

$$\sum_i \Phi_i e_{i\alpha} e_{i\beta} = F_\alpha u_\beta + F_\beta u_\alpha, \quad \alpha = x, y, z, \ \beta = x, y, z. \tag{4.20}$$

Now that we have the moments of all the terms, we can find the relation between the moments of f_i and $\bar{f}_i$. Generally,

$$\bar{\boldsymbol{m}} = \boldsymbol{m} - \frac{\Delta t}{2}\left(\left(\boldsymbol{S}^{-1} - \frac{\Delta t}{2}\mathbb{I}\right)^{-1}\left(\bar{\boldsymbol{m}} - \boldsymbol{m}^{eq}\right) + \left(\mathbb{I} - \frac{\Delta t}{2}\boldsymbol{S}\right)^{-1}\left(\boldsymbol{F} + \mathcal{O}\left(\Delta t^3\right)\right)\right). \tag{4.21}$$

If the a-th moment of the distribution f is conserved, then we have

$$\boldsymbol{m}_a = \boldsymbol{m}_a^{eq}, \tag{4.22}$$

and as a result,

$$\left(\mathbb{I} + \frac{\Delta t}{2}\left(\boldsymbol{S}^{-1} - \frac{\Delta t}{2}\mathbb{I}\right)^{-1}\right)_{ni} \bar{\boldsymbol{m}}_i = \left(\mathbb{I} + \frac{\Delta t}{2}\left(\boldsymbol{S}^{-1} - \frac{\Delta t}{2}\mathbb{I}\right)^{-1}\right)_{ni} \boldsymbol{m}_i - \frac{\Delta t}{2}\left(\mathbb{I} - \frac{\Delta t}{2}\boldsymbol{S}\right)^{-1}_{ni} \boldsymbol{F}_i. \tag{4.23}$$

This can be further simplified to get

$$\bar{\boldsymbol{m}}_n = \boldsymbol{m}_n - \frac{\Delta t}{2}\boldsymbol{F}_n. \tag{4.24}$$

As can be seen, the relaxation time matrix is absent in Eq. 4.24. This is the result of the conservation law. The above derivation is general and can be applied to any moment that is conserved. Let us show this for the simplest case of density of a single-relaxation time model. In this case, $\boldsymbol{S} = -\frac{1}{\tau}\delta_{ij}$ and $\boldsymbol{F} = 0$. Thus,

$$\bar{\rho} = \rho - \frac{\Delta t}{2}\left(\left(-\tau - \frac{\Delta t}{2}\right)^{-1}(\bar{\rho} - \rho) + \left(1 + \frac{\Delta t}{2\tau}\right)^{-1} F_0\right) \tag{4.25}$$

which can be rearranged to get

$$\bar{\rho}\left(1 - \frac{\Delta t}{2\tau + \Delta t}\right) = \rho\left(1 - \frac{\Delta t}{2\tau + \Delta t}\right) - \frac{\Delta t}{2}\left(\frac{2\tau}{2\tau + \Delta t}\right) F_0 \tag{4.26}$$

where ρ is the density. Finally, we can simplify this to get

$$\bar{\rho} = \rho - \frac{\Delta t}{2} F_0 = \rho \tag{4.27}$$

Similarly, for the macroscopic velocity, we multiply Eq. 4.8 by $e_{i\alpha}$ and sum over i:

$$\sum_i \left\{ \bar{f}_i e_{i\alpha} = f_i e_{i\alpha} - \frac{C_i e_{i\alpha}}{2} \Delta t \right\}. \tag{4.28}$$

Applying conservation of momentum and 4.19, we get

$$\bar{\rho}\bar{u}_\alpha = \rho\bar{u}_\alpha = \rho u_\alpha - \frac{\Delta t}{2} F_\alpha + \mathcal{O}\left(\Delta t^4\right) \tag{4.29}$$

where u_α is the macroscopic velocity in the α direction ($\alpha = x,\ y,\ z$).

The correction terms for the stress tensor can also be derived from Eq. 4.21. If conservation of energy is considered, a correction equation without any dependency on relaxation time can be derived for the temperature field as well. Conservation of total energy implies

$$\sum_i f_i e_i^2 = \sum_i f_i^{eq} e_i^2 = \frac{d}{2} \rho T + \rho u^2, \tag{4.30}$$

and

$$\sum_i \mathcal{L}_{ij} (f_j - f_j^{eq}) e_{i\alpha} e_{i\alpha} = 0 \tag{4.31}$$

where d is the dimension. Then the correction relation for the temperature is

$$\bar{T} = T - \frac{\Delta t}{2} (2 F_\alpha u_\alpha). \tag{4.32}$$

The error terms in the above equations are of order $\mathcal{O}\left(\Delta t^4\right)$. Therefore, the Lattice Boltzmann equation is the same as the velocity-discretized Boltzmann equation at least up to second order. We later use this result to perform the Chapman-Enskog on the velocity-discretized Boltzmann equation rather than the LBE. However, one has to be careful as the definition of the relaxation time would change from τ to $\tau + \Delta t/2$.

4.3 New Velocity discretization

As mentioned in the previous chapter, the standard Lattice Boltzmann Method solves the discretized Boltzmann equation. The discretization of the particle distribution f in the standard models is equivalent to using a delta function as the probability mass function:

$$f = \sum_i f_i p_i(\boldsymbol{e}_i) = \sum_i f_i \delta(\boldsymbol{\xi} - \boldsymbol{e}_i). \tag{4.33}$$

Then the Lattice Boltzmann Equation (LBE) is recovered by plugging Eq. 4.33 into the linearized Boltzmann equation

$$\partial_t f + \xi_\alpha \partial_\alpha f + \frac{F_\alpha}{\rho} \partial_{\xi_\alpha} f = -\frac{1}{\tau} \left(f - f^{eq}\right) \tag{4.34}$$

and integrating over the velocity space:

$$\begin{aligned}\partial_t \int \left(\sum_i f_i \delta(\boldsymbol{\xi} - \boldsymbol{e}_i)\right) d\boldsymbol{\xi} + \int \left(\xi_\alpha \partial_\alpha \sum_i f_i \delta(\boldsymbol{\xi} - \boldsymbol{e}_i)\right) d\boldsymbol{\xi} \\ + \int \left(\frac{F_\alpha}{\rho} \partial_{\xi_\alpha} \sum_i f_i \delta(\boldsymbol{\xi} - \boldsymbol{e}_i)\right) d\boldsymbol{\xi} \\ = -\frac{1}{\tau} \int \left(\sum_i f_i \delta(\boldsymbol{\xi} - \boldsymbol{e}_i) - \sum_i f_i^{eq} \delta(\boldsymbol{\xi} - \boldsymbol{e}_i)\right) d\boldsymbol{\xi}. \end{aligned} \tag{4.35}$$

This yields

$$\sum_i \left\{ \partial_t f_i + e_\alpha \partial_\alpha f_i = -\frac{1}{\tau}(f_i - f_i^{eq}) + \frac{F_\alpha}{\rho} f_i \right\} \tag{4.36}$$

which if we insist that it holds for all i, is the Lattice Boltzmann Equation (LBE) at the zeroth moment order. In this case, the moments of the distribution function are

$$\int f d\boldsymbol{\xi} = \sum_i \int f_i p_i d\boldsymbol{\xi} = \sum_i f_i = \rho \tag{4.37}$$

$$\int f \xi_\alpha d\boldsymbol{\xi} = \sum_i \int f_i p_i \xi_\alpha d\boldsymbol{\xi} = \sum_i f_i e_{i\alpha} = \rho u_\alpha \tag{4.38}$$

$$\int f \xi_\alpha \xi_\beta d\boldsymbol{\xi} = \sum_i \int f_i p_i \xi_\alpha \xi_\beta d\boldsymbol{\xi} = \sum_i f_i e_{i\alpha} e_{i\beta} = \Pi_{\alpha\beta} \tag{4.39}$$

$$\int f \xi_\alpha \xi_\beta \xi_\gamma d\boldsymbol{\xi} = \sum_i \int f_i p_i \xi_\alpha \xi_\beta \xi_\gamma d\boldsymbol{\xi} = \sum_i f_i e_{i\alpha} e_{i\beta} e_{i\gamma} = Q_{\alpha\beta\gamma} \tag{4.40}$$

where ρ and $\boldsymbol{u}$ are the macroscopic density and velocity, respectively. Using this discretization method on standard lattices (lattices with only nearest neighbour velocities), it is possible to set the zeroth to second moments of the equilibrium distribution function f_i^{eq} so that the macroscopic equations of hydrodynamic can be recovered. However, this is not possible for the third moments. This is because on standard lattices, the diagonal 3rd moment $Q_{\alpha\alpha\alpha}$ cannot be set independently and depends on the first moment:

$$Q_{\alpha\alpha\alpha} = \sum_i f_i e_{i\alpha} e_{i\alpha} e_{i\alpha} = |e_{i\alpha}|^2 \sum_i f_i e_{i\alpha} = \left(\frac{\Delta x}{\Delta t}\right)^2 \rho u_\alpha. \tag{4.41}$$

As a result, error terms of the form $\rho u_\alpha u_\beta u_\gamma$ and $u_\alpha \partial_\beta \rho$ (when $T \neq 1/3$) appear in the viscous stress tensor leading to lack of Galilean invariance.

In this work, we replace the delta function with a new probability mass function that has a variance, $b_{\alpha\beta}$, in addition to a mean, $e_{i\alpha}$. The continuous particle population can then be written as

$$f = \sum_i f_i p_i(\boldsymbol{e}_i, b_{\alpha\beta}) \tag{4.42}$$

where $b_{\alpha\beta}$ is a symmetric tensor that depends only on position $\boldsymbol{x}$ and time t. This term appears in the second moment of the distribution and can be interpreted as the microscopic stress tensor. In this formulation, the discrete moments are found from the continuous moments:

$$\int f d\boldsymbol{\xi} = \int \sum_i f_i p_i(\boldsymbol{e}_i, b_{\alpha\beta}) d\boldsymbol{\xi} \tag{4.43}$$

$$= \sum_i \int f_i p_i(\boldsymbol{e}_i, b_{\alpha\beta}) d\boldsymbol{\xi} \tag{4.44}$$

$$= \sum_i f_i = \rho. \tag{4.45}$$

Similarly,

$$\int f \xi_\alpha d\boldsymbol{\xi} = \sum_i f_i e_{i\alpha} = \rho u_\alpha. \tag{4.46}$$

The zeroth and first moments are similar to standard discretization. However, if we apply the same method to higher moments, we see the variance terms emerge:

$$\begin{aligned}\int f \xi_\alpha \xi_\beta d\boldsymbol{\xi} &= \int \sum_i f_i p_i(\boldsymbol{e}_i, b_{\alpha\beta}) \xi_\alpha \xi_\beta d\boldsymbol{\xi} \\ &= \sum_i f_i (e_{i\alpha} e_{i\beta} + b_{\alpha\beta}) = \Pi_{\alpha\beta}\end{aligned} \tag{4.47}$$

Similarly,

$$\int f \xi_\alpha \xi_\beta \xi_\gamma d\boldsymbol{\xi} = \sum_i f_i (e_{i\alpha} e_{i\beta} e_{i\gamma} + e_{i\alpha} b_{\beta\gamma} + e_{i\gamma} b_{\alpha\beta} + e_{i\beta} b_{\gamma\alpha}) = Q_{\alpha\beta\gamma} \tag{4.48}$$

$$\begin{aligned}\int f \xi_\alpha \xi_\beta \xi_\gamma \xi_\delta d\boldsymbol{\xi} = f_i (&e_{i\alpha} e_{i\beta} e_{i\gamma} e_{i\delta} + e_{i\alpha} e_{i\beta} b_{\gamma\delta} + e_{i\delta} e_{i\alpha} b_{\beta\gamma} + e_{i\gamma} e_{i\delta} b_{\alpha\beta} + e_{i\beta} e_{i\gamma} b_{\delta\alpha} \\ &+ e_{i\alpha} e_{i\gamma} b_{\beta\delta} + e_{i\delta} e_{i\beta} b_{\alpha\gamma} + b_{\alpha\beta} b_{\gamma\delta} + b_{\delta\alpha} b_{\beta\gamma} + b_{\alpha\gamma} b_{\beta\delta}) = S_{\alpha\beta\gamma\delta}.\end{aligned} \tag{4.49}$$

The variance terms $b_{\alpha\beta}$ present in the discrete moments above cannot simply be obtained from multiplying f_i by e_i and summing over i as in standard LBM. The introduction of the second moment b terms provide enough independent degrees of freedom to be able to set the third moments of the distribution function to that of the Maxwell-Boltzmann distribution exactly and eliminate the error terms in the macroscopic momentum equation.

Assuming that force F_α is independent of $\boldsymbol{\xi}$, we can find the moments of the discrete forcing term from the moments of the continuous forcing term:

$$\begin{aligned}\int \left(\frac{F_\alpha}{\rho} \partial_{\xi_\alpha} f \right) d\boldsymbol{\xi} &= \frac{F_\alpha}{\rho} \int \frac{\partial f}{\partial \xi_\alpha} d\boldsymbol{\xi} \\ &= \frac{F_\alpha}{\rho} f \bigg|_{\Omega_\xi} = 0\end{aligned} \tag{4.50}$$

where Ω_ξ indicates the velocity space. As f is a symmetric function, the result of the integral is zero. For the higher moments, we use the integration by parts method to evaluate the integrals

$$\begin{aligned}\int \left(\frac{F_\alpha}{\rho}\partial_{\xi_\alpha} f\right)\xi_\alpha d\boldsymbol{\xi} &= \frac{F_\alpha}{\rho}\int \partial_{\xi_\alpha} f \xi_\alpha d\boldsymbol{\xi} \\ &= \frac{F_\alpha}{\rho}\left[f\xi_\alpha\Big|_{\Omega_\xi} - \int f d\xi\right] \\ &= -\frac{F_\alpha}{\rho}\sum_i f_i = -F_\alpha \end{aligned} \tag{4.51}$$

We emphasize that the discrete moments are obtained from the continuous moments of f (i.e. integrals of f over the velocity space). Similarly,

$$\begin{aligned}\int \left(\frac{F_\alpha}{\rho}\partial_{\xi_\alpha} f\right)\xi_\alpha\xi_\beta d\boldsymbol{\xi} &= -\frac{F_\alpha}{\rho}\sum_i f_i e_{i\beta} - \frac{F_\beta}{\rho}\sum_i f_i e_{i\alpha} \\ &= -(F_\alpha u_\beta + F_\beta u_\alpha). \end{aligned} \tag{4.52}$$

The conservation of mass, momentum, and energy require the moments of the collision operator to be zero. For the linearized single-relaxation time collision operator, this manifests as

$$\int -\frac{1}{\tau}\left(f - f^{eq}\right) d\boldsymbol{\xi} = 0 \tag{4.53}$$

$$\int -\frac{1}{\tau}\left(f - f^{eq}\right) \xi_\alpha d\boldsymbol{\xi} = 0 \tag{4.54}$$

$$\int -\frac{1}{\tau}\left(f - f^{eq}\right) \xi_\alpha\xi_\alpha d\boldsymbol{\xi} = 0. \tag{4.55}$$

The Einstein summation convention is used for the last equation above (sum over xx, yy, and zz). We consider the single-relaxation time model in this section for sake of simplicity. The extension to Multi-Relaxation Time is straightforward. Substituting Eq. 4.42, we get

$$\begin{aligned}&\int -\frac{1}{\tau}\left(f - f^{eq}\right) d\boldsymbol{\xi} = \int -\frac{1}{\tau}\sum_i \left(f_i p_i(\boldsymbol{e}_i, b_{\alpha\beta}) - f_i^{eq} p_i(\boldsymbol{e}_i, b_{\alpha\beta}^{eq})\right) d\boldsymbol{\xi} \\ &= -\frac{1}{\tau}\sum_i \int \left(f_i p_i(\boldsymbol{e}_i, b_{\alpha\beta}) - f_i^{eq} p_i(\boldsymbol{e}_i, b_{\alpha\beta}^{eq})\right) d\boldsymbol{\xi} \\ &= -\frac{1}{\tau}\sum_i \left[\int f_i p_i(\boldsymbol{e}_i, b_{\alpha\beta}) d\boldsymbol{\xi} - \int f_i^{eq} p_i(\boldsymbol{e}_i, b_{\alpha\beta}^{eq}) d\boldsymbol{\xi}\right] \\ &= -\frac{1}{\tau}\sum_i (f_i - f_i^{eq}) = 0 \end{aligned} \tag{4.56}$$

To get the evolution equation of our Lattice Boltzmann model, we multiply the continuous Boltzmann equation by n continuous velocities ξ to get the n-th moment and integrate over the velocity space. Then we plug in the definition of the discretized distribution $f = \sum f_i p_i$ to obtain the discrete velocity evolution equations:

$$\sum_i \left\{ \partial_t f_i + \partial_\alpha (f_i e_{i\alpha}) = -\frac{1}{\tau}(f_i - f_i^{eq}) \right\}, \tag{4.57}$$

$$\sum_i \left\{ \partial_t f_i e_{i\beta} + \partial_\alpha (f_i (e_{i\alpha} e_{i\beta} + b_{\alpha\beta})) - \frac{F_\beta}{\rho} f_i = -\frac{1}{\tau}(f_i e_{i\beta} - f_i^{eq} e_{i\beta}) \right\}, \tag{4.58}$$

$$\begin{aligned} \sum_i \Bigg\{ & \partial_t (f_i (e_{i\beta} e_{i\gamma} + b_{\beta\gamma})) + \partial_\alpha (f_i (e_{i\alpha} e_{i\beta} e_{i\gamma} + e_{i\alpha} b_{\beta\gamma} + e_{i\gamma} b_{\alpha\beta} + e_{i\beta} b_{\gamma\alpha})) \\ & - \frac{F_\gamma e_{i\beta} + F_\beta e_{i\gamma}}{\rho} f_i = -\frac{1}{\tau} \Big(f_i (e_{i\beta} e_{i\gamma} + b_{\beta\gamma}) - f_i^{eq} (e_{i\beta} e_{i\gamma} + b_{\beta\gamma}^{eq}) \Big) \Bigg\}, \end{aligned} \tag{4.59}$$

$$\begin{aligned} \sum_i \Bigg\{ & \partial_t (f_i (e_{i\beta} e_{i\gamma} e_{i\delta} + e_{i\delta} b_{\beta\gamma} + e_{i\gamma} b_{\beta\delta} + e_{i\beta} b_{\gamma\delta})) + \partial_\alpha \Bigg(f_i (e_{i\alpha} e_{i\beta} e_{i\gamma} e_{i\delta} + e_{i\alpha} e_{i\delta} b_{\beta\gamma} \\ & + e_{i\gamma} e_{i\delta} b_{\alpha\beta} + e_{i\beta} e_{i\delta} b_{\gamma\alpha} + e_{i\alpha} e_{i\gamma} b_{\beta\delta} + e_{i\gamma} e_{i\beta} b_{\alpha\delta} + e_{i\beta} e_{i\alpha} b_{\gamma\delta} \\ & + b_{\alpha\beta} b_{\gamma\delta} + b_{\beta\gamma} b_{\alpha\delta} + b_{\alpha\gamma} b_{\beta\delta} \Bigg) \\ & - \frac{F_\delta (e_{i\beta} e_{i\gamma} + b_{\beta\gamma}) + F_\gamma (e_{i\beta} e_{i\delta} + b_{\beta\delta}) + F_\beta (e_{i\delta} e_{i\gamma} + b_{\delta\gamma})}{\rho} f_i \\ = -\frac{1}{\tau} \Bigg(& f_i (e_{i\alpha} e_{i\beta} e_{i\gamma} + e_{i\alpha} b_{\beta\gamma} + e_{i\gamma} b_{\alpha\beta} + e_{i\beta} b_{\gamma\alpha}) \\ & - f_i^{eq} (e_{i\alpha} e_{i\beta} e_{i\gamma} + e_{i\alpha} b_{\beta\gamma}^{eq} + e_{i\gamma} b_{\alpha\beta}^{eq} + e_{i\beta} b_{\gamma\alpha}^{eq}) \Bigg) \Bigg\}. \end{aligned} \tag{4.60}$$

Note that for the first moment and up, the variance terms b appear as we derive the evolution equations from the continuous moments and not from multiplying Eq. 4.57 by velocities e_i. Rearranging Eq. 4.58 and 4.57, we get

$$\sum_i \left\{ \partial_t f_i + \partial_\alpha (f_i e_{i\alpha}) = -\frac{1}{\tau}(f_i - f_i^{eq}) \right\}, \tag{4.61}$$

$$\sum_i \left\{ \partial_t f_i e_{i\beta} + \partial_\alpha (f_i e_{i\alpha} e_{i\beta}) = -\frac{1}{\tau}(f_i - f_i^{eq}) - \partial_\alpha (f_i b_{\alpha\beta}) + \frac{F_\alpha}{\rho} f_i \right\} \tag{4.62}$$

Comparing the new evolution equations to the standard model, the zeroth moment appears to be the same. However, in the first moment equation, an extra $-\partial_\alpha(\rho b_{\alpha\beta})$ term appears on the RHS of Eq. 4.62. The extra term resembles the forcing term $-\partial_\alpha P^{nid}$ proposed by He et al. to obtain the Navier-Stokes equation for nonideal gases [342, 343]. However, $-\partial_\alpha(\rho b_{\alpha\beta})$ term in our equation is more general as it includes the non-equilibrium contributions through $b_{\alpha\beta} = b_{\alpha\beta}^{eq} + b_{\alpha\beta}^{neq}$. $b_{\alpha\beta}^{eq}$ is related to the macroscopic stress tensor. We will further discuss the form of $b_{\alpha\beta}^{eq}$ later in the chapter.

For the the second moment, Eq. 4.59 cannot directly be evolved by standard LB algorithms. But, it can be split into two evolution equations that can be, one for the mean contribution and one for the variance contribution:

$$\begin{aligned}\sum_i \Big\{ &\partial_t \left(f_i \left(e_{i\beta} e_{i\gamma} - \frac{c^2}{3}\delta_{\alpha\beta}\right)\right) + \partial_\alpha \left(f_i e_{i\alpha} \left(e_{i\beta} e_{i\gamma} - \frac{c^2}{3}\delta_{\alpha\beta}\right)\right) \\ &= -\frac{1}{\tau}(f_i - f_i^{eq})\left(e_{i\beta}e_{i\gamma} - \frac{c^2}{3}\delta_{\alpha\beta}\right) - \partial_\alpha (f_i(e_{i\gamma}b_{\alpha\beta} + e_{i\beta}b_{\gamma\alpha})) + \frac{F_\gamma e_{i\beta} + F_\beta e_{i\gamma}}{\rho} f_i \Big\}, \end{aligned} \tag{4.63}$$

$$\sum_i \Big\{ \partial_t (f_i \bar{b}_{\beta\gamma}) + \partial_\alpha (f_i e_{i\alpha} \bar{b}_{\beta\gamma}) = -\frac{1}{\tau}(f_i \bar{b}_{\beta\gamma} - f_i^{eq} \bar{b}^{eq}_{\beta\gamma}) \Big\}. \tag{4.64}$$

where

$$\bar{b}_{\alpha\beta} = b_{\alpha\beta} + \frac{c^2}{3}\delta_{\alpha\beta}. \tag{4.65}$$

As evolving Eq. 4.63 and 4.64 simultaneously is a more strict condition than evolving their sum, the evolution of the sum is satisfied. The term $-\partial_\alpha(\rho u_\gamma b_{\alpha\beta} + \rho u_\beta b_{\gamma\alpha}))$ (after applying summation over i) can be added to the LB solver as a correction term and contributes to recovering the correct viscous stress term in the macroscopic equations. This correction term cannot be obtained by simply introducing a forcing term such as $-\partial_\alpha P^{nid}$ as that would only produce a term of form $-u_\beta \partial_\alpha P^{nid} - u_\alpha \partial_\beta P^{nid}$. This correction term also appears as a result of the discretization of the distribution function f. The consistent derivation of the correction terms makes the model easy to generalize.

Similarly for the third moment, we separate Eq. 4.60 into two equations:

$$\begin{aligned}\sum_i \Big\{ &\partial_t \left(f_i \left(e_{i\beta} e_{i\gamma} e_{i\delta} - \frac{c^2}{3}(e_{i\delta}\delta_{\beta\gamma} + e_{i\gamma}\delta_{\delta\beta} + e_{i\beta}\delta_{\gamma\delta})\right)\right) \\ &\qquad + \partial_\alpha \left(f_i e_{i\alpha} \left(e_{i\beta} e_{i\gamma} e_{i\delta} - \frac{c^2}{3}(e_{i\delta}\delta_{\beta\gamma} + e_{i\gamma}\delta_{\beta\delta} + e_{i\beta}\delta_{\gamma\delta})\right)\right) \\ &\qquad = -\frac{1}{\tau}(f_i - f_i^{eq}) \left(e_{i\beta} e_{i\gamma} e_{i\delta} - \frac{c^2}{3}(e_{i\delta}\delta_{\beta\gamma} + e_{i\gamma}\delta_{\delta\beta} + e_{i\beta}\delta_{\gamma\delta})\right) \\ &\qquad + \frac{1}{\rho}\Big((b_{\beta\gamma} + e_{i\beta}e_{i\gamma})F_\delta + (b_{\delta\beta} + e_{i\delta}e_{i\beta})F_\gamma + (b_{\gamma\delta} + e_{i\gamma}e_{i\delta})F_\beta \Big) f_i \\ &\qquad - \partial_\alpha \bigg(f_i \Big[b_{\alpha\beta}(b_{\gamma\delta} + e_{i\gamma}e_{i\delta}) + b_{\alpha\gamma}(b_{\delta\beta} + e_{i\delta}e_{i\beta}) + b_{\alpha\delta}(b_{\beta\gamma} + e_{i\beta}e_{i\gamma}) \Big] \bigg) \Big\}, \end{aligned} \tag{4.66}$$

$$\begin{aligned}\sum_i \Big\{ &\partial_t \Big(f_i \left[e_{i\delta}\bar{b}_{\beta\gamma} + e_{i\gamma}\bar{b}_{\delta\beta} + e_{i\beta}\bar{b}_{\gamma\delta} \right] \Big) + \partial_\alpha \Big(f_i e_{i\alpha} \left[e_{i\delta}\bar{b}_{\beta\gamma} + e_{i\gamma}\bar{b}_{\delta\beta} + e_{i\beta}\bar{b}_{\gamma\delta} \right] \Big) \\ &= -\frac{1}{\tau}(\Big(f_i \left[e_{i\delta}\bar{b}_{\beta\gamma} + e_{i\gamma}\bar{b}_{\delta\beta} + e_{i\beta}\bar{b}_{\gamma\delta} \right] \Big) - \Big(f_i^{eq} \left[e_{i\delta}\bar{b}_{\beta\gamma} + e_{i\gamma}\bar{b}_{\delta\beta} + e_{i\beta}\bar{b}_{\gamma\delta} \right] \Big) \Big\} \end{aligned} \tag{4.67}$$

where Eq. 4.67 is already satisfied by Eq. 4.64. Similar to the second moment, the standard LB algorithm (i.e. Eq. 4.15) with a modified forcing term Φ_i can be applied to the above equations for the evolution of f_i. The b's also can be evolved using the standard LB algorithm. However, there lies a challenge in realizing Eq. 4.66. Since the present model is applied on a standard lattice, the diagonal moments of the forcing term, i.e. $\beta = \gamma = \delta$, in the LBE are set by the first moments of this term. In other words,

$$\sum_i \Phi_i e_{i\alpha} e_{i\alpha} e_{i\alpha} = \frac{c^2}{3} \sum_i \Phi_i e_{i\alpha} \tag{4.68}$$

which cannot produce b cross terms, for example, $b_{\alpha\beta} b_{\gamma\delta}$. Therefore, the evolution equation of the third moment deviates from Eq. 4.66. There are possible ways to improve this constraint but we do not discuss this matter here as the current work only addresses an isothermal compressible flow and the exact form of the third moment evolution equation does not impact the systems addressed in this work. On the other hand, the third moment evolution equation plays an important role in systems with conserved energy and it will be discussed in future work.

In d dimensions, the quadrature is defined by the n discrete velocities $\boldsymbol{e}_i$ and a set of weights w_i giving rise to a $DdQn$ discrete Boltzmann equation. The new discretization method introduces 6 new variables $b_{\alpha\beta}$. This provides enough degrees of freedom on the $D3Q19$ lattice to set the equilibrium distributions such that all the moments up to the 3rd moment exactly match the moments of the Maxwell-Boltzmann distribution. We pick an isotropic choice of 4th central moments to have enough equations to get a unique solution. The central moments of f_i^{eq} are defined as

$$\boldsymbol{m}^{eq} = \begin{pmatrix} \rho \\ \rho u_x \\ \rho u_y \\ \rho u_z \\ \frac{2}{3}\rho u_x^2 \\ \frac{2}{3}\rho u_y^2 \\ \frac{2}{3}\rho u_z^2 \\ \frac{2}{3}\rho u_x u_y \\ \frac{2}{3}\rho u_x u_z \\ \frac{2}{3}\rho u_y u_z \\ 0 \\ 0 \\ 0 \\ 0 \\ 0 \\ 0 \\ \frac{1}{9}\rho\left(\left(u_x^2+u_y^2-2u_z^2\right)\mathrm{c}^2-6u_y^2u_z^2+6u_x^2\left(2u_y^2-u_z^2\right)\right) \\ \frac{1}{9}\rho\left(u_x^2-u_y^2\right)\left(6u_z^2+\mathrm{c}^2\right) \\ \frac{1}{9}\rho\left(\left(u_x^2+u_y^2+u_z^2\right)\mathrm{c}^2-6\left(\left(u_y^2+u_z^2\right)u_x^2+u_y^2u_z^2\right)\right) \end{pmatrix} \tag{4.69}$$

Note that the second moments are $\frac{2}{3}\rho u_\alpha u_\beta$ which is different from the standard model where they are $\rho u_\alpha u_\beta$. The rest $\frac{1}{3}u_\alpha u_\beta$ is carried by the microscopic stress tensor $b_{\alpha\beta}$:

$$b_{\alpha\beta} = \frac{P_{\alpha\beta}}{\rho} - \frac{c^2}{3} + \frac{u_\alpha u_\beta}{3} \tag{4.70}$$

where $P_{\alpha\beta}$ is the deviatoric stress. Now we can solve the linear system of 19 equations

$$m_a^{eq} = \sum M_{ai} f_i^{eq} \tag{4.71}$$

and find the set of f_i^{eq} that satisfies it. After some algebra, we find the transformation matrix $\boldsymbol{M}$ shown in Table 4.1

As we convert between the moment and f-space at several points in the algorithm, it would be ideal to avoid the need for computing the inverse of the M matrix. Therefore, M is orthogonlized by using combinations of the central moments. Then the equilibrium distributions can be found using

$$f_i^{eq} = w_i \sum_a M_{ai} m_a^{eq} N_a \tag{4.72}$$

where w_i is the Hermite quadrature weights, and N is the normalization vector. We use the transpose of M as $M^{-1} = M^T$ (M is orthogonal).

4.3.1 Chapman-Enskog Analysis

Here we perform the Chapman-Enskog analysis to show that our model recovers the governing macroscopic equations, i.e. Navier-Stokes-Fourier equations. We do this in a slightly nontraditional way. Typically the Chapman-Enskog expansion is applied to the LB equation. We showed in section 4.2.1 that the discrete velocity Lattice Boltzmann Equation is accurate up to at least second order in time. Thus, we can perform our Chapman-Enskog on the discrete velocity LB equation (continuous in time and space) instead. The only caveat is to remember that the relaxation times in these derivations are $\tau + \Delta t/2$.

4.3.2 Zeroth-order Approximation

If we substitute $f_i \approx f_i^{eq}$ into Eq. 4.57 and 4.58 and sum over i (integrate), we get

$$\partial_t \rho + \partial_\alpha(\rho u_\alpha) = 0 \tag{4.73}$$

$$\partial_t(\rho u_\beta) + \partial_\alpha \Pi_{\alpha\beta}^{eq} + F_\beta = 0 \tag{4.74}$$

In the simplest model, the energy is defined as half of the trace of the stress tensor

$$E_{tot} = \frac{1}{2}\sum_i f_i e_i^2 = \frac{1}{2}\Pi_{\alpha\alpha} = \frac{3}{2}\rho T + \frac{1}{2}\rho u^2 \tag{4.75}$$

where an ideal gas model relates the stress tensor $P_{\alpha\beta}$ to the temperature of the system

$$P_{\alpha\beta} = \rho T \delta_{\alpha\beta}. \tag{4.76}$$

Therefore, the evolution equation for the energy reads

$$\begin{aligned}\frac{1}{2}\left(\partial_t \Pi_{\gamma\gamma}^{eq} + \partial_\alpha Q_{\alpha\gamma\gamma}^{eq} + 2F_{\gamma\gamma}u_\gamma\right) =& \frac{1}{2}\partial_t(\Pi_{xx}^{eq} + \Pi_{yy}^{eq} + \Pi_{zz}^{eq}) \\ &+ \frac{1}{2}\partial_\alpha(Q_{\alpha xx}^{eq} + Q_{\alpha yy}^{eq} + Q_{\alpha zz}^{eq}) + F_{xx}u_x + F_{yy}u_y + F_{zz}u_z = 0\end{aligned} \tag{4.77}$$

where $\mathrm{Tr}\boldsymbol{\Pi}^{(1)} = \Pi_{\gamma\gamma}^{(1)} = 0$. For sake of brevity, we can simply multiply both sides by 2 to avoid

$$\begin{pmatrix}
1 & 1 & 1 & 1 & 1 & 1 & 1 & 1 & 1 & 1 & 1 & 1 & 1 & 1 & 1 & 1 & 1 & 1 & 1 \\
0 & \mathrm{c} & 0 & -\mathrm{c} & 0 & 0 & 0 & \mathrm{c} & \mathrm{c} & -\mathrm{c} & -\mathrm{c} & \mathrm{c} & \mathrm{c} & -\mathrm{c} & -\mathrm{c} & 0 & 0 & 0 & 0 \\
0 & 0 & \mathrm{c} & 0 & -\mathrm{c} & 0 & 0 & \mathrm{c} & -\mathrm{c} & \mathrm{c} & -\mathrm{c} & 0 & 0 & 0 & 0 & \mathrm{c} & \mathrm{c} & -\mathrm{c} & -\mathrm{c} \\
0 & 0 & 0 & 0 & 0 & \mathrm{c} & -\mathrm{c} & 0 & 0 & 0 & 0 & \mathrm{c} & -\mathrm{c} & \mathrm{c} & -\mathrm{c} & \mathrm{c} & -\mathrm{c} & \mathrm{c} & -\mathrm{c} \\
-\frac{\mathrm{c}^2}{3} & \frac{2\mathrm{c}^2}{3} & -\frac{\mathrm{c}^2}{3} & \frac{2\mathrm{c}^2}{3} & -\frac{\mathrm{c}^2}{3} & -\frac{\mathrm{c}^2}{3} & -\frac{\mathrm{c}^2}{3} & \frac{2\mathrm{c}^2}{3} & \frac{2\mathrm{c}^2}{3} & \frac{2\mathrm{c}^2}{3} & \frac{2\mathrm{c}^2}{3} & \frac{2\mathrm{c}^2}{3} & \frac{2\mathrm{c}^2}{3} & \frac{2\mathrm{c}^2}{3} & \frac{2\mathrm{c}^2}{3} & -\frac{\mathrm{c}^2}{3} & -\frac{\mathrm{c}^2}{3} & -\frac{\mathrm{c}^2}{3} & -\frac{\mathrm{c}^2}{3} \\
-\frac{\mathrm{c}^2}{3} & -\frac{\mathrm{c}^2}{3} & \frac{2\mathrm{c}^2}{3} & -\frac{\mathrm{c}^2}{3} & \frac{2\mathrm{c}^2}{3} & -\frac{\mathrm{c}^2}{3} & -\frac{\mathrm{c}^2}{3} & \frac{2\mathrm{c}^2}{3} & \frac{2\mathrm{c}^2}{3} & \frac{2\mathrm{c}^2}{3} & \frac{2\mathrm{c}^2}{3} & -\frac{\mathrm{c}^2}{3} & -\frac{\mathrm{c}^2}{3} & -\frac{\mathrm{c}^2}{3} & -\frac{\mathrm{c}^2}{3} & \frac{2\mathrm{c}^2}{3} & \frac{2\mathrm{c}^2}{3} & \frac{2\mathrm{c}^2}{3} & \frac{2\mathrm{c}^2}{3} \\
-\frac{\mathrm{c}^2}{3} & -\frac{\mathrm{c}^2}{3} & -\frac{\mathrm{c}^2}{3} & -\frac{\mathrm{c}^2}{3} & -\frac{\mathrm{c}^2}{3} & \frac{2\mathrm{c}^2}{3} & \frac{2\mathrm{c}^2}{3} & -\frac{\mathrm{c}^2}{3} & -\frac{\mathrm{c}^2}{3} & -\frac{\mathrm{c}^2}{3} & -\frac{\mathrm{c}^2}{3} & \frac{2\mathrm{c}^2}{3} & \frac{2\mathrm{c}^2}{3} & \frac{2\mathrm{c}^2}{3} & \frac{2\mathrm{c}^2}{3} & \frac{2\mathrm{c}^2}{3} & \frac{2\mathrm{c}^2}{3} & \frac{2\mathrm{c}^2}{3} & \frac{2\mathrm{c}^2}{3} \\
0 & 0 & 0 & 0 & 0 & 0 & 0 & \mathrm{c}^2 & -\mathrm{c}^2 & -\mathrm{c}^2 & \mathrm{c}^2 & 0 & 0 & 0 & 0 & 0 & 0 & 0 & 0 \\
0 & 0 & 0 & 0 & 0 & 0 & 0 & 0 & 0 & 0 & 0 & \mathrm{c}^2 & -\mathrm{c}^2 & -\mathrm{c}^2 & \mathrm{c}^2 & 0 & 0 & 0 & 0 \\
0 & 0 & 0 & 0 & 0 & 0 & 0 & 0 & 0 & 0 & 0 & 0 & 0 & 0 & 0 & \mathrm{c}^2 & -\mathrm{c}^2 & -\mathrm{c}^2 & \mathrm{c}^2 \\
0 & -\frac{2\mathrm{c}^3}{3} & 0 & \frac{2\mathrm{c}^3}{3} & 0 & 0 & 0 & \frac{\mathrm{c}^3}{3} & \frac{\mathrm{c}^3}{3} & -\frac{\mathrm{c}^3}{3} & -\frac{\mathrm{c}^3}{3} & \frac{\mathrm{c}^3}{3} & \frac{\mathrm{c}^3}{3} & -\frac{\mathrm{c}^3}{3} & -\frac{\mathrm{c}^3}{3} & 0 & 0 & 0 & 0 \\
0 & 0 & -\frac{2\mathrm{c}^3}{3} & 0 & \frac{2\mathrm{c}^3}{3} & 0 & 0 & \frac{\mathrm{c}^3}{3} & -\frac{\mathrm{c}^3}{3} & \frac{\mathrm{c}^3}{3} & -\frac{\mathrm{c}^3}{3} & 0 & 0 & 0 & 0 & \frac{\mathrm{c}^3}{3} & \frac{\mathrm{c}^3}{3} & -\frac{\mathrm{c}^3}{3} & -\frac{\mathrm{c}^3}{3} \\
0 & 0 & 0 & 0 & 0 & -\frac{2\mathrm{c}^3}{3} & \frac{2\mathrm{c}^3}{3} & 0 & 0 & 0 & 0 & \frac{\mathrm{c}^3}{3} & -\frac{\mathrm{c}^3}{3} & \frac{\mathrm{c}^3}{3} & -\frac{\mathrm{c}^3}{3} & \frac{\mathrm{c}^3}{3} & -\frac{\mathrm{c}^3}{3} & \frac{\mathrm{c}^3}{3} & -\frac{\mathrm{c}^3}{3} \\
0 & 0 & 0 & 0 & 0 & 0 & 0 & \mathrm{c}^3 & \mathrm{c}^3 & -\mathrm{c}^3 & -\mathrm{c}^3 & -\mathrm{c}^3 & -\mathrm{c}^3 & \mathrm{c}^3 & \mathrm{c}^3 & 0 & 0 & 0 & 0 \\
0 & 0 & 0 & 0 & 0 & 0 & 0 & \mathrm{c}^3 & -\mathrm{c}^3 & \mathrm{c}^3 & -\mathrm{c}^3 & 0 & 0 & 0 & 0 & -\mathrm{c}^3 & -\mathrm{c}^3 & \mathrm{c}^3 & \mathrm{c}^3 \\
0 & 0 & 0 & 0 & 0 & 0 & 0 & 0 & 0 & 0 & 0 & \mathrm{c}^3 & -\mathrm{c}^3 & \mathrm{c}^3 & -\mathrm{c}^3 & -\mathrm{c}^3 & \mathrm{c}^3 & -\mathrm{c}^3 & \mathrm{c}^3 \\
0 & \frac{\mathrm{c}^4}{2} & \frac{\mathrm{c}^4}{2} & \frac{\mathrm{c}^4}{2} & \frac{\mathrm{c}^4}{2} & -\mathrm{c}^4 & -\mathrm{c}^4 & -\mathrm{c}^4 & -\mathrm{c}^4 & -\mathrm{c}^4 & -\mathrm{c}^4 & \frac{\mathrm{c}^4}{2} & \frac{\mathrm{c}^4}{2} & \frac{\mathrm{c}^4}{2} & \frac{\mathrm{c}^4}{2} & \frac{\mathrm{c}^4}{2} & \frac{\mathrm{c}^4}{2} & \frac{\mathrm{c}^4}{2} & \frac{\mathrm{c}^4}{2} \\
0 & \frac{\mathrm{c}^4}{2} & -\frac{\mathrm{c}^4}{2} & \frac{\mathrm{c}^4}{2} & -\frac{\mathrm{c}^4}{2} & 0 & 0 & 0 & 0 & 0 & 0 & -\frac{\mathrm{c}^4}{2} & -\frac{\mathrm{c}^4}{2} & -\frac{\mathrm{c}^4}{2} & -\frac{\mathrm{c}^4}{2} & \frac{\mathrm{c}^4}{2} & \frac{\mathrm{c}^4}{2} & \frac{\mathrm{c}^4}{2} & \frac{\mathrm{c}^4}{2} \\
\frac{\mathrm{c}^4}{6} & -\frac{\mathrm{c}^4}{3} & -\frac{\mathrm{c}^4}{3} & -\frac{\mathrm{c}^4}{3} & -\frac{\mathrm{c}^4}{3} & -\frac{\mathrm{c}^4}{3} & -\frac{\mathrm{c}^4}{3} & \frac{\mathrm{c}^4}{6} & \frac{\mathrm{c}^4}{6} & \frac{\mathrm{c}^4}{6} & \frac{\mathrm{c}^4}{6} & \frac{\mathrm{c}^4}{6} & \frac{\mathrm{c}^4}{6} & \frac{\mathrm{c}^4}{6} & \frac{\mathrm{c}^4}{6} & \frac{\mathrm{c}^4}{6} & \frac{\mathrm{c}^4}{6} & \frac{\mathrm{c}^4}{6} & \frac{\mathrm{c}^4}{6}
\end{pmatrix}$$

Table 4.1: The population-to-moment transformation. $\mathrm{c} = \Delta x/\Delta t$ is the lattice velocity.

carrying the 1/2 factor through the derivation. Substituting the definitions of the moments, we get

$$\begin{aligned}\partial_t \Pi^{eq}_{\gamma\gamma} + \partial_\alpha Q^{eq}_{\alpha\gamma\gamma} + 2F_{\gamma\gamma}u_\gamma =& \partial_t(P_{xx} + \rho u_x^2 + P_{yy} + \rho u_y^2 + P_{zz} + \rho u_z^2) \\ &+ \partial_\alpha(2P_{\alpha x}u_x + P_{xx}u_\alpha + \rho u_x^2 u_\alpha) \\ &+ \partial_\alpha(2P_{\alpha y}u_y + P_{yy}u_\alpha + \rho u_y^2 u_\alpha) \\ &+ \partial_\alpha(2P_{\alpha z}u_z + P_{zz}u_\alpha + \rho u_z^2 u_\alpha). \end{aligned} \tag{4.78}$$

Substituting the equation of state in Eq. 4.76 and applying the product rule

$$\partial_\alpha(abc) = c\partial_\alpha(ab) + b\partial_\alpha(ac) - bc\partial_\alpha(a), \tag{4.79}$$

we get

$$\begin{aligned}\partial_t \Pi^{eq}_{\gamma\gamma} + \partial_\alpha Q^{eq}_{\alpha\gamma\gamma} + 2F_{\gamma\gamma}u_\gamma =& 3\partial_t(\rho T) - 2\partial_\alpha(\rho T\delta_{\alpha x} + \rho u_\alpha u_x)u_x \\ &- 2\partial_\alpha(\rho T\delta_{\alpha y} + \rho u_\alpha u_y)u_y - 2\partial_\alpha(\rho T\delta_{\alpha z} + \rho u_\alpha u_z)u_z \\ &+ \partial_\alpha(\rho u_\alpha)\left(u_x^2 + u_y^2 + u_z^2\right) + \partial_\alpha\left(\rho u_\alpha(u_x^2 + u_y^2 + u_z^2)\right) \\ &+ 3\partial_\alpha(\rho T u_\alpha) + 2\partial_\alpha(\rho T u_\alpha) \end{aligned} \tag{4.80}$$

If we simplify the above equation, we finally get

$$\partial_t \Pi^{eq}_{\gamma\gamma} + \partial_\alpha Q^{eq}_{\alpha\gamma\gamma} = 3\rho(\partial_t T + u_\alpha \partial_\alpha T) - 2\partial_\alpha(\rho T)u_\alpha + 2\partial_\alpha(\rho T u_\alpha) = 0, \tag{4.81}$$

which leads to

$$(\partial_t T + u_\alpha \partial_\alpha T) = -\frac{2}{3}T\partial_\alpha u_\alpha. \tag{4.82}$$

4.3.3 First-order Approximation

Now let's assume a small deviation from the equilibrium such that $f_i \approx f_i^{eq} + f^{(1)}$. Then for a single relaxation time model, macroscopic evolution equations are

$$\partial_t \rho + \partial_\alpha(\rho u_\alpha) = 0 \tag{4.83}$$

$$\partial_t(\rho u_\beta) + \partial_\alpha \Pi^{eq}_{\alpha\beta} = -\partial_\alpha \Pi^{(1)}_{\alpha\beta} \tag{4.84}$$

$$\partial_t \Pi^{eq}_{\beta\gamma} + \partial_\alpha Q^{eq}_{\alpha\beta\gamma} = -\frac{1}{\tau}\Pi^{(1)}_{\beta\gamma} \tag{4.85}$$

$$\partial_t Q^{eq}_{\beta\gamma\delta} + \partial_\alpha S^{eq}_{\alpha\beta\gamma\delta} = -\frac{1}{\tau}Q^{(1)}_{\beta\gamma\delta}. \tag{4.86}$$

Thus, one can find the non-equilibrium moments at a certain level by solving the equation one order higher using the equilibrium moments. For the momentum equation, we have to find $\Pi^{(1)}_{\alpha\beta}$ and therefore have to solve the third-moment equation (4.85):

$$\begin{aligned}\partial_t \Pi^{eq}_{\beta\gamma} + \partial_\alpha Q^{eq}_{\alpha\beta\gamma} &= \partial_t(P_{\beta\gamma} + \rho u_\beta u_\gamma) + \partial_\alpha(P_{\alpha\beta}u_\gamma + P_{\gamma\alpha}u_\beta + P_{\beta\gamma}u_\alpha + \rho u_\alpha u_\beta u_\gamma) && (4.87) \\ &= \partial_t(P_{\beta\gamma}) + \partial_t(\rho u_\beta u_\gamma) + \partial_\alpha(P_{\alpha\beta}u_\gamma + P_{\gamma\alpha}u_\beta + P_{\beta\gamma}u_\alpha) + \partial_\alpha(\rho u_\alpha u_\beta u_\gamma). && (4.88)\end{aligned}$$

Applying the product rule of Eq. 4.79 and using the first and second moment equations

$$\partial_t \rho = -\partial_\alpha(\rho u_\alpha), \tag{4.89}$$

$$\partial_t(\rho u_\beta) = -\partial_\alpha \Pi^{eq}_{\alpha\beta}, \tag{4.90}$$

we can write

$$\begin{aligned}
\partial_t \Pi^{eq}_{\beta\gamma} + \partial_\alpha Q^{eq}_{\alpha\beta\gamma} &= \partial_t(P_{\beta\gamma}) + \partial_t(\rho u_\beta)u_\gamma + \partial_t(\rho u_\gamma)u_\beta - (\partial_t\rho)u_\beta u_\gamma \\
&\qquad + \partial_\alpha(P_{\alpha\beta}u_\gamma + P_{\gamma\alpha}u_\beta + P_{\beta\gamma}u_\alpha) + \partial_\alpha(\rho u_\alpha u_\beta u_\gamma) \qquad (4.91)\\
&= \partial_t(P_{\beta\gamma}) - \partial_\alpha \Pi^{eq}_{\alpha\beta}u_\gamma - \partial_\alpha \Pi^{eq}_{\alpha\gamma}u_\beta + (\partial_\alpha \rho u_\alpha)u_\beta u_\gamma \\
&\qquad + \partial_\alpha(P_{\alpha\beta}u_\gamma + P_{\gamma\alpha}u_\beta + P_{\beta\gamma}u_\alpha) + \partial_\alpha(\rho u_\alpha u_\beta u_\gamma) \qquad (4.92)\\
&= \partial_t(P_{\beta\gamma}) - \partial_\alpha(P_{\alpha\beta} + \rho u_\alpha u_\beta)u_\gamma - \partial_\alpha(P_{\alpha\gamma} + \rho u_\alpha u_\gamma)u_\beta + (\partial_\alpha \rho u_\alpha)u_\beta u_\gamma \\
&\qquad + \partial_\alpha(P_{\alpha\beta}u_\gamma + P_{\gamma\alpha}u_\beta + P_{\beta\gamma}u_\alpha) + \partial_\alpha(\rho u_\alpha u_\beta u_\gamma) \qquad (4.93)\\
&= \partial_t(P_{\beta\gamma}) - \partial_\alpha(P_{\alpha\beta})u_\gamma - \partial_\alpha(P_{\alpha\gamma})u_\beta - (\partial_\alpha \rho u_\alpha u_\beta u_\gamma) \\
&\qquad + \partial_\alpha(P_{\alpha\beta}u_\gamma + P_{\gamma\alpha}u_\beta + P_{\beta\gamma}u_\alpha) + \partial_\alpha(\rho u_\alpha u_\beta u_\gamma) \qquad (4.94)\\
&= \partial_t(P_{\beta\gamma}) - \partial_\alpha(P_{\alpha\beta})u_\gamma - \partial_\alpha(P_{\alpha\gamma})u_\beta + \partial_\alpha(P_{\alpha\beta}u_\gamma + P_{\gamma\alpha}u_\beta + P_{\beta\gamma}u_\alpha) \qquad (4.95)
\end{aligned}$$

Assuming that $P_{\alpha\beta} = P(\rho, T)$, we have

$$\begin{aligned}
\partial_t \Pi^{eq}_{\beta\gamma} + \partial_\alpha Q^{eq}_{\alpha\beta\gamma} &= \partial_\rho(P_{\beta\gamma})\partial_t\rho + \partial_T(P_{\beta\gamma})\partial_t T - \partial_\alpha(P_{\alpha\beta})u_\gamma - \partial_\alpha(P_{\alpha\gamma})u_\beta \\
&\qquad + \partial_\alpha(P_{\alpha\beta}u_\gamma + P_{\gamma\alpha}u_\beta + P_{\beta\gamma}u_\alpha) \qquad (4.96)\\
&= -\partial_\rho(P_{\beta\gamma})\partial_\alpha(\rho u_\alpha) + \partial_T(P_{\beta\gamma})\partial_t T - \partial_\alpha(P_{\alpha\beta})u_\gamma - \partial_\alpha(P_{\alpha\gamma})u_\beta \\
&\qquad + \partial_\alpha(P_{\alpha\beta}u_\gamma + P_{\gamma\alpha}u_\beta + P_{\beta\gamma}u_\alpha) \\
&= -\partial_\rho(P_{\beta\gamma})u_\alpha\partial_\alpha\rho - \partial_\rho(P_{\beta\gamma})\rho\partial_\alpha u_\alpha + \partial_T(P_{\beta\gamma})\partial_t T - \partial_\alpha(P_{\alpha\beta})u_\gamma \qquad (4.97)\\
&\qquad - \partial_\alpha(P_{\alpha\gamma})u_\beta + \partial_\alpha(P_{\alpha\beta}u_\gamma + P_{\gamma\alpha}u_\beta + P_{\beta\gamma}u_\alpha) \\
&= -\partial_\rho(P_{\beta\gamma})u_\alpha\partial_\alpha\rho - \partial_\rho(P_{\beta\gamma})\rho\partial_\alpha u_\alpha + \partial_T(P_{\beta\gamma})\partial_t T + P_{\alpha\beta}\partial_\alpha u_\gamma \\
&\qquad + P_{\alpha\gamma}\partial_\alpha u_\beta + \partial_\alpha(P_{\beta\gamma}u_\alpha) \qquad (4.98)\\
&= -\partial_\rho(P_{\beta\gamma})u_\alpha\partial_\alpha\rho - \partial_\rho(P_{\beta\gamma})\rho\partial_\alpha u_\alpha + \partial_T(P_{\beta\gamma})\partial_t T + P_{\alpha\beta}\partial_\alpha u_\gamma \\
&\qquad + P_{\alpha\gamma}\partial_\alpha u_\beta + u_\alpha\partial_\alpha P_{\beta\gamma} + P_{\beta\gamma}\partial_\alpha u_\alpha \qquad (4.99)\\
&= (P_{\beta\gamma} - \rho\partial_\rho(P_{\beta\gamma}))\partial_\alpha u_\alpha + \partial_T(P_{\beta\gamma})(\partial_t T + \partial_\alpha T u_\alpha) \\
&\qquad + P_{\alpha\beta}\partial_\alpha u_\gamma + P_{\alpha\gamma}\partial_\alpha u_\beta. \qquad (4.100)
\end{aligned}$$

Substituting $P_{\alpha\beta} = \rho T\delta_{\alpha\beta}$, gives

$$\begin{aligned}
\partial_t \Pi^{eq}_{\beta\gamma} + \partial_\alpha Q^{eq}_{\alpha\beta\gamma} &= (\rho T\delta_{\beta\gamma} - \rho\partial_\rho(\rho T\delta_{\beta\gamma}))\partial_\alpha u_\alpha \\
&\qquad + \partial_T(\rho T\delta_{\beta\gamma})(\partial_t T + \partial_\alpha T u_\alpha) + \rho T\delta_{\alpha\beta}\partial_\alpha u_\gamma + \rho T\delta_{\alpha\gamma}\partial_\alpha u_\beta \qquad (4.101)\\
&= \rho\delta_{\beta\gamma}(\partial_t T + \partial_\alpha T u_\alpha) + \rho T\partial_\beta u_\gamma + \rho T\partial_\gamma u_\beta. \qquad (4.102)
\end{aligned}$$

The term with derivative of temperature can be further simplified by invoking the isothermal condition:

$$\rho\delta_{\beta\gamma}(\partial_t T + \partial_\alpha T u_\alpha) = 0. \tag{4.103}$$

The final momentum equation is

$$\partial_t(\rho u_\beta) + \partial_\alpha \Pi^{eq}_{\alpha\beta} = \partial_\alpha \left(\eta \Big(\partial_\beta u_\gamma + \partial_\gamma u_\beta \Big) \right) \tag{4.104}$$

On the other hand, if the conservation of energy and Eq. 4.82 are invoked, the momentum equation turns out to be

$$\partial_t(\rho u_\beta) + \partial_\alpha \Pi^{eq}_{\alpha\beta} = \partial_\alpha \left(\eta \Big(\partial_\beta u_\gamma + \partial_\gamma u_\beta - \frac{2}{3}\delta_{\beta\gamma}\partial_\alpha u_\alpha \Big) \right) \tag{4.105}$$

where the viscosity $\eta = \rho T \tau$. Eq. 4.104 and 4.105 are the Navier-Stokes equation with different bulk viscosities. In either case, the equations are exactly recovered with no error terms in the macroscopic momentum equation.

4.4 Implementation

So far, we have discussed and covered the theoretical basis of the model and showed that it correctly recovers the Navier-Stokes (NS) equation. In this section, we focus on the numerical aspect and implementation of the model.

Evolution Equation As demonstrated in Eq. 4.61-4.66, one can separate the evolution equation of the first moment contribution e_i and second moment contribution b. For a single-relaxation time, this yields the set of evolution equations that are solved in our algorithm

$$\sum_i \left\{ \partial_t f_i + \partial_\alpha (f_i e_{i\alpha}) = -\frac{1}{\tau}(f_i - f_i^{eq}) \right\}, \tag{4.106}$$

$$\sum_i \left\{ \partial_t f_i e_{i\beta} + \partial_\alpha (f_i e_{i\alpha} e_{i\beta}) + \frac{F_\alpha}{\rho} f_i = -\frac{1}{\tau}(f_i - f_i^{eq}) - \partial_\alpha (f_i b_{\alpha\beta}) \right\}, \tag{4.107}$$

$$\begin{aligned} \sum_i \Bigg\{ & \partial_t \left(f_i \left(e_{i\beta} e_{i\gamma} - \frac{c^2}{3}\delta_{\alpha\beta} \right) \right) + \partial_\alpha \left(f_i e_{i\alpha} \left(e_{i\beta} e_{i\gamma} - \frac{c^2}{3}\delta_{\alpha\beta} \right) \right) \\ & = -\frac{1}{\tau}(f_i - f_i^{eq}) \left(e_{i\beta} e_{i\gamma} - \frac{c^2}{3}\delta_{\alpha\beta} \right) - \partial_\alpha (f_i (e_{i\gamma} b_{\alpha\beta} + e_{i\beta} b_{\gamma\alpha})) - \frac{F_\alpha e_{i\beta} + F_\beta e_{i\alpha}}{\rho} f_i \Bigg\}, \end{aligned} \tag{4.108}$$

$$\sum_i \left\{ \partial_t (f_i \bar{b}_{\beta\gamma}) + \partial_\alpha (f_i e_{i\alpha} \bar{b}_{\beta\gamma}) = -\frac{1}{\tau}(f_i \bar{b}_{\beta\gamma} - f_i^{eq} \bar{b}^{eq}_{\beta\gamma}) \right\}, \tag{4.109}$$

where

$$\bar{b}_{\alpha\beta} = b_{\alpha\beta} + \frac{c^2}{3}\delta_{\alpha\beta}. \tag{4.110}$$

Consequently,

$$\bar{b}^{eq}_{\alpha\beta} = \frac{P_{\alpha\beta}}{\rho} + \frac{u_\alpha u_\beta}{3} \tag{4.111}$$

As can be seen, the evolution of f_i's and b's are coupled through the b derivative terms. These derivative terms are calculated on the interior sites using the isotropic differential operators proposed by Ramadugu et al. [344]:

$$\partial_\alpha(\rho b_{\alpha\beta}) = \frac{1}{3}\sum_{i=1}^{q} w_i e_{i\alpha} \rho b_{\alpha\beta}(\boldsymbol{x} + \boldsymbol{e}_i) + \mathcal{O}(\partial^3) \tag{4.112}$$

where the prefactor 1/3 is a lattice dependent constant. At the boundaries, however, we do not use the isotropic derivatives as a Halfway bounce-back method is employed. We further discuss the boundary conditions later in this chapter. A consequence of using the Halfway bounce-back is that we do not define any nodes inside the wall and therefore the isotropic derivatives cannot be used. Instead, we utilize second-order finite differences for the boundaries such that:

$$\partial_x(\rho b_{x\beta}) = \frac{\rho b_{x\beta}(x+\Delta x) - \rho b_{x\beta}(x-\Delta x)}{2\Delta x} \tag{4.113}$$

$$\partial_y(\rho b_{y\beta}) = \frac{\rho b_{y\beta}(y+\Delta y) - \rho b_{y\beta}(y-\Delta y)}{2\Delta y} \tag{4.114}$$

$$\partial_z(\rho b_{z\beta}) = \pm\frac{\rho b_{z\beta}(x \pm 2\Delta x) - 4\rho b_{z\beta}(x \pm \Delta x) + \rho b_{z\beta}(x)}{2\Delta z} \tag{4.115}$$

where forward and backward (+ and − in Eq. 4.115) finite differences are applied in the z direction for the bottom and top walls, respectively.

At the beginning of each simulation, the geometry is set up and $\bar{f}_i$, ρ, $\bar{u}$, and T arrays are initialized. $\bar{f}_i$ is defined in 4.8. The macroscopic properties are received from the user and the $\bar{f}_i$'s are set to the equilibrium values. The collision step is then performed in the moment space and the post-collision $\bar{f}_i^*$ is found from transforming the post-collision moments. Next, the collision is performed on the $\rho\bar{b}$ terms to get the post-collision $\bar{b}^*$. This is followed by a streaming step where the populations travel to neighbouring sites via e_i velocities. The second moment $\bar{b}$ is carried by the $\bar{f}$'s such that:

$$\rho(x + \boldsymbol{e}_i\Delta t, t+\Delta t)\bar{b}_{\alpha\beta}(x + \boldsymbol{e}_i\Delta t, t+\Delta t) = \sum_i \bar{f}_i^*(x,t)\bar{b}_{\alpha\beta}^*(x,t). \tag{4.116}$$

Then the macroscopic variables are computed from the moments of $\bar{f}_i$:

$$\rho(t+\Delta t) = \sum_i \bar{f}(t+\Delta t) \tag{4.117}$$

$$\rho(t+\Delta t)\bar{u}_\alpha(t+\Delta t) = \sum_i \bar{f}(t+\Delta t)e_{i\alpha} \tag{4.118}$$

$$\tag{4.119}$$

where for the isothermal case, T is left as the initial value. The MD calculations are then done and forces exerted on the fluid by the particles and by the fluid on the particles are found. We will shortly discuss the coupling between the MD particles and the fluid. Finally, the macroscopic properties are corrected as described in Sec. 4.2.1. The total mass, velocity, and energy can be outputted as a LAMMPS *thermo* output. The local properties can output into an .xdmf file and be visualized in visualization software. A concise summary of the algorithm is provided in the form of a pseudo-code in Algorithm 1.

Algorithm 1 LAMMPS psuedo-code illustrating calls for lb/fluid

```
for $n = 1$ to $N_t$ do                                                    ▷ Loop over $N_t$ timesteps
    ev_set()

    fix→initial_integrate()
        lb/fluid:
            calculate $m*/m - m^{eq}(\rho(t), \boldsymbol{u}(t), T)$ on local subgrid
            calculate $f_i^*$ on local subgrid
            calculate $\bar{b}^*$ on local subgrid
            calculate/comm $\bar{f}_k(t + \Delta t)$, $\bar{\boldsymbol{b}}(t + \Delta t) = \sum \bar{f}_k \bar{\boldsymbol{b}}$
            calculate/comm $\rho = \sum_k \bar{f}_k$, $\rho\bar{\mathbf{u}} = \sum_k \bar{f}_k \mathbf{e}_k$
            calculate $\partial_\alpha(\rho b_{\alpha\beta})$
    fix→post_integrate()

    LAMMPS neighbor list update and particle communication

    force_clear()
    fix→pre_force()

    force→compute(),
        where force $\in$ {pair, bond, angle,dihedral, improper, kspace}

    comm→reverse_comm()

    fix→post_force()
        lb/fluid: if (fixviscouslb)
                      calculate and comm interpolation weights
                      calculate and comm Force on fluid $\mathbf{F}_f$
                      comm particle $\mathbf{F}_H(t + \Delta t)$ mass field
                  end if
        lb/viscous: $\mathbf{F}_i(t + \Delta t) = \mathbf{F}_{H,i} + m_i/(m_i + m_{n,i})\,\mathbf{F}_{x,i}$
    fix→final_integrate()
        lb/fluid:
            calculate $\partial_\alpha(\rho u_\gamma b_{\alpha\beta} + \rho u_\beta b_{\alpha\gamma})$
            calculate/comm $\boldsymbol{u}(t + \Delta t) = \bar{\mathbf{u}} + \Delta t/(2\rho)\,(\partial_\alpha(\rho b_{\alpha\beta}) + \boldsymbol{F})$
    fix→end_of_step()
        lb/fluid: output fluid                                             ▷ If output to write

    output→write()                                                         ▷ If output to write
end for
```

4.4.1 Boundary Conditions

For anyone who has worked with Partial Differential Equation (PDE)s before, the necessity of boundary conditions is obvious. The specific solution to a PDE and the integration constants can be only determined based on the initial and boundary conditions. Physically, the initial and boundary conditions set the geometry of the problem. So it is very clear that from both the mathematical and physical point of view, these conditions need to be specified to be able to model a particular physical problem.

When it comes to hydrodynamics, the LBM recovers the Navier-Stokes (NS) equations at the macro-scale. Thus, the initial and boundary conditions typically applied to NS equations can be applied to LBE at the macro-scale. But the LBE solves the evolution equation of the particle populations f_i. Therefore, it requires initial and boundary conditions for these particle populations. It would not be an exaggeration to state that finding the right boundary conditions for an LBM is one of the most important and challenging parts of the design. This is particularly because the physical macroscopic conditions do not generate enough constraints to uniquely determine the boundary conditions for all of the mesoscopic distributions. As a result, a great number of approaches have been proposed to handle the LBE boundary conditions. Examples of different methods can be found in the literature [20, 345–349]. For the current work, we used a halfway bounce back method for the solid walls and periodic boundary conditions everywhere else which we will describe in the next section.

Periodic Boundary Conditions

Periodic boundary conditions can be used when the solution of a flow is periodic in a specific direction. Physically, this corresponds to isolating a unit cell in a repeating flow pattern. The particle distributions that leave the simulation box are assumed to re-enter the box instantaneously in the periodic directions. Therefore, the periodic boundary conditions always conserves mass and momentum.

Implementing periodic boundary conditions in the LBM is straightforward. During the streaming step, the unknown incoming populations on one side are given by the exiting populations on the other side:

$$f_i(x_\alpha, t + \Delta t) = f_i^*(x_\alpha + L - e_{i\alpha}\Delta t, t) \tag{4.120}$$

where L is the length of the box in the α direction.

Bounce Back Boundary Conditions

The no-flow, no-slip boundary condition is the most commonly used boundary condition in hydrodynamics. The most popular method that is used to impose a no-slip boundary condition in LBM is the bounce-back method. The main idea behind the bounce-back approach is quite simple; the populations that hit a rigid wall are reflected to where they came from. The no-slip boundary condition is enforced by bouncing back the populations rather than streaming forward which implies that the fluid and the boundary have the same velocity. The bounce-back also ensures conservation of mass as no particle passes through the boundary and all are returned to the fluid (no-flow).

There are two approaches to the bounce-back method:

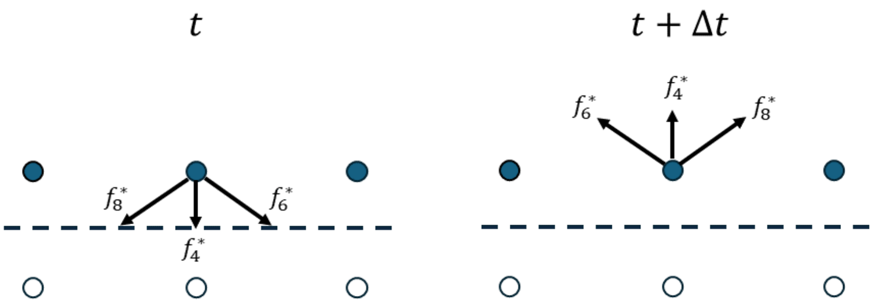

Figure 4.1: Time evolution of the bounce-back method at the bottom wall. The incoming populations are reflected in the opposite direction at the next timestep.

1. Fullway bounce-back: In the fullway bounce-back, solid nodes inside the wall are created. The population entering the wall first resides on the solid node and is returned into the bulk in the next streaming step.
2. Halfway bounce-back: In the halfway bounce-back, there is no need for solid nodes. The populations entering the wall are returned to their current site immediately and leave in the opposite direction in the next timestep.

Both bounce-back schemes result in a boundary located approximately $+\frac{\Delta x}{2}$ from the boundary nodes. It has been shown that the fullway bounce-back method is a first order method while the halfway method is accurate up to second order [20]. In our simulations, we use the halfway bounce-back method. For a stationary wall, this means

$$f_j(\boldsymbol{x}, t + \Delta t) = f_i^*(\boldsymbol{x}, t) \tag{4.121}$$

where $e_i = -e_j$. This is demonstrated for a bottom wall in Fig. 4.1 The bounce-back can be easily extended to include moving walls. The main principle is adding/taking a certain amount of momentum to/from the bounce-back populations so that the outcome is Galilean invariant. Thus, the modified bounce-back for a moving wall with the velocity $\boldsymbol{U}$ is

$$f_j(\boldsymbol{x}, t + \Delta t) = f_i^*(\boldsymbol{x}, t) - 2w_i \rho_w (e_{i\alpha} U_\alpha)/c^2 \tag{4.122}$$

where w_i is the discretization weight, ρ_w is the density at the wall, and c is the lattice constant.

4.4.2 Coupling MD particles to the fluid

The production of fiber-reinforced thermoplastics is often done under flow conditions, for example, extrusion and injection molding. Thus, it is crucial to understand the dynamics of fibers in flow to obtain high quality fiber-reinforced composites. To study the dynamics and behaviour of fibers and nanorods in a flow, we couple our Lattice Boltzmann Method to the Molecular Dynamics particles in LAMMPS (Large-scale Atomic/Molecular Massively Parallel Simulator) [253]. In this section, we will derive the force coupling between the Molecular Dynamics (MD) particles and the fluid. The goal here is to achieve an immersed boundary style method [350] where the velocity of the particle (or node on the surface of the extended particle) exactly matches the velocity of the fluid (interpolated to the location of the particle/surface node) at the end of each time step. This section has been published in the journal of Computer Physics Communications in collaboration with C Denniston, M.G. Cole-André, F.E. Mackay, S.T.T. Ollila, and T. Whitehead [314]. This was included as a modification to lb/fluid package in the open-source software LAMMPS.

Similar to other constraints in LAMMPS such as the SHAKE algorithm [351, 352], the force coupling is done by finding the set of constraining forces (equal and opposite for the particles/fluid) that ensure that particles' velocity match the (interpolated) velocity of the fluid at the particles' location at the end of the time step. As we will see, the algorithm below does this exactly in two limits, first when the particles are far apart and second when they are very densely packed. Between these limits there is a finite, but bounded, error (difference between the velocities). Just as with other constraints in LAMMPS, the total number of degrees of freedom (DOF) in the system are reduced by these constraints.

An interpolation *stencil* is used to interpolate values from the fluid mesh to the particle location (which typically does not coincide with a mesh point). The weight from mesh site j at particle (node) i location is denoted as ζ_{ij}. By construction we require that $\sum_j \zeta_{ij} = 1$. This can then be used to interpolate the value of the fluid density to particle i's location as

$$\rho_i = \sum_j \rho(x_j)\zeta_{ij}, \tag{4.123}$$

where $\rho(x_j)$ is the density at the mesh site x_j. However, for the fluid velocity we use a mass-weighted average for the interpolation so that

$$\mathbf{u}_i = \frac{\sum_j \rho(x_j)\mathbf{u}(x_j)\zeta_{ij}}{\sum_j \rho(x_j)\zeta_{ij}}. \tag{4.124}$$

In other words, we actually interpolate the momentum density to the location of the particle and then divide by the mass density interpolated to the particle site. This helps ensure an exact conservation of momentum in the algorithm.

"Spreading" is the converse process to interpolation, and is the term used to describe how the particle properties are distributed onto the fluid mesh. The main thing needed to be "spread" is the equal-and-opposite force to the hydrodynamic force on the i'th particle F_H^i. In the previous version of the package the spreading weight of particle i onto fluid mesh site j was always equal to the interpolation weight ζ_{ij}. In the current version this will only be true for a limiting case. We denote the spreading weight of particle i at lattice site j as η_{ij}. We will not require this sum to be one but will need the normalization which is denoted

$$\eta_{iA} = \sum_j \eta_{ij}. \tag{4.125}$$

To derive the required constraining forces, we need to also consider the velocity-Verlet algorithm [353] typically used in MD (variants work fairly similarly). In LAMMPS, the particle velocity at the end of the step is computed from the half-step velocity (cf. Algorithm 1) in the `final_integrate` step:

$$\mathbf{v}_i(t+\Delta t) = \mathbf{v}_i(t+\Delta t/2) + \frac{\Delta t}{2m_i}\left[-\mathbf{F}_H^i + \frac{m_i}{m_i+m_n^i}\mathbf{F}_x^i\right], \tag{4.126}$$

where m_i is the particle mass, m_n^i is the fluid mass constrained to move with the particle (which we will determine below), $\mathbf{F}_H^i$ is the constraining force on the particle (making it move with the fluid), and $\mathbf{F}_x^i$ is the other forces (inter-particle or other MD forces) on the particle. Note that the particle and accompanying fluid move *together* so form a pseudo-particle with total mass $m_i + m_n^i$. The corresponding step for the fluid is from Eq. (4.29) which in terms of the specific forces in Eq. (4.126) and converted from momentum densities to total momentum for fluid site j is

$$\rho_j \mathbf{u}_j \Delta x^3 = \rho_j \bar{\mathbf{u}}_j \Delta x^3 + \frac{\Delta t}{2}\sum_i \left[\mathbf{F}_H^i + \frac{m_n^i}{m_i+m_n^i}\mathbf{F}_x^i\right]\frac{\eta_{ij}}{\eta_{iA}}. \tag{4.127}$$

As an aside, we note that these equations conserve the total momentum $\mathbf{P}$ in the system:

$$\begin{aligned}
\Delta P &= \Delta P_{particles} + \Delta P_{fluid} && (4.128)\\
&= \sum_i \left[m_i \mathbf{v}_i(t+\Delta t) - m_i \mathbf{v}_i(t+\frac{\Delta t}{2})\right] && (4.129)\\
&\quad + \sum_j \left[\rho_j \mathbf{u}(\mathbf{x}_j) - \rho_j \bar{\mathbf{u}}(\mathbf{x}_j)\right]\Delta x^3 && (4.130)\\
&= \frac{\Delta t}{2}\sum_i \left[-\mathbf{F}_H^i + \frac{m_i}{m_i+m_n^i}\mathbf{F}_x^i\right] && (4.131)\\
&\quad + \frac{\Delta t}{2}\sum_i \left[\mathbf{F}_H^i + \frac{m_n^i}{m_i+m_n^i}\mathbf{F}_x^i\right]\sum_j \frac{\eta_{ij}}{\eta_{iA}} && (4.132)\\
&= \frac{\Delta t}{2}\sum_i \mathbf{F}_x^i. && (4.133)
\end{aligned}$$

where in Eq.(4.132) we have made use of Eq. (4.126) and (4.127) and switched the order of summation for the second term. To go from Eq.(4.132) to Eq. (4.133) we have made use of Eq. (4.125) to find the sum over j to be one. Note that if Newton's third law is obeyed by the MD algorithm (which is the case) we should have $\sum_i \mathbf{F}_x^i = 0$ if the $\mathbf{F}_x^i$ are inter-particle forces and this sum will result in the total external force on the system if external forces are present. As a result, total momentum is conserved, or changes in accordance to Newton's laws in the presence of external forces.

We now turn to determining $\mathbf{F}_H^i$ and m_n^i using the constraint that we want the end-of-step velocities $\mathbf{v}_i(t+\Delta t)$ and $\mathbf{u}_j$ interpolated to the i'th particle position to be identical. Using the interpolated velocity definition Eq. (4.124) with the final fluid velocity we get

$$\begin{aligned}
\mathbf{u}_i(t+\Delta t) &= \frac{\sum_j \zeta_{ij}\left(\rho_j \bar{\mathbf{u}}(\mathbf{x}_j) + \frac{\Delta t}{2\Delta x^3}\sum_s \left\{\mathbf{F}_H^s + \frac{m_n^s}{m_s+m_n^s}\mathbf{F}_x^s\right\}\frac{\eta_{sj}}{\eta_{sA}}\right)}{\sum_j \rho_j \zeta_{ij}}, && (4.134)\\
&= \bar{\mathbf{u}}_i + \frac{\Delta t}{2\Delta x^3}\sum_s \left\{\mathbf{F}_H^s + \frac{m_n^s}{m_s+m_n^s}\mathbf{F}_x^s\right\}\frac{\sum_j \zeta_{ij}\eta_{sj}}{\eta_{sA}\sum_j \rho_j \zeta_{ij}}, && (4.135)
\end{aligned}$$

where the first term is the interpolated half-step fluid velocity at particle i's location, and we have switched the order of summation in the second term. Now taking the difference between the interpolated final fluid velocity and the particle velocity (Eq. (4.126)) we get

$$\begin{aligned}
\mathbf{u}_i(t+\Delta t) \quad - \quad & \mathbf{v}_i(t+\Delta t) = (\bar{\mathbf{u}}_i - \mathbf{v}_i(t+\Delta t/2)) & (4.136)\\
+ \quad & \frac{\Delta t}{2}\mathbf{F}_H^i \left(\frac{\sum_j \zeta_{ij}\eta_{ij}}{\eta_{iA}\sum_j \rho_j \zeta_{ij}\Delta x^3} + \frac{1}{m_i} \right) & (4.137)\\
+ \quad & \frac{\Delta t}{2}\frac{\mathbf{F}_x^i m_n^i}{m_i + m_n^i} \left(\frac{\sum_j \zeta_{ij}\eta_{ij}}{\eta_{iA}\sum_j \rho_j \zeta_{ij}\Delta x^3} - \frac{1}{m_n^i} \right) & (4.138)\\
+ \quad & \frac{\Delta t}{2\Delta x^3}\sum_{s\neq i}\left\{ \mathbf{F}_H^s + \frac{m_n^s}{m_s + m_n^s}\mathbf{F}_x^s \right\} \frac{\sum_j \zeta_{ij}\eta_{sj}}{\eta_{sA}\sum_j \rho_j \zeta_{ij}}, & (4.139)
\end{aligned}$$

where we have separated out the term in the sum over particles corresponding to particle i. At this point we have not specified m_n^i, $\mathbf{F}_H^i$, or η_{ij} and we will use the goal of minimizing the magnitude of this expression (difference between the final velocities) to determine these quantities.

We note two limiting cases:

1. *Isolated Particles case* where there is only one particle or all particles are separated. In this case for any mesh site j only one particle contributes and $\zeta_{ij}\eta_{sj} = 0$ for $i \neq s$. As a result the last line is zero and the choice

$$m_n^i \overset{?}{=} \frac{\eta_{iA}\sum_j \rho_j \zeta_{ij}\Delta x^3}{\sum_j \zeta_{ij}\eta_{ij}} \qquad (4.140)$$

   will zero the third line (the $\overset{?}{=}$ is used here as we will modify this slightly below). Finally

$$\mathbf{F}_H^i = \frac{2}{\Delta t}\frac{m_i m_n^i}{m_i + m_n^i}(\bar{\mathbf{u}}_i - \mathbf{v}_i(t+\Delta t/2)) \qquad (4.141)$$

   will zero the first two lines yielding $\mathbf{u}_i(t+\Delta t) = \mathbf{v}_i(t+\Delta t)$ as desired. Note that this is the same coupling force expression derived in Ref.[313] except that now m_n^i and the times scale for the impulse are fully specified.

2. *Coinciding Particles case* where particles are either isolated or exactly coincide so for any mesh site j either only one particle i has $\zeta_{ij} \neq 0$ or there are Q particles that exactly coincide. With a slight modification of m_n^i,

$$m_n^i \equiv \frac{\eta_{iA}^2\sum_j \rho_j \zeta_{ij}\Delta x^3}{\sum_j \zeta_{ij}\eta_{ij}} \qquad (4.142)$$

   and defining the spreading weight η_{ij} as

$$\eta_{ij} = \zeta_{ij}\frac{|\zeta_{ij}|}{\sum_{r=1}^{Q}|\zeta_{rj}|}, \qquad (4.143)$$

   we will show below that this zeros the difference between the particle and interpolated fluid velocity in both this case and in the isolated particle case, with the choice of Eq.(4.141) in all cases.

To see that Equations (4.141), (4.142), and (4.143) work for both limiting cases, first note that in case 1 the sum in the denominator Eq.(4.143) always has only one term, which cancels with the term in the numerator and the spreading weight $\eta_{ij} = \zeta_{ij}$, the interpolation weight. As a result, in case

1 the spreading normalization $\eta_{iA} = 1$ and so Eq.(4.142) and (4.140) become numerically identical. Thus these expressions again yield $\mathbf{u}_i(t + \Delta t) = \mathbf{v}_i(t + \Delta t)$ as desired for case 1.

For limiting case 2, the denominator in Eq.(4.143) is $Q|\zeta_{ij}|$, where particle i is one of the Q coinciding particles (so all have same interpolation weight), and $\eta_{ij} = \frac{1}{Q}\zeta_{ij}$. The normalization then becomes $\eta_{iA} = 1/Q$. In this case, the effect will be that the Q coinciding particles equally split the properties of one "super" pseudo-particle with a total full weight of ζ_{ij}. Further, the last line in the velocity difference equation, Eq.(4.139) can be rewritten as identical terms to the first terms in the brackets on the previous two lines (so a total of Q such terms). As $\eta_{iA} = 1/Q$ in this case, we once again get $\mathbf{u}_i(t + \Delta t) = \mathbf{v}_i(t + \Delta t)$ as desired.

In the more general case where the interpolation weights for multiple particles may overlap, but not perfectly coincide, Eq.(4.143) is a weighted sum of the Q particles contributing to a fluid mesh site j. In this case we may not get $\mathbf{u}_i(t + \Delta t) = \mathbf{v}_i(t + \Delta t)$ exactly, but it should be very close.

One downside to using Eq.(4.143) is that it requires two passes over the particles to compute. The first pass works out

$$w_{1,j} = \sum_s |\zeta_{sj}|, \tag{4.144}$$

which is stored in an array (with dimensions of the fluid mesh size) and in the second pass over the particles we work out

$$\eta_{ij} = \frac{1}{w_{1,j}} \zeta_{ij} |\zeta_{ij}|, \tag{4.145}$$

for each particle. While more expensive that a single pass, the overall fluid-particle force calculation is still $\mathcal{O}(N)$ for N particles. In most examples of using the *lb/fluid* package this calculation is a small part of the total computational load so that the extra work is negligible and well worth the cost. Significantly, this removes the need for the user to specify a correct value for m_n^i. This seemed to be a significant issue for many users of the first version of *lb/fluid* as poor choices for m_n^i resulted in poor performance, especially in thermostating of the particles when a fluid with thermal fluctuations was used.

4.4.3 Interpolation Stencils [1]

The algorithm above requires a choice of interpolation stencil with weights ζ_{ij} which interpolated particle i information at location $\mathbf{r}_{pi} = (x_{pi}, y_{pi}, z_{pi})$ to fluid mesh site $\mathbf{r}_{fj} = (x_{fj}, y_{fj}, z_{fj})$. The stencil weight

$$\zeta_{ij} = \phi(\Delta x_{ij})\phi(\Delta y_{ij})\phi(\Delta z_{ij})$$

where $\Delta \mathbf{r}_{ij} = (\mathbf{r}_{pi} - \mathbf{r}_{fj})/\Delta x$ and Δx is the lattice spacing. Three different stencils are provided in the package with the choice specified by the user in the input script:

1. *Trilinear stencil*: This is a standard 2-point linear interpolation (in each dimension) so

$$\phi(\Delta) = 1 - |\Delta|, \qquad |\Delta| < 1. \tag{4.146}$$

---

[1] This section has been published in the journal of Computer Physics Communications in collaboration with C Denniston, M.G. Cole-André, F.E. Mackay, S.T.T. Ollila, and T. Whitehead [314]

2. *Three-point immersed boundary stencil*: This is a commonly used immersed boundary stencil [350],

$$\phi(\Delta) = \begin{cases} \frac{1}{3}(1+\sqrt{1-3\Delta^2}), & |\Delta| \leq 0.5 \\ \frac{1}{6}(5-3\Delta-\sqrt{1-3(1-\Delta)^2}), & 0.5 < |\Delta| < 1.5. \end{cases} \tag{4.147}$$

3. *Keys' cubic spline interpolation stencil*: This 4-point stencil is often used for scaling images and video as it preserves detail better than linear interpolation. Keys showed that this produces third-order accuracy [354]. The stencil is

$$\phi(\Delta) = \begin{cases} \frac{3}{2}|\Delta|^3 - \frac{5}{2}\Delta^2 + 1, & |\Delta| \leq 1 \\ -\frac{1}{2}|\Delta|^3 + \frac{5}{2}\Delta^2 - 4|\Delta| + 2, & 1 < |\Delta| < 2. \end{cases} \tag{4.148}$$

These stencils are all zero outside their defined range. The default stencil (used if not otherwise specified by the user) is the trilinear stencil.

There are advantages and disadvantages to each stencil. The trilinear stencil's main advantage is that it extends at most Δx from the particle which allows particles to approach walls (and each other) without significant overlap of the stencil. The disadvantage of the trilinear stencil is that it has stronger commensurability effects from the underlying mesh [355]. The immersed boundary stencil reduces these mesh effects [350] but at the cost of reduced accuracy. In addition, the reweighting necessary for densely packed nodes in the spreading stencil η_{ij} somewhat negates the stencil smoothness over the mesh. The 4-point stencil produces similar results to the trilinear stencil. It produces a more accurate interpolation at the cost of extending up to $2\Delta x$ from the particle. However, the stencil accuracy appears to be one of the smaller discretization errors overall so usually one of the other two stencils would be preferred.

4.5 Results

4.5.1 Fourier Analysis

The governing macroscopic equations of our model were derived in section 4.3.1. In this section, we measure the physical properties of our fluid. We also compare these results to our theoretical predictions to validate our model. The dynamic/shear viscosity and bulk viscosity are related to the rate of decay of density waves in the system. Thus, we initially introduce a sound wave in the system and measure these quantities from the decay of such waves. As a starting point, we perform a Fourier analysis of the sound waves in our LB fluid. The analysis is applied to a Single-Relaxation Time (SRT) model. The continuity equation reads

$$\partial_t \rho + \partial_\alpha(\rho u_\alpha) = 0 \tag{4.149}$$

and the momentum equation is

$$\partial_t(\rho u_\beta) + \partial_\alpha(\rho u_\alpha u_\beta) = -\partial_\beta(\rho T) + \eta \partial_\alpha \Bigg(\partial_\beta u_\alpha + \partial_\alpha u_\beta \Bigg). \tag{4.150}$$

The momentum equation 4.150 can be simplified by using the product rule in Eq. 4.79 and the continuity equation

$$\rho \partial_t u_\beta + \rho u_\alpha \partial_\alpha u_\beta = -\partial_\beta(\rho T) + \partial_\alpha \Bigg(\eta(\partial_\alpha u_\beta + \partial_\beta u_\alpha) \Bigg) \tag{4.151}$$

Now let's assume a small perturbation in the form of a right travelling wave with the wave number k and angular frequency ω ($k, \omega > 0$)

$$\rho = \rho_0 + a_0 e^{-\gamma t} e^{i(kx - \omega t)} \tag{4.152}$$

$$u = b_0 e^{-\gamma t} e^{i(kx - \omega t)} \tag{4.153}$$

$$\tag{4.154}$$

where a_0, and b_0 are constants with no dependence on space or time. The constants can be complex but they are small in value:

$$a_0 = |a_0| \, e^{i\delta_a}, \qquad |a_0| \sim 0 \tag{4.155}$$

Plugging 4.152 and 4.153 into 4.149, we get

$$a_0(-\gamma - i\omega) e^{-\gamma t} e^{i(kx-\omega t)} + \rho_0 b_0 (ik) e^{-\gamma t} e^{i(kx-\omega t)} + \mathcal{O}\left(a_0 b_0\right) = 0 \tag{4.156}$$

which in turn gives

$$b_0 = a_0 \frac{(\gamma + i\omega)}{ik\rho_0}. \tag{4.157}$$

The complex coefficient relating a_0 and b_0 implies ρ and u are not in phase but have a phase shift.

Similarly, if we plug 4.152-4.153 into the momentum equation 4.151, we get

$$\rho_0 b_0(-\gamma - i\omega) + \mathcal{O}\left(b_0^2, a_0 b_0\right) = -ik\left(a_0 T\right) + \mathcal{O}\left(a_0 c_0\right) + (ik)\eta_0(ik)(2)b_0 + \mathcal{O}\left(a_0 b_0, b_0 c_0\right). \quad (4.158)$$

where $\eta_0 = \rho_0 T\tau$. Substituting for b_0, we have

$$\rho_0(\gamma + i\omega)a_0\frac{(\gamma + i\omega)}{ik\rho_0} = ik\left(a_0 T\right) + 2k^2\eta_0 a_0\frac{(\gamma + i\omega)}{ik\rho_0} \quad (4.159)$$

which can be further simplified to

$$(\gamma + i\omega)^2 = -k^2\left(T\right) + 2k^2\frac{\eta_0}{\rho_0}(\gamma + i\omega). \quad (4.160)$$

An equation for the decay rate γ can be found by equating the imaginary parts on each side of this equation:

$$\gamma = k^2\frac{\eta_0}{\rho_0} \quad (4.161)$$

And the real part can be solved to get a dispersion relation:

$$\gamma^2 - \omega^2 = -k^2 T + 2\frac{\eta_0}{\rho_0}k^2\gamma. \quad (4.162)$$

It is worth noting that since a bulk viscosity is $2/3\eta_0$, the effective viscosity appearing in Eq. 4.161 is equal to the shear viscosity. Substituting Eq. 4.161 in Eq. 4.162, we get an equation for ω

$$\omega^2 = k^2 T - k^4\frac{\eta_0^2}{\rho_0^2} \quad (4.163)$$

Eq. 4.161 and 4.163 can be used to measure η_0 from a sound wave analysis. To do so, we initialize our system with a sinusoidal perturbation

$$\rho_{ijk} = \rho_0 + Acos(2\pi\frac{k}{N_z}) \quad (4.164)$$

where ρ_0 is the base density inputted by the user. $\rho_0 = 1$ and $A = 0.0001$ in the rest of this chapter unless mentioned otherwise. The size of the simulation box for the simulations in this section is set to 20μm $\times$ 20μm $\times$ 80μm and $k = 2\pi/80 = 0.07854$.

Fig. 4.2(a) shows the evolution of the density at centre of the simulation box. The results for viscosities $\eta_0 = 0.0625, 0.125, 0.25, 0.5$ are shown. We see that the waves are damped out faster at higher viscosities. This qualitative observation agrees with the prediction of Eq. 4.161. To check if our model reproduces the correct bulk viscosity, we fit the ρ versus t data to find the damping factor γ. Fig. 4.2 shows the measured damping factor as a function of the input viscosity. As can be seen, the damping factor is a linear function of the viscosity. The slope of the line is found to be 0.0062317 which matches the expected value $k^2/\rho_0 = 0.0061685$ with about 1% error.

Moreover, one would expect changing the effective viscosity η_0 to have a negligible impact on the angular frequency as it only appears as the coefficient of k^4. This is also observed in Fig. 4.2(a) where the frequency of the waves seem to coincide.

One of the advantages of our new LBM is the flexibility in setting the temperature. Fig. 4.3 shows the square of the measured angular frequency as a function of temperature for input viscosities

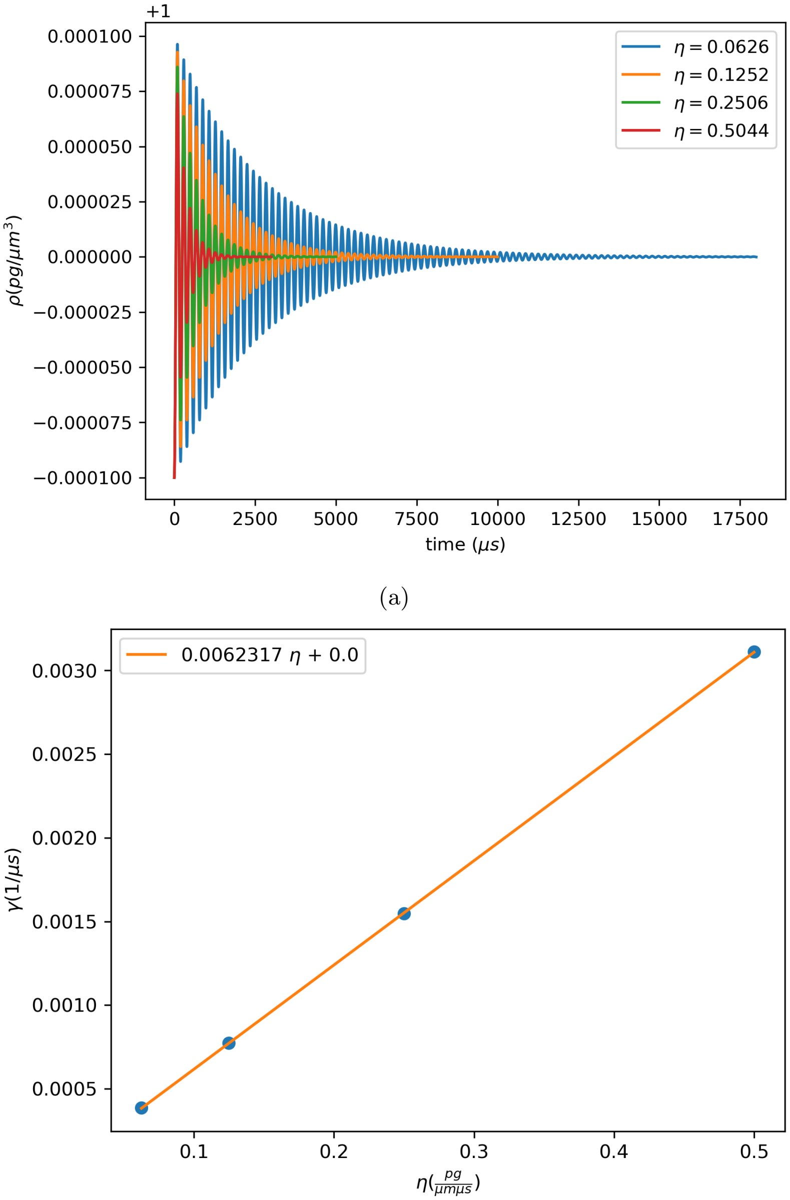

(a)

(b)

Figure 4.2: (a) shows the density oscillation at z=0 for different viscosities as a function of time. (b) shows the damping factor of the sound waves as function of viscosity. Higher viscosities damp out the waves faster as expected. A linear relation between γ and η is found as predicted by the wave analysis. The slope of the line is k^2/ρ_0

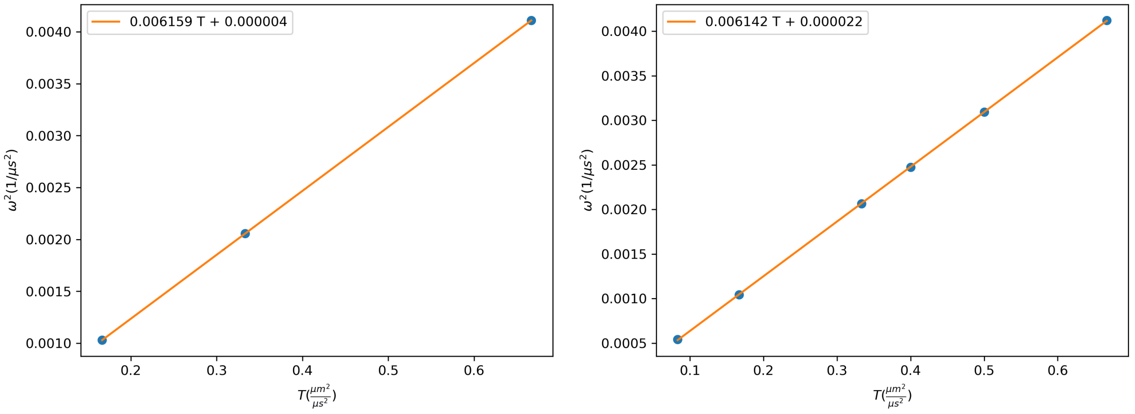

(a)

(b)

Figure 4.3: The squared angular frequency ω^2 is plotted versus T for $\eta = 0.125$ (a) and $\eta = 0.5$ (b)

$\eta = 0.125$pg/μmμs (a) and $\eta = 0.5$pg/μmμs (b). A linear relationship between the ω^2 and T is observed at both viscosities. This is expected, based on Eq. 4.162, as the k^4 term is small compared to k^2T term and $\omega^2 \approx k^2T$. The slope of the fitted lines correctly correspond to the value of k^2 with less than 1% error.

4.5.2 Poiseuille Flow

The bulk viscosity was measured above based on the damping of the sound waves. In this section, we measure the shear viscosity using a Poiseuille flow. A Poiseuille flow can be generated by applying a body force or a pressure gradient along the channel and parallel to stationary walls. In our case, we apply a body force acceleration of $a = 0.00001\frac{\mu m}{\mu s^2}$, which is very close to the gravitational acceleration on earth g, in the y direction. the velocity profile when a body force acceleration a in the y direction is applied can be found from the momentum equation (Eq. 4.150):

$$\partial_t(\rho u_\beta) + \partial_\alpha(\rho u_\alpha u_\beta) = -\partial_\beta(\rho T) + \eta\partial_\alpha\Bigg(\partial_\beta u_\alpha + \partial_\alpha u_\beta\Bigg) + \rho a_\beta. \tag{4.165}$$

In steady-state, nothing changes with time. Thus, $\partial_t = 0$. The walls of the channel are set up with normals in the z direction and a bounce back boundary condition (BC) is applied at the walls. Periodic boundary condition (BC)s are used in the x and y directions. Therefore, everything is translationally invariant in these directions, i.e. $\partial_x = \partial_y = 0$. There is also no driving force applied in the x direction resulting in no velocity in that direction, i.e. $u_x = 0$. The walls and conservation of mass impose $u_z = 0$. Considering all the above conditions and an incompressible regime ($Ma = u_{max}/c_s < 0.35$), Eq. 4.165 transforms into

$$0 = 0 + \eta\partial_z\Bigg(\partial_y u_z + \partial_z u_y\Bigg) + \rho a_y. \tag{4.166}$$

which in turn has a solution of form

$$u_y(z) = -\frac{1}{2\eta}\rho a_y z(z - H) \tag{4.167}$$

where u_y is the velocity in the y-direction, η is the dynamic viscosity, a_y is the y component of the acceleration (rest of them are zero), and H is the height of the channel in the z-direction. Fig. 4.4(a) and (b) illustrate the u_y profile for fluids at different temperatures and two relaxation times $\tau = 1\mu$s and $\tau = 2\mu$s, respectively. For these simulations, we observe that the fluid reaches larger velocities at higher temperatures. Based the Chapman-Enskog expansion, we expect the viscosity and temperature to be related by

$$\eta = \rho T \tau \tag{4.168}$$

where τ is the relaxation time. To confirm this relation, we measure the viscosity η from the Poiseuille flow profiles and fit a linear equation to the data. The viscosity is found using

$$\eta = \frac{\rho a_y H^2}{8 u_y^{max}}. \tag{4.169}$$

Fig. 4.4(c) shows the measured η as a function of temperature for both relaxation times. As can be seen, the viscosity versus temperature data fits perfectly to a line and the slope of the lines correspond to the correct value of $\rho\tau$ for both systems confirming Eq. 4.168.

4.5.3 Couette Flow and Galilean Invariance

As discussed in section 4.3, the standard LBM on standard lattices is not capable of generating independent third moments. This leads to appearance of error terms in the macroscopic momentum equation and limits the applicability of the model to the incompressible limit. The error terms also introduce a dependence on the frame and break the Galilean invariance of the model [20, 303]. These error terms are typically negligible in the incompressible and low velocity regimes but significant when a density gradient is applied. In this section, we show that our model is Galilean invariant even in the presence of density gradients and in the compressible regime.

We test the Galilean invariance of our system in a Couette flow example. Two simulations are conducted: In the first system, the bottom wall is stationary and the top wall moves in the y direction at the speed of $2U$. In the second system, the bottom wall moves at the speed of U in the -y direction and the top wall moves in the y direction at the speed of U. In both systems, a body force is applied in the -z direction to create a density gradient. A periodic boundary condition is applied in the x and y directions. The solid walls are set up normal to the z direction and bounce back boundary conditions are invoked. Schematic diagrams of both systems are illustrated in Fig. 4.5.

The velocity profile for this problem can be analytically found by solving Eq. 4.104:

$$\partial_t(\rho u_\beta) + \partial_\alpha(\rho u_\alpha u_\beta) = -\partial_\beta(\rho T) + \partial_\alpha\bigg(\eta(\partial_\alpha u_\beta + \partial_\beta u_\alpha)\bigg) + \rho a_\beta \tag{4.170}$$

where ρa_β is the body force term. For the above geometry and under steady state conditions, Eq.

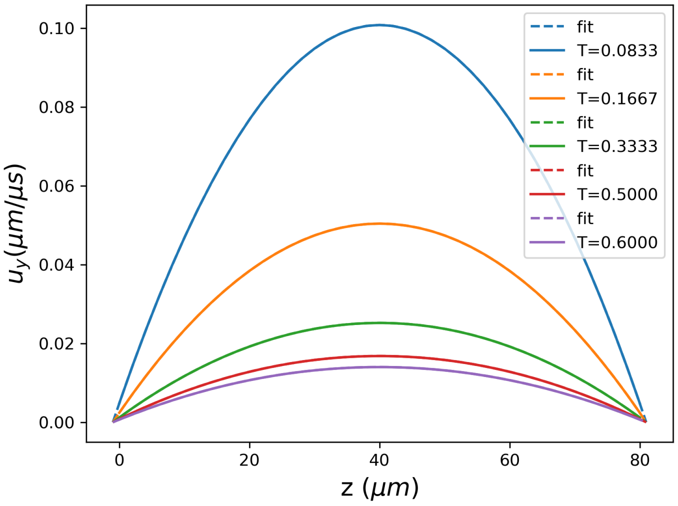

(a)

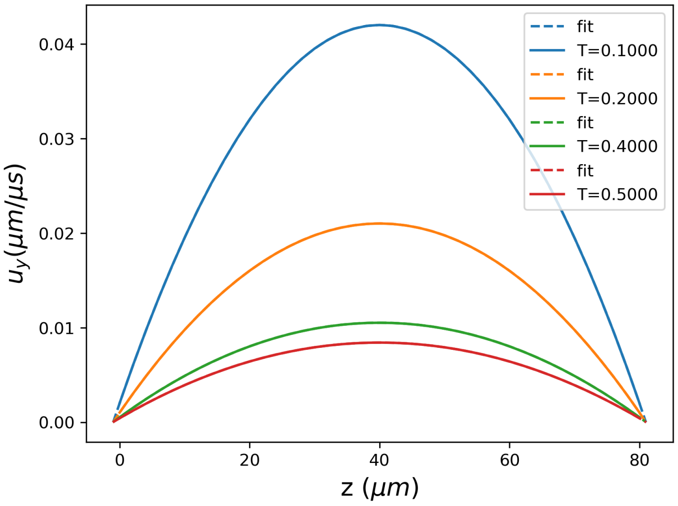

(b)

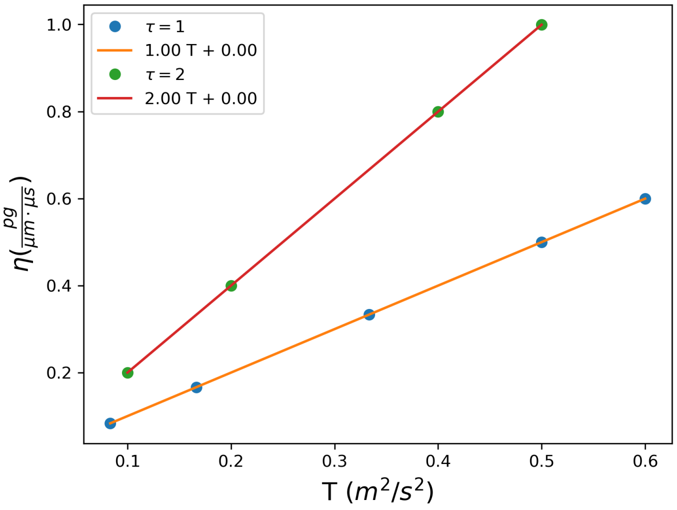

(c)

Figure 4.4: The velocity profile for a Poiseuille flow at different temperatures and $\tau = 1\mu s$ is shown in (a). (b) shows the velocity profile for a system with the relaxation time $\tau = 2\mu s$. (c) shows the measured viscosity as a function of temperature. A linear relation between viscosity and temperature is obtained. The slope of the line is $\rho\tau$ which agrees with the theoretical prediction.

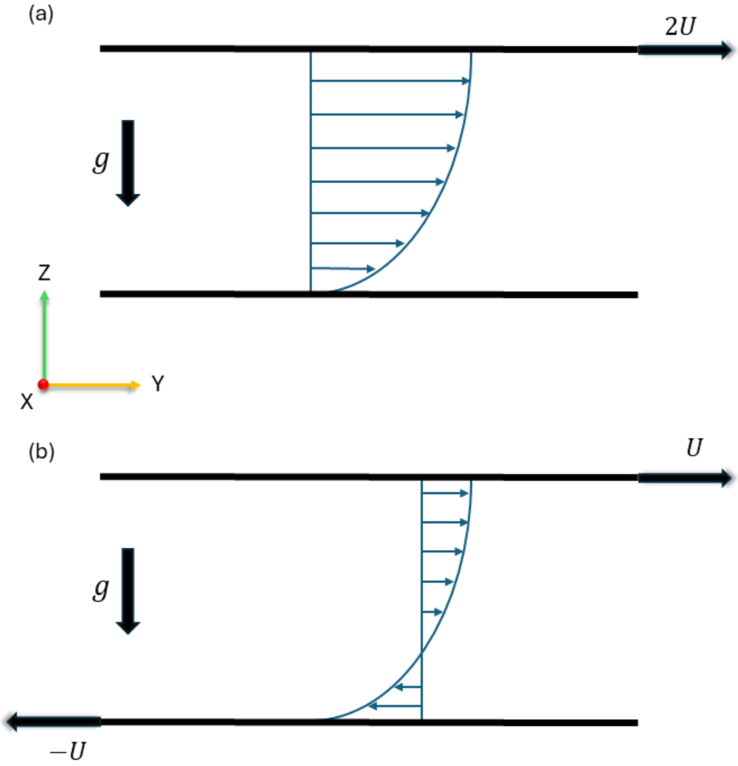

Figure 4.5: The velocity profile for a Couette flow in the presence of a gravitational field is depicted. (a) stationary bottom wall and moving top wall (b) top and bottom walls moving at the same velocity in the opposite directions

4.170 can be simplified to get

$$0 = \partial_\alpha \bigg(\eta(\partial_\alpha u_x + \partial_x u_\alpha) \bigg) \tag{4.171}$$

$$0 = \partial_\alpha \bigg(\eta(\partial_\alpha u_y + \partial_y u_\alpha) \bigg) \tag{4.172}$$

$$0 = -\partial_z(\rho T) + \partial_\alpha \bigg(\eta(\partial_\alpha u_z + \partial_z u_\alpha) \bigg) + \rho a_z. \tag{4.173}$$

After further simplification, we get

$$0 = \tau T \partial_z \bigg(\rho(\partial_z u_y) \bigg) \tag{4.174}$$

$$0 = -T\partial_z(\rho) + \rho a_z. \tag{4.175}$$

The density profile obtained from integrating Eq. 4.175 is

$$\ln(\rho) = \frac{a_z}{T} z + c_0, \tag{4.176}$$

or in the exponential form

$$\rho = c_1 \exp\left(\frac{a_z}{T} z \right). \tag{4.177}$$

Substituting 4.177 into Eq. 4.174 and integrating, the velocity comes out to be

$$u_y = \frac{c_2}{c_1} \exp\left(\frac{-a_z}{T} z \right) + c_3. \tag{4.178}$$

To find the integration constants $c_1,\ c_2,\ c_3$, we apply the boundary conditions:

$$u_y(z = 0) = u_b \tag{4.179}$$

$$u_y(z = H) = u_t \tag{4.180}$$

where H is the hight of the channel (distance between the plates), u_b is the velocity of the bottom plate, and u_t is the velocity of the top wall. The final velocity profile has the form of

$$u_y = (u_t - u_b) \left[\frac{1 - e^{-(a_z/T)z}}{1 - e^{-(a_z/T)H}} \right] + u_b. \tag{4.181}$$

In our system, $a_z = -g = -980$ cm/s^2, $\Delta u = u_t - u_b = 2U = 1$ cm/s, $T = 1/6$ cm^2/s^2, and $\rho = 0.001184$ g/cm^3. Fig. 4.6 demonstrates the velocity profiles obtained from analytical solution above as well as the results for the standard LB and our new model. The profiles for the current model, the standard model, and the analytical solution are shown as solid lines, dashed lines, and star points. As can be seen, switching the frame of reference results in a new profile in the standard model and Galilean invariance is broken. On the other hand, the velocity profile remains the same after a change of reference frame for the model proposed in this chapter. The profiles also exactly overlap with the analytical solution.

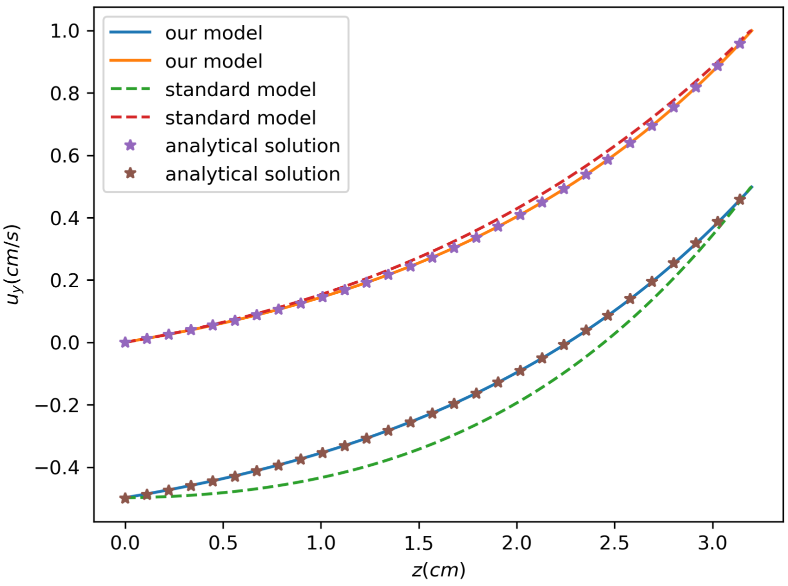

Figure 4.6: The velocity profile obtained from standard LB, our model, and analytical solutions for two types of Couette flow are shown. Our model produces velocity profiles that exactly match the analytical solution (star points) and do not depend on the frame of reference.

4.6 Extension to Viscoelastic Fluids

The proposed LBM in this chapter can be easily extended to thermal and viscoelastic flows. As mentioned earlier in the chapter, the b terms can be interpreted as the microscopic stress tensor. The viscoelasticity then can be included through a constitutive equation and equilibrium values of the b's. A common viscoelastic model is the Oldroyd-B model, originally introduced by Oldroyd in 1950 [356]. The main feature of viscoelastic material is the memory effects and dependence of stress and strain on their past values. This could be accounted for through time derivatives and integrals. However, Oldroyd realized that the basis vectors of the reference frames are also affected by these operations. So to have equations of state that do not depend on the observer's reference frame, Oldroyd suggested using the material reference frame, i.e. the frame that is moving with the material. This methodology was later given the name of "Material Frame Indifference".

The Oldroyd-B model utilizes the upper convected time-derivative, defined as

$$\frac{\delta \boldsymbol{\sigma}}{\delta t} = \frac{D\boldsymbol{\sigma}}{Dt} - \boldsymbol{\sigma} \cdot \nabla \boldsymbol{u} - (\nabla \boldsymbol{u})^T \cdot \boldsymbol{\sigma} \tag{4.182}$$

where D/Dt is the material derivative, and $\varepsilon = \frac{1}{2}(\nabla \boldsymbol{u} + \nabla \boldsymbol{u}^T)$ is the strain rate tensor. The Oldroyd-A model, on the other hand, emerges from the lower convected time-derivative of the stress tensor:

$$\frac{\delta \boldsymbol{\sigma}}{\delta t} = \frac{D\boldsymbol{\sigma}}{Dt} + \boldsymbol{\sigma} \cdot \nabla \boldsymbol{u} + (\nabla \boldsymbol{u})^T \cdot \boldsymbol{\sigma}. \tag{4.183}$$

Then, the constitutive equations for Oldoryd-A and Oldroyd-B are

$$\left(1 + \lambda_x \frac{\delta}{\delta t}\right) \boldsymbol{\sigma} = 2\mu_{\text{eff}} \left(1 + \lambda_d \frac{\delta}{\delta t}\right) \boldsymbol{\varepsilon} \tag{4.184}$$

where for Oldroyd-A, $\delta/\delta t$ is defined by Eq. 4.183 and for Oldroyd-B, $\delta/\delta t$ is defined by Eq. 4.182.In Eq. 4.184, λ_x is the relaxation time, λ_d is the retardation time, and μ_{eff} is an effective viscosity.

The Oldroyd-B model is the more popular model used by the polymer community as it provides more consistent results with experiments. For example, the Weissenberg effect, where fluid rises near the inner cylinder in flow between vertical concentric rotating cylinders, is correctly predicted by the Oldroyd-B model. In contrast, the Oldroyd-A model predicts that the fluid falls near the inner cylinder. In steady simple shear, both models predict a viscosity independent of shear rate and a first normal stress difference quadratic in the shear rate. However, the Oldroyd-B model's second normal stress difference vanishes, while in the Oldroyd-A model, it is negative and equal in magnitude to the first normal stress difference. In uniaxial extensional flow, the extensional viscosity for Oldroyd-B becomes infinite at $\lambda_x \varepsilon = \frac{1}{2}$, whereas for Oldroyd-A, it becomes infinite at $\lambda_x \varepsilon = 1$. These differences underline the importance of selecting the appropriate model based on the physical context and the mathematical representation of the material properties.

Using our model and defining a viscous stress contribution to the stress tensor, one can impose a constitutive equation that has the form of a lower convected Maxwell model on the viscous stress tensor. More detailed investigation of this will be done in future work.

4.6.1 Nanofibers in shear flow: Jeffery's Orbits

The production of fiber-reinforced thermoplastics involves processes performed under flow conditions. Therefore, it is crucial to understand the dynamics of fibers in flow to obtain high quality fiber-reinforced composites. The behaviour of fibers under flow conditions directly impacts the orientation, distribution, and mechanical properties of the final composite materials [357]. Accurate modelling and simulation of fiber dynamics, which take into account factors like fiber-matrix interactions and fiber flexibility, non-uniform stiffness, and surface characteristics, enable better prediction and control of these properties [358]. As mentioned before, the LBM implemented in LAMMPS has the ability to include particles and can be utilized to simulate behaviour of fibers under flow. In this section, we demonstrate this for nanorods in a simple fluid.

Jeffery Orbits Investigation of the dynamics of non-spherical particles in a flow dates back as early as 1922 with Jeffery's work on ellipsoidal particles in a laminar viscous flow [359]. In this theoretical work, Jeffery derived the equations of motion for an ellipsoidal particle in a simple shear flow. For an ellipsoid of aspect ratio $a_r = \frac{\text{length of semi-major axis}}{\text{length of semi-minor axis}}$ in a flow with far-field velocity U, he showed that the angular motion of the ellipsoid can be described by

$$\tan\theta = \frac{C a_r}{\sqrt{a_r^2 \cos\phi + \sin\phi}} \tag{4.185}$$

$$\tan\phi = a_r \tan\left(\frac{2\pi}{T_J} t\right) \tag{4.186}$$

where θ is the angle between the particle's major axis and the vorticity axis, and ϕ is the angle between the projection of the major axis onto the flow plane and the direction of the gradient of the velocity. These angles are shown in a schematic plot in Fig. 4.7(a). The period of the motion T_J is then found to be

$$T_J = \frac{2\pi}{\dot{\gamma}} \left(a_r + \frac{1}{a_r}\right) \tag{4.187}$$

where $\dot{\gamma} = U/H$ is the shear rate and H is the length of the channel (distance between the plates in a Couette flow). The orbit constant C is determined by the initial orientation of the particle. According to Eq. 4.185 and 4.186, the ellipsoid is expected to follow a family of closed loops around the vorticity axis, known as Jeffery orbits. The specific orbit depends on C and the initial orientation of the particle. The existence of such orbits were verified by the experimental work of Trevelyan et al. [360].

Jeffery's work, although groundbreaking, only applied to inertialess ellipsoidal particles and far from any solid boundary. Bretherton showed that Jeffery orbits would describe the motion of any body of revolution if the appropriate "equivalent aspect ratio" is used [361]. Cox studied the total force and torque on a long slender body in a shear flow [362] and found a relationship between the geometric and equivalent aspect ratios such that

$$a_e = \frac{1.24 a_r}{\sqrt{\ln(a_r)}} \tag{4.188}$$

where a_e is the equivalent aspect ratio.

The original Jeffery's model did not account for inertia or confinement effects. Subramanian and Koch conducted a theoretical investigation of motion of a torque-free slender axisymmetric fiber in a simple shear flow [363]. They found that for small Reynolds numbers Re, the fiber slowly drifts towards the flow plane (i.e. $\theta = \pi/2$). Reynolds number Re is a dimensionless number that shows the balance between inertial and viscous forces in a flow [20]. At Re beyond a critical value, the fiber was found to cease rotation and stay close to the shear plane (i.e. $\phi = \pi/2$) and align with the flow direction. Yu and coworkers studied the rotation of a neutrally buoyant spheroid in a Couette flow [364]. They found that increasing the Reynolds number shifts the behaviour of the particle away from the $Re = 0$ limit where the particle follows the Jeffery orbits. They also discovered that the initial orientation can affect the shape of the orbits when inertial effects are strong.

Mao and Alexeev studied the motion of a solid spheroid particle in a simple shear flow using a Lattice Boltzmann-Immersed Boundary method [365]. They particularly examined the individual effects of particle and fluid inertia on the motion of the particle. They found that the total inertial effects can be estimated using superposition of the particle and fluid effects. They also found that increasing Reynolds number results in an increase in the period of rotation. Our algorithm accounts for inertial effects as the MD particles and LB fluid carry a mass. However, the purpose of this section is not to study such effects and to only showcase the capability of our algorithm in incorporating fibers in a fluid. Therefore, we focus on low Reynolds number regimes where the impact of inertia is not strong.

Simulation Details Our simulation is set up with a single nanorod randomly placed in the fluid. The rod, similar to the ones used in chapter 2, consists of 4 threads. This configuration was used in chapter 2 to avoid commensurability between the different components of the melt. In this section, we use the multithreaded configuration as it gives the rods a mesh independent size [355]. The rod initial configuration is generated using the open-source package moltemplate [254]. The geometric aspect ratio of the rod is 7.12 with a diameter equal to 2 μm and a length equal to 14.24 μm.

The simulation box has dimensions of $60\mu\text{m} \times 60\mu\text{m} \times 60\mu\text{m}$. This box size is selected to minimize confinement and finite-size effect while keeping the simulation time reasonable. Periodic boundary

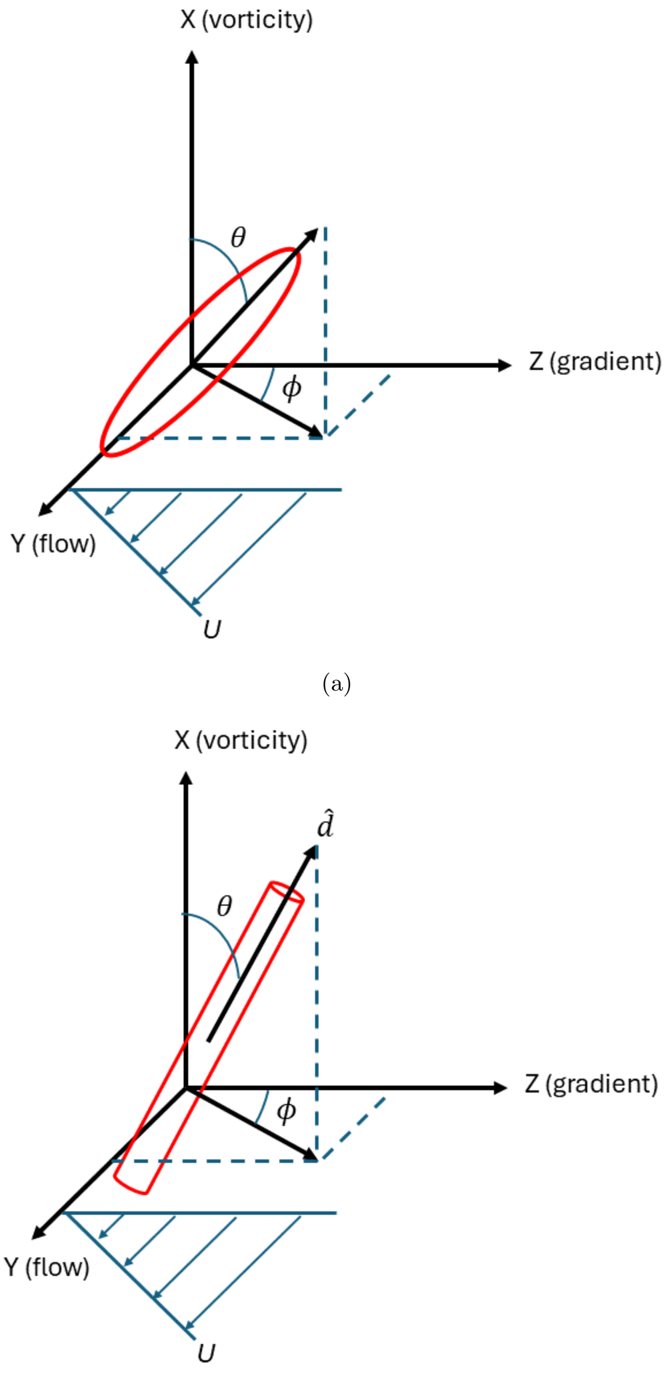

(a)

(b)

Figure 4.7: The geometry and relevant angles for Jeffery's orbits are illustrated for (a) an ellipsoid and (b) a rod. The director of the rod is used as the major axis.

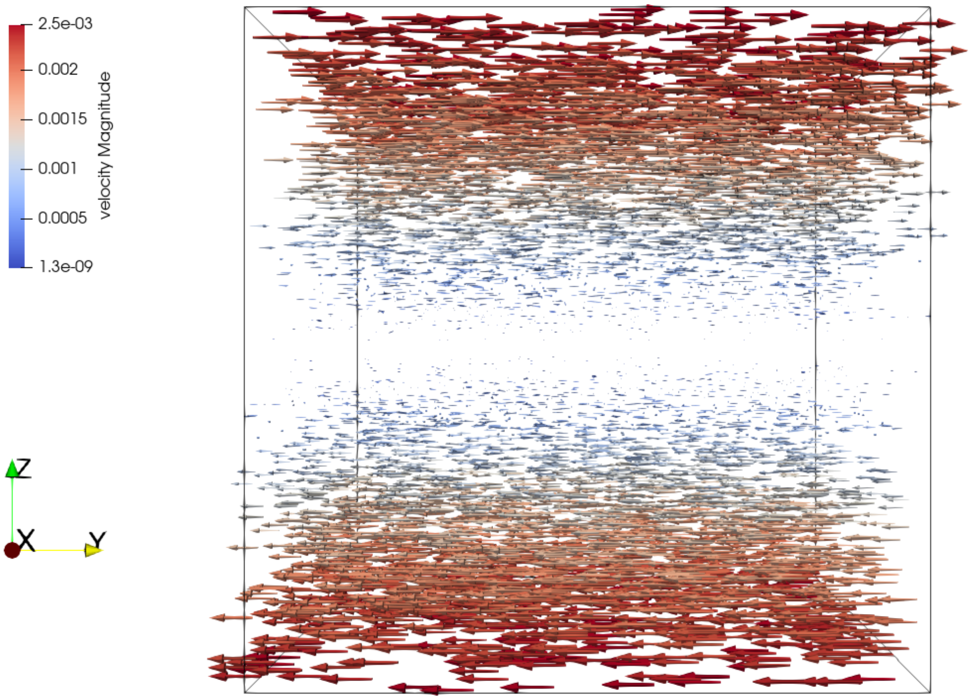

Figure 4.8: The simple shear flow induced by moving the bottom and top walls is illustrated.

conditions are applied in the x and y directions. Two parallel plates with bounce back boundary conditions are used in the z direction. The bottom and top plates move at the same speed $0.0025\mu m/\mu s$ and in the opposite directions in the y direction. The flow field is illustrated in Fig. 4.8.

Results To study the angular motion of the rod, we define angle coordinates similar to those by Jeffery. We use the director $\hat{d}$ of the rod as the major axis as shown in Fig. 4.7(b). θ is angle between the vorticity axis (i.e. X) and the director $\hat{d}$. ϕ is the angle between the projection of the director on to the flow plane (i.e. YZ) and the gradient axis (i.e. Z). Fig. 4.9(a) shows the rod's trajectory. The motion of the rod follows closed loops as predicted by the Jeffery's model. Depending on the initial orientation and orbit constant, the path falls on different orbits. For particles starting in the flow plane, i.e. $C = \infty$, the particle stays in the flow plane and undergoes circular motion.

In Fig. 4.9(b) and (c), we show the evolution of the ϕ and θ. As can be seen, both angles follow a period motion as predicted by Jeffery's model. The period of the oscillation is found to be 1.03s. The equivalent aspect ratio is found to be 6.68μm. This value is slightly higher than predictions based on Cox's equation (Eq. 4.188). This is not unexpected as his model provides an estimation for a long slender rod while our rods are small-sized bead rods with non-negligible thickness.

As demonstrated in this section, our MD-LBM algorithm is capable of simulating systems of fiber/nanorod-fluid and can be utilized to study behaviour of fiber-reinforced polymers.

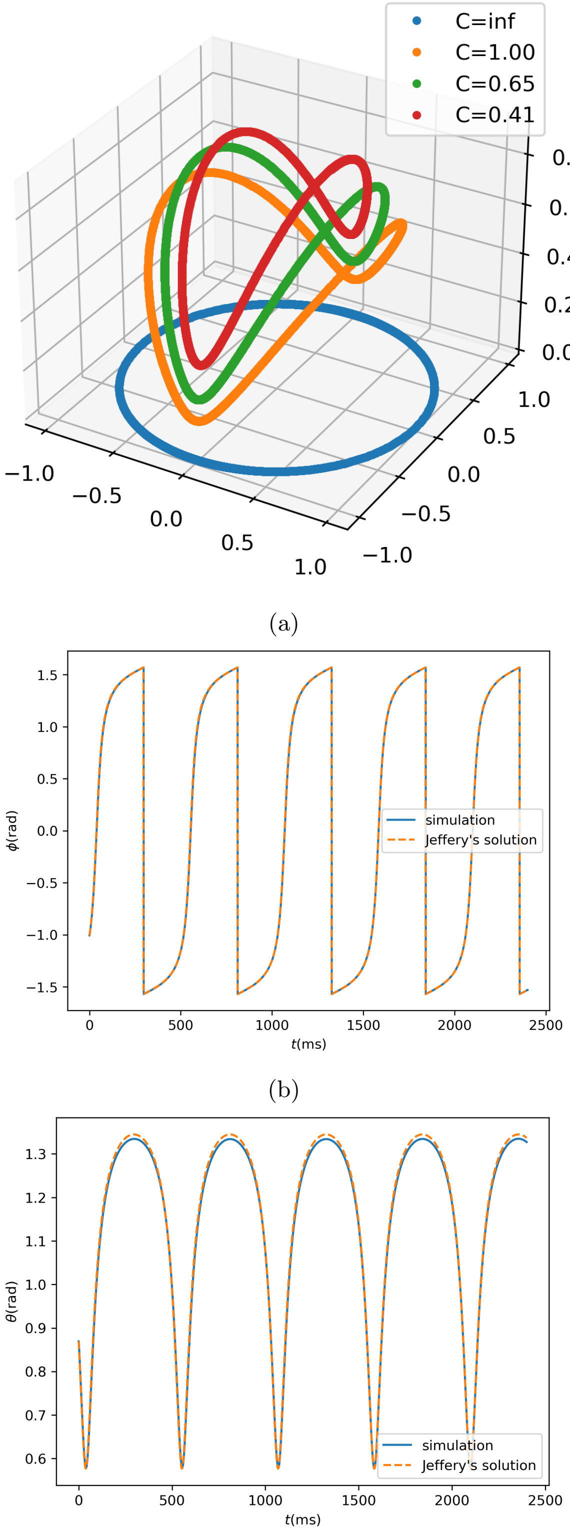

(a)

(b)

(c)

Figure 4.9: The director trajectories for a rod is depicted in (a). Depending on the initial angle (indicated by parameter C), the rod rotates on different trajectories. (b) shows the evolution of the azimuthal angle of the director of the rod and (c) shows the evolution of the polar angle. Our results (blue solid curves) match the orbits obtained from theoretical methods (orange dashed curves)

4.7 Conclusion

In this chapter, we have developed a new Lattice Boltzmann Method. The new model discretizes the particle distribution function using a mass function that has a mean and a variance. This provides enough independent degrees of freedom to be able to match the moments of the discretized distribution with the moments of the Maxwell-Boltzmann distribution. As a result, the hydrodynamic equations generated by the model do not contain the error terms typically present in the standard LBM and are suitable for compressible flows.

The Chapman-Enskog expansion of our LBE recovers the Navier-Stokes equations where the shear viscosity is found to be $\eta = \rho T \tau$ and τ is the relaxation time. We conducted Poiseuille flow simulations at different temperatures and measured the viscosity to confirm this relation. We found that the measured viscosity as a function of temperature creates a line with the slope $\rho\tau$ as expected. Under isothermal conditions that we studied in this work, from the Chapman-Enskog expansion, we expect the secondary viscosity of the fluid to be $\frac{2}{3}\eta$. This was confirmed by analyzing the damping of sound waves in the fluid.

One of the challenges of modelling compressible flows using the standard LBM is the lack of Galilean invariance when there is a density gradient. We showed that our model does not suffer this issue by simulating a Couette flow in the presence of gravity. The velocity profiles obtained from our simulations exactly match the analytical solutions.

The production of fiber-reinforced thermoplastics involves processes performed under flow or press conditions. Therefore, it is crucial to understand the dynamics of fibers in flow or under pressure to obtain high quality fiber-reinforced composites. As an example, we coupled our model with Molecular Dynamics particles and studied the dynamics of nanorods under shear flow. We found that our nanorods follow the Jeffery orbits as expected.

One of the main advantages of the new formulation is that it is generalizable as the equilibrium variance terms (microscopic stress) are set directly by the choice of the equilibrium moments. The work presented here is the first step in creating a Lattice Boltzmann Method (LBM) that can model compressible, thermal, and viscoelastic flows. The impact of processing on the behaviour of nanocomposites then can be studied by including MD particles as demonstrated for simple fluids above.

Chapter 5

Conclusion

One approach to addressing issues like global warming and transportation safety is through lightweighting. This involves replacing materials used in vehicles with lighter alternatives without sacrificing performance. Composite materials, which combine the best properties of different substances, enable the creation of high-performance lightweight materials. However, producing these advanced materials is complex, requiring a thorough understanding of the interactions and assembly of components at various scales, as well as the effects of processing on the final product.

Predictive models are a powerful tool to understand physical systems and advance technology. Predictive models not only can be used to improve current materials, but they also gain fundamental understanding of the underlying processes. There are numerous theoretical and numerical models introduced in the field of polymer composites and nanocomposites. Different methods best describe a system at a specific time and length scale. In the introduction chapter, a survey of available computational and theoretical methods and the state of each field was provided. In this thesis, I utilized coarse-grained Molecular Dynamics, Phase-Field, and Lattice Boltzmann methods to study different aspect of polymer composites and nanocomposites.

In chapter 2, the dispersion and orientation patterns of nanorods in polymer melts with either attractive or repulsive rod-polymer interactions were examined as a function of the rod concentration. The phase behaviour of the nanocomposites was mainly controlled by the interplay of three competing effects: i) entropy of the rods; ii) energetic interactions between the rods and polymers and; iii) entropy of the polymers. We observe when only repulsive interactions were applied between all components, the rods completely phase separate at all rod concentrations whereas the system with attractive polymer-rod interactions does not behave as such. This strongly implicates the role of entropy, in the form of the depletion effect (related to the free volume per particle), as the main driver of phase separation in the system.

The attractive polymer-rod interactions set up a competition between entropic and enthalpic effects (as this is a constant pressure system it is more appropriate to discuss in terms of enthalpy than energy). Since the strength of the enthalpic effects is proportional to the number of rods in the system, the dispersion patterns show direct correlation with the rod concentration. At lower concentrations, entropic processes are dominant and ordered clusters of nanorods are created. However, due to the presence of the attractive forces, the rods do not completely phase separate and polymers interpenetrate between the rods of a cluster. At higher concentrations, the energetic effects become significant and the dispersion of the rods improves with the overall cluster size diminishing with concentration. The polymer interpenetration between the rods is typically referred to as ”polymer bridging” and, at least at very strong polymer-rod interactions, is often argued to create an effective rod-rod attraction leading to the formation of rod clusters. As mentioned above, this does not appear to be the case here as the phase separation seems entirely entropically driven at the strength of polymer-rod interaction we studied.

One interesting question that has not been thoroughly investigated yet is the impact of polymer and rod polydispersity on the phase behaviour of the composite. This is an important question as most polymerization processes produce some level of polydispersity. Moreover, depending on the processing method, the fibers and nanofibers used as enforcement agents could contain some level of size distribution. Our group is currently conducting Molecular Dynamics simulation of polydisperse polymer-nanorod systems to shed light on the impact of polydispersity on dispersion and orientation patterns of polymer nanocomposites.

In chapter 3, we studied the crystallization process of PolyAmide-6 (PA6) and introduced a Multiphase-field model to study heterogeneity in such systems. Physical and mechanical properties of semi-crystalline polymers depend on their degree of crystallization and crystal morphology. Producing semi-crystalline material with desired properties is only possible when the crystallization process and structure is well-understood and can be predicted. In chapter 3, we introduced a multiphase-field method coupled with the Nakamura model and heat conduction equation to model the non-local crystallization of polymeric materials on a microstructural length scale. The multiphase-field base of our model provides an efficient and easy way to track the boundaries of the crystalline areas. This makes it possible to study heterogeneous crystal structures. It also allows for adding any number of phases with different properties making the model a good candidate to study polymer blends and composites. The crystallization inside crystalline areas is controlled by a kinetic model, which was the Nakamura model in this work. The dependency of the crystal growth rate on temperature is added by a Turnbell-Fisher type of equation. The kinetic model and temperature dependency can be adjusted to match the processing conditions and specific materials under study.

We applied our model to pure PA6 and PA6 with fibers. For the pure matrix, lower cooling rates produced more homogeneous structures with larger grains, while higher cooling rates resulted in more heterogeneous structures due to sharper temperature gradients and shorter crystallization times. At lower cooling rates, the initial grain size had minimal impact on final morphology as grains had sufficient time to reach maximum crystallinity. However, the initial number of grains significantly influenced morphology. At higher cooling rates, both the initial grain size and number significantly affected the final structure.

In the presence of carbon fibers, we observed more homogeneous morphology around the fibers due to higher initial crystal grain volume fraction and the high thermal conductivity of the fibers. This resulted in similar cooling rates and crystallization times for grains near the fiber surface, with rapid heat transfer from the region. The higher initial volume fraction meant simultaneous crystallization in most regions, leading to homogeneity. Additionally, crystalline grains grew perpendicular to the fiber surface, reflecting geometrical constraints on interfacial grains.

Overall, our model’s results align qualitatively with experiments, but further understanding of coarse-grained crystal grains, their relation to spherulites, and detailed knowledge of initial nuclei density is needed for better quantitative agreement with experiments. Choosing the right kinetic model and parameters play an important role and requires further investigation as well. The current model does not include any mechanical elements. Future work will be dedicated to including mechanical properties in the multiphase-field model to examine the impact of crystal morphology on such properties.

In chapter 4, we have developed a new Lattice Boltzmann Method. The new model discretizes the particle distribution function using a mass function that has a variance in addition to a mean value. This provides enough independent degrees of freedom to be able to match the moments of the discretized distribution with the moments of the Maxwell-Boltzmann distribution. As a result, the hydrodynamic equations generated by the model do not contain the error terms, present in the standard LBM, making the model suitable for compressible flows.

As demonstrated above, our model is capable of simulating fluids at different temperatures. It was also shown that the expected hydrodynamic equations from the Chapman-Enskog expansion were recovered. And last but not least, we showed that our model is Galilean invariant under all conditions including in the presence of a density gradient.

The natural next step is to expand the developed LBM to viscoelastic fluids as outlined in the chapter.

Appendix A

A.1 Equilibration

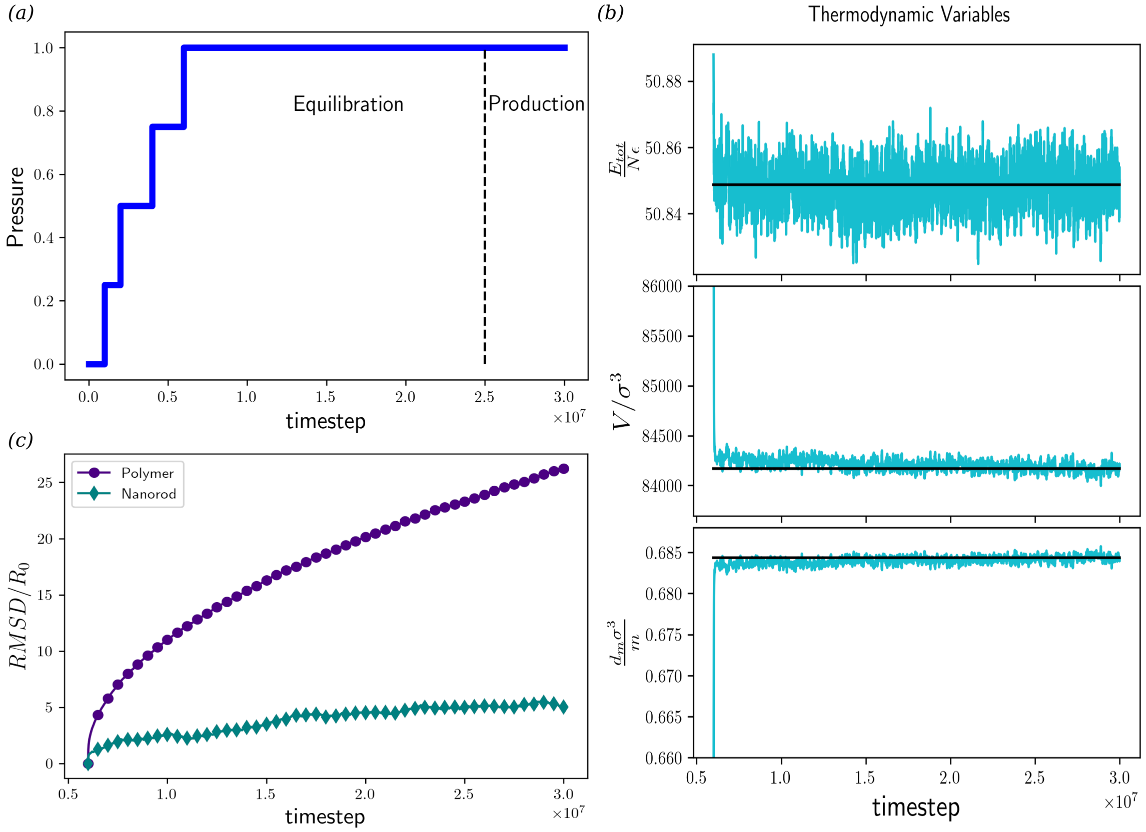

Figure A.1: Equilibration procedure is schematically shown in (a). Thermodynamic parameters (b) and RMSD (c) are shown for the system at $\phi_c = 0.44$ and all-repulsive interactions. The thermodynamic properties plateau for the last 5×10^6 steps which shows that the system is properly equilibrated. Both the polymers and the rods move a considerable distance during the equilibration process which shows that the system is not trapped in a kinetically favourable state.

The equilibration of the all-repulsive system, like the original simulations, consists of 5 stages:

1. 10^6 steps of NVT at $T = 1.0$ and low packing density

2. 10^6 steps of NPT at $T = 1.0$ and $P = 0.25$

3. 2×10^6 steps of NPT at $T = 1.0$ and $P = 0.5$
4. 2×10^6 steps of NPT at $T = 1.0$ and $P = .75$
5. 14×10^6 (or 24×10^6 for $\phi_c = 0.44$) steps of NPT at $T = 1.0$ and $P = 1.0$

The final pressure is chosen to achieve a system with a melt-like packing density of $0.3 \leq d_p \leq 0.5$. The analysis is done based on the last 5×10^6 steps (production). The reported results are averaged over at least 11 uncorrelated configurations for each realization. Fig. A.1 presents the thermodynamic and the particle Root-Mean-Squared-Displacement (RMSD) for an all-repulsive system at the highest concentration $\phi_c = 0.44$. As can be seen, the thermodynamic parameters are reasonably constant and stable for the last 5×10^6 timesteps which shows that the system has at least reached a steady state. The RMSD for both the polymers and the rods takes values of a several times the average radius of gyration of polymers in pure melt R_0 implying that the system is not stuck in a local minimum and is truly equilibrated.

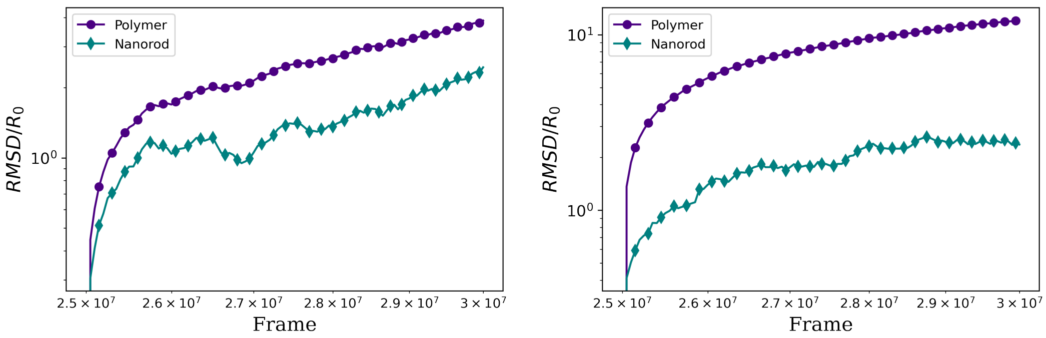

(a) (b)

Figure A.2: The Root-Mean-Squared-Displacement of the centre of mass for the attractive (a) and repulsive (b) cases are shown.

The RMSD's shown in Fig. 2.2 and A.1 are particle RMSD and take into account the rotational motion of the molecules. We also track the RMSD of centre of mass (COM) of the molecules to further ensure that the nanorods and the polymers move at least a couple of R_0 before production. We show the RMSD of COM for the polymers and the nanorods in Fig. A.2 (a) for the original system and in Fig. A.2 (b) for the all-repulsive system.

References

[1] *Bakelite: First Synthetic Plastic - National Historic Chemical Landmark*, `https://archive.ph/20120722150229/http://portal.acs.org/portal/PublicWebSite/education/whatischemistry/landmarks/bakelite/index.htm%5C#selection-517.461-517.479` (visited on 07/08/2023).

[2] H. Frey and T. Johann, "Celebrating 100 years of "polymer science": Hermann Staudinger's 1920 manifesto", Polymer Chemistry **11**, 8–14 (2019).

[3] J. Karger-Kocsis, H. Mahmood, and A. Pegoretti, "Recent advances in fiber/matrix interphase engineering for polymer composites", Progress in Materials Science **73**, 1–43 (2015).

[4] M. F. Ashby and Y. J. M. Bréchet, "Designing hybrid materials", Acta Materialia **51**, 5801–5821 (2003).

[5] S. C. Glotzer and W. Paul, "Molecular and mesoscale simulation methods for polymer materials", Annual Review of Materials Science **32**, 401–436 (2002).

[6] *Finite element method*, `https://en.wikipedia.org/wiki/Finite_element_method` (visited on 08/10/2024).

[7] M. Born and R. Oppenheimer, "Zur Quantentheorie der Molekeln", Annalen der Physik **389**, 457–484 (1927).

[8] H. Sun, "COMPASS: An ab Initio Force-Field Optimized for Condensed-Phase ApplicationssOverview with Details on Alkane and Benzene Compounds", Journal of Physical Chemistry B **102**, 7338–7364 (1998).

[9] M. E. Tuckerman, "Ab initio molecular dynamics: basic concepts, current trends and novel applications", J. Phys.: Condens. Matter **14** (2002).

[10] D. Marx and J. Hutter, *Ab Initio Molecular Dynamics* (Cambridge University Press, Cambridge, MA, US, 2009).

[11] J. Jin, A. J. Pak, A. E. P. Durumeric, T. D. Loose, and G. A. Voth, "Bottom-up Coarse-Graining: Principles and Perspectives", Journal of Chemical Theory and Computation **18**, 5759–5791 (2022).

[12] M. E. Tuckerman, *Statistical Mechanics: Theory and Molecular Simulation*, First, Oxford Graduate Texts (Oxford University Press, Oxford, New York, 2010).

[13] N. Metropolis and S. Ulam, "The Monte Carlo Method", Journal of the American Statistical Association **44**, 335–341 (1949).

[14]N. Metropolis, A. W. Rosenbluth, M. N. Rosenbluth, A. H. Teller, and E. Teller, "Equation of State Calculations by Fast Computing Machines", The Journal of Chemical Physics **21**, 1087–1092 (1953).

[15]M. Kalos and P. Whitlock, *Monte Carlo Methods* (Wiley, Weinheim, Germany, 2009).

[16]M. Allen and D. Tildesley, *Computer Simulation of Liquids* (OUP Oxford, Oxford, England, 2017).

[17]P. Español and P. Warren, "Statistical Mechanics of Dissipative Particle Dynamics", Europhysics Letters (EPL) **30**, 191–196 (1995).

[18]H. B. Callen and T. A. Welton, "Irreversibility and Generalized Noise", Physical Review **83**, 34–40 (1951).

[19]R. Kubo, "The fluctuation-dissipation theorem", Reports on Progress in Physics **29**, 255–284 (1966).

[20]T. Krüger, H. Kusumaatmaja, A. Kuzmin, O. Shardt, G. Silva, and E. Viggen, *The lattice boltzmann method: Principles and practice*, Graduate Texts in Physics (Springer International Publishing, Switzerland, 2016).

[21]X. He and L. S. Luo, "Theory of the lattice Boltzmann method: From the Boltzmann equation to the lattice Boltzmann equation", Physical Review E - Statistical Physics, Plasmas, Fluids, and Related Interdisciplinary Topics **55**, 6811–6820 (1997).

[22]M. Kardar, *Statistical physics of particles* (Cambridge University Press, Cambridge, MA, US, 2007).

[23]L. Pareschi and G. Russo, "Numerical Solution of the Boltzmann Equation I: Spectrally Accurate Approximation of the Collision Operator", SIAM Journal on Numerical Analysis **37**, 1217–1245 (2000).

[24]I. M. Gamba, J. R. Haack, C. D. Hauck, and J. Hu, "A Fast Spectral Method for the Boltzmann Collision Operator with General Collision Kernels", SIAM Journal on Scientific Computing **39**, B658–B674 (2017).

[25]P. L. Bhatnagar, E. P. Gross, and M. Krook, "A model for collision processes in gases. I. Small amplitude processes in charged and neutral one-component systems", Physical Review **94**, 511–525 (1954).

[26]A. Wagner, "Theory and Applications of the Lattice Boltzmann Method", PhD thesis (University of Oxford, 1997).

[27]C. K. Aidun and Y. Lu, "Lattice Boltzmann simulation of solid particles suspended in fluid", Journal of Statistical Physics **81**, 49–61 (1995).

[28]S. Changizrezaei and C. Denniston, "Photonic band structure of diamond colloidal crystals in a cholesteric liquid crystal", Physical Review E **96**, 32702 (2017).

[29]O. Malaspinas, N. Fiétier, and M. Deville, "Lattice Boltzmann method for the simulation of viscoelastic fluid flows", Journal of Non-Newtonian Fluid Mechanics **165**, 1637–1653 (2010).

[30]P. C. Hohenberg and B. I. Halperin, "Theory of dynamic critical phenomena", Reviews of Modern Physics **49**, 435–479 (1977).

[31] J. D. Van Der Waals, “The thermodynamic theory of capillarity under the hypothesis of a continuous variation of density”, Journal of Statistical Physics **20**, 200–244 (1979).

[32] J. W. Cahn and J. E. Hilliard, “Free Energy of a Nonuniform System. I. Interfacial Free Energy”, The Journal of Chemical Physics **28**, 258–267 (1958).

[33] J. S. Langer, “Models of pattern formation in first-order phase transitions”, in *Directions in Condensed Matter Physics*, Vol. Volume 1, Series on Directions in Condensed Matter Physics (WORLD SCIENTIFIC, Aug. 1986), pp. 165–186.

[34] S. M. Allen and J. W. Cahn, “A microscopic theory for antiphase boundary motion and its application to antiphase domain coarsening”, Acta Metallurgica **27**, 1085–1095 (1979).

[35] B. Nestler, H. Garcke, and B. Stinner, “Multicomponent alloy solidification: Phase-field modeling and simulations”, Physical Review E **71**, 041609 (2005).

[36] K. Janssens, D. Raabe, E. Kozeschnik, M. Miodownik, and B. Nestler, *Computational materials engineering: An introduction to microstructure evolution* (Elsevier Science, Amsterdam, Netherlands, 2010).

[37] N. Moelans, B. Blanpain, and P. Wollants, “An introduction to phase-field modeling of microstructure evolution”, Calphad **32**, 268–294 (2008).

[38] L. Q. Chen, “Phase-field models for microstructure evolution”, Annual Review of Materials Science **32**, 113–140 (2002).

[39] I. Steinbach, F. Pezzolla, B. Nestler, M. Seeßelberg, R. Prieler, G. Schmitz, and J. Rezende, “A phase field concept for multiphase systems”, Physica D: Nonlinear Phenomena **94**, 135–147 (1996).

[40] J. Tiaden, B. Nestler, H. J. Diepers, and I. Steinbach, “The multiphase-field model with an integrated concept for modelling solute diffusion”, Physica D: Nonlinear Phenomena **115**, 73–86 (1998).

[41] B. Stinner, B. Nestler, and H. Garcke, “A Diffuse Interface Model for Alloys with Multiple Components and Phases”, SIAM Journal on Applied Mathematics **64**, 775–799 (2004).

[42] C. Herrmann, E. Schoof, D. Schneider, F. Schwab, A. Reiter, M. Selzer, and B. Nestler, “Multiphase-field model of small strain elasto-plasticity according to the mechanical jump conditions”, Computational Mechanics **62**, 1399–1412 (2018).

[43] H. Goldstein, C. Poole, and J. Safko, *Classical mechanics* (Addison Wesley, San Francisco, CA, US, 2002).

[44] D. W. Oxtoby, “Density Functional Methods in the Statistical Mechanics of Materials”, Annual Review of Materials Research **32**, 39–52 (2002).

[45] J. Wu, “Density functional theory for chemical engineering: From capillarity to soft materials”, AIChE Journal **52**, 1169–1193 (2006).

[46] C. Ebner, W. F. Saam, and D. Stroud, “Density-functional theory of simple classical fluids. I. Surfaces”, Physical Review A **14**, 2264–2273 (1976).

[47] H. Graf and H. Löwen, “Density functional theory for hard spherocylinders: phase transitions in the bulk and in the presence of external fields”, Journal of Physics: Condensed Matter **11**, 1435 (1999).

[48]W. E. McMullen and K. F. Freed, “A density functional theory of polymer phase transitions and interfaces”, The Journal of Chemical Physics **92**, 1413–1426 (1990).

[49]L. M. Hall, A. Jayaraman, and K. S. Schweizer, “Molecular theories of polymer nanocomposites”, Current Opinion in Solid State and Materials Science **14**, 38–48 (2010).

[50]V. Ganesan and A. Jayaraman, “Theory and simulation studies of effective interactions, phase behavior and morphology in polymer nanocomposites”, Soft Matter **10**, 13–38 (2014).

[51]L. J. D. Frink and A. L. Frischknecht, “Density functional theory approach for coarse-grained lipid bilayers”, Physical Review E **72**, 041923 (2005).

[52]J. Hansen and I. McDonald, *Theory of simple liquids: with applications to soft matter* (Elsevier Science, Oxford, England, 2013).

[53]D. Henderson, *Fundamentals of inhomogeneous fluids* (Taylor & Francis, New York, US, 1992).

[54]C. P. Emborsky, Z. Feng, K. R. Cox, and W. G. Chapman, “Recent advances in classical density functional theory for associating and polyatomic molecules”, Fluid Phase Equilibria, 20 Years of the SAFT Equation of State **306**, 15–30 (2011).

[55]D. Chandler, J. D. McCoy, and S. J. Singer, “Density functional theory of nonuniform polyatomic systems. I. General formulation”, The Journal of Chemical Physics **85**, 5971–5976 (1986).

[56]H. C. Andersen and D. Chandler, “Optimized Cluster Expansions for Classical Fluids. I. General Theory and Variational Formulation of the Mean Spherical Model and Hard Sphere Percus-Yevick Equations”, The Journal of Chemical Physics **57**, 1918–1929 (1972).

[57]D. Chandler and H. C. Andersen, “Optimized Cluster Expansions for Classical Fluids. II. Theory of Molecular Liquids”, The Journal of Chemical Physics **57**, 1930–1937 (1972).

[58]J. G. Curro and K. S. Schweizer, “Theory of polymer melts: an integral equation approach”, Macromolecules **20**, 1928–1934 (1987).

[59]K. S. Schweizer and J. G. Curro, “PRISM theory of the structure, thermodynamics, and phase transitions of polymer liquids and alloys”, in *Atomistic Modeling of Physical Properties*, edited by L. Monnerie and U. W. Suter, Advances in Polymer Science (Springer, Berlin, Heidelberg, 1994), pp. 319–377.

[60]T. B. Martin, T. E. I. Gartner, R. L. Jones, C. R. Snyder, and A. Jayaraman, “pyPRISM: A Computational Tool for Liquid-State Theory Calculations of Macromolecular Materials”, Macromolecules **51**, 2906–2922 (2018).

[61]K. S. Schweizer and A. Yethiraj, “Polymer reference interaction site model theory: New molecular closures for phase separating fluids and alloys”, The Journal of Chemical Physics **98**, 9053–9079 (1993).

[62]J. B. Hooper, K. S. Schweizer, T. G. Desai, R. Koshy, and P. Keblinski, “Structure, surface excess and effective interactions in polymer nanocomposite melts and concentrated solutions”, Journal of Chemical Physics **121**, 6986–6997 (2004).

[63]J. B. Hooper and K. S. Schweizer, “Contact aggregation, bridging, and steric stabilization in dense polymer-particle mixtures”, Macromolecules **38**, 8858–8869 (2005).

[64]J. B. Hooper and K. S. Schweizer, “Theory of phase separation in polymer nanocomposites”, Macromolecules **39**, 5133–5142 (2006).

[65]L. M. Hall and K. S. Schweizer, “Many body effects on the phase separation and structure of dense polymer-particle melts”, Journal of Chemical Physics **128**, 234901 (2008).

[66]Y. Zhou and K. S. Schweizer, “PRISM Theory of Local Structure and Phase Behavior of Dense Polymer Nanocomposites: Improved Closure Approximation and Comparison with Simulation”, Macromolecules **53**, 9962–9972 (2020).

[67]A. Jayaraman and K. S. Schweizer, “Structure and assembly of dense solutions and melts of single tethered nanoparticles”, The Journal of Chemical Physics **128**, 164904 (2008).

[68]A. Jayaraman and K. S. Schweizer, “Effect of the Number and Placement of Polymer Tethers on the Structure of Concentrated Solutions and Melts of Hybrid Nanoparticles”, Langmuir **24**, 11119–11130 (2008).

[69]A. Jayaraman and K. S. Schweizer, “Effective Interactions, Structure, and Phase Behavior of Lightly Tethered Nanoparticles in Polymer Melts”, Macromolecules **41**, 9430–9438 (2008).

[70]A. Jayaraman and K. S. Schweizer, “Effective Interactions and Self-Assembly of Hybrid Polymer Grafted Nanoparticles in a Homopolymer Matrix”, Macromolecules **42**, 8423–8434 (2009).

[71]K. S. Schweizer, K. G. Honnell, and J. G. Curro, “Reference interaction site model theory of polymeric liquids: Self-consistent formulation and nonideality effects in dense solutions and melts”, The Journal of Chemical Physics **96**, 3211–3225 (1992).

[72]J. Melenkevitz, K. S. Schweizer, and J. G. Curro, “Self-consistent integral equation theory for the equilibrium properties of polymer solutions”, Macromolecules **26**, 6190–6196 (1993).

[73]A. Yethiraj and K. S. Schweizer, “Self-consistent polymer integral equation theory: Comparisons with Monte Carlo simulations and alternative closure approximations”, The Journal of Chemical Physics **97**, 1455–1464 (1992).

[74]M. Pütz, J. G. Curro, and G. S. Grest, “Self-consistent integral equation theory for polyolefins: Comparison to molecular dynamics simulations and x-ray scattering”, The Journal of Chemical Physics **114**, 2847–2860 (2001).

[75]N. Nair and A. Jayaraman, “Self-Consistent PRISM Theory-Monte Carlo Simulation Studies of Copolymer Grafted Nanoparticles in a Homopolymer Matrix”, Macromolecules **43**, 8251–8263 (2010).

[76]A. Jayaraman and N. Nair, “Integrating PRISM theory and Monte Carlo simulation to study polymer-functionalised particles and polymer nanocomposites”, Molecular Simulation **38**, 751–761 (2012).

[77]G. Fredrickson, *The equilibrium theory of inhomogeneous polymers*, International Series of Monographs on Physics (OUP Oxford, New York, US, 2006).

[78]F. Schmid, “Self-consistent-field theories for complex fluids”, Journal of Physics: Condensed Matter **10**, 8105 (1998).

[79]K. F. Freed, “Interrelation between density functional and self-consistent-field formulations for inhomogeneous polymer systems”, The Journal of Chemical Physics **103**, 3230–3239 (1995).

[80]M. W. Matsen, “The standard Gaussian model for block copolymer melts”, Journal of Physics: Condensed Matter **14**, R21–R47 (2002).

[81]M. W. Matsen, “Field theoretic approach for block polymer melts: SCFT and FTS”, The Journal of Chemical Physics **152**, 110901 (2020).

[82]Q. H. Zeng, A. B. Yu, and G. Q. Lu, “Multiscale modeling and simulation of polymer nanocomposites”, Progress in Polymer Science **33**, 191–269 (2008).

[83]T. Böhlke, F. Henning, A. Hrymak, L. Kärger, K. Weidenmann, and J. Wood, *Continuous–Discontinuous fiber-reinforced polymers: An integrated engineering approach* (Carl Hanser Verlag GmbH & Company KG, Cincinnati, OH, US, 2019).

[84]G. Pal and S. Kumar, “Modeling of carbon nanotubes and carbon nanotube-polymer composites”, Progress in Aerospace Sciences **80**, 33–58 (2016).

[85]L. Kehrer, P. Pinter, and T. Böhlke, “Mean field homogenization and experimental investigation of short and long fiber reinforced polymers”, PAMM **16**, 531–532 (2016).

[86]L. Kehrer, P. Pinter, and T. Böhlke, “Mean and full field homogenization of artificial long fiber reinforced thermoset polymers”, PAMM **17**, 603–604 (2017).

[87]B. Raju, S. R. Hiremath, and D. Roy Mahapatra, “A review of micromechanics based models for effective elastic properties of reinforced polymer matrix composites”, Composite Structures **204**, 607–619 (2018).

[88]K. tak Lau, C. Gu, and D. Hui, “A critical review on nanotube and nanotube/nanoclay related polymer composite materials”, Composites Part B: Engineering **37**, 425–436 (2006).

[89]A. Karatrantos, N. Clarke, and M. Kröger, “Modeling of polymer structure and conformations in polymer nanocomposites from atomistic to mesoscale: A review”, Polymer Reviews **56**, 385–428 (2016).

[90]J. Zhao, L. Wu, C. Zhan, Q. Shao, Z. Guo, and L. Zhang, “Overview of polymer nanocomposites: Computer simulation understanding of physical properties”, Polymer **133**, 272–287 (2017).

[91]G. G. Vogiatzis and D. N. Theodorou, “Multiscale Molecular Simulations of Polymer-Matrix Nanocomposites: or What Molecular Simulations Have Taught us About the Fascinating Nanoworld”, Archives of Computational Methods in Engineering **25**, 591–645 (2018).

[92]J. Moon, S. Yang, and M. Cho, “Interfacial strengthening between graphene and polymer through Stone-Thrower-Wales defects: Ab initio and molecular dynamics simulations”, Carbon **118**, 66–77 (2017).

[93]V. Bala, S. K. Tripathi, and R. Kumar, “Optical properties of Ga and in doped CdS nanocomposites: An experimental and first principles study”, Materials Letters **149**, 18–21 (2015).

[94]F. Sheng, C. Xu, Z. Jin, J. Guo, S. Fang, Z. Shi, and J. Wang, “Simulation on Field Enhanced Electron Transfer between the Interface of ZnO–Ag Nanocomposite”, The Journal of Physical Chemistry C **117**, 18627–18633 (2013).

[95]K. Mylvaganam and L. Zhang, “Fabrication of Graphene–Polymer Nanocomposites Through Ionic Polymerization”, The Journal of Physical Chemistry A **120**, 7689–7693 (2016).

[96]F. K. Schwab and C. Denniston, “Reaction and characterisation of a two-stage thermoset using molecular dynamics”, Polymer Chemistry **10**, 4413–4427 (2019).

[97]L. Schöller, B. Nestler, and C. Denniston, “Modeling of a two-stage polymerization considering glass fibre sizing using molecular dynamics”, Nanoscale Advances **5**, 106–118 (2023).

[98] G. Milano, G. Santangelo, F. Ragone, L. Cavallo, and A. Di Matteo, "Gold Nanoparticle/Polymer Interfaces: All Atom Structures from Molecular Dynamics Simulations", The Journal of Physical Chemistry C **115**, 15154–15163 (2011).

[99] T. V. M. Ndoro, E. Voyiatzis, A. Ghanbari, D. N. Theodorou, M. C. Böhm, and F. Müller-Plathe, "Interface of Grafted and Ungrafted Silica Nanoparticles with a Polystyrene Matrix: Atomistic Molecular Dynamics Simulations", Macromolecules **44**, 2316–2327 (2011).

[100] F. W. Starr, T. B. Schrøder, and S. C. Glotzer, "Molecular dynamics simulation of a polymer melt with a nanoscopic particle", Macromolecules **35**, 4481–4492 (2002).

[101] J. Liu, Y. Wu, J. Shen, Y. Gao, L. Zhang, and D. Cao, "Polymer – nanoparticle interfacial behavior revisited: A molecular dynamics study", Physical Chemistry Chemical Physics **13**, 13058–13069 (2011).

[102] L. Chen, K. Zheng, X. Tian, K. Hu, R. Wang, C. Liu, Y. Li, and P. Cui, "Double Glass Transitions and Interfacial Immobilized Layer in in-Situ-Synthesized Poly(vinyl alcohol)/Silica Nanocomposites", Macromolecules **43**, 1076–1082 (2010).

[103] J. S. Smith, D. Bedrov, and G. D. Smith, "A molecular dynamics simulation study of nanoparticle interactions in a model polymer-nanoparticle composite", Composites Science and Technology, Modeling and Characterization of Nanostructured Materials **63**, 1599–1605 (2003).

[104] G. N. Toepperwein, N. C. Karayiannis, R. A. Riggleman, M. Kröger, and J. J. De Pablo, "Influence of nanorod inclusions on structure and primitive path network of polymer nanocomposites at equilibrium and under deformation", Macromolecules **44**, 1034–1045 (2011).

[105] S. K. Sukumaran, G. S. Grest, K. Kremer, and R. Everaers, "Identifying the primitive path mesh in entangled polymer liquids", Journal of Polymer Science Part B: Polymer Physics **43**, 917–933 (2005).

[106] Y. Gao, J. Liu, J. Shen, L. Zhang, and D. Cao, "Molecular dynamics simulation of dispersion and aggregation kinetics of nanorods in polymer nanocomposites", Polymer **55**, 1273–1281 (2014).

[107] S. Lu, Z. Wu, and A. Jayaraman, "Molecular Modeling and Simulation of Polymer Nanocomposites with Nanorod Fillers", Journal of Physical Chemistry B, `10.1021/acs.jpcb.1c00097` (2021).

[108] X. Li, B. Huang, J. Liu, X. Hu, and Z.-J. Zheng, "Revealing the reinforcing effect of a nanorod network on a polymer matrix through molecular dynamics simulations", Physical Chemistry Chemical Physics **25**, 18757–18765 (2023).

[109] P. G. Bolhuis, A. Stroobants, D. Frenkel, and H. N. Lekkerkerker, "Numerical study of the phase behavior of rodlike colloids with attractive interactions", Journal of Chemical Physics **107**, 1551–1564 (1997).

[110] M. Dijkstra, J. M. Brader, and R. Evans, "Phase behaviour and structure of model colloid-polymer mixtures", Journal of Physics Condensed Matter **11**, 10079–10106 (1999).

[111] M. Vacatello, "Monte Carlo Simulations of Polymer Melts Filled with Solid Nanoparticles", Macromolecules **34**, 1946–1952 (2001).

[112] M. Vacatello, "Chain dimensions in filled polymers: An intriguing problem", Macromolecules **35**, 8191–8193 (2002).

[113] P. G. Bolhuis, E. J. Meijer, and A. A. Louis, "Colloid-Polymer Mixtures in the Protein Limit", Physical Review Letters **90**, 4 (2003).

[114] Q. W. Yuan, A. Kloczkowski, J. E. Mark, and M. A. Sharaf, "Simulations on the reinforcement of poly(dimethylsiloxane) elastomers by randomly distributed filler particles", Journal of Polymer Science Part B: Polymer Physics **34**, 1647–1657 (1996).

[115] Q. Zhang and L. A. Archer, "Monte Carlo simulation of structure and nanoscale interactions in polymer nanocomposites", The Journal of Chemical Physics **121**, 10814–10824 (2004).

[116] K. C. Daoulas, V. A. Harmandaris, and V. G. Mavrantzas, "Detailed Atomistic Simulation of a Polymer Melt/Solid Interface: Structure, Density, and Conformation of a Thin Film of Polyethylene Melt Adsorbed on Graphite", Macromolecules **38**, 5780–5795 (2005).

[117] M. S. Ozmusul, C. R. Picu, S. S. Sternstein, and S. K. Kumar, "Lattice Monte Carlo simulations of chain conformations in polymer nanocomposites", Macromolecules **38**, 4495–4500 (2005).

[118] X.-W. Huang, Y. Peng, and J.-H. Huang, "Universal behaviors of polymer conformations in crowded environment", Colloid and Polymer Science **296**, 689–696 (2018).

[119] M. Vacatello, "Predicting the Molecular Arrangements in Polymer-Based Nanocomposites", Macromolecular Theory and Simulations **12**, 86–91 (2003).

[120] Y. Termonia, "Monte-Carlo modeling of dense polymer melts near nanoparticles", Polymer **50**, 1062–1066 (2009).

[121] J. C. Owicki and H. A. Scheraga, "Preferential sampling near solutes in monte carlo calculations on dilute solutions", Chemical Physics Letters **47**, 600–602 (1977).

[122] Y. N. Pandey and M. Doxastakis, "Detailed atomistic Monte Carlo simulations of a polymer melt on a solid surface and around a nanoparticle", Journal of Chemical Physics **136**, 094901 (2012).

[123] J. M. Scheutjens and G. J. Fleer, "Statistical theory of the adsorption of interacting chain molecules. 2. Train, loop, and tail size distribution", Journal of Physical Chemistry **84**, 178–190 (1980).

[124] S. V. Savenko and M. Dijkstra, "Phase behavior of a suspension of colloidal hard rods and nonadsorbing polymer", Journal of Chemical Physics **124**, 244909 (2006).

[125] G. Jiang, M. J. A. Hore, S. Gam, and R. J. Composto, "Gold Nanorods Dispersed in Homopolymer Films: Optical Properties Controlled by Self-Assembly and Percolation of Nanorods", ACS Nano **6**, 1578–1588 (2012).

[126] K. P. Santo and A. V. Neimark, "Dissipative particle dynamics simulations in colloid and Interface science: a review", Advances in Colloid and Interface Science **298**, 102545 (2021).

[127] Y. Kong, C. W. Manke, W. G. Madden, and A. G. Schlijper, "Simulation of a confined polymer in solution using the dissipative particle dynamics method", International Journal of Thermophysics **15**, 1093–1101 (1994).

[128] V. Pryamitsyn and V. Ganesan, "Strong Segregation Theory of Block Copolymer-Nanoparticle Composites", Macromolecules **39**, 8499–8510 (2006).

[129] G. Scocchi, P. Posocco, A. Danani, S. Pricl, and M. Fermeglia, "To the nanoscale, and beyond!. Multiscale molecular modeling of polymer-clay nanocomposites", Fluid Phase Equilibria **261**, 366–374 (2007).

[130] A. Gooneie and R. Hufenus, “Polymeric Solvation Shells around Nanotubes: Mesoscopic Simulation of Interfaces in Nanochannels”, Macromolecules **52**, 8803–8813 (2019).

[131] Y.-L. Lin, C.-S. Chiou, S. K. Kumar, J.-J. Lin, Y.-J. Sheng, and H.-K. Tsao, “Self-Assembled Superstructures of Polymer-Grafted Nanoparticles: Effects of Particle Shape and Matrix Polymer”, The Journal of Physical Chemistry C **115**, 5566–5577 (2011).

[132] S. Khani, S. Jamali, A. Boromand, M. J. A. Hore, and J. Maia, “Polymer-mediated nanorod self-assembly predicted by dissipative particle dynamics simulations”, Soft Matter **11**, 6881–6892 (2015).

[133] N. Patel and S. A. Egorov, “Interactions between colloidal particles in polymer solutions: A density functional theory study”, The Journal of Chemical Physics **121**, 4987–4997 (2004).

[134] N. Patel and S. A. Egorov, “Interactions between nanocolloidal particles in polymer solutions: Effect of attractive interactions”, Journal of Chemical Physics **123**, 144916 (2005).

[135] X. Chen, J. Cai, H. Liu, and Y. Hu, “Depletion interaction in colloid/polymer mixtures: application of density functional theory”, Molecular Simulation **32**, 877–885 (2006).

[136] A. L. Frischknecht and A. Yethiraj, “Two- and three-body interactions among nanoparticles in a polymer melt”, Journal of Chemical Physics **134**, 174901 (2011).

[137] Z. Shou, G. A. Buxton, and A. C. Balazs, “Predicting the self-assembled morphology and mechanical properties of mixtures of diblocks and rod-like nanoparticles”, Composite Interfaces **10**, 343–368 (2003).

[138] P. Bryk, “Density functional theory and demixing of binary hard-rod–polymer mixtures”, Physical Review E **68**, 062501 (2003).

[139] L. M. Hall and K. S. Schweizer, “Structure, scattering patterns and phase behavior of polymer nanocomposites with nonspherical fillers”, Soft Matter **6**, 1015–1025 (2010).

[140] U. K. Sankar and M. Tripathy, “Dispersion, depletion, and bridging of athermal and attractive nanorods in polymer melt”, Macromolecules **48**, 432–442 (2015).

[141] U. Erigi, U. Dhumal, and M. Tripathy, “Phase behavior of polymer-nanorod composites: A comparative study using PRISM theory and molecular dynamics simulations”, Journal of Chemical Physics **154**, 124903 (2021).

[142] A. I. Chervanyov, “Polymer-mediated interactions and their effect on the coagulation–fragmentation of nano-colloids: a self-consistent field theory approach”, Soft Matter **11**, 1038–1053 (2015).

[143] V. V. Ginzburg, “Modeling the Morphology and Phase Behavior of One-Component Polymer-Grafted Nanoparticle Systems”, Macromolecules **50**, 9445–9455 (2017).

[144] H. Chao, B. J. Lindsay, and R. A. Riggleman, “Field-Theoretic Simulations of the Distribution of Nanorods in Diblock Copolymer Thin Films”, The Journal of Physical Chemistry B **121**, 11198–11209 (2017).

[145] J. P. Koski, R. C. Ferrier, N. M. Krook, H. Chao, R. J. Composto, A. L. Frischknecht, and R. A. Riggleman, “Comparison of Field-Theoretic Approaches in Predicting Polymer Nanocomposite Phase Behavior”, Macromolecules **50**, 8797–8809 (2017).

[146]J. P. Koski, N. M. Krook, J. Ford, Y. Yahata, K. Ohno, C. B. Murray, A. L. Frischknecht, R. J. Composto, and R. A. Riggleman, “Phase Behavior of Grafted Polymer Nanocomposites from Field-Based Simulations”, Macromolecules **52**, 5110–5121 (2019).

[147]W. Li, K. T. Delaney, and G. H. Fredrickson, “Self-consistent field theory study of polymer-mediated colloidal interactions in solution: Depletion effects and induced forces”, The Journal of Chemical Physics **155**, 154903 (2021).

[148]A. T. Lakkas, A. P. Sgouros, C. J. Revelas, and D. N. Theodorou, “Structure and thermodynamics of grafted silica/polystyrene dilute nanocomposites investigated through self-consistent field theory”, Soft Matter **17**, 4077–4097 (2021).

[149]M. Surve, V. Pryamitsyn, and V. Ganesan, “Nanoparticles in solutions of adsorbing polymers: Pair interactions, percolation, and phase behavior”, Langmuir **22**, 969–981 (2006).

[150]M. Surve, V. Pryamitsyn, and V. Ganesan, “Dispersion and percolation transitions of nanorods in polymer solutions”, Macromolecules **40**, 344–354 (2007).

[151]L. G. Tang and J. L. Karoos, “A review of methods for improving the interfacial adhesion between carbon fiber and polymer matrix”, Polymer Composites **18**, 100–113 (1997).

[152]R. L. Zhang, Y. Liu, Y. D. Huang, and L. Liu, “Effect of particle size and distribution of the sizing agent on the carbon fibers surface and interfacial shear strength (IFSS) of its composites”, Applied Surface Science **287**, 423–427 (2013).

[153]S. Zhang, W. B. Liu, L. F. Hao, W. C. Jiao, F. Yang, and R. G. Wang, “Preparation of carbon nanotube/carbon fiber hybrid fiber by combining electrophoretic deposition and sizing process for enhancing interfacial strength in carbon fiber composites”, Composites Science and Technology **88**, 120–125 (2013).

[154]R. Paul and L. Dai, “Interfacial aspects of carbon composites”, Composite Interfaces **25**, 539–605 (2018).

[155]J. H. Park, V. Kalra, and Y. L. Joo, “Controlling the dispersion and orientation of nanorods in polymer melt under shear: Coarse-grained molecular dynamics simulation study”, Journal of Chemical Physics **140**, `10.1063/1.4868986` (2014).

[156]D. Aztatzi-Pluma, E. O. Castrejón-González, A. Almendarez-Camarillo, J. F. Alvarado, and Y. Durán-Morales, “Study of the Molecular Interactions between Functionalized Carbon Nanotubes and Chitosan”, Journal of Physical Chemistry C **120**, 2371–2378 (2016).

[157]K. Liao and S. Li, “Interfacial characteristics of a carbon nanotube-polystyrene composite system”, Applied Physics Letters **79**, 4225–4227 (2001).

[158]X. Xu, M. M. Thwe, C. Shearwood, and K. Liao, “Mechanical properties and interfacial characteristics of carbon-nanotube-reinforced epoxy thin films”, Applied Physics Letters **81**, 2833–2835 (2002).

[159]M. Wong, M. Paramsothy, X. J. Xu, Y. Ren, S. Li, and K. Liao, “Physical interactions at carbon nanotube-polymer interface”, Polymer **44**, 7757–7764 (2003).

[160]Y. R. Huang, Y. Jiang, J. L. Hor, R. Gupta, L. Zhang, K. J. Stebe, G. Feng, K. T. Turner, and D. Lee, “Polymer nanocomposite films with extremely high nanoparticle loadings via capillary rise infiltration (CaRI)”, Nanoscale **7**, 798–805 (2015).

[161] N. Manohar, K. J. Stebe, and D. Lee, "Solvent-Driven Infiltration of Polymer (SIP) into Nanoparticle Packings", ACS Macro Letters **6**, 1104–1108 (2017).

[162] R. B. Venkatesh, S. H. Han, and D. Lee, "Patterning polymer-filled nanoparticle films via leaching-enabled capillary rise infiltration (LeCaRI)", Nanoscale Horizons **4**, 933–939 (2019).

[163] Y. Jiang, J. L. Hor, D. Lee, and K. T. Turner, "Toughening Nanoparticle Films via Polymer Infiltration and Confinement", ACS Applied Materials and Interfaces **10**, 44011–44017 (2018).

[164] A. Swain, N. Das A, S. Chandran, and J. K. Basu, "Kinetics of high density functional polymer nanocomposite formation by tuning enthalpic and entropic barriers", Soft Matter **18**, 1005–1012 (2022).

[165] L. Sperling, *Introduction to physical polymer science* (Wiley, Hoboken, NJ, US, 2015).

[166] Z. .-. Wang, B. S. Hsiao, E. B. Sirota, and S. Srinivas, "A simultaneous small- and wide-angle X-ray scattering study of the early stages of melt crystallization in polyethylene", Polymer **41**, 8825–8832 (2000).

[167] J.-B. Jheng, W.-T. Chuang, P.-D. Hong, Y.-C. Huang, U.-S. Jeng, C.-J. Su, and G.-R. Pan, "Formation of mesomorphic domains associated with dimer aggregates of phenyl rings in cold crystallization of poly(trimethylene terephthalate)", Polymer **54**, 6242–6252 (2013).

[168] W.-T. Chuang, W.-B. Su, U.-S. Jeng, P.-D. Hong, C.-J. Su, C.-H. Su, Y.-C. Huang, K.-F. Laio, and A.-C. Su, "Formation of Mesomorphic Domains and Subsequent Structural Evolution during Cold Crystallization of Poly(trimethylene terephthalate)", Macromolecules **44**, 1140–1148 (2011).

[169] M. Muthukumar, "Molecular modelling of nucleation in polymers", Philosophical Transactions of the Royal Society of London. Series A: Mathematical, Physical and Engineering Sciences **361**, edited by G. W. Greenwood, A. L. Greer, D. M. Herlach, and K. F. Kelton, 539–556 (2003).

[170] M. Anwar and T. Schilling, "Crystallization of polyethylene: A molecular dynamics simulation study of the nucleation and growth mechanisms", Polymer **76**, 307–312 (2015).

[171] K. Esselink, P. A. J. Hilbers, and B. W. H. van Beest, "Molecular dynamics study of nucleation and melting of n-alkanes", The Journal of Chemical Physics **101**, 9033–9041 (1994).

[172] E. Piorkowska, A. Galeski, and J.-M. Haudin, "Critical assessment of overall crystallization kinetics theories and predictions", Progress in Polymer Science **31**, 549–575 (2006).

[173] M. C. Zhang, B.-H. Guo, and J. Xu, "A Review on Polymer Crystallization Theories", Crystals **7**, 4 (2017).

[174] H. Yokota and T. Kawakatsu, "Nucleation theory of polymer crystallization with conformation entropy", Polymer **186**, 121975 (2020).

[175] A. Kolmogorov, "On Statistical Theory of the Crystallization of Metals", Bulletin of the Academy of Sciences of the USSR, Mathematics **1**, 355–359 (1937).

[176] M. Avrami, "Kinetics of Phase Change. I General Theory", The Journal of Chemical Physics **7**, 1103–1112 (1939).

[177] W. A. Johnson and R. F. Mehl, "Reaction kinetics in processes of nucleation and growth", TRANSACTIONS OF THE AMERICAN INSTITUTE OF MINING AND METALLURGICAL ENGINEERS **135**, 416–442 (1939).

[178] M. Avrami, "Kinetics of Phase Change. II Transformation-Time Relations for Random Distribution of Nuclei", The Journal of Chemical Physics **8**, 212–224 (1940).

[179] T. Ozawa, "Kinetics of non-isothermal crystallization", Polymer **12**, 150–158 (1971).

[180] K. Nakamura, T. Watanabe, K. Katayama, and T. Amano, "Some aspects of nonisothermal crystallization of polymers. I. Relationship between crystallization temperature, crystallinity, and cooling conditions", Journal of Applied Polymer Science **16**, 1077–1091 (1972).

[181] J. D. Hoffman and J. I. Lauritzen, "Crystallization of bulk polymers with chain folding: theory of growth of lamellar spherulites", Journal of Research of the National Bureau of Standards Section A: Physics and Chemistry **65A**, 297 (1961).

[182] S. Z. D. Cheng and B. Lotz, "Enthalpic and entropic origins of nucleation barriers during polymer crystallization: the Hoffman–Lauritzen theory and beyond", Polymer, To Honor the Memory of John D. Hoffman **46**, 8662–8681 (2005).

[183] R. Becker and W. Döring, "Kinetische Behandlung der Keimbildung in übersättigten Dämpfen", Annalen der Physik **416**, 719–752 (1935).

[184] S. Auer and D. Frenkel, "Prediction of absolute crystal-nucleation rate in hard-sphere colloids", Nature **409**, 1020–1023 (2001).

[185] A. Keller and A. O'connor, "Large Periods in Polyethylene: the Origin of Low-Angle X-ray Scattering", Nature **180**, 1289–1290 (1957).

[186] E. W. Fischer, "Notizen: Stufen- und spiralförmiges Kristallwachstum bei Hochpolymeren", Zeitschrift für Naturforschung A **12**, 753–754 (1957).

[187] P. H. Till Jr., "The growth of single crystals of linear polyethylene", Journal of Polymer Science **24**, 301–306 (1957).

[188] J. D. Hoffman, G. T. Davis, and J. I. Lauritzen, "The Rate of Crystallization of Linear Polymers with Chain Folding", in *Treatise on Solid State Chemistry: Volume 3 Crystalline and Noncrystalline Solids*, edited by N. B. Hannay (Springer US, Boston, MA, 1976), pp. 497–614.

[189] J. D. Hoffman, "Theoretical aspects of polymer crystallization with chain folds: Bulk polymers", Polymer Engineering & Science **4**, 315–362 (1964).

[190] D. Turnbull and J. C. Fisher, "Rate of Nucleation in Condensed Systems", The Journal of Chemical Physics **17**, 71–73 (1949).

[191] J. D. Hoffman and J. J. Weeks, "Rate of Spherulitic Crystallization with Chain Folds in Polychlorotrifluoroethylene", The Journal of Chemical Physics **37**, 1723–1741 (1962).

[192] R. M. Patel and J. E. Spruiell, "Crystallization kinetics during polymer processing—Analysis of available approaches for process modeling", Polymer Engineering & Science **31**, 730–738 (1991).

[193] T. Huang and M. R. Kamal, "Morphological modeling of polymer solidification", Polymer Engineering & Science **40**, 1796–1808 (2000).

[194] F. C. Frank, "I. Liquid crystals. On the theory of liquid crystals", Discussions of the Faraday Society **25**, 19 (1958).

[195] J. Molnár, Ö. Sepsi, B. Gaál, Z. Zuba, M. Dobrzyńska-Mizera, and A. Menyárd, "Probabilistic numerical simulation for predicting spherulitic morphology from calorimetric crystallization conversion curves: An isothermal case", Materials & Design **212**, 110245 (2021).

[196] I. Steinbach, “Phase-field models in materials science”, Modelling and Simulation in Materials Science and Engineering **17**, 073001 (2009).

[197] H. Xu, R. Matkar, and T. Kyu, “Phase-field modeling on morphological landscape of isotactic polystyrene single crystals”, Physical Review E **72**, 011804 (2005).

[198] X.-D. Wang, J. Ouyang, J. Su, and W. Zhou, “A phase-field model for simulating various spherulite morphologies of semi-crystalline polymers”, Chinese Physics B **22**, 106103 (2013).

[199] R. Kobayashi, “Modeling and numerical simulations of dendritic crystal growth”, Physica D: Nonlinear Phenomena **63**, 410–423 (1993).

[200] A. Bahloul, I. Doghri, and L. Adam, “An enhanced phase field model for the numerical simulation of polymer crystallization”, POLYMER CRYSTALLIZATION **3**, e10144 (2020).

[201] K. Taguchi, H. Miyaji, K. Izumi, A. Hoshino, Y. Miyamoto, and R. Kokawa, “Growth shape of isotactic polystyrene crystals in thin films”, Polymer **42**, 7443–7447 (2001).

[202] K. L. Beers, J. F. Douglas, E. J. Amis, and A. Karim, “Combinatorial Measurements of Crystallization Growth Rate and Morphology in Thin Films of Isotactic Polystyrene”, Langmuir **19**, 3935–3940 (2003).

[203] A. Bahloul, I. Doghri, and L. Adam, “Linking a phase field model for polymer crystallization to full-field micromechanical simulations of semi-crystalline polymers”, Computational Materials Science **199**, 110685 (2021).

[204] T. Krause, G. Kalinka, C. Auer, and G. Hinrichsen, “Computer simulation of crystallization kinetics in fiber-reinforced composites”, Journal of Applied Polymer Science **51**, 399–406 (1994).

[205] N. A. Mehl and L. Rebenfeld, “Computer simulation of crystallization kinetics and morphology in fiber-reinforced thermoplastic composites. I. Two-dimensional case”, Journal of Polymer Science Part B: Polymer Physics **31**, 1677–1686 (1993).

[206] N. A. Mehl and L. Rebenfeld, “Computer simulation of crystallization kinetics and morphology in fiber-reinforced thermoplastic composites. III. Thermal nucleation”, Journal of Polymer Science Part B: Polymer Physics **33**, 1249–1257 (1995).

[207] A. Benard and S. G. Advani, “An analytical model for spherulitic growth in fiber-reinforced polymers”, Journal of Applied Polymer Science **70**, 1677–1687 (1998).

[208] J.-M. Haudin and J.-L. Chenot, “Numerical and Physical Modeling of Polymer Crystallization: Part I: Theoretical and Numerical Analysis”, International Polymer Processing **19**, 267–274 (2004).

[209] A. Durin, N. Boyard, J.-L. Bailleul, N. Billon, J.-L. Chenot, and J.-M. Haudin, “Semianalytical models to predict the crystallization kinetics of thermoplastic fibrous composites”, Journal of Applied Polymer Science **134**, `10.1002/app.44508` (2017).

[210] S. Galeski, E. Piorkowska, A. Rozanski, G. Regnier, A. Galeski, and K. Jurczuk, “Crystallization kinetics of polymer fibrous nanocomposites”, European Polymer Journal **83**, 181–201 (2016).

[211] C. Ruan, J. Ouyang, S. Liu, and L. Zhang, “Computer modeling of isothermal crystallization in short fiber reinforced composites”, Computers & Chemical Engineering **35**, 2306–2317 (2011).

[212] C. Ruan, J. Ouyang, and S. Liu, "Multi-scale modeling and simulation of crystallization during cooling in short fiber reinforced composites", International Journal of Heat and Mass Transfer **55**, 1911–1921 (2012).

[213] S. Iijima, "Helical microtubules of graphitic carbon", Nature **354**, 56–58 (1991).

[214] P. M. Ajayan, O. Stephan, C. Colliex, and D. Trauth, "Aligned carbon nanotube arrays formed by cutting a polymer resin-nanotube composite", Science **265**, 1212–1214 (1994).

[215] B. Arash, Q. Wang, and V. K. Varadan, "Mechanical properties of carbon nanotube/polymer composites", Scientific Reports **4**, 6479 (2014).

[216] R. Zhu, E. Pan, and A. K. Roy, "Molecular dynamics study of the stress-strain behavior of carbon-nanotube reinforced Epon 862 composites", Materials Science and Engineering A **447**, 51–57 (2007).

[217] N. G. Sahoo, S. Rana, J. W. Cho, L. Li, and S. H. Chan, "Polymer nanocomposites based on functionalized carbon nanotubes", Progress in Polymer Science **35**, 837–867 (2010).

[218] M. Moniruzzaman and K. I. Winey, "Polymer nanocomposites containing carbon nanotubes", Macromolecules **39**, 5194–5205 (2006).

[219] K. Lozano and E. V. Barrera, "Nanofiber-reinforced thermoplastic composites. I. Thermoanalytical and mechanical analyses", Journal of Applied Polymer Science **79**, 125–133 (2001).

[220] V. Z. Mordkovich, "Carbon nanofibers: A new ultrahigh-strength material for chemical technology", Theoretical Foundations of Chemical Engineering **37**, 429–438 (2003).

[221] M. H. Al-Saleh and U. Sundararaj, "Review of the mechanical properties of carbon nanofiber/polymer composites", Composites Part A: Applied Science and Manufacturing **42**, 2126–2142 (2011).

[222] S. Kumar, H. Doshi, M. Srinivasarao, J. O. Park, and D. A. Schiraldi, "Fibers from polypropylene/nano carbon fiber composites", Polymer **43**, 1701–1703 (2002).

[223] J. N. Coleman, U. Khan, and Y. K. Gun'ko, "Mechanical reinforcement of polymers using carbon nanotubes", Advanced Materials **18**, 689–706 (2006).

[224] J. Sapkota, A. Gooneie, A. Shirole, and J. C. Martinez Garcia, "A refined model for the mechanical properties of polymer composites with nanorods having different length distributions", Journal of Applied Polymer Science **134**, 45279 (2017).

[225] X.-l. Xie, Y.-w. Mai, and X.-p. Zhou, "Dispersion and alignment of carbon nanotubes in polymer matrix : A review", **49**, 89–112 (2006).

[226] J. N. Coleman, U. Khan, W. J. Blau, and Y. K. Gun'ko, "Small but strong: A review of the mechanical properties of carbon nanotube-polymer composites", Carbon **44**, 1624–1652 (2006).

[227] A. Hirsch, "Functionalization of Single-Walled Carbon Nanotubes", Angewandte Chemie International Edition **41**, 1853–1859 (2002).

[228] F. Severini, L. Formaro, M. Pegoraro, and L. Posca, "Chemical modification of carbon fiber surfaces", Carbon **40**, 735–741 (2002).

[229] R. Ramasubramaniam, J. Chen, and H. Liu, "Homogeneous carbon nanotube/polymer composites for electrical applications", Applied Physics Letters **83**, 2928–2930 (2003).

[230]J. Zhu, J. D. Kim, H. Peng, J. L. Margrave, V. N. Khabashesku, and E. V. Barrera, "Improving the dispersion and integration of single-walled carbon nanotubes in epoxy composites through functionalization", Nano Letters **3**, 1107–1113 (2003).

[231]N. Grossiord, J. Loos, O. Regev, and C. E. Koning, "Toolbox for dispersing carbon nanotubes into polymers to get conductive nanocomposites", Chemistry of Materials **18**, 1089–1099 (2006).

[232]L. Vaisman, H. D. Wagner, and G. Marom, "The role of surfactants in dispersion of carbon nanotubes", Advances in Colloid and Interface Science **128–130**, 37–46 (2006).

[233]".-C. Ma, N. A. Siddiqui, G. Marom, and J.-K. Kim", "Dispersion and functionalization of carbon nanotubes for polymer-based nanocomposites: A review", Composites Part A: Applied Science and Manufacturing **41**, 1345–1367 (2010).

[234]V. Kalra, F. Escobedo, and Y. L. Joo, "Effect of shear on nanoparticle dispersion in polymer melts: A coarse-grained molecular dynamics study", Journal of Chemical Physics **132**, `10.1063/1.3277671` (2010).

[235]H. N. Lekkerkerker and A. Stroobants, "Phase behaviour of rod-like colloid+flexible polymer mixtures", Il Nuovo Cimento D **16**, 949–962 (1994).

[236]S. W. Hu, Y. J. Sheng, and H. K. Tsao, "Depletion-induced size fractionation of nanorod dispersions", Soft Matter **9**, 7261–7266 (2013).

[237]M. J. A. Hore and R. J. Composto, "Functional Polymer Nanocomposites Enhanced by Nanorods", Macromolecules **47**, 875–887 (2014).

[238]A. Milchev, S. A. Egorov, J. Midya, K. Binder, and A. Nikoubashman, "Entropic Unmixing in Nematic Blends of Semiflexible Polymers", ACS Macro Letters **9**, 1779–1784 (2020).

[239]N. Afrasiabian, M. Wei, and C. Denniston, "Enhanced Pulley Effect for Translocation: The Interplay of Electrostatic and Hydrodynamic Forces", Biomacromolecules **24**, 4103–4112 (2023).

[240]K. Kremer and G. S. Grest, "Dynamics of entangled linear polymer melts: A molecular-dynamics simulation", The Journal of Chemical Physics **92**, 5057–5086 (1990).

[241]W. Humphrey, A. Dalke, and K. Schulten, "VMD: Visual molecular dynamics", Journal of Molecular Graphics **14**, 33–38 (1996).

[242]G. N. Toepperwein, R. A. Riggleman, and J. J. De Pablo, "Dynamics and deformation response of rod-containing nanocomposites", Macromolecules **45**, 543–554 (2012).

[243]J. H. Park and Y. L. Joo, "Tailoring nanorod alignment in a polymer matrix by elongational flow under confinement: Simulation, experiments, and surface enhanced Raman scattering application", Soft Matter **10**, 3494–3505 (2014).

[244]Y. Gao, D. Cao, J. Liu, J. Shen, Y. Wu, and L. Zhang, "Molecular dynamics simulation of the conductivity mechanism of nanorod filled polymer nanocomposites", Physical Chemistry Chemical Physics **17**, 22959–22968 (2015).

[245]J. Shen, X. Li, L. Zhang, X. Lin, H. Li, X. Shen, V. Ganesan, and J. Liu, "Mechanical and Viscoelastic Properties of Polymer-Grafted Nanorod Composites from Molecular Dynamics Simulation", Macromolecules **51**, 2641–2652 (2018).

[246]F. Paiva, A. Boromand, J. Maia, A. Secchi, V. Calado, and S. Khani, "Interfacial aggregation of Janus rods in binary polymer blends and their effect on phase separation", Journal of Chemical Physics **151**, 114905 (2019).

[247]A. Karatrantos, R. J. Composto, K. I. Winey, and N. Clarke, "Structure and conformations of polymer/SWCNT nanocomposites", Macromolecules **44**, 9830–9838 (2011).

[248]R. Tuinier, T. Taniguchi, and H. H. Wensink, "Phase behavior of a suspension of hard spherocylinders plus ideal polymer chains", European Physical Journal E **23**, 355–365 (2007).

[249]Y. Wang, S. Liu, H. Zhu, H. Ji, G. Li, Z. Wan, Y. Ma, and L. Xie, "The Entangled Conductive Structure of CB/PA6/PP MFCs and Their Electromechanical Properties", Polymers **13**, 961 (2021).

[250]S. Lu and A. Jayaraman, "Effect of Nanorod Physical Roughness on the Aggregation and Percolation of Nanorods in Polymer Nanocomposites", ACS Macro Letters **10**, 1416–1422 (2021).

[251]M. Robbins and M. Müser, "Computer Simulations of Friction, Lubrication, and Wear", in *Modern Tribology Handbook: Volume One: Principles of Tribology* (CRC Press, Boca Raton, Dec. 2000), pp. 717–765.

[252]D. Berman, A. Erdemir, and A. V. Sumant, "Approaches for Achieving Superlubricity in Two-Dimensional Materials", ACS Nano **12**, 2122–2137 (2018).

[253]A. P. Thompson, H. M. Aktulga, R. Berger, D. S. Bolintineanu, W. M. Brown, P. S. Crozier, P. J. in 't Veld, A. Kohlmeyer, S. G. Moore, T. D. Nguyen, R. Shan, M. J. Stevens, J. Tranchida, C. Trott, and S. J. Plimpton, "LAMMPS - a flexible simulation tool for particle-based materials modeling at the atomic, meso, and continuum scales", Computer Physics Communications **271**, 108171 (2022).

[254]A. I. Jewett, D. Stelter, J. Lambert, S. M. Saladi, O. M. Roscioni, M. Ricci, L. Autin, M. Maritan, S. M. Bashusqeh, T. Keyes, R. T. Dame, J. E. Shea, G. J. Jensen, and D. S. Goodsell, "Moltemplate: A Tool for Coarse-Grained Modeling of Complex Biological Matter and Soft Condensed Matter Physics", Journal of Molecular Biology **433**, 166841 (2021).

[255]R. Auhl, R. Everaers, G. S. Grest, K. Kremer, and S. J. Plimpton, "Equilibration of long chain polymer melts in computer simulations", Journal of Chemical Physics **119**, 12718–12728 (2003).

[256]T. Schneider and E. Stoll, "Molecular-dynamics study of a three-dimensional one-component model for distortive phase transitions", Physical Review B **17**, 1302–1322 (1978).

[257]N. Grønbech-Jensen and O. Farago, "A simple and effective Verlet-type algorithm for simulating Langevin dynamics", Molecular Physics (2013).

[258]H. J. Berendsen, J. P. Postma, W. F. Van Gunsteren, A. Dinola, and J. R. Haak, "Molecular dynamics with coupling to an external bath", The Journal of Chemical Physics **81**, 3684–3690 (1984).

[259]O. Mozafar and C. Denniston, "Effects of structural inhomogeneity on equilibration processes in Langevin dynamics", Physical Review E **105**, 64109 (2022).

[260]T. E. Gartner and A. Jayaraman, "Modeling and Simulations of Polymers: A Roadmap", Macromolecules **52**, 755–786 (2019).

[261]F. Du, J. E. Fischer, and K. I. Winey, “Coagulation method for preparing single-walled carbon nanotube/poly(methyl methacrylate) composites and their modulus, electrical conductivity, and thermal stability”, Journal of Polymer Science Part B: Polymer Physics **41**, 3333–3338 (2003).

[262]Y. Zhao, M. Byshkin, Y. Cong, T. Kawakatsu, L. Guadagno, A. De Nicola, N. Yu, G. Milano, and B. Dong, “Self-assembly of carbon nanotubes in polymer melts: simulation of structural and electrical behaviour by hybrid particle-field molecular dynamics”, Nanoscale **8**, 15538–15552 (2016).

[263]R. Mahnke, J. Kaupužs, and I. Lubashevsky, *Physics of Stochastic Processes: How Randomness Acts in Time* (Wiley, Weinheim, Germany, 2009).

[264]S. Asakura and F. Oosawa, “On interaction between two bodies immersed in a solution of macromolecules”, The Journal of Chemical Physics **22**, 1255–1256 (1954).

[265]A. Vrij, “POLYMERS AT INTERFACES AND THE INTERACTIONS IN COLLOIDAL DISPERSIONS”, in *Colloid and Surface Science* (Pergamon, Oxford, England, Jan. 1977), pp. 471–483.

[266]T. Biben, P. Bladon, and D. Frenkel, “Depletion effects in binary hard-sphere fluids”, Journal of Physics Condensed Matter **8**, 10799–10821 (1996).

[267]A. Striolo, C. M. Colina, K. E. Gubbins, N. Elvassore, and L. Lue, “The depletion attraction between Pairs of colloid particles in polymer solution”, Molecular Simulation **30**, 437–449 (2004).

[268]G. J. Vroege and H. N. Lekkerkerker, “Phase transitions in lyotropic colloidal and polymer liquid crystals”, Reports on Progress in Physics **55**, 1241–1309 (1992).

[269]N. J. Mottram and C. J. P. Newton, *Introduction to Q-tensor theory*, 2014.

[270]A. Majumdar, “Equilibrium order parameters of nematic liquid crystals in the Landau-de Gennes theory”, European Journal of Applied Mathematics **21**, 181–203 (2010).

[271]T. Aoyagi, J. I. Takimoto, and M. Doi, “Molecular dynamics study of polymer melt confined between walls”, Journal of Chemical Physics **115**, 552–559 (2001).

[272]M. V. Gorkunov and M. A. Osipov, “Mean-field theory of a nematic liquid crystal doped with anisotropic nanoparticles”, Soft Matter **7**, 4348–4356 (2011).

[273]N. Afrasiabian, V. Balasubramanian, and C. Denniston, “Dispersion and orientation patterns in nanorod-infused polymer melts”, The Journal of Chemical Physics **158**, 054902 (2023).

[274]P. K. Mallick, *Fiber-Reinforced Composites: Materials, Manufacturing, and Design, Third Edition*, 3rd ed. (CRC Press, Boca Raton, Nov. 2007).

[275]N. Meyer, A. N. Hrymak, and L. Kärger, “Modeling Short-Range Interactions in Concentrated Newtonian Fiber Bundle Suspensions”, International Polymer Processing **36**, 255–263 (2021).

[276]L. Schöller, D. Schneider, C. Herrmann, A. Prahs, and B. Nestler, “Phase-field modeling of crack propagation in heterogeneous materials with multiple crack order parameters”, Computer Methods in Applied Mechanics and Engineering **395**, 114965 (2022).

[277]T. Kannenberg, L. Schöller, A. Prahs, D. Schneider, and B. Nestler, “Microstructure evolution accounting for crystal plasticity in the context of the multiphase-field method”, Computational Mechanics, `10.1007/s00466-023-02423-7` (2023).

[278]A. Prahs, M. Reder, D. Schneider, and B. Nestler, "Thermomechanically coupled theory in the context of the multiphase-field method", International Journal of Mechanical Sciences **257**, 108484 (2023).

[279]A. Prahs, L. Schöller, F. K. Schwab, D. Schneider, T. Böhlke, and B. Nestler, "A multiphase-field approach to small strain crystal plasticity accounting for balance equations on singular surfaces", Computational Mechanics, `10.1007/s00466-023-02389-6` (2023).

[280]A. Karma and W.-J. Rappel, "Phase-field method for computationally efficient modeling of solidification with arbitrary interface kinetics", Physical Review E **53**, R3017–R3020 (1996).

[281]I. Steinbach and F. Pezzolla, "A generalized field method for multiphase transformations using interface fields", Physica D: Nonlinear Phenomena **134**, 385–393 (1999).

[282]A. Ziabicki, "Generalized Theory of Nucleation Kinetics. II. Athermal Nucleation Involving Spherical Clusters", The Journal of Chemical Physics **48**, 4374–4380 (1968).

[283]M. L. Di Lorenzo and C. Silvestre, "Non-isothermal crystallization of polymers", Progress in Polymer Science **24**, 917–950 (1999).

[284]P. Sajkiewicz, "Kinetics of Crystallisation of Polymers - A Review", Progress in Rubber, Plastics and Recycling Technology **18**, 195–215 (2002).

[285]G. Ehrenstein, G. Riedel, and P. Trawiel, *Thermal analysis of plastics: Theory and practice* (Carl Hanser Verlag GmbH & Company KG, Cincinnati, OH, US, 2012).

[286]N. Kocic, S. Lederhofer, K. Kretschmer, M. Bastian, and P. Heidemeyer, "Nucleation parameter and size distribution of critical nuclei for nonisothermal polymer crystallization: The influence of the cooling rate and filler", Journal of Applied Polymer Science **132**, `10.1002/app.41433` (2015).

[287]Y. Long, R. A. Shanks, and Z. H. Stachurski, "Kinetics of polymer crystallisation", Progress in Polymer Science **20**, 651–701 (1995).

[288]S. Bose, A. R. Bhattacharyya, P. V. Kodgire, and A. Misra, "Fractionated crystallization in PA6/ABS blends: Influence of a reactive compatibilizer and multiwall carbon nanotubes", Polymer **48**, 356–362 (2007).

[289]Y. Lin, W. Zhong, L. Shen, P. Xu, and Q. Du, "Study on the Relationship Between Crystalline Structures and Physical Properties of Polyamide-6", Journal of Macromolecular Science, Part B **44**, 161–175 (2005).

[290]M. Yuan, L.-S. Turng, S. Gong, A. Winardi, and D. Caulfield, "Crystallization Behavior of Polyamide-6 Microcellular Nanocomposites", Journal of Cellular Plastics **40**, 397–409 (2004).

[291]N. Chen, X. Yao, C. Zheng, Y. Tang, M. Ren, Y. Ren, M. Guo, S. Zhang, and L.-Z. Liu, "Study on the miscibility, crystallization and crystalline morphology of polyamide-6/polyvinylidene fluoride blends", Polymer **124**, 30–40 (2017).

[292]T. Ferreira, P. E. Lopes, A. J. Pontes, and M. C. Paiva, "Microinjection molding of polyamide 6", Polymers for Advanced Technologies **25**, 891–895 (2014).

[293]X. Zhang, A. Gohn, G. Mendis, J. F. Buzinkai, S. J. Weigand, and A. M. Rhoades, "Probing Three Distinct Crystal Polymorphs of Melt-Crystallized Polyamide 6 by an Integrated Fast Scanning Calorimetry Chip System", Macromolecules **54**, 7512–7528 (2021).

[294] V. Ferreiro, Y. Pennec, R. Séguéla, and G. Coulon, “Shear banding in polyamide 6 films as revealed by atomic force microscopy”, Polymer **41**, 1561–1569 (2000).

[295] J. Sierra, M. Noriega Escobar, J. Gómez, and J. Pastor, “Isothermal and non-isothermal Crystallization Kinetics for Blends of Polyamide 6 and Polypropylene”, Zeitschrift Kunststofftechnik/Journal of Plastics Technology (2006).

[296] J. E. Mark, *Physical Properties of Polymers Handbook* (Springer Science & Business Media, New York, US, Mar. 2007).

[297] R. E. (E. Kirk, D. F. (F. Othmer, J. I. Kroschwitz, and M. Howe-Grant, *Encyclopedia of chemical technology*, 4th ed. (Wiley, New York, 1991).

[298] M. Li, Y. Wan, Z. Gao, G. Xiong, X. Wang, C. Wan, and H. Luo, “Preparation and properties of polyamide 6 thermal conductive composites reinforced with fibers”, Materials & Design **51**, 257–261 (2013).

[299] M. Salmerón Sánchez, V. B. F. Mathot, G. Vanden Poel, and J. L. Gómez Ribelles, “Effect of the Cooling Rate on the Nucleation Kinetics of Poly(l-Lactic Acid) and Its Influence on Morphology”, Macromolecules **40**, 7989–7997 (2007).

[300] J. Varga and J. Karger-Kocsis, “Interfacial morphologies in carbon fibre-reinforced polypropylene microcomposites”, Polymer **36**, 4877–4881 (1995).

[301] J. L. Thomason and A. A. Van Rooyen, “Transcrystallized interphase in thermoplastic composites”, Journal of Materials Science **27**, 889–896 (1992).

[302] S. Chen and G. D. Doolen, “LATTICE BOLTZMANN METHOD FOR FLUID FLOWS”, Annual Review of Fluid Mechanics **30**, 329–364 (1998).

[303] D. J. Holdych, D. Rovas, J. G. Georgiadis, and R. O. Buckius, “An Improved Hydrodynamics Formulation for Multiphase Flow Lattice-Boltzmann Models”, International Journal of Modern Physics C **09**, 1393–1404 (1998).

[304] Q. Li and A. J. Wagner, “Symmetric free-energy-based multicomponent lattice Boltzmann method”, Physical Review E **76**, 036701 (2007).

[305] K. S. Ridl and A. J. Wagner, “Lattice Boltzmann simulation of mixtures with multicomponent van der Waals equation of state”, Physical Review E **98**, 043305 (2018).

[306] C. Denniston, E. Orlandini, and J. M. Yeomans, “Lattice Boltzmann simulations of liquid crystal hydrodynamics”, Physical Review E **63**, 056702 (2001).

[307] S. Changizrezaei and C. Denniston, “Heterogeneous colloidal particles immersed in a liquid crystal”, Physical Review E **95**, 052703 (2017).

[308] Z. Guo and T. S. Zhao, “Lattice Boltzmann model for incompressible flows through porous media”, Physical Review E **66**, 036304 (2002).

[309] N. Afrasiabian and C. Denniston, “The journey of a single polymer chain to a nanopore”, Soft Matter **16**, 9101–9112 (2020).

[310] V. Balasubramanian and C. Denniston, “Polymer margination in uniform shear flows”, Soft Matter **14**, 9209–9219 (2018).

[311] A. J. Wagner, *Derivation of a non-objective Oldroyd model from the Boltzmann equation*, May 2001.

[312] P. Lallemand, D. d'Humières, L.-S. Luo, and R. Rubinstein, "Theory of the lattice Boltzmann method: Three-dimensional model for linear viscoelastic fluids", Physical Review E **67**, 021203 (2003).

[313] F. E. Mackay and C. Denniston, "Coupling MD particles to a lattice-Boltzmann fluid through the use of conservative forces", Journal of Computational Physics **237**, 289–298 (2013).

[314] C. Denniston, N. Afrasiabian, M. G. Cole-André, F. E. Mackay, S. T. Ollila, and T. Whitehead, "LAMMPS lb/fluid fix version 2: Improved hydrodynamic forces implemented into LAMMPS through a lattice-Boltzmann fluid", Computer Physics Communications **275**, 108318 (2022).

[315] F. Bösch, S. S. Chikatamarla, and I. V. Karlin, "Entropic multirelaxation lattice Boltzmann models for turbulent flows", Physical Review E **92**, 043309 (2015).

[316] A.-G. Xu, G.-C. Zhang, Y.-B. Gan, F. Chen, and X.-J. Yu, "Lattice Boltzmann modeling and simulation of compressible flows", Frontiers of Physics **7**, 582–600 (2012).

[317] F. J. Alexander, H. Chen, S. Chen, and G. D. Doolen, "Lattice Boltzmann model for compressible fluids", Physical Review A **46**, 1967–1970 (1992).

[318] Y. Guangwu, C. Yaosong, and H. Shouxin, "Simple lattice Boltzmann model for simulating flows with shock wave", Physical Review E **59**, 454–459 (1999).

[319] T. Kataoka and M. Tsutahara, "Lattice Boltzmann method for the compressible Euler equations", Physical Review E **69**, 056702 (2004).

[320] C. Z. Ji, C. Shu, and N. Zhao, "A lattice boltzmann method-based flux solver and its application to solve shock tube problem", Modern Physics Letters B **23**, 313–316 (2009).

[321] C.-H. Sun, "Thermal Lattice Boltzmann Model for Compressible Fluid", Chinese Physics Letters **17**, 209 (2000).

[322] F. J. Alexander, S. Chen, and J. D. Sterling, "Lattice Boltzmann thermohydrodynamics", Physical Review E **47**, R2249–R2252 (1993).

[323] Y. H. Qian, "Simulating thermohydrodynamics with lattice BGK models", Journal of Scientific Computing **8**, 231–242 (1993).

[324] Y. Chen, H. Ohashi, and M. Akiyama, "Thermal lattice Bhatnagar-Gross-Krook model without nonlinear deviations in macrodynamic equations", Physical Review E **50**, 2776–2783 (1994).

[325] G. R. McNamara, A. L. Garcia, and B. J. Alder, "Stabilization of thermal lattice Boltzmann models", Journal of Statistical Physics **81**, 395–408 (1995).

[326] S. Ansumali and I. V. Karlin, "Consistent lattice Boltzmann method", Physical Review Letters **95**, `10.1103/PhysRevLett.95.260605` (2005).

[327] N. I. Prasianakis and I. V. Karlin, "Lattice Boltzmann method for thermal flow simulation on standard lattices", Physical Review E - Statistical, Nonlinear, and Soft Matter Physics **76**, `10.1103/PhysRevE.76.016702` (2007).

[328] I. V. Karlin and S. Succi, "Equilibria for discrete kinetic equations", Physical Review E **58**, R4053–R4056 (1998).

[329]X. He, S. Chen, and G. D. Doolen, “A Novel Thermal Model for the Lattice Boltzmann Method in Incompressible Limit”, Journal of Computational Physics **146**, 282–300 (1998).

[330]I. V. Karlin, D. Sichau, and S. S. Chikatamarla, “Consistent two-population lattice Boltzmann model for thermal flows”, Physical Review E **88**, 063310 (2013).

[331]N. Frapolli, S. S. Chikatamarla, and I. V. Karlin, “Lattice Kinetic Theory in a Comoving Galilean Reference Frame”, Physical Review Letters **117**, 010604 (2016).

[332]N. G. Kallikounis and I. V. Karlin, “Particles on demand method: Theoretical analysis, simplification techniques, and model extensions”, Physical Review E **109**, 015304 (2024).

[333]B. Dorschner, F. Bösch, and I. V. Karlin, “Particles on Demand for Kinetic Theory”, Physical Review Letters **121**, 130602 (2018).

[334]L. Giraud, D. d'HumièRes, and P. Lallemand, “A Lattice-Boltzmann Model for Visco-Elasticity”, International Journal of Modern Physics C **08**, 805–815 (1997).

[335]A. J. Wagner, L. Giraud, and C. E. Scott, “Simulation of a cusped bubble rising in a viscoelastic fluid with a new numerical method”, Computer Physics Communications **129**, 227–232 (2000).

[336]P. Lallemand and L.-S. Luo, “Theory of the lattice Boltzmann method: Acoustic and thermal properties in two and three dimensions”, Physical Review E **68**, 036706 (2003).

[337]R. B. Bird, W. E. Stewart, and E. N. Lightfoot, *Transport Phenomena* (J. Wiley, New York, US, 2002).

[338]I. Ispolatov and M. Grant, “Lattice Boltzmann method for viscoelastic fluids”, Physical Review E **65**, 056704 (2002).

[339]T. N. Phillips and G. W. Roberts, “Lattice Boltzmann models for non-Newtonian flows”, IMA Journal of Applied Mathematics **76**, 790–816 (2011).

[340]Y. H. Qian and S. A. Orszag, “Lattice BGK Models for the Navier-Stokes Equation: Nonlinear Deviation in Compressible Regimes”, Europhysics Letters (EPL) **21**, 255–259 (1993).

[341]P. J. Dellar, “Bulk and shear viscosities in lattice Boltzmann equations”, Physical Review E **64**, 031203 (2001).

[342]X. He, X. Shan, and G. D. Doolen, “Discrete Boltzmann equation model for nonideal gases”, Physical Review E **57**, R13–R16 (1998).

[343]A. J. Wagner, “Thermodynamic consistency of liquid-gas lattice Boltzmann simulations”, Physical Review E **74**, 056703 (2006).

[344]R. Ramadugu, S. P. Thampi, R. Adhikari, S. Succi, and S. Ansumali, “Lattice differential operators for computational physics”, Europhysics Letters **101**, 50006 (2013).

[345]S. Chen, D. Martínez, and R. Mei, “On boundary conditions in lattice Boltzmann methods”, Physics of Fluids **8**, 2527–2536 (1996).

[346]R. S. Maier, R. S. Bernard, and D. W. Grunau, “Boundary conditions for the lattice Boltzmann method”, Physics of Fluids **8**, 1788–1801 (1996).

[347]S. Ansumali and I. V. Karlin, “Kinetic boundary conditions in the lattice Boltzmann method”, Physical Review E **66**, 026311 (2002).

[348]M. Hecht and J. Harting, "Implementation of on-site velocity boundary conditions for D3Q19 lattice Boltzmann simulations", Journal of Statistical Mechanics: Theory and Experiment **2010**, P01018 (2010).

[349]L. Li, R. Mei, and J. F. Klausner, "Boundary conditions for thermal lattice Boltzmann equation method", Journal of Computational Physics **237**, 366–395 (2013).

[350]C. S. Peskin, "The immersed boundary method", Acta Numerica **11**, 479–517 (2002).

[351]J.-P. Ryckaert, G. Ciccotti, and H. J. C. Berendsen, "Numerical integration of the cartesian equations of motion of a system with constraints: molecular dynamics of *n*-alkanes", Journal of Computational Physics **23**, 327–341 (1977).

[352]H. C. Andersen, "Rattle: A "velocity" version of the shake algorithm for molecular dynamics calculations", Journal of Computational Physics **52**, 24–34 (1983).

[353]L. Verlet, "Computer "Experiments" on Classical Fluids. I. Thermodynamical Properties of Lennard-Jones Molecules", Physical Review **159**, 98–103 (1967).

[354]R. Keys, "Cubic convolution interpolation for digital image processing", IEEE Transactions on Acoustics, Speech, and Signal Processing **29**, 1153–1160 (1981).

[355]S. T. Ollila, C. J. Smith, T. Ala-Nissila, and C. Denniston, "The hydrodynamic radius of particles in the hybrid lattice boltzmann-molecular dynamics method", Multiscale Modeling and Simulation **11**, 213–243 (2013).

[356]J. Hinch and O. Harlen, "Oldroyd B, and not A?", Journal of Non-Newtonian Fluid Mechanics **298**, 104668 (2021).

[357]P. Skjetne, R. F. Ross, and D. J. Klingenberg, "Simulation of single fiber dynamics", The Journal of Chemical Physics **107**, 2108–2121 (1997).

[358]M. S. Ingber and L. A. Mondy, "A numerical study of three-dimensional Jeffery orbits in shear flow", Journal of Rheology **38**, 1829–1843 (1994).

[359]G. B. Jeffery and L. N. G. Filon, "The motion of ellipsoidal particles immersed in a viscous fluid", Proceedings of the Royal Society of London. Series A, Containing Papers of a Mathematical and Physical Character **102**, 161–179 (1922).

[360]B. J. Trevelyan and S. G. Mason, "Particle motions in sheared suspensions. I. Rotations", Journal of Colloid Science **6**, 354–367 (1951).

[361]F. P. Bretherton, "The motion of rigid particles in a shear flow at low Reynolds number", Journal of Fluid Mechanics **14**, 284–304 (1962).

[362]R. G. Cox, "The motion of long slender bodies in a viscous fluid. Part 2. Shear flow", Journal of Fluid Mechanics **45**, 625–657 (1971).

[363]G. Subramanian and D. L. Koch, "Inertial effects on fibre motion in simple shear flow", Journal of Fluid Mechanics **535**, 383–414 (2005).

[364]Z. Yu, N. Phan-Thien, and R. I. Tanner, "Rotation of a spheroid in a Couette flow at moderate Reynolds numbers", Physical Review E **76**, 026310 (2007).

[365]W. Mao and A. Alexeev, "Motion of spheroid particles in shear flow with inertia", Journal of Fluid Mechanics **749**, 145–166 (2014).